NOTE TO USERS

Materials and Magnetic Studies of Cobalt-Doped Anatase Titanium Dioxide and Perovskite Strontium Titanate as Potential Dilute Magnetic Semiconductors

Tiffany C. Kaspar

A dissertation submitted in partial fulfillment
of the requirements for the degree of

Doctor of Philosophy

University of Washington

2004

Program Authorized to Offer Degree:
Department of Chemical Engineering

University of Washington
Graduate School

This is to certify that I have examined this copy of a doctoral dissertation by

Tiffany C. Kaspar

and have found that it is complete and satisfactory in all respects,
and that any and all revisions required by the final
examining committee have been made.

Co-chairs of Supervisory Committee:

J.W. Rogers, Jr.

Eric M. Stuve

Reading Committee:

J.W. Rogers, Jr.

Eric M. Stuve

Scott A. Chambers

Fumio Ohuchi

May 27, 2004
Date

In presenting this dissertation in partial fulfillment of the requirements for the doctoral degree at the University of Washington, I agree that the Library shall make its copies freely available for inspection. I further agree that extensive copying of the dissertation is allowable only for scholarly purposes, consistent with "fair use" as prescribed in the U.S. Copyright Law. Requests for copying or reproduction of this dissertation may be referred to Proquest Information and Learning, 300 North Zeeb Road, Ann Arbor, MI 48106-1346, to whom the author has granted "the right to reproduce and sell (a) copies of the manuscript in microform and/or (b) printed copies of the manuscript made from microform."

Signature Tiffany C. Kasper

Date 6-10-04

University of Washington

Abstract

Materials and Magnetic Studies of Cobalt-Doped Anatase Titanium Dioxide and Perovskite Strontium Titanate as Potential Dilute Magnetic Semiconductors

Tiffany C. Kaspar

Co-chairs of Supervisory Committee:
Affiliate Professor J.W. Rogers, Jr.
Professor Eric M. Stuve
Department of Chemical Engineering

Deposition of cobalt-doped anatase TiO_2 and cobalt-doped perovskite $SrTiO_3$ (STO) utilizing molecular beam epitaxy (MBE) was investigated in an effort to achieve a dilute magnetic semiconductor (DMS) system with desirable materials and magnetic properties for application in future Si-based spintronic devices. A prospective DMS material must have a uniform dopant distribution within the semiconductor lattice without the presence of secondary phases, and the dopant must ferromagnetically order such that the semiconductor carriers are spin-polarized. Compatibility with Si requires the DMS material to be deposited under mildly oxidizing conditions to protect the Si interface from oxidation. Epitaxial anatase TiO_2 can be realized on Si utilizing an epitaxial $SrTiO_3$ buffer layer. Despite the use of the oxygen plasma during Co:TiO_2 deposition, which was confirmed to result in significant oxidation of the Si interface, the charge state of Co in the resultant film was found to be a mixture of Co(0), Co(II), and Co(III). Although no secondary phases were observed, faceted Co-enriched surface particles were present on all films. The observed room temperature ferromagnetism of the films could not be conclusively attributed to a true Co-doped anatase DMS phase. The inability to fully oxidize Co to Co(II) under

strongly oxidizing conditions and incorporate it uniformly into the anatase lattice, preclude the use of Co-doped anatase TiO_2 as a DMS material in future spintronic devices based on Si technology. Alternatively, Co-doped perovskite STO was explored. To evaluate the materials and magnetic properties of Co:STO as a potential DMS material, Co:STO films were deposited on STO(001) substrates. Smooth, epitaxial films free of surface particles or clusters were obtained; further evidence showed Co substituted as Co(II) for Ti in the STO lattice. Films doped with < 5% Co were ferromagnetic at room temperature. *F*-center mediated exchange was proposed as the mechanism of ferromagnetic ordering in these insulating films ($\rho > 5$ kΩcm). For doping concentrations > 5%, no ferromagnetic hysteresis was observed. From these results, Co:STO is a prime candidate as a ferromagnetic semiconductor for integration into future Si-based spintronic devices.

TABLE OF CONTENTS

Page

TABLE OF CONTENTS, CONTINUED

Page

LIST OF FIGURES

LIST OF FIGURES, CONTINUED

LIST OF TABLES

ACKNOWLEDGMENTS

The research contained in this dissertation was performed in the W.R. Wiley Environmental Molecular Sciences Laboratory (EMSL), a national scientific user facility sponsored by the Department of Energy's Office of Biological and Environmental Research and located at Pacific Northwest National Laboratory (PNNL) in Richland, WA. I wish to acknowledge the financial support I have received from Achievement Rewards for College Scientists, the National Science Foundation, and the UW / PNNL Joint Institute for Nanoscience.

I want to thank my advisor, Prof. Bill Rogers, for giving me the opportunity to pursue research projects in EMSL, and Dr. Scott Chambers, who has provided me with a wealth of support and knowledge. I also want to express my appreciation for the support and patience of my family and friends throughout my graduate career.

INTRODUCTION

The emerging field of *spintronics* (spin transport electronics or spin-based electronics)[1] aims to revolutionize microelectronic devices by utilizing the property of quantum mechanical spin for device operation. Current microelectronic device design employs only the charge of the electron to carry and store information. Scaling of components, such as metal-oxide-semiconductor field effect transistors (MOSFETs), has succeeded thus far in increasing packing density according to Moore's Law.[2,3] However, fundamental physical limits will be reached as soon as 2010 in the miniaturization of certain components.[4] These limits cannot be overcome with traditional technology and materials.

Many avenues are being actively explored to overcome the fundamental issues facing microelectronics in the next few years. One promising approach is to utilize electron, hole, or nuclear spin, in addition to or in place of charge, to carry and store information in spintronic devices. Proposed spintronic devices promise "nonvolatility, increased data processing speed, decreased electric power consumption, and increased integration densities compared with conventional semiconductor devices."[5] Eventually, spintronics may be the basis for quantum computation utilizing the quantum properties of superposition and entanglement.[6]

One of the many advances required to realize spin functionality in practical devices is the development of materials which can generate, maintain, and transfer spin-polarized carrier populations. For applications in near-term spintronic devices, such as FETs which incorporate spin functionality, ferromagnetic materials must be developed which can efficiently inject spin-polarized carriers into traditional semiconductor heterostructures. One promising class of materials for this purpose are dilute magnetic semiconductors (DMSs). A DMS consists of magnetic dopants incorporated into a host semiconductor material; the magnetic ordering of the

dopants results in spin polarization of the semiconductor host carriers. In practice, the semiconductor host can be a traditional III-V semiconductor such as GaAs, a transition metal oxide semiconductor such as ZnO or TiO_2, or more unconventional materials. The magnetic dopant is generally a transition metal such as Cr, Mn, Fe, or Co.

In this work, two candidate material systems were investigated for potential application as a DMS spin injector in future spintronic devices: Co-doped anatase TiO_2 and Co-doped perovskite $SrTiO_3$. Due to recent advances in the deposition of epitaxial oxide materials on Si by molecular beam epitaxy (MBE),[7] both anatase TiO_2 and $SrTiO_3$ are prime candidates for integration with this technologically relevant semiconductor. By doping these semiconducting oxide systems with small concentrations of Co, a DMS with desirable materials and magnetic properties could be integrated into existing Si semiconductor technology.

Co-doped anatase deposited on oxide substrates has received considerable attention as a room temperature ferromagnetic semiconductor. Epitaxial Co-doped anatase films were successfully deposited by MBE on single crystal Si(001) utilizing a $SrTiO_3$ buffer layer, although oxidation of the Si interface during anatase deposition could not be eliminated. The films had promising ferromagnetic properties at room temperature, with saturation magnetic moments of 2.5 - 3 μ_B/Co. Unfortunately, preferential segregation of Co to anatase surface particles, as well as the presence of mixed valence Co including Co(0), precludes the utilization of Co-doped anatase on Si as a DMS material for spintronic devices.

Co-doped $SrTiO_3$ (STO) was found to be significantly more promising as a potential DMS material. As an initial evaluation of Co:STO, epitaxial films were deposited on single crystal STO(001) substrates by MBE. Smooth films free of particles or clusters were obtained for all Co doping concentrations, and further evidence showed

that Co(II) substituted for Ti(IV) in the STO lattice with no evidence of Co(0). Co-doped STO films were found to be ferromagnetic at room temperature for doping concentrations less than approximately 5% Co. In the absence of a significant quantity of free carriers in these insulating films, *F*-center mediated exchange was proposed as the mechanism of ferromagnetic ordering. From these preliminary results, Co:STO is considered a promising candidate as a DMS material integrated with Si.

Notes to Introduction

1. D.D. Awschalom, D. Loss, and N. Samarth, ed. *Semiconductor Spintronics and Quantum Computation.* (Springer-Verlag, New York, 2002).

2. G.E. Moore, "Cramming more components onto integrated circuits." *Electronics* **38**, 114 (1965).

3. P.A. Packan, "Pushing the limits." *Science* **285** (5436), 2079 (1999).

4. B.T. Jonker, "Progress toward electrical spin injection of spin-polarized electrons into semiconductors." *Proc. IEEE* **91** (5), 727 (2003).

5. S.A. Wolf, D.D. Awschalom, R.A. Buhrman, J. Daughton, S. von Molnar, M.L. Roukes, A.Y. Chtchelkanova, and D.M. Treger, "Spintronics: a spin-based electronics vision for the future." *Science* **294**, 1488 (2001).

6. S. Das Sarma, "Spintronics." *Am. Sci.* **89** (6), 516 (2001).

7. R.A. McKee, F.J. Walker, and M.F. Chisholm, "Crystalline oxides on silicon: the first five monolayers." *Phys. Rev. Lett.* **81** (14), 3014 (1998).

CHAPTER I: BACKGROUND

Spintronics

The utilization of electron, hole, or nuclear spin in spintronic devices promises a revolution in microelectronic device functionality. Successful development of spintronic devices will require significant innovations in materials and device architecture, as well as an increased understanding of the fundamental physical properties of spin and the ordering of spins in magnetic materials.

Spin and magnetism[1]

In order to understand the properties and applications of spintronic materials, it is necessary to understand some fundamentals of magnetism and magnetic materials. The macroscopic results of magnetism, described by classical physics, can be represented by two model systems: a bar magnet and a circulating electrical current. A bar magnet, shown in Figure 1.1(a), has its magnetic orientation along its axis. This results in a magnetic pole at either end of the magnet, labeled north (N) and south (S). Each magnetic pole creates a magnetic field, ***H***, which acts on the other pole. By convention, the source of the magnetic field is the north pole and the sink is the south pole, so field lines of the magnetic field around the magnet can be represented as emanating from the north pole and flowing to the south pole. If an electrical current flows through a coiled wire, as illustrated in Figure 1.1(b), a

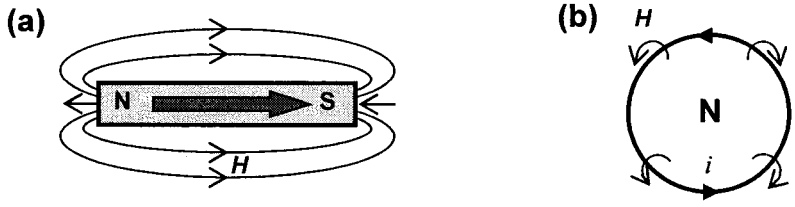

Figure 1.1. (a) Bar magnet. Large arrow indicates orientation of magnetization in bar material. Lines represent magnetic field (***H***) originating from the north pole (N) and flowing to the south pole (S). (b) Coil of wire with current (*i*) flowing counterclockwise. Magnetic field (***H***) is produced by circulating current; center of coil is analogous to north pole (N) of bar magnet.

magnetic field results that is identical to the pole of a bar magnet. This illustrates the fundamental origin of magnetism: magnetic fields are produced by the movement of electric charge. In the case of a circulating current in a wire, the bulk movement of negative electrons as the flowing current produces the magnetic field. In a bar magnet, the magnetic field is generated by the movement of electrons orbiting the atomic nuclei in the material.

When a bar magnet is placed at an angle to an external magnetic field ($\boldsymbol{H}$), each pole feels a force, proportional to $\boldsymbol{H}$, to align with the field. The combined force on each pole results in a moment, $\boldsymbol{m}$, exerted around the center of mass of the bar to rotate into alignment with the field. Similarly, a coiled wire with a current flow feels a moment whose magnitude is the product of the current and the area enclosed by the wire. In the limit of a small bar magnet or coiled wire encompassing a small area, the magnetic moment becomes a magnetic dipole. The energy of a magnetic dipole placed in an external magnetic field is $-\boldsymbol{m}\cdot\boldsymbol{H}$.

When a material is placed in an external magnetic field ($\boldsymbol{H}$), a magnetic response is induced in the material. This magnetic induction, $\boldsymbol{B}$, is a combination of the external magnetic field and the magnetization of the material, $\boldsymbol{M}$. The magnitude of M is a material property dependent on the magnetic moments of the constituent atoms and their interaction. The ratio of $\boldsymbol{M}$ to $\boldsymbol{H}$ is the susceptibility of the material, χ, which describes the magnitude of the magnetization of the material in an applied field. A material with a large susceptibility experiences a large induced magnetization in the presence of a small applied magnetic field. The permeability, μ, is defined as the ratio of $\boldsymbol{B}$ to $\boldsymbol{H}$ and is related to the susceptibility by $\mu = 1 + 4\pi\chi$ (in cgs units).

The macroscopic magnetization of a material is a consequence of the magnetic properties of the constituent atoms. Specifically, the movement of the electrons in a material's atoms, ions, or molecules gives rise to the magnetic properties of the

material. Although atomic nuclei also have a magnetic moment, their moments are approximately three orders of magnitude smaller than those exhibited by electrons and thus can be neglected. To understand the atomic origins of magnetism, it is necessary to move from classical physics to quantum mechanics. The solution of the Schrödinger equation for an atom reveals the quantization of the allowed energy of its electrons. This quantization is represented by three fundamental quantum numbers. The principle quantum number, n, determines the energy of the electron shell. The orbital quantum number, l, represents the orbital angular momentum of the electrons in shell n. l can take values from 0 to n-1, and the values $l = 0, 1, 2, 3$ correspond to atomic orbitals s, p, d, and f. Analogous to the magnetic field generated by an electrical current in a coiled wire, the orbital angular momentum of an electron around the atomic nucleus results in an orbital magnetic dipole moment. The s orbital, with $l = 0$, has no net orbital angular momentum and thus no magnetic dipole, and the magnitude of the orbital magnetic moment increases with increasing values of l. The magnetic quantum number, m_l, determines the orientation of the orbital angular momentum relative to an applied magnetic field. The magnetic quantum number can take values from $-l$ to $+l$; therefore, for the p orbital with $l = 1$, m_l has three values (-1, 0, +1) and thus there are three orientations of the orbital angular momentum vector in relation to the external field. Due to this quantization, the orbital momentum vector, and thus the orbital magnetic moment, can never point in exactly the same direction as the external magnetic field, and instead precesses in a cone around the field direction. The component of the orbital angular momentum perpendicular to the applied field averages to zero. The quantization and precession of the orbital angular momentum is illustrated in Figure 1.2(a) for a p orbital. In the absence of an external magnetic field, the possible orientations of the orbital angular momentum are equal in energy. However, in the presence of an external magnetic field the orbital energies are split according to their orientation relative to the field. This is known as the normal Zeeman effect and is observed in the atomic absorption spectrum of a material in an applied field as splitting of the lines involving $l > 0$

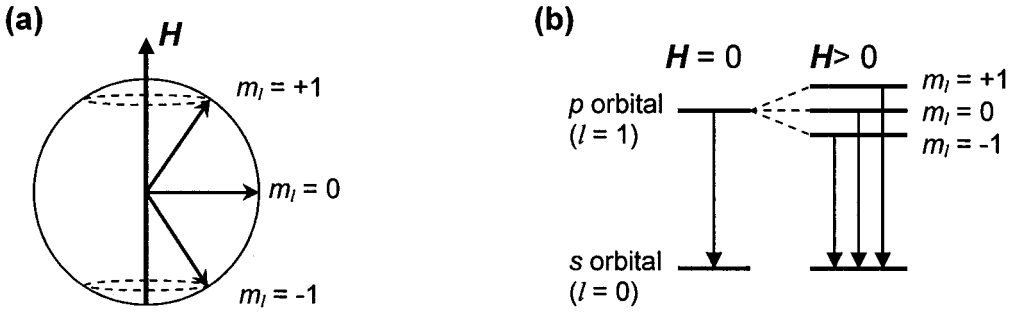

Figure 1.2. (a) Representation of the three possible orbital angular momentum vectors relative to an external magnetic field for a *p* orbital ($l = 1$). The orbital magnetic moment of $m_l = 0$ is zero. The orbital magnetic moments of $m_l = -1$ and $m_l = +1$ can never point in exactly the same direction as ***H***; instead they precess in a cone around ***H***. (b) Zeeman splitting of the *p* orbital in an external magnetic field. When the magnetic field is applied, the single *p*-*s* transition is split into a triplet.

transitions, as shown schematically in Figure 1.2(b).

Although only three quantum numbers arise from solution of the Schrödinger equation (n, l, and m_l), two additional quantum numbers are required to fully specify the state of an electron in an atom. The spin quantum number, s, describes the angular momentum of the spin of the electron around its own axis (analogous to l for orbital angular momentum). Unlike l, which can take several values, the value of s for electrons is always ½. Analogous to m_l, the spin magnetic quantum number, m_s, determines the orientation of the spin angular momentum and can have the values +½ and -½, often referred to as "spin up" and "spin down." The spin angular momentum cannot point exactly in the direction of an applied field, and instead precesses in a cone around the field. The spin magnetic quantum number plays an important role in determining how atomic orbitals are filled. One consequence of the Pauli exclusion principle is that no two electrons in an atom can have the same values for all the quantum numbers. Thus, two electrons can occupy each atomic orbital, with the same values of n, l, and m_l, but they must have opposite values of spin (m_s must be +½ for one and –½ for the other). In addition, Hund's first rule states that the lowest energy state of electrons in a given shell is that which maximizes the total spin, S, without violating the Pauli exclusion principle. For example, there are three *p*

orbitals of equivalent energy (for a free atom in the absence of an external magnetic field) so in the lowest energy state a single electron will fill each orbital with all spins parallel; the total spin S is then the maximum value of ½ + ½ + ½ = 3/2. A fourth electron will be forced to pair up with one of the three, and by the Pauli exclusion principle will have opposite spin. This reduces the total spin to (½ - ½) + ½ + ½ = 1.

Both the orbital and spin angular momenta produce magnetic moments. The orbital magnetic moment is given by:

$$\boldsymbol{m} = -\mu_B m_l \qquad (1.1)$$

where $\boldsymbol{m}$ is the magnetic moment vector, μ_B is the Bohr magneton (the elementary unit of orbital magnetic moment in an atom, defined as $e\hbar/2m_ec$ in cgs units), and m_l is the orbital magnetic quantum number. Since m_l always takes integer values, the orbital moment will be an integer number of Bohr magnetons. The spin magnetic moment is given by a similar expression:

$$\boldsymbol{m} = -g_e\mu_B m_s \qquad (1.2)$$

where g_e is referred to as the g-factor of the electron. For a single electron, g_e = 2.002319 (which can be approximated as $g_e = 2$) such that the spin magnetic moment of a single electron is one Bohr magneton. Due to the negative charge of the electron, the spin and spin magnetic moment point in opposite directions.

Spin-orbit coupling occurs when the orbital magnetic moment of an electron orbiting the atomic nucleus produces a magnetic field that interacts with its spin magnetic moment. The magnitude of the spin-orbit coupling depends on the charge of the atomic nucleus. Similarly, orbit-orbit and spin-spin interactions can occur between electrons in the atom.

For all but the heaviest atoms, Russell-Saunders coupling describes the total angular momentum of the atom. Completely filled shells have no net angular momentum and thus do not contribute to the overall magnetic moment of the atom. Therefore only

the incomplete outer shells need to be considered in the calculation. Vector addition of the orbital momenta determines the total orbital angular momentum (L), and similar vector addition of the spin momenta determines the total spin angular momentum (S). The total orbital and spin momenta are then combined by vector addition to calculate the total angular momentum of the atom (J). From the total angular momentum of the atom, the total magnetic moment can be determined as:

$$\boldsymbol{m} = -g\mu_B M_J \tag{1.3}$$

where M_J is the magnetic quantum number representing the projection of the total angular momentum onto the magnetic field axis and can have values of $-J$ to $+J$, and g is the Landé g-factor. Because the spin moment of an electron has a g-factor of 2 (see Equation 1.2), while the orbital moment has a g-factor of 1, the total moment of the atom depends not just on the total angular momentum, J, but also on L and S. This is reflected in the Landé g-factor, which is a function of L, S, and J. If the total spin angular momentum is zero ($S = 0$), then $J = L$ and the Landé g-factor is 1 for all values of L. Since the total magnetic moment does not depend on L, the magnetic moment and thus the Zeeman splitting of all electron energy levels is equal, and the normal Zeeman effect is observed as discussed above (see Figure 1.2(b)). However, for $S \neq 0$, the Landé g-factor takes a different value for each level, which results in a different magnitude of Zeeman splitting for each level. This is referred to as the anomalous Zeeman effect and produces a complex set of transitions in the atomic absorption spectrum.

The orbital and spin magnetic moments of electrons in an atom lead to three general classes of magnetic behavior in bulk materials: diamagnetism, paramagnetism, and ferromagnetism. Diamagnetism occurs weakly in all atoms; however, it is only readily observed in atoms with filled shells, in which no stronger magnetic properties obscure the effect. Diamagnetic materials have a negative susceptibility, meaning their internal magnetization decreases as the applied magnetic field increases. The applied field induces electromagnetic currents, and thus magnetic dipole moments, in

the material that oppose the applied field. Even in nonmagnetic atoms (in which the magnetic dipole moments cancel), the individual magnetic moments still change to oppose the applied field, resulting in a diamagnetic effect.

Paramagnetism occurs in materials in which the atoms have net magnetic moments, but the moments of individual atoms are weakly coupled. In the absence of an applied field, thermal energy overcomes the weak coupling between moments, resulting in a random alignment of moments and no net magnetization for the material. When a moderately strong magnetic field is applied, the moments shift slightly to align with the field, but only a small fraction are able to point in the field direction. To overcome thermal disorder and fully align the magnetic moments with the applied field, very large magnetic fields or very low temperatures (near absolute zero) are necessary. However, upon cooling many paramagnets undergo a spontaneous phase transition, at a characteristic Curie temperature, to become ferromagnets.

In ferromagnetic materials, the magnetic coupling overcomes thermal disorder and the magnetic moments align. This magnetic ordering occurs even in the absence of an applied magnetic field, leading to the characteristic magnetic hysteresis behavior of ferromagnets (Figure 1.3(a)). Although Fe, Co, and Ni are the only transition metal elements that are ferromagnetic at room temperature, there are a wide variety of oxides, alloys, and other compounds that exhibit ferromagnetism. In the quantum mechanics solution of the many-body Hamiltonian, the magnetic coupling between neighboring atoms emerges as an energy term referred to as the exchange interaction. The exchange interaction is of electrostatic, not magnetic, origin, and is a consequence of the Pauli exclusion principle. If two electrons have antiparallel spins, they can occupy the same atomic or molecular orbital. This means they will overlap spatially, increasing the (unfavorable) Coulomb repulsion between them. However, if the electrons have parallel spin, they must occupy different orbitals,

which reduces the overall Coulomb repulsion. Thus the exchange energy of the system is minimized if all the electrons have the same spin. Minimization of the exchange energy by aligning electron spins is opposed by the energy required to promote the electrons to higher electronic levels such that they are unpaired and can reverse their spin. In simple metals such as K and Ca, the energy required to promote a valence 4*s* electron to a higher level is greater than the gain of exchange energy minimization, so these metals are not ferromagnetic. In the first row transition metals Sc through Mn, the 4*s* and 3*d* densities of states overlap, creating lower-lying states for electrons to reverse their spin, but the energy balance is such that ferromagnetism is not observed. Mn and Cr are antiferromagnetic, meaning each atomic row is magnetically aligned antiparallel to the neighboring rows. Although the material is magnetically ordered, the magnetic dipoles cancel out and bulk ferromagnetic behavior is not observed. For Fe, Co, and Ni, the overlap of the 3*d* and 4*s* bands, and the large density of states of the 3*d* band at the Fermi level, provides many low-lying states to allow electrons to reverse their spin, so the exchange effect dominates, resulting in ferromagnetism. For the later transition metals Cu and Zn, the Fermi level lies above the 3*d* band, eliminating the density of states at the Fermi level required for electrons to reverse their spin and thus preventing the exchange interaction.

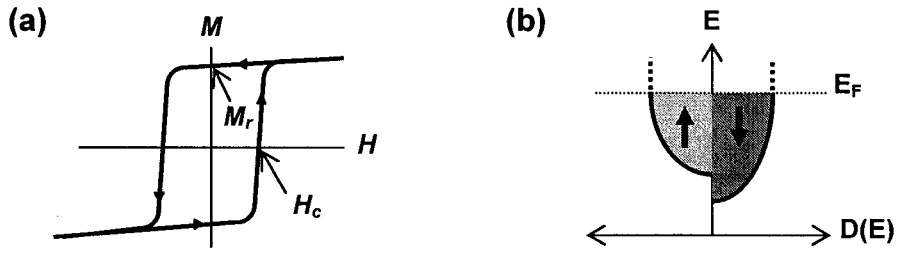

Figure 1.3. (a) Sketch of a ferromagnetic hysteresis loop, showing the material's magnetization, ***M***, versus the applied magnetic field, ***H***. At zero applied field, the material retains it's magnetic alignment; M_r is the magnetic remanence. A coercive applied field, H_c, is required to bring the magnetization to zero. (b) Sketch of the density of states (D) near the Fermi level (E_F) for a ferromagnetic material. The exchange interaction shifts the densities of states for spin-up and spin-down electrons relative to each other, resulting in permanent spin polarization and magnetic alignment. For the first row transition metals, the density of states at the Fermi level is an overlap of the 3*d* and 4*s* states.

A simplified sketch of the density of states of a ferromagnetic material is given in Figure 1.3(b). The effect of the exchange interaction on ferromagnetic materials is a shift of the energy of the spin-up and spin-down densities of states relative to each other. (This shift also occurs for paramagnets when placed in a magnetic field.) The unequal number of electrons in one spin state relative to the other results in permanent spin polarization and ferromagnetic alignment. Spin polarization is conventionally defined as[2]

$$P_{spin} = (n\uparrow - n\downarrow) / (n\uparrow + n\downarrow) \qquad (1.4)$$

where P_{spin} is the spin polarization (usually reported as a percentage), and $n\uparrow$ and $n\downarrow$ are the electron populations of the spin-up and spin-down densities of states. For ferromagnetic metals, the spin polarization is typically ~50%.[2] The distribution of electrons in the spin-up and spin-down densities of states also determines the magnetic moment per atom.

GMR spin valve

In 1988 the modern field of spintronics was born[3] when the first report of giant magnetoresistance (GMR), a spintronic effect that combines the properties of electron spin and charge, was published.[4] Within 10 years, magnetic read heads for computer hard disk drives based on GMR were introduced which revolutionized the hard drive industry. Simply incorporating GMR read heads increased the storage on a hard drive from 1 to 20 Gbit,[5] and further improvements have allowed miniature high-density hard disks for applications such as laptop computers. GMR magnetic read heads now dominate the hard drive industry.[3]

Magnetoresistance refers to the change in electrical resistance of a material in the presence of a magnetic field. Giant magnetoresistance is best illustrated by a spin valve, as shown in Figure 1.4(a). A spin valve consists of two ferromagnetic conducting layers sandwiching a nonmagnetic conducting layer. Assume for

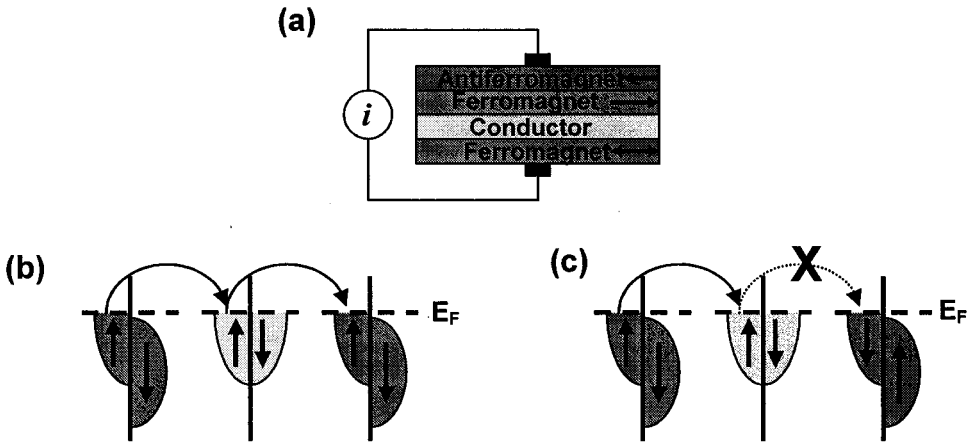

Figure 1.4. (a) GMR spin valve consisting of a conducting metal layer sandwiched between two ferromagnetic metal layers. (b) Sketch of density of states for 100% polarized ferromagnetic layers when the magnetization orientation is parallel. Spin up electrons from the top ferromagnetic layer can flow through the conductor and into the bottom layer with low resistance. (c) Sketch of same density of states if the magnetization orientation is antiparallel. There are no density of states to accommodate spin up electrons in the bottom layer. The electrons are scattered, creating a high resistance state. Modified from [5].

simplicity that the spin polarization of both ferromagnetic layers is 100% (all conduction electrons in the layer have the same spin orientation). Current injected from the top layer into the conducting layer will be also be 100% spin-polarized. If the two ferromagnetic layers have a parallel magnetization direction, their conduction electrons will have the same spin orientation and efficient electron transport to the bottom layer can occur, as illustrated in Figure 1.4(b). This is the low resistance state. If the magnetization orientation of one ferromagnetic layer is switched by 180°, the spin-polarized conduction electrons entering the bottom layer will have the opposite spin direction of electrons in the layer. As shown in Figure 1.4(c), for 100% polarized material there is no density of states at the Fermi level that can accommodate these electrons. They are scattered, reducing the overall conduction. This is the high resistance state, and the dependence of the electrical resistance on magnetization is the phenomena of magnetoresistance.

In a GMR spin valve such as those employed in magnetic hard drive read heads, the ferromagnetic layers are constructed from metallic alloys of Fe, Co, and Ni, with a

spin polarization of about 40%,[6] and the nonmagnetic layer is a highly conducting nonmagnetic metal such as Cu. The "hard" ferromagnetic layer has its magnetization direction pinned by coupling to an antiferromagnetic layer, making its magnetization direction difficult to change. The "soft" layer is free, and its magnetization direction is relatively easy to change. Resistance changes of 5-10% between parallel and antiparallel magnetic orientation in these devices are typical,[3] although improvements such as incorporating a nano-oxide layer on the outside surface of the soft magnetic layer, which lowers the background resistance due to surface scattering,[3] can increase the change in resistance to 20%.[7] As the GMR read head passes over the magnetic bits on the hard disk, the change in the orientation of a bit from its neighbor changes the magnetization of the soft layer of the read head. This results in a change in the resistance of the spin valve, and by monitoring this change in resistance the hard disk can be read.

Another application of GMR that is expected to produce significant commercial success within the next few years is magnetic random access memory (MRAM). MRAM would likely be based on a grid of magnetic tunnel junctions. A magnetic tunnel junction (MTJ) is a variation of the GMR spin valve in which the nonmagnetic conductor of the spin valve is replaced with a very thin insulating layer, commonly Al_2O_3, that acts as a tunnel barrier.[3] Data would be stored by magnetic hysteresis as the magnetic orientation of the soft layer of the tunnel junction, and read by the magnetoresistance change in the junction.[3] MRAM is expected to offer the advantage of nonvolatile memory storage, in which the information is not lost when the power is turned off, but unlike current nonvolatile memory technologies such as electrically erasable programmable read-only memory (EEPROM) and flash memory,[3] the switching rates and rewritability cycles will be comparable to conventional dynamic random access memory (DRAM).[8] While MRAM is not yet available commercially, Motorola recently announced[9] the production of 4 Mbit MRAM for evaluation purposes.

Spin-FET

The considerable technological and commercial success of magnetic sensors utilizing GMR has opened the door for a wide array of other spintronic devices. For the microelectronics industry, it is highly desirable to integrate spintronics devices into existing semiconductor technology. As a near-term goal, adding spin functionality to existing device architecture could lead to significant improvements in device speed and power consumption. In 1990, Datta and Das[10] proposed a spin-based field effect transistor (spin-FET). To fully understand the operation of the spin-FET, it is instructive to first look at a conventional metal-oxide-semiconductor field effect transistor (MOSFET).

A schematic of a typical MOSFET is shown in Figure 1.5. The source and drain are highly *n*-type doped regions of the bulk *p*-type silicon substrate. The gate is formed from a metal contact and dielectric oxide. When positive voltage is applied to the gate contact, the positive charge at the oxide interface with Si repels holes and attracts electrons from the Si bulk, creating a two-dimensional inversion layer at the Si surface that is highly *n*-type doped. This highly doped region allows carriers to flow from the source to the drain. When the gate voltage is removed, the inversion layer disappears and no current can flow. Thus current flow through the transistor is

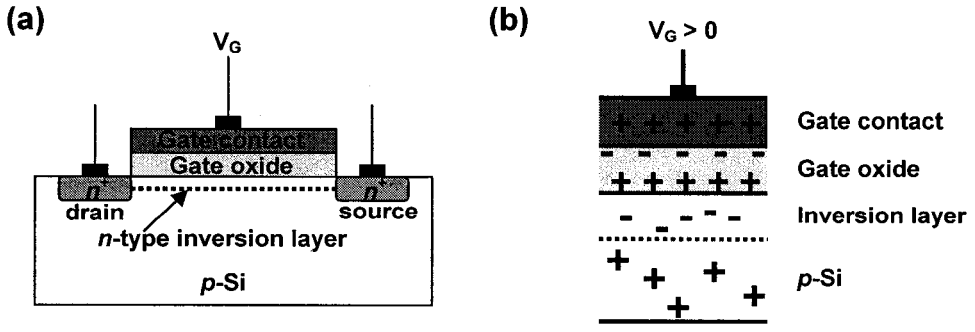

Figure 1.5. (a) Geometry of MOSFET device. The *n*-type inversion layer is only present when a voltage is applied to the gate contact. (b) Illustration of charge distribution in the gate and Si when a positive voltage is applied to the gate contact.

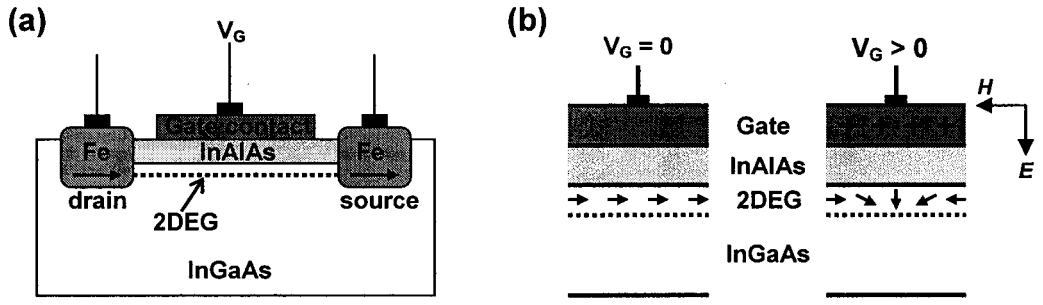

Figure 1.6. (a) Geometry of spin-FET device. The high mobility two-dimensional electron gas (2DEG) region at the InGaAs surface allows current to flow from the ferromagnetic source to drain. (b) Illustration of electron spin direction with and without applied gate voltage. When no voltage is applied, no spin precession occurs and electrons can enter the drain (left). When a positive voltage is applied, the resultant magnetic field causes the spins to precess until they are antiparallel to the drain; electrons are scattered and cannot enter the drain (right).

turned on or off by the application of a relatively small gate voltage.

A spin-FET would perform the same transistor function as a conventional MOSFET with a similar geometry, but the principle of operation would be significantly different.[2,8,11] A sketch of the spin-FET device proposed by Datta and Das based on an InGaAs substrate is given in Figure 1.6. The highly doped semiconductor source and drain of the MOSFET have been replaced with ferromagnetic materials (Fe for the Datta and Das structure). A permanent "inversion layer," or two-dimensional electron gas (2DEG), is created by replacing the gate oxide with a thin layer of InAlAs. Without a voltage applied to the gate, current can flow from the ferromagnetic source. This current will have the same spin polarization as the source, and can flow into the drain if the drain has the same magnetization direction as the source. This is analogous to the low resistance state of the GMR spin valve. If a voltage is applied to the gate, an electric field is set up in the 2DEG. Because InGaAs has a large spin-orbit interaction, meaning the external magnetic field generated by the electric field has a large effect on electron spin[11] (known as the Rashba interaction[12]), the spin-polarized electrons will tend to precess in the direction of the magnetic field. The strength of the electric field applied to the gate determines the amount of precession of the spin-polarized current. If the spin is rotated 180°, the

electrons will have spin antiparallel to the drain and will be scattered, similar to the high resistance state of the GMR spin valve. Analogous to a MOSFET, the current flow through the transistor is controlled by the applied gate voltage. A spin-FET would have several advantages over a conventional MOSFET, such as significantly reduced electric fields required to control current flow and much faster switching speeds.[8] In addition, the spin-FET could be "reprogrammed" by changing the magnetization direction of the source or drain such that they were antiparallel. In this configuration, spin-polarized current could not flow into the drain *unless* a voltage was applied to the gate to rotate the spin direction. Despite its relative simplicity, to date there has been no experimental demonstration of a spin-FET device.[11]

Challenges

The proposed spin-FET illustrates the challenges facing semiconductor spintronics. The primary challenges can be subdivided into four categories:[2]

- injection of spin-polarized carriers into the host semiconductor
- transport of the carriers through the semiconductor
- manipulation of spin polarization for device functionality
- detection of spin polarization

The last three points will be discussed first. In the transport of spin-polarized carriers through a nonmagnetic semiconductor, spin lifetime and spin diffusion length must be considered. In studies of bulk GaAs with spin-polarized carriers generated by optical pumping, both the spin lifetime and spin diffusion length of electrons have been found to be promising for spintronic devices, with spin lifetimes greater than 100 ns and diffusion lengths of several microns at low temperature.[2,13-15] In quantum dots and heterostructures, nanosecond-scale lifetimes persist to room temperature.[3] While studies of optically pumped semiconductors provide important fundamental information on spin behavior, the behavior of electrically injected spin-polarized electrons in a 2DEG is more technologically relevant. Hammar *et al.*[16] have found a

spin diffusion length of at least 4.6 μm and spin lifetime of at least 3.8 ps for spin-polarized electrons injected from ferromagnetic electrodes into a high-mobility InAs 2DEG at low temperature. Spin-polarized holes have been found to have very short spin lifetimes due to valence band mixing[13] and thus are not promising for application in spintronic devices.

Successful spintronic devices developed thus far, such as GMR spin valves and magnetic tunnel junctions, are passive devices in which the spin polarization of the electron current is not altered before detection; instead, the polarization of the current is passively read by the detector. In an active device such as a spin-FET, the spin polarization of the carriers will be altered to produce the desired device functionality. It has been shown experimentally that the spin orientation of spin-polarized carriers can be altered by an external magnetic field through the Rashba spin-orbit interaction.[2,17]

Detection of spin-polarized carriers in semiconductor spintronic devices would use spin selectivity[3] similar to the magnetoresistance employed in GMR spin valves. The interface between a nonmagnetic semiconductor and ferromagnetic material is spin-selective, and only electrons with the same spin orientation as the magnetic material are allowed to cross the interface without scattering. However, all the issues arising in spin injection into semiconductors, discussed next, also apply to spin-polarized electrons crossing the interface in the other direction for spin detection.

The most difficult challenge thus far has been the efficient injection of spin-polarized carriers from a ferromagnetic material into a semiconductor. The original spin-FET proposal by Datta and Das featured ferromagnetic Fe as the source and drain electrodes. Ferromagnetic metals, which have Curie temperatures well above room temperature, are an appealing source of spin-polarized carriers. However, subsequent work on injection of spin-polarized electrons from ferromagnetic metals

into semiconductors has found that the spin injection efficiency is very poor, on the order of 0.1 – 1%, due to the conductivity mismatch between the metal and semiconductor.[18,19] Forming a tunnel barrier between the metal and semiconductor can alleviate the conductivity mismatch problem,[19] and several tunnel barrier schemes have been investigated. Since Al_2O_3 has been successfully implemented in all-metal magnetic tunnel junctions, adding a thin layer of Al_2O_3 at the interface of the metal and semiconductor has been explored, with a resultant improved spin polarization efficiency of 9%.[20] Another approach is to utilize the Schottky barrier that forms naturally at the ferromagnetic metal / semiconductor interface. With appropriate doping profiles to narrow the depletion width in the semiconductor, a sharp tunnel barrier can be formed. Injected spin polarization as high as 30% has been realized by this structure.[21]

Another significant issue in the injection of spin-polarized carriers is the interface between the ferromagnetic material and the semiconductor. Even at high-quality heteroepitaxial interfaces, a significant density of defects (such as stacking faults) are present. Stroud *et al.*[22] have experimentally observed a reduction in spin injection polarization correlated to an increase in stacking faults at the ferromagnetic semiconductor / GaAs interface, and theoretical calculations showed a high probability of spin-flip scattering at interfacial defects. In general, spin-flip scattering at the interface between the ferromagnetic material and the semiconductor may play a significant role in spin-polarized injection.

An alternative approach to improve the spin injection efficiency is to explore other ferromagnetic materials whose conductivity more closely matches the host semiconductor. Dilute magnetic semiconductors (DMSs) have received considerable attention as an alternative electrode material. A DMS is a host nonmagnetic semiconductor with a small amount of magnetic impurity dopant, such that the carriers of the semiconductor become spin-polarized. A DMS with conductivity

tuned to the host semiconductor could realize efficient spin-polarized injection for spin-FET and other applications.

Dilute Magnetic Semiconductors (DMSs)

History

Due to the issues with conductivity mismatch between ferromagnetic metals and nonmagnetic semiconductors, an obvious choice for a replacement magnetic material in semiconductor spintronic devices would be a ferromagnetic semiconductor. The first ferromagnetic semiconductor, $CrBr_3$, was synthesized in 1960.[23] Ferromagnetic semiconductors such as EuO, europium chalcogenides (such as EuS and EuSe), and chalcogenide spinels (such as $CdCr_2Se_4$) were extensively studied in the 1960's and 1970's and found to exhibit ferromagnetic properties including magnetic hysteresis and spin-polarized carrier populations.[2] However, interest waned due to low Curie temperatures and difficulty in preparing both single crystals and thin films integrated with semiconductor device materials.[2,24] Recent work on the ferromagnetic semiconductor $CdCr_2Se_4$ has demonstrated epitaxial growth on GaAs and GaP, although spin injection across the heterojunction has not been demonstrated.[2] Ferromagnetic semiconductors such as $(La,Sr)MnO_3$ are also finding new application as colossal-magnetoresistance (CMR) materials, in which the magnetoresistance is several orders of magnitude greater than that observed in multilayered GMR films.[23]

In the 1980's another class of magnetic semiconductor received significant attention. Dilute (or diluted) magnetic semiconductors (DMSs) are materials in which a magnetic element such as a transition metal or rare earth is alloyed in small quantities (usually less than 20 atomic %) in a nonmagnetic semiconductor lattice. The first promising DMS materials were II-VI semiconductors, such as ZnSe, CdTe, and

HgTe, doped with Mn.[25] These materials were extensively studied as bulk single crystals. Epitaxial thin films, superlattices, and heterostructures grown by nonequilibrium techniques such as molecular beam epitaxy (MBE) allowed the study of compositions and crystal structures not accessible in bulk form. While study of these materials provided deep scientific insights into magnetism in DMSs, the doped II-VI materials themselves exhibited only paramagnetic or antiferromagnetic behavior; ferromagnetic behavior was never observed.[24]

Recent progress

In 1989 the first DMS based on a III-V semiconductor, Mn-doped InAs, was reported by Munekata *et al.*[26] When deposited by MBE at 200°C, phase-pure *n*-$In_{1-x}Mn_xAs$ ($x \leq 0.18$) exhibited paramagnetic behavior; deposition at higher temperature resulted in phase-segregated MnAs clusters. In *p*-type $In_{0.987}Mn_{0.013}As$, partial ferromagnetic ordering was observed below a Curie temperature of 7 K. The discovery of ferromagnetic DMS behavior in InMnAs opened the possibility of developing DMS materials which could be incorporated into existing III-V semiconductor technology. In 1996, H. Ohno *et al.*[27,28] reported ferromagnetic DMS behavior in *p*-type Mn-doped GaAs, with a Curie temperature as high as 60 K. Since this discovery, significant effort has been directed towards developing a DMS based on a technologically relevant host lattice, such as GaAs, and exhibiting a Curie temperature at or above room temperature. For conventionally doped GaMnAs, the highest Curie temperature reported to date is 140-150 K.[29,30] By δ-doping 0.3 ML Mn between GaAs layers, a DMS with a Curie temperature of 172 K was obtained by Nazmul *et al.*[31] Y. Ohno *et al.*[32] demonstrated electrical spin injection from GaMnAs into an InGaAs quantum well in a light-emitting diode (LED) configuration, in which the spin polarization of the injected holes was inferred from polarization of the emitted electroluminescence. Below the GaMnAs Curie temperature of 40-90 K, spin-polarized injection of holes was achieved in the absence of an external magnetic

field. Despite the impractical Curie temperature of the material in this study, the feasibility of utilizing a ferromagnetic DMS for spin injection into a semiconductor was successfully demonstrated.

The desire for a ferromagnetic DMS material with a Curie temperature well above room temperature, combined with improved nonequilibrium growth techniques such as MBE and pulsed laser deposition (PLD), has resulted in the investigation of possible DMS behavior in a wide variety of materials. Applying the Zener model of magnetism, Dietl *et al.*[33] calculated the theoretical Curie temperature for several Group V, III-V, and II-VI materials, as well as semiconducting ZnO, assuming a Mn doping of 5% and a carrier concentration of 3.5×10^{20} holes/cm^3. Mn-doped GaN and Mn-doped ZnO were the only materials predicted to have a Curie temperature above 300 K. Although attempts to fabricate bulk microcrystallites of Mn-doped GaN resulted in paramagnetic behavior, thin films fabricated by post-growth dopant diffusion into chemical vapor deposited GaN[34] or deposition of Mn-doped GaN by MBE[35] produced ferromagnetism at room temperature. However, these results have been called into question due to the possibility of ferromagnetic and/or ferrimagnetic secondary phases such as Mn_3GaN and Mn_xN_y. If undetected, the magnetic response of these phases could be inappropriately attributed to $Ga_{1-x}Mn_xN$.[36] Room-temperature ferromagnetism has also been observed recently in Mn-doped GaP.[37]

Initial results on Mn-doped ZnO were not promising. Thin film material exhibiting non-ferromagnetic[38] or ferromagnetic behavior with a low Curie temperature (45 K)[39] was obtained, with a Mn doping concentration of approximately 30 at.% for both studies. Recently, room temperature ferromagnetism has been reported by Sharma *et al.*[40] for < 0.4 at.% Mn-doped ZnO bulk crystals and thin films deposited by PLD. Low-temperature processing was found to be critical for maintenance of the ferromagnetic properties. It was speculated that high temperature annealing (above 700°C) resulted in the formation of Mn clusters, which are antiferromagnetic and will

suppress the ferromagnetic ordering in the material.

Dietl *et al.*'s prediction of ferromagnetism in the oxide semiconductor ZnO led to the investigation of ferromagnetic DMS behavior in other oxide semiconductors. Prompted by theoretical calculations predicting ferromagnetism in *n*-type ZnO doped with Fe, Co, or Ni,[41] ZnO thin films doped with Co, Mn, Cr, or Ni were deposited by PLD, and *n*-type Co-doped ZnO was found to be ferromagnetic near room temperature.[42] Doping with Cr, Ni, or Mn did not result in ferromagnetism. Using a combinatorial approach with laser MBE, Matsumoto *et al.*[43,44] doped both the rutile and anatase phases of *n*-TiO_2 with each of the 3*d* transition metals to screen for room temperature ferromagnetism. Anatase TiO_2 doped with Co was found to be ferromagnetic at room temperature, and will be discussed in more detail in the following section. The success of Co-doped anatase TiO_2 has led to further investigations of doped TiO_2; recently room temperature ferromagnetism has been reported in Co-doped rutile TiO_2,[45-47] Cr-doped anatase TiO_2,[48] and Fe-, Ni-, and V-doped anatase TiO_2.[49,50]

In addition to investigating various transition metal dopants in the III-V, III-nitride, and oxide semiconductors discussed above, room temperature ferromagnetism is being explored in more unconventional materials. Some examples include Co,Mn-codoped Ge,[51] II-VI materials such as Cr-doped ZnTe,[52] half-metallic ferromagnetic oxides such as CrO_2 and Fe_3O_4 (magnetite) whose band structures exhibit 100% spin polarization,[6] and Heusler alloys (X_2YZ or XYZ in which X and Y are transition metals, and Z is a Group III, IV, or V element), many of which are ferromagnetic half-metals.[53]

The development of a feasible semiconductor spintronic material is still a very active research area. All the materials investigated thus far have significant potential; however, they each have drawbacks both fundamental and practical that have

prevented the demonstration of a successful spintronic device thus far. A deeper understanding of the fundamental mechanisms governing the magnetic properties of DMS materials is one necessary step to developing the materials for practical spintronic devices.

Theory of magnetism in DMS materials

The specific mechanism of magnetism in DMS materials is still under vigorous debate. To understand the general features of magnetism in DMSs, and appreciate the complexity of the problem, it is necessary to first look at some variations on the exchange interaction discussed above for ferromagnetic materials. The most easily understood exchange interaction is direct exchange, illustrated in Figure 1.7(a). In direct exchange, there is a direct Coulomb interaction of electrons from the two magnetic ions, resulting in magnetic ordering (either ferromagnetic or antiferromagnetic). If the magnetic ions are separated by non-magnetic ions, as may occur in a periodic crystal lattice, the electrons from the two magnetic ions do not overlap, preventing direct exchange. Magnetic ordering can still occur, however, if

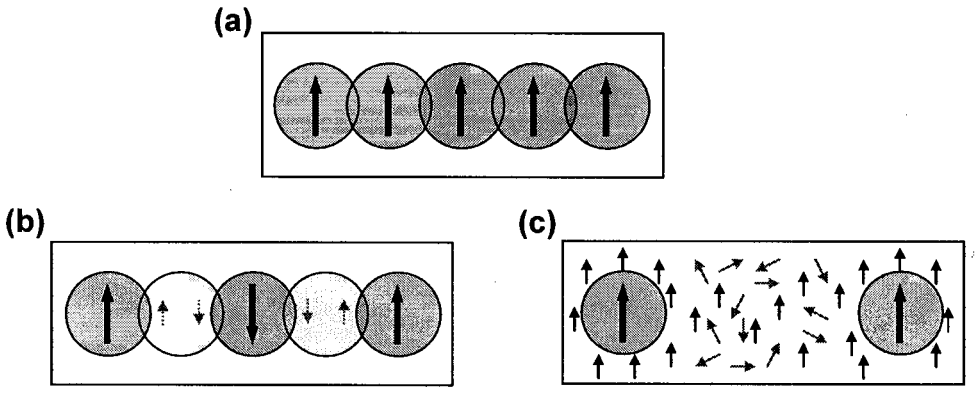

Figure 1.7. (a) Direct exchange interaction from overlap of valence orbitals of magnetic atoms, resulting in ferromagnetic behavior. (b) Superexchange interaction of non-overlapping spin-polarized valence orbitals mediated by filled orbital on the non-magnetic atom between them, resulting in antiferromagnetism. (c) RKKY-type carrier mediated interaction of two isolated magnetic atoms through their exchange interactions with free carriers. For clarity, the spin-polarized carriers are shown in black and the non-polarized carriers in gray; the magnitude of the magnetic moment of both types of carriers is the same.

the electrons from the magnetic ions couple to the non-magnetic ion in a mechanism known as superexchange (Figure 1.7(b)). Superexchange across a non-magnetic (closed-shell) ion can occur due to fluctuations in the transfer of electrons between the ions. Assuming it is energetically favorable for some degree of covalent bonding between the ions, there is some probability that the non-magnetic ion will temporarily transfer an electron to one of the magnetic ions, leaving it with an unpaired electron that can interact via direct exchange with the other magnetic ion. In this way the magnetic ions interact indirectly. Superexchange is responsible for antiferromagnetic order in compounds such as rock salt MnO.

In a DMS, the magnetic dopant ions are spatially separated such that neither direct exchange nor superexchange can explain the observed ferromagnetic order. Instead, the mechanism is an exchange interaction between the isolated magnetic ions and the semiconductor carriers. Essentially, the localized electrons of the isolated magnetic ion can interact via exchange with carriers in the vicinity, resulting in a spin-polarized cloud of carriers surrounding the magnetic ion, as illustrated in Figure 1.7 (c). These carriers move through the material and interact with other magnetic ions, facilitating long-range ferromagnetic ordering of the magnetic ions. This interaction is often described by Ruderman-Kittel-Kasuya-Yoshida (RKKY) theory, which gives the exchange coupling of two isolated magnetic ions as a function of the density of states of carriers at the Fermi level and the exchange interaction between the carriers and the localized magnetic ions.[54] The interaction oscillates between ferromagnetic and antiferromagnetic as the distance between the magnetic ions changes. A similar model was first proposed by Zener[55-57] to explain the ferromagnetism of magnetic metals. In this model, a mean-field approach is employed to describe the interactions between two spin systems: the spins of the carriers and the spins of the localized *d* electrons.[24] The model failed to take into consideration several properties that are now known to be key aspects of the theory of magnetic metals; however, the model is appropriate for isolated magnetic ions in a semiconductor host.[33] In the case where

the carrier concentration is less than the number of localized magnetic ions, the mean field approximation to RKKY theory and the Zener model of magnetism, as applied by Dietl *et al.* to calculate the Curie temperature of several potential DMS materials, become equivalent.[52]

The RKKY / Zener model of magnetic exchange in DMS materials successfully explains much experimental data for Mn-doped II-VI and III-V materials.[52] This agreement between theory and experiment has provided a fairly clear picture of the physical mechanism of magnetism in these materials.[52,54,58] Mn substitutes as Mn(II) in both II-VI and III-V compounds; thus, Mn is isoelectronic in II-VI materials but introduces a hole in III-V materials. In both cases the localized *d*-states of the Mn ion fall within the valence band of the semiconductor. Hybridization of the Mn *d*-states and the valence *p*-states results in an exchange interaction between the magnetic Mn *d* electrons and the free carriers in the valence band (holes), leading to carrier-mediated ferromagnetism of the isolated Mn ions. This exchange interaction has the effect of spin-splitting the free carrier energy bands, analogous to the case for ferromagnetic metals (see Figure 1.3(b)), resulting in a spin-polarized carrier concentration. Since the Mn *d*-states lie in the valence band of the semiconductor, holes are expected to mediate the exchange interaction much more effectively than conduction band electrons, as observed in experimental results of ferromagnetism in *p*-type Mn-doped DMS materials.[58] Only under certain circumstances, such as quantum wells at a temperature of less than 2 K, has ferromagnetism been observed in *n*-type Mn-doped semiconductors.[52,59] If spaced closely enough in the crystal lattice, Mn(II) ions undergo a strong, short-range antiferromagnetic superexchange interaction that reduces the effective bulk ferromagnetism (since the antiferromagnetic Mn ions are no longer participating in ferromagnetic ordering), and lowers the ferromagnetic Curie temperature (through the RKKY interaction). Thus, the ferromagnetic response and Curie temperature of Mn-doped DMS materials can be increased in several ways: by increasing the number of free carriers (holes), by

decreasing the Mn concentration, or by increasing the Mn position disorder in the lattice.

Some experimental evidence does not support the RKKY / Zener model of ferromagnetism in DMSs. A significant number of free carriers are required to mediate the RKKY interaction, and the ferromagnetic ordering is expected to increase with an increase in carriers. In GaMnAs, each substitutional Mn(II) ion acts as an acceptor, introducing one free carrier hole per ion. However, the number of carriers has been found experimentally to be almost an order of magnitude less than the number of Mn ions.[60] The high level of carrier compensation in the GaMnAs system is believed to be a key component of the observed ferromagnetism, although the role it plays is under active debate.[60] In addition, ferromagnetism has been observed in GaMnAs regardless of the carrier concentration; ferromagnetism has even been observed in insulating samples.[60] These experimental results have led to the development of an alternate theory of the ferromagnetism in DMS materials by Das Sarma *et al.*[60] For systems with sufficient free carriers to be metallic, Das Sarma *et al.* modify the mean-field RKKY model to include the effects of an impurity band which is formed in the gap and consists of free carriers interacting with the Mn ions. When the interaction of the carriers with the Mn ions becomes strong enough, the carriers become trapped and the material becomes insulating. In this case, Das Sarma *et al.* introduce the concept of a bound magnetic polaron, which consists of one localized hole and many magnetic impurities whose spins are polarized by the exchange interaction with the localized hole. As the polarons increase in size, they begin to coalesce, eventually forming a single polaron throughout the material. This results in a ferromagnetic DMS. These two models are able to explain certain characteristics of the experimental data collected on GaMnAs, but there has been no experimental or theoretical proof of their validity and they are generally less accepted than the RKKY / Zener model proposed by Dietl *et al.*

Unfortunately, the RKKY / Zener model of magnetism as applied to Mn-doped *p*-type II-VI and III-V semiconductors does not apply to other host lattices such as *n*-type oxides, or to alternative magnetic dopants such as Cr or Co. In these cases, the *d*-states of the magnetic dopant fall within the bandgap of the semiconductor. For dopants such as Cr and Co in *p*-type II-VI and III-V semiconductors, this prevents hybridization of the valence band carriers and the transition metal *d*-states, eliminating the possibility of a RKKY-type exchange interaction. Additionally, in *n*-type oxides a significant quantity of valence band carriers do not exist to mediate the RKKY interaction, and instead the ferromagnetism appears to be mediated by free carrier electrons. Understanding the origin of magnetic ordering in these materials is necessary since spin-polarized electrons are preferred over spin-polarized holes for spin injection in practical spintronic devices. [13] Recent theories have suggested ferromagnetism in these materials arises from double exchange.[58,61,62] Double exchange was proposed as part of Zener's model of magnetism[56] to explain the ferromagnetic ordering in mixed-valence semiconducting compounds such as $La_xCa_{1-x}MnO_3$, which contains both Mn(III) and Mn(IV) separated by oxygen anions. In the double exchange mechanism, a *d* electron is transferred from Mn(III) through a neighboring oxygen anion to Mn(IV). Since this electron transfer can only occur if the spin of the electron hopping from the Mn(III) is the same as the spin of the Mn (IV) electrons, ferromagnetic ordering results. As applied to DMS materials such as Co-doped ZnO and Co-doped anatase TiO_2, the double exchange mechanism may explain the ferromagnetic ordering of the magnetic dopant in an *n*-type material, in the absence of an RKKY-type interaction.

The study of magnetism in DMS materials is providing significant insight into the physical mechanisms of magnetism and magnetic ordering. These results have shown the possibility of achieving nearly 100% spin polarization in DMS materials.[63] It should be emphasized, however, that spin-polarized carrier populations, not localized electrons or holes, are necessary for spin injection in spintronic devices.

Thus, a semiconductor with small inclusions of ferromagnetic metal clusters may have the properties of a ferromagnetic material with a high degree of ordering, but since the spin polarization is restricted to localized electrons in the metallic cluster and does not extend to the semiconductor carriers, the material would not be a true DMS and could not be used as a source of spin-polarized carriers.

When investigating a new material for potential DMS behavior, it is difficult to determine *a priori* the expected properties of the system. Even the magnetic properties which are easily measured experimentally, such as the magnetic moment per magnetic dopant atom, are difficult to obtain theoretically. The magnetic moment on an isolated atom or ion, such as Co(II) which has d^7 electrons, is readily obtained by filling the *d* orbitals with the proper number of electrons, then applying the appropriate spin-orbit coupling scheme, such as Russell-Saunders coupling, to determine the overall magnetic moment of the ion. However, the situation is much more complicated when the magnetic ion is placed in a host crystal lattice. The geometric positions of the electron orbitals of the surrounding host atoms can lift the degeneracy of the *d* orbitals of the dopant ion, since some *d* orbitals may interact much more closely with the orbitals of neighboring atoms. This is known as crystal field splitting, and is illustrated in Figure 1.8. Many transition metal oxides, such as TiO_2, have octahedral coordination, which split the *d* orbitals into three lower-energy

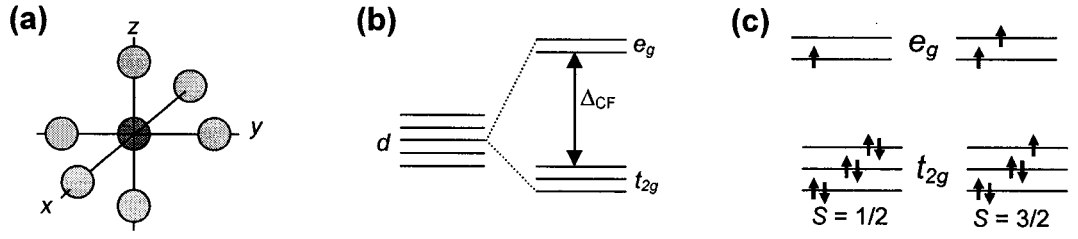

Figure 1.8. (a) Octahedral coordination of a transition metal cation surrounded by six neighboring oxygen anions in a transition metal oxide. (b) The *d* orbitals of the cation that lie along the x, y, and z axes (d_{z^2} and $d_{x^2-y^2}$) feel more Coulomb repulsion from the oxygen anions than the *d* orbitals that lie between the anions (d_{xy}, d_{yz}, d_{xz}). This lifts the degeneracy of the *d* orbitals into higher energy e_g and lower energy t_{2g} orbitals. The energy separation is known as the crystal field splitting (Δ_{CF}). (c) Depending on the magnitude of Δ_{CF}, electrons can assume either a low-spin state ($S = 1/2$) or a high-spin state ($S = 3/2$) (shown using a d^7 system, such as Co(II), as an example).

orbitals which lie between neighboring atoms, referred to as t_{2g} orbitals, and two higher-energy orbitals which point towards neighboring atoms, referred to as e_g orbitals. If the crystal field splitting between the t_{2g} and e_g orbitals is sufficient, it may be more energetically favorable for electrons to pair up in the lower t_{2g} orbitals instead of filling the higher e_g orbitals, resulting in a low-spin configuration with the minimum magnetic moment. Alternatively, a high-spin configuration results if the crystal field splitting is such that electrons fill the higher e_g orbitals, resulting in the maximum magnetic moment. It is also possible for intermediate-spin configurations to occur. To know which spin configuration will be most energetically favorable for a given magnetic dopant in a given host lattice, the detailed density of states of the system must be determined. Density functional theory (DFT) calculations are often employed for this; however, approximations must be made in the calculations that may not hold in the actual material system. In addition, the role of free carriers in the overall magnetization of the system must be taken into account. Due to these difficulties, it is nearly impossible to determine with confidence the expected magnetic behavior of a proposed material system; instead, experimental results and careful materials characterization are necessary.

Cobalt-doped Anatase TiO_2

Titanium dioxide, TiO_2, occurs in three crystal structures: rutile, anatase, and brookite. Rutile, the most stable form, has a tetragonal crystal structure. Brookite is a metastable phase with a rhombohedral crystal structure. The crystal structure of metastable anatase, shown in Figure 1.9, is a distorted form of the tetragonal rutile structure, with lattice constants $a = 3.785$ Å and $c = 9.514$ Å and distorted octahedral coordination of the Ti(IV) ions. The Ti-O bond lengths are 1.94 Å for oxygens in the *a-b* plane and 1.97 Å for oxygens in the *c* plane.[64] Since anatase is a metastable phase and undergoes a transition to rutile at relatively low temperatures, it is difficult

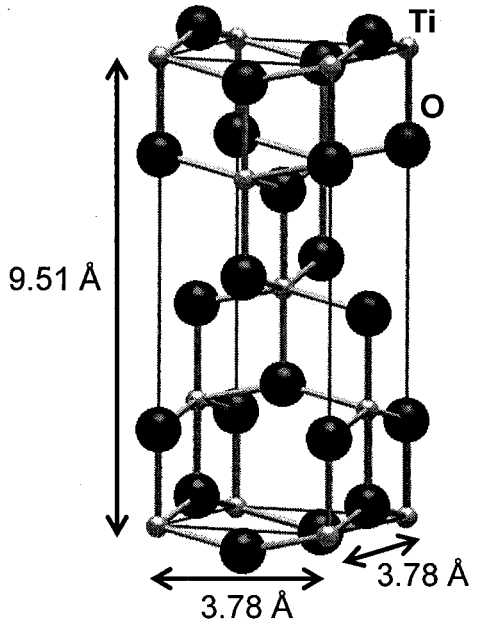

Figure 1.9. Anatase TiO_2 unit cell (space group $I4_1/amd$). Light spheres are Ti, dark spheres are O.

to obtain in bulk form.[65] However, anatase is favored over rutile in fine TiO_2 powders.[66] In addition, thin films of anatase can be obtained by deposition on suitable lattice-matched substrates, such as the (001) surface of $LaAlO_3$ (LAO), which has a lattice mismatch of $(a_{anatase} - a_{LAO}) / a_{LAO} = 0.13\%$, and $SrTiO_3(001)$, which has a lattice mismatch of –3.1%. Anatase TiO_2 is a wide bandgap semiconductor with an indirect bandgap of 3.2 – 3.3 eV.[66,67] Anatase can easily be reduced to *n*-type by the introduction of oxygen vacancies; each oxygen vacancy introduces two free carrier electrons in a donor band just below the conduction band.[65]

Titanium dioxide has been studied extensively for a wide variety of applications. TiO_2 is already employed as a pigment in paint (at a production rate of 4 million tons a year worldwide[66]), as a component in heterogeneous catalysts, and as a component in thin film optical interference coatings, among others. In addition, there is ongoing research into its catalytic, photocatalytic, photoelectric, photochemical, optical, and dielectric properties for applications ranging from solar cells to the replacement gate

dielectric in MOSFET devices. For spintronic devices, it is especially appealing to combine the optical properties of TiO_2, such as its transparency in the visible and near-infrared regions, with ferromagnetic DMS behavior.[43]

Cobalt is one of only three transition metals that are ferromagnetic at room temperature, with a magnetic moment of 1.72 μ_B/Co atom and a Curie temperature of 1388 K (1115°C). Cobalt forms two oxides which are stable in bulk form, both of which are antiferromagnetic. CoO, with an oxidation state of Co(II) and the rock salt crystal structure, is antiferromagnetic due to superexchange interactions between the Co cations through the oxygen anions. The Neél temperature (T_N, the transition temperature from antiferromagnetic to paramagnetic behavior) of CoO is 291 K.[68] Spinel Co_3O_4, which is a mixed-valence compound containing both Co(II) and Co(III), has a low T_N of 40 K.[68] Co_2O_3, which has an inverse spinel structure containing only Co(III), is not easily obtained in bulk form unless hydrated.[69] The magnetic properties of Co_2O_3 are not well established, although it has been reported to be antiferromagnetic with a T_N of 33 K;[70] recent theoretical calculations have predicted an antiferromagnetic ground state.[71] Cobalt also forms a stable titanate, $CoTiO_3$, with the ilmenite crystal structure and a low T_N of 38 K.[68] The local environment of Co in $CoTiO_3$ is a distorted octahedron, with bond lengths to the nearest-neighbor oxygens of 2.08 Å (three bonds) and 2.20 Å (three bonds).[64] With Ti as the next-nearest-neighbors, this local environment is very similar to that predicted for Co substitution for Ti in anatase. Crystal structure and magnetic data for common Co compounds are given in Table 1.1.

When Co substitutes for Ti(IV) in anatase, it is expected to adopt either the +2 or +3 oxidation state,[43] with crystal field splitting of the *d* orbitals into t_{2g} and e_g levels. Since the 4*s* electrons are ionized before the 3*d* electrons, Co(II) has 7 *d* electrons. In the high spin state ($S = 3/2$), Co(II) would exhibit a spin magnetic moment of 3 μ_B/ Co, and in the low spin state ($S = 1/2$) it would exhibit a spin magnetic moment of 1

Table 1.1. Crystal structure and magnetic properties of Co metal and several Co oxides. Data from [68],[70].

Compound	Crystal structure	Magnetization	Moment / Co	T_C or T_N
Co	hcp	ferromagnetic	1.72 μ_B	1388 K
CoO	rock salt	antiferromagnetic		291 K
Co_3O_4	spinel	antiferromagnetic		40 K
Co_2O_3	inverse spinel	antiferromagnetic (?)		33 K (?)
$CoTiO_3$	ilmenite	antiferromagnetic		38 K

μ_B/Co (see Figure 1.8(c) and Equation 1.2). Likewise, if Co adopted the +3 oxidation state, it would exhibit a spin magnetic moment of 0 μ_B/Co in the low spin state ($S = 0$) and 4 μ_B/Co in the high spin state ($S = 4/2$). In transition metals, the orbital magnetic moment is often quenched by strong coupling of the orbital angular momentum to the crystal field, which prevents alignment with a magnetic field. If the orbital angular momentum of the Co ion is fully quenched, the measured magnetic moment will be the spin magnetic moment, which will be an integer number of Bohr magnetons. However, in the presence of an asymmetric crystal field, such as that felt by a transition metal ion in octahedral coordination, the orbital magnetic moment is not fully quenched. In this case, the orbital magnetic moment makes a contribution to the overall magnetic moment of the ion.

Literature review of Co:TiO_2

Interest in anatase TiO_2 as a host lattice for DMS materials originated with the discovery by Matsumoto *et al.*[43,44] of room temperature ferromagnetism in anatase doped with up to 8% Co. Films were deposited by laser MBE on $LaAlO_3$(001) (LAO) and $SrTiO_3$(001) (STO) substrates. Doping in a similar manner with other 3*d* transition metals did not result in room temperature ferromagnetism. Unlike work on GaN and ZnO, which began with theoretical calculations by Dietl *et al.*[33] indicating the possibility of room temperature ferromagnetism, anatase TiO_2 was chosen for its

favorable optical, dielectric, and semiconducting properties. This discovery spurred significant interest in Co-doped anatase as a potential DMS material.

By far the most widely implemented deposition technique for Co-doped anatase has been pulsed laser deposition (PLD), which is sometimes referred to as laser MBE when used at low deposition rates (< 0.2 nm/min).[72] PLD is performed in a high vacuum chamber with base pressure on the order of $1x10^{-6}$ to $1x10^{-7}$ Torr. Ceramic targets of the desired composition are ablated with a pulsed laser, which locally heats the target and produces a plume of vaporized and ejected target material during each pulse. Deposition rates are typically 2-6 nm/min, allowing the growth of epitaxial materials, although the instantaneous deposition rate during each laser pulse is much higher than the overall rate. Oxygen gas is generally introduced into the chamber to provide additional oxidant for the deposition of oxide materials.

The reported properties of Co-doped anatase deposited by PLD vary widely. Kennedy *et al.*[73,74] studied the deposition of both anatase and rutile on LAO(001) and STO(001), (011), and (111), with a deposition temperature of 750°C, oxygen pressure of $1x10^{-3}$ Torr, and high deposition rate of 20 nm/min. Deposition of anatase on STO(001) resulted in a small fraction of rutile inclusions, while deposition on LAO, which is better lattice-matched to anatase, produced pure anatase films, as determined by x-ray diffraction (XRD). When 7% Co-doped anatase was deposited on LAO, the Co was found to segregate entirely to the film surface and form faceted Co metal particles at the tip of surface anatase particles. No Co was detected in the anatase film, and the measured magnetic moment of the film was 1.7 μ_B/Co, identical to the value for Co metal. Similarly, Li *et al.*[75] deposited 5% Co-doped anatase on STO at 750°C. When deposited in $1.5x10^{-4}$ Torr O_2, a secondary phase identified as $CoTi_2O_5$ was observed in XRD. These films were insulating and not ferromagnetic. Films deposited at 630°C in vacuum resulted in anatase and rutile phases, and no secondary Co phases were observed. This led the authors to speculate the Co was

incorporated into the rutile phase. The film was conductive and ferromagnetic with a moment of 0.16 μ_B/Co.

Shinde *et al.*[76] deposited 7% Co-doped anatase on STO and LAO at 700°C and $1x10^{-5}$ to $1x10^{-4}$ Torr O_2, and observed strongly ferromagnetic behavior with a moment of 1.4 μ_B/Co and a Curie temperature of 1180 K. While no secondary phases were observed in XRD, further investigation by scanning transmission electron microscopy (STEM) revealed the presence of Co metal clusters distributed throughout the film. In contrast to the results of Kennedy *et al.*,[74] the authors reported some Co incorporation into the anatase lattice, and estimated the solubility limit of Co in anatase as less than 2%. Surprisingly, annealing the film to 1200 K appeared to dissolve the Co metal clusters into the anatase lattice, as indicated by STEM images and Rutherford backscattering (RBS) channeling measurements. The room temperature magnetic moment after annealing remained unchanged (1.4 μ_B/ Co), although the Curie temperature was reduced to 650 K.

In an effort to clarify the conflicting results reported for PLD-grown Co-doped anatase films, D.H. Kim *et al.*[72,77] performed a detailed study of 4% Co-doped anatase films deposited slowly (< 0.2 nm/min) on STO at 600°C under various oxygen pressures from $1x10^{-7}$ to $1x10^{-4}$ Torr. For deposition under high oxygen pressure, the *in situ* reflection high energy electron diffraction (RHEED) patterns remained streaky throughout the deposition, and the smooth surface was confirmed with *ex situ* atomic force microscopy (AFM). Deposition under lower oxygen pressure resulted in spotty final RHEED images, implying three dimensional island growth. AFM confirmed the presence of surface islands 10-100 nm in diameter. For all films, XRD indicated phase-pure anatase; the presence of Co metal or other secondary phases was not observed. Both the ferromagnetic moment and electrical conductivity increased as the oxygen pressure decreased, with a magnetic moment of 1.7 μ_B/Co for the film deposited at $1x10^{-7}$ Torr O_2. TEM was utilized to observe Co

cluster formation. Single crystal Co metal clusters of 11 ± 6 nm diameter were observed at the film / substrate interface for films deposited at less than $1x10^{-5}$ Torr O_2; for films deposited at higher oxygen pressure no metal clusters were observed. These results were confirmed by Co K-edge x-ray absorption spectroscopy (XAS), which clearly indicated Co in the +2 charge state (similar to CoO) for films deposited at $1x10^{-5}$ Torr O_2 and above. For the film deposited at $1x10^{-7}$ Torr O_2, the XAS spectrum was almost identical to Co metal, indicating nearly all the Co in the film was in the form of Co(0). In an extension of this work, J.-Y. Kim *et al.*[78] investigated the effect of annealing on the Co distribution and magnetic properties. Films were deposited on LAO at 650°C in $1x10^{-5}$ to $1x10^{-6}$ Torr O_2, and the Co concentration was varied from 4% to 10%. Co L-edge XAS of the as-deposited films indicated Co was in the +2 high spin charge state. The room temperature ferromagnetic moment, measured by magnetic circular dichroism (MCD), was low (~0.1 μ_B/Co), and the MCD lineshape resembled that for Co metal. The films were then annealed at 400°C under $1x10^{-6}$ Torr O_2. After annealing, the XAS spectra indicated Co metal, and the ferromagnetic MCD signal increased significantly without changing lineshape, with a final moment of 1.55 μ_B/Co. The presence of Co metal clusters on the film surface was confirmed by scanning electron microscopy (SEM). The overall intensity of the XAS spectra did not increase after annealing, indicating there was no bulk movement of Co into the surface region (the authors reported their XAS measurement has a probe depth of ~ 10 nm). Films that were annealed at 650°C under the same conditions also showed evidence of Co clustering into metallic clusters. In addition, bulk movement of Co to the surface was implied by the significant increase in the Co XAS signal relative to the Ti and O signals. Interestingly, if the as-deposited film was annealed in air at 400°C, the magnetism was lost. The authors attribute this phenomenon to oxidation of the Co clusters during the anneal. These annealing results are in direct contrast to the results of Shinde *et al.*,[76] who observed the dissolution of Co metal clusters into the anatase lattice upon annealing and the retention of ferromagnetism.

Two key points can be made regarding the deposition of Co-doped anatase by PLD. The first is the difficulty of the material system. The distribution of Co in the anatase film depends sensitively on the growth conditions, such as substrate temperature, oxygen pressure, and growth rate. Small changes in one of these parameters can have a dramatic effect on the resultant film. For example, the reported magnetic moment per Co atom ranges from 0.32 μ_B/Co[43] to 1.4 μ_B/Co[76] for films which are nominally free of Co clusters. For films in which Co metal clusters are present, they have been observed at the film / substrate interface,[77] distributed throughout the film,[76] or on the film surface.[74] This variation in morphology and properties leads to the second key point, which is that careful and thorough materials characterization is necessary before any claims of DMS behavior can be made. In all these studies, XRD was employed to determine the crystal structure of the Co-doped film. While secondary phases such as rutile and $CoTi_2O_5$ were detected in some films, Co metal was never observed, even in films in which Co metal clusters were clearly observed by TEM. The necessity of thorough materials characterization is exemplified by the reports of Yang *et al.*,[79] who deposited 7% Co-doped anatase films on LAO at 400-700°C and $3x10^{-5}$ Torr O_2. The film properties were improved by UV-PLD, in which an UV lamp was used to dissociate oxygen molecules near the substrate into more reactive excited atomic species. Films grown at 400°C by UV-PLD were ferromagnetic at room temperature, with a Curie temperature > 350 K. XRD indicated the film consisted of epitaxial anatase with no impurity phases. An Auger electron spectroscopy (AES) depth profile found Co segregation at the film / LAO interface, but no further materials characterization was performed to determine if the Co was present in metallic clusters at the interface, as observed by D.H. Kim *et al.*[72,77] Without substantial proof that metallic Co is not present in their films, the reported results cannot be considered reliable.

Utilizing oxygen-plasma-assisted molecular beam epitaxy (OPAMBE), Chambers *et*

al.[64,80-82] have reported a detailed materials characterization study of Co-doped anatase deposited on STO and LAO. For this study, metallic Ti in an electron beam evaporator was employed as the Ti source and Co was evaporated from a high temperature effusion cell. Oxygen gas was introduced through an electron cyclotron resonance (ECR) plasma to produce atomic and excited oxygen species. By controlling the oxygen pressure and Ti / O ratio, the concentration of oxygen vacancies in the anatase films could be varied, resulting in electrical conductivity ranging from insulating to *n*-type semiconducting. The initial report by the authors[80] focused on deposition on STO at a growth rate of 1.8 – 2.4 nm/min. Without Co doping, epitaxial anatase was obtained at substrate temperatures of 550°C and above with good crystal quality. However, the introduction of Co during the deposition was found to affect the nucleation and growth of the epitaxial film in a complex way. Additionally, x-ray photoelectron spectroscopy (XPS) measurements of the Co concentration in the surface region of the film consistently resulted in a lower Co concentration than expected. Further depth profiling measurements indicated Co may diffuse into the STO substrate at elevated temperature ($\geq$ 550°C). Surprisingly, the Co distribution in the film was also found to depend critically on the method of growth termination. If the film was allowed to cool from the growth temperature in the presence of the oxygen plasma, a significant concentration of Co was observed to diffuse to the surface of the film, resulting in a near-surface concentration as high as 50% Co. Depth profiling confirmed the surface segregation of Co, with essentially no Co in the middle of the film and a slight increase in Co at the film / substrate interface. However, if the film was allowed to cool in vacuum, no surface segregation of Co was observed. Co L-edge XAS of films with surface segregation indicated the films contained a mixture of Co(II) and Co(III), while films without surface segregation appeared to be Co(II) with a local environment similar to $CoTiO_3$; Co metal was not detected in any of the films. The concentration profile of Co also affected the magnetic properties of the film. Co-doped anatase films in which surface segregation was observed were consistently nonmagnetic. Films in

which no surface segregation of Co was observed were found to be ferromagnetic at room temperature, with a magnetic moment of 1.26 μ_B/Co. This value is slightly higher than the moment expected for Co(II) in the low spin state (1 μ_B/Co), but the authors speculate that the asymmetric crystal field associated with the octahedral site in anatase is not sufficient to fully quench the orbital moment, giving rise to an additional contribution to the magnetic moment.

Due to the difficulties encountered in depositing Co-doped anatase on STO, subsequent reports by Chambers *et al.*[64,81,82] focused on depositions on LAO. With a relatively fast deposition rate of 2.2 nm/min, deposition of anatase on LAO produced epitaxial anatase films with rutile inclusions. TEM images indicated the rutile inclusions nucleate near, but not at, the film / substrate interface, and grow during film deposition to become rutile protrusions on the film surface. When Co-doped anatase was deposited under these conditions, the Co was found to preferentially segregate to the rutile inclusions. At slower growth rates (0.6 nm/min), rutile inclusions were not observed. However, subtle changes in the deposition conditions at this growth rate dramatically altered the film morphology. In some films, a smooth surface with Co incorporation into the bulk of the film was observed. In other cases, large particles (up to 80-100 nm diameter, 7-14 nm high) were observed on the film surface. Investigation by scanning AES showed the particles were Co-enriched TiO_2 with a Co concentration up to approximately 40%, and negligible Co was observed in the continuous anatase film. TEM images confirmed the particles were epitaxial anatase, and no indication of Co metal or other secondary phases was observed. Using Co K-edge XAS, the charge state and local environment of Co atoms in an insulating smooth film and a semiconducting film with Co-enriched particles, both with 5% Co, were compared. No significant differences were observed in the near-edge or extended fine structure of the two films. The near-edge structure of both films closely matched $CoTiO_3$, indicating Co is in the +2 charge state. No evidence of CoO or Co metal was observed. Fitting of the extended fine

structure gave Co to O bond lengths intermediate between the values expected for Ti-O bond lengths in anatase and Co-O bond lengths in $CoTiO_3$. The effective coordination number (number of nearest-neighbor oxygens) was calculated to be 5.45. For an ion in an octahedral site in fully stoichiometric anatase, a coordination of 6.0 is expected. The authors hypothesize that, to maintain charge neutrality, one electrically inactive oxygen vacancy must be produced for every Co(II) ion that substitutes for a Ti(IV) in anatase. In this case, the true film stoichiometry would be written $Ti_{1-x}Co_xO_{2-x}$. If each oxygen vacancy remains correlated with the Co ion that necessitated it, the coordination number for Co would be 5.0. However, if the oxygen vacancies were distributed randomly throughout the lattice, it was calculated that the effective coordination number of Co would be 5.82 for 6% Co doping. Since the calculated coordination number of 5.45 falls between these values, the authors inferred partial but incomplete structural correlation of the oxygen vacancies and Co ions. Magnetic measurements of both smooth films and films with Co-enriched anatase particles consistently produced a room temperature magnetic moment of 1.1-1.2 μ_B/Co for semiconducting samples (insulating samples were not ferromagnetic). Since no evidence of Co metal or secondary phases has been observed, the authors speculate Co-doped anatase deposited by OPAMBE exhibits true DMS behavior.

In addition to PLD and MBE, a few studies of Co-doped anatase deposited by other techniques have been reported. Han *et al.*[83] investigated the deposition of Co-doped anatase on LAO with reactive co-sputtering. Ceramic TiO_2 and metallic Co targets were ablated with an Ar ion beam for a growth rate of 0.53 nm/min at a substrate temperature of 750°C. The pressure was maintained at $5x10^{-3}$ Torr Ar; no oxygen gas was introduced. The amount of Co incorporated into the film was found to be significantly less than expected, although no Co segregation was observed in the as-deposited films. Despite the oxygen-poor deposition conditions, as-grown samples were found to be insulating. Annealing in vacuum ($<10^{-8}$ Torr) at 750°C significantly reduced the resistivity. Room temperature ferromagnetism was

observed for an as-deposited film, with a magnetic moment of 1.135 μ_B/Co. Annealing in vacuum was found to significantly increase the saturation magnetization of the film. The authors speculate this increase could be due to Co clustering into metallic particles in the oxygen-poor annealing conditions.

D.H. Kim *et al.*[84] studied the magnetic properties of Co-ion-implanted anatase films. Pure epitaxial anatase films 500 nm thick were deposited on STO by PLD. Co^+ ions of 250 keV energy were then implanted at a doping level of $3x10^{16}$ ions/cm^2 or $5x10^{16}$ ions/cm^2, resulting in 3% or 5% Co doping and ~200 nm incorporation depth. The films were then annealed at 300-600°C under $1x10^{-6}$ or $1x10^{-1}$ Torr O_2. The retention of the anatase phase after ion implantation and annealing was confirmed by XRD. As-implanted films appeared to be ferromagnetic at 5 K but paramagnetic at room temperature. The authors interpreted the magnetic results as superparamagnetic behavior. Superparamagnetism arises from small ferromagnetic particles or precipitates in which the anisotropy energy, which holds the magnetization along an easy crystal direction, is reduced with size. At a critical particle size, the anisotropy energy becomes comparable to the thermal energy, and the magnetization of the particle can spontaneously switch direction; the temperature at which this occurs for a given particle size is known as the blocking temperature (T_B). In this regime, the particles behave as paramagnetic materials, but with a much larger magnetic moment. Kim *et al.* calculated that Co metal clusters of approximately 3 nm diameter would produce the observed superparamagnetic behavior. STEM images confirmed the presence of 3-5 nm diameter particles in the as-deposited film. Energy-dispersive x-ray spectroscopy (EDS) confirmed the particles are significantly enriched in Co, although it could not be determined whether the particles were metallic Co or a ferromagnetic Co intermetallic compound. Post-annealing increased the particle size, and above a certain particle size room temperature ferromagnetism was observed, with a magnetic moment of 1.5 μ_B/Co attributed to the ferromagnetic Co metal clusters.

Metalorganic chemical vapor deposition (MOCVD) utilizing a liquid delivery system for the solid metalorganic precursors of Ti and Co was employed by Seong *et al.*[85] for Co-doped anatase deposition onto SiO_2 (200 nm) / Si. The growth pressure was held at 1 Torr, with a gas flow of 50 sccm O_2 / 50 sccm Ar. As-deposited films were annealed in vacuum ($1x10^{-6}$ Torr) at 700°C. Weak polycrystalline anatase was observed by XRD for annealed films deposited at 400°C regardless of Co content; annealed films deposited above 400°C were polycrystalline rutile. Annealed films deposited at 400°C with Co concentrations of 3%-12% were ferromagnetic at room temperature. For Co concentrations $\leq$ 5%, no surface particles were observed after annealing and the ferromagnetism was attributed to Co-doped anatase. For Co concentrations > 5%, large $Co_{1-x}Ti_x$ particles were observed on the surface, with a corresponding increase in the saturation magnetic moment. The magnetization of these samples was attributed by the authors to both ferromagnetism of Co-doped anatase and soft magnetic properties of the $Co_{1-x}Ti_x$ precipitate phase.

Several groups have produced Co-doped anatase by sol-gel processing. Soo *et al.*[86] produced 6% Co-doped anatase powder which was annealed at 220°C, 450°C, or 1000°C in air. XRD indicated the as-grown and 220°C annealed powders were amorphous, the powder annealed at 450°C was primarily anatase with some rutile, and the 1000°C annealed sample was entirely rutile. The as-grown and 1000°C annealed powders were paramagnetic at room temperature, but the powders annealed at 220°C and 450°C were ferromagnetic. The near edge structure of Co K-edge XAS confirmed Co was in the +2 oxidation state. The extended fine structure confirmed the amorphous morphology of the low temperature samples. For the 450°C annealed powder, the extended structure was fit an anatase-like local environment. Unexpectedly, the extended structure of the 1000°C annealed sample also appeared to be anatase-like, despite the rutile crystal structure observed in XRD. Manivannan *et al.*[87] produced 10% Co-doped anatase powder which was annealed to 475°C. In

contrast to the result by Soo *et al.*,[86] the powder exhibited paramagnetic behavior at room temperature. Room temperature ferromagnetism was induced by passing H_2 gas over the powder at 300°C. After hydrogenation, no Co metal was detected by XPS. The authors speculate that H_2 increased the conductivity by removing oxygen from the powder, although the conductivity of the powder was not measured. Shim *et al.*[88] used sol-gel processing to spin-coat thin films onto LAO and SiO_2/Si substrates. Films annealed in air at $\geq$ 500°C crystallized into anatase, with (001)-preferred orientation on LAO. The films were found to be ferromagnetic at room temperature.

Theoretical calculations have been performed on the Co-doped anatase material system in an attempt to clarify the experimental discrepancies from an *ab initio* first-principles approach. The calculations were all based on density functional theory (DFT). DFT calculations are based on minimization of the total energy of an interacting electron system. For a magnetic system, the exact mechanism resulting in magnetic ordering is not assumed nor revealed in calculation; instead, the local spin density approximation (LSDA) is utilized, in which the electron-correlation properties are determined at each point in space by the local charge density of interacting electrons. The spin-orbit coupling is neglected, implying zero orbital magnetic moment, unless another term in the calculation is explicitly included.[89]

Park *et al.*[62] used the linearized muffin tin orbital (LMTO) band method with the LSDA to calculate the density of states of an anatase supercell ($Ti_{16}O_{32}$) in which zero, one, or two Ti atoms are replaced by Co atoms (x = 0, 0.0625, or 0.125). For the case of pure anatase, the calculated band structure was consistent with previous results, although the calculated TiO_2 bandgap, 4.0 eV, is an overestimation of the known bandgap of anatase (3.2 eV). The top of the valence band was calculated to consist primarily of O 2*p* character, while the bottom of the conduction band was primarily Ti 3*d*. Replacing one Ti with an isoelectronic Co (as Co(IV)) in the lattice

placed the Co *d*-states in the bandgap of TiO_2, as expected. The *d*-states were split by the crystal field into e_g and t_{2g} levels, and to a lesser extent the levels were split by the exchange interaction. The Fermi level was calculated to fall above the spin-down t_{2g} band but within the spin-up t_{2g} band, resulting in 100% spin-polarized half-metallic character. This band arrangement led the authors to speculate the mechanism of ferromagnetic ordering in Co-doped anatase is a double exchange mechanism involving the Co *d*-states. Since the exchange splitting of the t_{2g} band was less than the crystal field splitting of the t_{2g} and e_g bands, the Co was predicted to be in a low spin state, with a spin magnetic moment of 1 μ_B/Co atom. However, the calculations showed the orbital magnetic moment was not fully quenched by the crystal field, resulting in an orbital moment of 0.9 μ_B/Co and thus a total magnetic moment of 1.9 μ_B/Co. The effect of oxygen vacancies, which allow Co to assume the +2 charge state, was also investigated. The calculations indicated that an O vacancy in a Ti octahedron was most stable and had little effect on the overall band structure. However, an O vacancy in a Co octahedron, which may occur during a nonequilibrium growth technique such as MBE, resulted in further asymmetry in the crystal field, entirely lifting the degeneracy of the Co *d*-states. In this case, the Co assumed an intermediate spin state with a total magnetic moment of 2.53 μ_B/Co. Calculations were also performed on a supercell containing two Co ions separated by two nearest-neighbor O atoms and one Ti atom, and it was found that the ferromagnetic ground state was slightly more energetically favorable than the antiferromagnetic ground state.

Utilizing the all-electron full-potential linearized augmented plane-wave (FLAPW) method and CASTEP pseudopotential code, as well as LSDA to describe the exchange-correlation interaction, Yang *et al.*[90] calculated the electronic structure and magnetic properties of Co-doped anatase and rutile. The lattice constants and atomic positions of both anatase and rutile were optimized through the LSDA total energy and atomic forces, and found to be in agreement with the known experimental values,

although the calculated bandgap of 2.5 eV is a significant underestimation. In all cases, the Co *d*-states were calculated to fall within the bandgap of TiO_2, with a half-metallic configuration. The quantitative substitution energies calculated for Co substitution into TiO_2 were large (7.23 eV/atom for rutile, 8.51 eV/atom for anatase), indicating low solubility of Co in either lattice. Uniform doping of Co in anatase was calculated to be less energetically favorable than uniform doping of Co in rutile. Calculation of the magnetic properties of Co uniformly distributed in rutile and anatase yielded the ferromagnetic ground state for both lattices, with 0.56 μ_B/Co for rutile and 0.71 μ_B/Co for anatase. However, non-uniform Co distribution with shorter Co-Co bond lengths was found to be more energetically favorable than uniform distribution in anatase. Several configurations of non-uniform Co distribution in anatase produced a ferromagnetic ground state, with a magnetic moment ranging from 0.68 μ_B/Co to 0.71 μ_B/Co. A ferrimagnetic state was only slightly less energetically favorable. The effect of oxygen vacancies was not investigated. In all cases, the exchange interaction between Co atoms was found to be strong despite the low magnetic moment and spatial separation of the atoms. The authors speculate this property results in the experimentally observed high Curie temperature.

Sullivan *et al.*[91] used DFT to calculate the formation energies of interstitial Co, substitutional Co, oxygen vacancies, interstitial Ti, and a defect complex consisting of a substitutional Co and nearest-neighbor oxygen vacancy. The calculations were performed assuming an equilibrium temperature of 700°C, which is a typical deposition temperature for Co-doped anatase thin films. The calculations were evaluated in the local density approximation (LDA) within the ultrasoft pseudopotential formalism. The LDA is known to underestimate the bandgap; the bandgap calculated for anatase was 2.2 eV. Calculations of Co substituting for Ti indicated the Co *d*-states, which fall within the TiO_2 bandgap, were split by the crystal field into e_g and t_{2g} states, separated by 1 eV. In addition, the e_g states were

further split by 0.3 eV, and the t_{2g} states were split by 0.2 eV. The exchange splitting further separated the spin-up and spin-down states. The authors assumed the orbital magnetic moment is fully quenched. For both substitutional and interstitial Co(II), the magnetic moment was calculated to be 1 μ_B /Co. The defect formation energies were calculated in the oxygen-rich thermodynamic limit, which is the condition assumed by Chambers *et al.*[64,82] for OPAMBE deposition conditions. However, the calculations predict several properties known to be incorrect from experiment: Co was found to be substitutional with a magnetic moment of 1.0 μ_B/Co, not 1.26 μ_B/ Co,[64,82] placement of the Fermi energy below midgap is incompatible with the known *n*-type doping of anatase, and Co(IV) was calculated to be the stable oxidation state of substitutional Co, in contrast to numerous experimental results indicating Co is in the +2 charge state. Calculations in the oxygen-poor limit, however, predicted both substitutional and interstitial Co ions. The interstitial Co ions were predicted to be in the +1 charge state, with a magnetic moment of 2 μ_B/Co. In combination with Co(II) in substitutional sites, the authors speculate interstitial Co (I) may account for the measured magnetic moment of 1.26 μ_B/Co. Co(I) has not been directly observed or ruled out in experimental studies. In addition, calculations show the *n*-type carrier density may not be the result of oxygen vacancies, but instead incomplete compensation of the interstitial Co(I) by substitutional Co(II). Oxygen vacancies were found to have a negligible effect on the electronic structure or carrier density of Co-doped anatase, although this may be a limitation of LDA, which also does not predict *n*-type doping by oxygen vacancies in pure anatase.

The theoretical calculations performed to date agree on several key points. In all cases, the Co *d*-states are found to fall within the TiO_2 bandgap, with half-metallic behavior predicted due to the position of the Fermi level in one of the spin-split t_{2g} levels. Ferromagnetic ground states at room temperature are calculated for several Co doping configurations, although none of the calculations are able to reproduce the magnetic moments observed experimentally. A hint of the energetics favoring Co

clustering was observed by Yang *et al.*,[90] who calculated non-uniform Co doping in anatase. Disagreement amongst the calculations occurs on the role of oxygen vacancies, which Park *et al.*[62] found to strongly influence the calculated magnetic moment but Sullivan *et al.*[91] found to have negligible effect on the electronic or magnetic properties. This may be due to inherent inadequacies in the calculations employed, such as the underestimation of the TiO_2 bandgap by LDA. Alternatively, it may originate in the assumption by Park *et al.* that the orbital magnetic moment of substitutional Co is not fully quenched in anatase, while Sullivan *et al.* assume a fully quenched orbital moment. It is evident that the assumptions, implicit and explicit, in the theoretical calculations of the electronic and magnetic structure of Co-doped anatase must be refined to reproduce the experimental results. Thus it appears that, instead of guiding experiment, theory will evolve along with experiment such that theoretical results will be investigated experimentally and experimental results will be explored theoretically, eventually resulting in a detailed understanding of the Co-doped anatase material system. The discrepancies in both the experimental and theoretical results to date indicate significant contributions must still be made before a detailed understanding emerges.

Cobalt-doped $SrTiO_3$

Strontium titanate, $SrTiO_3$, has the cubic perovskite structure shown in Figure 1.10 (a), with a lattice constant of $a = 3.905$ Å. The Ti(IV) ion has undistorted octahedral coordination, with a Ti-O bond length of 1.95 Å. $SrTiO_3$ (STO) is a wide bandgap oxide with a bandgap of 3.3 eV.[92] In contrast to anatase TiO_2, reducing STO to achieve *n*-type semiconducting behavior is hindered by the ease with which secondary phases form. For bulk single crystals of STO, secondary phases have been observed near the surface for crystals processed under either oxidizing or reducing conditions at 950-1000°C.[93] Ruddlesden-Popper phases of rock salt SrO layers

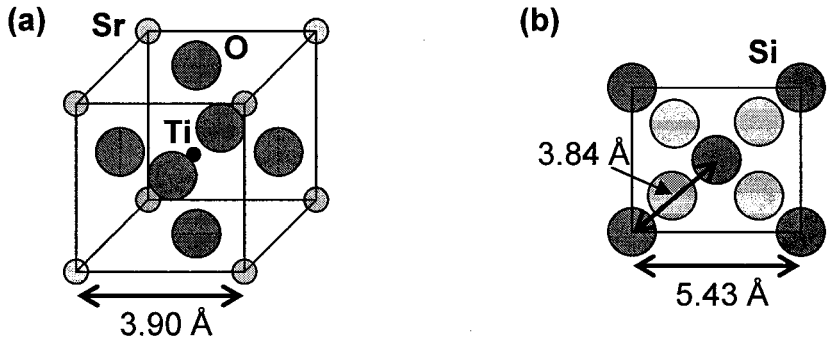

Figure 1.10. (a) Perovskite $SrTiO_3$ unit cell (space group $Pm\bar{3}m$). Light spheres are Sr, black sphere is Ti, dark spheres are O. (b) Unreconstructed Si(001) surface. Dark spheres are top layer Si atoms, light spheres are Si atoms below top surface. Lattice spacing of atoms in a cubic cell rotated 45° from the Si unit cell is indicated.

interspersed in the STO lattice ($SrO{\cdot}(SrTiO_3)_n$), as well as reduced titanium oxide phases (such as TiO and Ti_2O) were observed by XRD after thermal treatment. Formation of these secondary phases to accommodate oxygen (or cation) non-stoichiometry makes evaluation of the electrical properties difficult. Secondary phases are generally observed in a 50-100 nm thick surface region in bulk crystals; secondary phase formation in thin films (whose total thickness is generally on the order of 100 nm or less) is much less well understood, although both Ruddlesden-Popper phases and Ti-rich amorphous regions have been observed in homoepitaxial STO thin films.[94,95] To achieve *n*-type conductivity, bulk STO can be doped with donor impurities such as La[96,97] or Nb.[80]

Literature review of Co:$SrTiO_3$

Magnetic studies of perovskites have focused almost exclusively on ferromagnetic manganites, which exhibit colossal magnetoresistance (CMR) associated with a significant drop in resistivity at their Curie transition temperature.[98] The perovskites are based on $T_{1-x}D_xMnO_3$, in which T is a trivalent lanthanide cation such as La(III) and D is a divalent alkaline earth cation such as Ca(II), Sr(II), or Ba(II). The end compositions (i.e. $LaMnO_3$ and $CaMnO_3$) are antiferromagnetic, resulting from superexchange between Mn cations. Doping with 20-40% Ca, Sr, or Ba produces a

ferromagnetic ground state[98] (which can be above room temperature[23]) with associated CMR behavior at the Curie temperature. The double-exchange mechanism is believed to be at least partially responsible for the ferromagnetic ordering in manganite perovskites.[23,98]

Interest in $SrCoO_3$ originated with the discovery of unusual electrical and magnetic properties in $La_{1-x}Sr_xCoO_3$, which undergoes a transition to a metallic ferromagnet as x increases.[99,100] $SrCoO_3$ is a cubic perovskite (a = 3.83 Å)[100] containing Co(IV), and is also metallic and ferromagnetic below a Curie temperature of approximately 220 K,[100] with an effective saturation magnetic moment of 2.1 – 3 μ_B.[100,101] An intermediate spin state for Co(IV) has been inferred for this system.[99,101] Fully oxygen-stoichiometric $SrCoO_3$ is difficult to obtain by bulk ceramic processing methods. Oxygen-deficient $SrCoO_{3-\delta}$ undergoes order-disorder phase transitions to form perovskite-related structures such as brownmillerite ($SrCoO_{2.5}$),[102,103] in which the oxygen vacancies are ordered within the lattice and reduced Co cations occupy an equal number of distorted tetragonal and distorted octahedral sites. While Co(III) is generally assumed to occupy both sites,[102] there is evidence that Co(II) occupies the tetragonal sites and Co(IV) occupies the octahedral sites.[103] Oxygen-deficient $SrCoO_{3-\delta}$ has received attention recently for application as oxygen separation membranes and as electrodes in solid oxide fuel cells.[103,104]

Kharton *et al.*[104] studied the oxygen permeability characteristics of bulk ceramic solid solutions of $SrCoO_{3-\delta}$ – $SrTiO_3$. Results indicated $SrCo_{1-x}Ti_xO_{3-\delta}$ formed a solid solution for $x < 0.2$ and $x > 0.7$; material with intermediate values of x exhibited phase segregation. From this, the equilibrium solid solubility of Co in $SrTiO_3$ is predicted to be approximately 30%. However, the study focused on the oxygen diffusion through the ceramics, and the magnetic properties were not measured.

Very little work has been attempted on developing DMS materials based on

perovskites. Nakayama *et al.*[105] performed DFT calculations utilizing the FLAPW method within the framework of the LSDA to determine the magnetic ground state of perovskite $BaTiO_3$ doped with 25% of 3*d* transition metals (Sc through Cu). Placing a transition metal dopant in the octahedral Ti(IV) site was calculated to result in crystal field splitting of the *d*-states, creating impurity states in the bandgap of $BaTiO_3$. $BaTiO_3$ doped with Cr or Fe was predicted to be ferromagnetic at room temperature, and it was speculated that the mechanism of magnetism was double exchange. Mn doping was calculated to be antiferromagnetic due to the superexchange interaction between Mn ions. However, the ferromagnetic state was stabilized by adding free carrier holes. Doping with Co was calculated to result in a nonmagnetic material, although due to inherent deficiencies in LSDA the authors hypothesized that Co-doped $BaTiO_3$ should be ferromagnetic, although a high Curie temperature was not expected.

Following the theoretical prediction by Nakayama *et al.*, Lee *et al.*[106] studied the magnetic properties of bulk single crystal $BaTiO_3$, $SrTiO_3$, and $KTaO_3$ ion-implanted with Co or Mn. The ion implantation was performed at 350°C with 250 keV ions at a dose of $3x10^{16}$ ions/cm^2 or $5x10^{16}$ ions/cm^2, resulting in an incorporation depth of approximately 200 nm and a transition metal concentration of 3 or 5%, respectively. The crystals were then annealed at 700°C under flowing N_2 to partially repair implantation damage. No secondary phases were observed by XRD for the implanted samples. $BaTiO_3$ was found to be ferromagnetic near room temperature when doped with Mn, while ferromagnetism at room temperature was observed for Co-implanted $BaTiO_3$. For $SrTiO_3$, implantation with 5% Mn resulted in paramagnetic behavior, while doping with 3% Mn produced ferromagnetism near room temperature. The authors attribute this to antiferromagnetic coupling of the Mn ions at the higher doping concentration. Implantation with Co resulted in room temperature ferromagnetism for both concentrations. Similar results were obtained for $KTaO_3$, where Mn implantation produced ferromagnetism with a Curie

temperature of ~ 250 K, and implantation by Co resulted in room temperature ferromagnetism.

Zhao *et al.*[96] deposited Co-doped $La_{0.5}Sr_{0.5}TiO_{3-\delta}$ on LAO substrates by PLD. High quality perovskite structure films were obtained, with no secondary phases observed by XRD. Ferromagnetism of 1.5% Co:(La,Sr)TiO_3 was observed at room temperature, with an estimated Curie temperature of 450 K. STEM images confirmed the high crystalline quality of the film without evidence of clusters or inclusions, although electron energy loss spectroscopy (EELS) indicated an inhomogeneous Co distribution on the scale of 1-2 nm for the 7% Co-doped sample. The role of carriers on the magnetic properties was investigated. It was found that ferromagnetism only occurred for intermediate film resistivity values of 10^2-10^4 $\mu\Omega$·cm, which the authors interpreted as evidence of the complex role of carriers, provided both by oxygen vacancies and Co substitution, in mediating the magnetism. The highest magnetic moments obtained, for 1.5% Co doping and a film resistivity of 10^2-10^3 $\mu\Omega$ cm, was ~ 2.5 μ_B/Co. The authors speculate this high moment may result from high and low spin admixtures of Co(II) and Co(III) present in the film.

Oxide growth on silicon

Perovskites such as $SrTiO_3$ are prime candidates for epitaxial deposition on Si(001) due to the close lattice match of $SrTiO_3$(001) and Si(001) if the *a-b* plane of the STO lattice is rotated 45° relative to Si, such that (001)$SrTiO_3$ // (001)Si and [100] $SrTiO_3$ // [110]Si (see Figure 1.10(b)). However, the deposition of oxides on Si is greatly complicated by the ease with which Si oxidizes to form an amorphous SiO_2 layer, which destroys the epitaxial Si template. Successful deposition of an oxide on Si without the formation of an interfacial SiO_2 layer was first demonstrated by McKee *et al.*,[107] who deposited epitaxial $SrTiO_3$ on Si by MBE utilizing intermediate

Sr silicide and SrO layers. Deposition of ¼ ML Sr on clean (2x1) Si at 850°C was found to produce a 4x2 reconstructed surface as observed by RHEED. Subsequent deposition of additional Sr metal at low temperature (200°C), followed by deposition of 1 ML SrO, was found to satisfactorily protect the Si surface from oxidation while preserving the epitaxial template. STO deposition was then initiated by deposition of 1 ML TiO_2 followed by 1 ML SrO, resulting in 1 ML of STO(001). High resolution TEM images of the interface led the authors to conclude the initial ¼ ML Sr formed $SrSi_2$ silicide, in which Sr atoms have replaced and displaced Si atoms at the interface. The presence of this silicide was hypothesized to thermodynamically protect the Si interface from oxidation. As a candidate replacement gate oxide material in MOSFET devices, 10 nm STO deposited by this method was demonstrated to have an equivalent oxide thickness of 5.4 Å and favorable electrical properties, although a forming gas anneal was necessary to passivate defects.[108]

The deposition of STO on silicon as a replacement gate oxide has been extensively studied by Motorola.[109-114] To clean Si(001) in UHV, the surface was exposed to Sr at < 800°C.[113] At this temperature, Sr scavenged oxygen from surface contaminants and SiO_2 to form volatile SrO, which then thermally desorbed from the surface. Additional Sr remained on the surface as an ordered sub-monolayer silicide. This silicide layer was exposed to a low pressure of oxygen ($1 - 5 \times 10^{-8}$ Torr) at 200-300°C, producing a silicate structure, before codeposition of Sr and Ti was initiated to deposit STO. Recrystallizing the STO at high temperature and low oxygen pressure ($< 5 \times 10^{-9}$ Torr) after each deposition of approximately 1-3 ML produced epitaxial STO without an interfacial oxide.

The results of McKee *et al.*[107] and Li *et al.* from Motorola[113] illustrate the importance of the Sr silicide layer in protecting the Si surface from oxidation. However, the exact structure of this layer, and the optimum structure for maximum oxidation resistance and favorable electrical properties, is still debated. Liang *et al.*[115] observed

several surface reconstructions, as observed by RHEED, as the clean Si(2x1) surface was exposed to Sr. At approximately 0.35 ML Sr, a 3x2 reconstruction was observed. Increasing the Sr dosage to 0.5 ML produced a 2x1 reconstruction. Further Sr exposure resulted in 5x1, 7x1, and 8x1 reconstructions. Of these, only 0.5 ML Sr (2x1 reconstruction) was found to be oxidation resistant when exposed to $1x10^{-6}$ Torr O_2 a temperatures <200°C. Subsequent annealing in vacuum at <500°C was required to recrystallize the surface, which was then found to be oxidation resistant at high temperature (450°C) and high oxygen pressure ($5x10^{-7}$ Torr). Investigation of this structure by XPS revealed a small peak in the Si spectrum that was attributed to an interfacial silicate with Sr_2SiO_4 stoichiometry. In contrast, Lettieri *et al.*[116] found that, in deposition of both ¼ ML and ½ ML Sr deposited on clean Si(2x1), the RHEED pattern of Si[110] underwent a transition from 2x to 3x and back to the 2x reconstruction. Epitaxial deposition of SrO could be achieved with either ¼ or ½ ML Sr, with subsequent deposition of physisorbed Sr metal (3/8 ML) at low temperature before oxidant was introduced.

Recent theoretical calculations based on DFT have attempted to clarify the role of the Sr silicide in the deposition of oxides on Si.[117,118] Introduction of ½ ML Sr onto clean reconstructed Si(001) was found to passivate the surface Si dangling bonds, with Sr atoms sitting in the surface troughs between four Si dimers. Introduction of 1 ML oxygen to this surface resulted in oxygen bonding to the dimerized Si atoms; addition of further oxygen results in oxygen insertion into the dimer bonds to form Si-O-Si. These interface structures are simpler than the structures observed experimentally. Calculations showed that both the oxygen-free surface and surface with 1 ML oxygen were insulating, with no interface states in the gap. The conduction band offset between STO and Si was found to depend strongly on the interface structure, with a much larger offset for the oxidized silicide structure. This large barrier to conduction electron injection from STO to Si is necessary for gate oxide applications. In addition, Peacock *et al.* calculated the properties of the

interface structure proposed by McKee *et al.*[107] and found the interface would behave as a metallic conductor, with poor electrical properties for gate oxide applications. McKee *et al.* demonstrated favorable electrical characteristics of STO on Si with the interface structure observed in TEM; Peacock *et al.*[117] speculate this discrepancy may be due to differences in the interface structure of the film prepared for TEM and the film prepared for capacitance measurement.

For spin injection in spintronic devices, a small conduction band offset between the DMS and silicon is necessary. Despite the theoretical predictions of a large conduction band offset for the oxidized interface structure, experimental determination of the conduction band offset of STO on Si by XPS has produced a very small offset (0 – 0.1 eV).[119,120] While detrimental for gate oxide applications, this is a promising result for spin injection from Co-doped STO into silicon. Additionally, Tuan *et al.*[92] have measured the band offsets for 5 ML anatase TiO_2 / 5 ML STO / ¼ ML Sr / Si(001) deposited by MBE, and found the conduction band offsets to be 0.1 ± 0.1 eV at both interfaces, indicating the possibility of spin injection from anatase through STO to Si. STO is a well-suited template layer for the deposition of anatase on Si; the lattice mismatch between anatase and STO is only -3%. However, aside from the report of Tuan *et al.*, there have been very few reports of the deposition of epitaxial anatase on Si. Utilizing PLD, Sugiharto *et al.*[67] deposited a thick TiN buffer layer (227 nm) on clean Si(001), followed by deposition of thick $SrTiO_3$ (450 nm), and finally anatase TiO_2 (762 nm). Although epitaxy of the TiN, STO, and anatase films was observed by XRD, rocking curve measurements indicate the layers are of poor crystalline quality. In addition, RBS data indicated significant diffusion of Si and TiN.

To date, neither epitaxial Co-doped anatase nor Co-doped STO deposited on Si for evaluation as a potential DMS spin injector material has been reported. Deposition on Si is expected to significantly complicate the growth procedure due to attempts to

limit or eliminate interfacial reactions. In addition, the film strain and defect formation are expected to differ on Si versus oxide substrates. These issues need to be investigated and addressed through careful experimental work and detailed materials characterization to realize successful integration of a DMS material onto Si for practical spintronic devices.

Notes to Chapter I

1. N. Spaldin, *Magnetic Materials: Fundamentals and Device Applications.* (University Press, Cambridge, 2003).

2. B.T. Jonker, "Progress toward electrical spin injection of spin-polarized electrons into semiconductors." *Proc. IEEE* **91** (5), 727 (2003).

3. S.A. Wolf, D.D. Awschalom, R.A. Buhrman, J. Daughton, S. von Molnar, M.L. Roukes, A.Y. Chtchelkanova, and D.M. Treger, "Spintronics: a spin-based electronics vision for the future." *Science* **294**, 1488 (2001).

4. M.N. Baibich, J.M. Broto, A. Fert, F. Nguyen Van Dau, F. Petroff, P. Eitenne, G. Creuzet, A. Friederich, and J. Chazelas, "Giant magnetoresistance of (001)Fe/ (001)Cr magnetic superlattices." *Phys. Rev. Lett.* **61** (21), 2472 (1988).

5. G.A. Prinz, "Magnetoelectronics." *Science* **282**, 1660 (1998).

6. J.M.D Coey and C.L. Chien, "Half-metallic ferromagnetic oxides." *MRS Bull.* **28** (10), 720 (2003).

7. J. Daughton, "Spin-dependent sensors." *Proc. IEEE* **91** (5), 681 (2003).

8. D.D. Awschalom, M.E. Flatte, and N. Samarth, "Spintronics." *Sci. Am.* **286** (6), 66 (2002).

9. Motorola Press Release, "Motorola produces world's first 4 MBit MRAM chip." *http://www.motorola.com/mediacenter/news/detail/0,,3158_2591_23,00.html* (Oct. 27, 2003).

10. S. Datta and B. Das, "Electronic analog of the electro-optic modulator." *Appl. Phys. Lett.* **56** (7), 665 (1990).

11. S. Das Sarma, "Spintronics." *Am. Sci.* **89** (6), 516 (2001).

12. A.F. Morpurgo, J.P. Heida, T.M. Klapwijk, B.J. van Wees, and G. Borghs, "Ensemble-average spectrum of Aharonov-Bohm conductance oscillations: evidence for spin-orbit-induced Berry's phase." *Phys. Rev. Lett.* **80** (5), 1050 (1998).

13. J.M. Kikkawa and D.D. Awschalom, "Resonant spin amplification in *n*-type GaAs." *Phys. Rev. Lett.* **80** (19), 4313 (1998).

14. J.M. Kikkawa and D.D. Awschalom, "Lateral drag of spin coherence in gallium arsenide." *Nature* **397**, 139 (1999).

15. D. Hagele, M. Oestreich, W.W. Ruhle, Nestle. N., and K. Eberl, "Spin transport in GaAs." *Appl. Phys. Lett.* **73** (11), 1580 (1998).

16. P.R. Hammar and M. Johnson, "Detection of spin-polarized electrons injected into a two-dimensional electron gas." *Phys. Rev. Lett.* **88** (6), 066806 (2002).

17. J. Nitta, F. Meijer, Y. Narita, and H. Takayanagi, "Gate voltage-dependent Aharanov-Bohm experiment in the presence of Rashba spin-orbit interaction." *Physica E* **6**, 318 (2000).

18. G. Schmidt, D. Ferrand, L.W. Molencamp, A.T. Filip, and B.J. van Wees, "Fundamental obstacle for electrical spin injection from a ferromagnetic metal into a diffusive semiconductor." *Phys. Rev. B* **62** (8), R4790 (2000).

19. E.I. Rashba, "Theory of electrical spin injection: Tunnel contacts as a solution of the conductivity mismatch problem." *Phys. Rev. B* **62** (24), R16267 (2000).

20. V.F. Motsnyi, J. De Boeck, J. Das, W. Van Roy, G. Borghs, E. Goovaerts, and V.I. Safarov, "Electrical spin injection in a ferromagnet/tunnel barrier/ semiconductor heterostructure." *Appl. Phys. Lett.* **81** (2), 265 (2002).

21. A.T. Hanbicki, B.T. Jonker, G. Itskos, G. Kioseoglou, and A. Petrou, "Efficient electrical spin injection from a magnetic metal/tunnel barrier contact into a semiconductor." *Appl. Phys. Lett.* **80** (7), 1240 (2002).

22. R.M. Stroud, A.T. Hanbicki, Y.D. Park, G. Kioseoglou, A.G. Petukhov, B.T. Jonker, G. Itskos, and A. Petrou, "Reduction of spin injection efficiency by interface defect spin scattering in ZnMnSe / AlGaAs-GaAs spin-polarized light-emitting diodes." *Phys. Rev. Lett.* **89** (16), 166602 (2002).

23. E.L. Nagaev, "Colossal-magnetoresistance materials: manganites and conventional ferromagnetic semiconductors." *Phys. Rep.* **346**, 387 (2001).

24. H. Ohno, in *Semiconductor Spintronics and Quantum Computation*, edited by D.D. Awschalom, D. Loss, and N. Samarth (Springer-Verlag, New York, 2002).

25. W. Giriat and J.K. Furdyna, in *Diluted Magnetic Semiconductors*, edited by J.K. Furdyna and J. Kossut (Academic Press, Inc., San Diego, 1988), Vol. 25.

26. H. Munekata, H. Ohno, S. von Molnar, A. Segmuller, L.L. Chang, and L. Esaki, "Diluted magnetic III-V semiconductors." *Phys. Rev. Lett.* **63** (17), 1849 (1989).

27. H. Ohno, A. Shen, F Matsukura, A. Oiwa, A. Endo, S. Katsumoto, and Y. Iye, "(Ga,Mn)As: A new diluted magnetic semiconductor based on GaAs." *Appl. Phys. Lett.* **69** (3), 363 (1996).

28. H. Ohno, "Making nonmagnetic semiconductors ferromagnetic." *Science* **281**, 951 (1998).

29. K.C. Ku, J. Potashnik, R.F. Wang, S.H. Chun, P. Schiffer, N. Samarth, M.J. Seong, A. Mascarenhas, E. Johnston-Halperin, R.C. Myers, A.C. Gossard, and D.D. Awschalom, "Highly enhanced Curie temperature in low-temperature annealed [Ga,Mn]As epilayers." *Appl. Phys. Lett.* **82** (14), 2302 (2003).

30. K.W. Edmonds, K.Y. Wang, R.P. Campion, A.C. Neumann, N.R.S. Farley, B.L. Gallagher, and C.T. Foxon, "High-Curie-temperature $Ga_{1-x}Mn_xAs$ obtained by resistance-monitored annealing." *Appl. Phys. Lett.* **81** (26), 4991 (2002).

31. A. Nazmul, S. Sugahara, and M. Tanaka, "Ferromagnetism and high Curie temperature in semiconductor heterostructures with Mn δ-doped GaAs and *p*-type selective doping." *Phys. Rev. B* **67**, 241308 (2003).

32. Y. Ohno, D.K. Young, B. Beschoten, F Matsukura, H. Ohno, and D.D. Awschalom, "Electrical spin injection in a ferromagnetic semiconductor heterostructure." *Nature* **402** (6763), 790 (1999).

33. T. Dietl, H. Ohno, F. Matsukura, J. Cibert, and D. Ferrand, "Zener model description of ferromagnetism in zinc-blende magnetic semiconductors." *Science* **287**, 1019 (2000).

34. M.L. Reed, N.A. El-Masry, H.H. Stadelmaier, M.K. Ritums, M.J. Reed, C.A. Parker, J.C. Roberts, and S.M. Bedair, "Room temperature ferromagnetic properties of (Ga,Mn)N." *Appl. Phys. Lett.* **79** (21), 3473 (2001).

35. G.T. Thaler, M.E. Overberg, B. Gila, R. Frazier, C.R. Abernathy, S.J. Pearton, J.S. Lee, S.Y. Lee, Y.D. Park, and Z.G. Khim, "Magnetic properties of *n*-GaMnN thin films." *Appl. Phys. Lett.* **80** (21), 3964 (2002).

36. M. Zajac, J. Gosk, E. Grzanda, M. Kaminska, A. Twardowski, B. Strojek, T. Szyszko, and S. Podsiadlo, "Possible origin of ferromagnetism in (Ga,Mn)N."

J. Appl. Phys. **93** (8), 4715 (2003).

37. S.J. Pearton, M.E. Overberg, G.T. Thaler, C.R. Abernathy, J. Kim, F. Ren, N. Theodoropoulou, A.F. Hebard, and Y.D. Park, "Room temperature ferromagnetism in GaMnN and GaMnP." *Phys. Stat. Sol. (a)* **195** (1), 222 (2003).

38. T. Fukumura, Z. Jin, M. Kawasaki, T. Shono, T. Hasegawa, S. Koshihara, and H. Koinuma, "Magnetic properties of Mn-doped ZnO." *Appl. Phys. Lett.* **78** (7), 958 (2001).

39. S.W. Jung, S.-J. An, G.-C. Yi, C.U. Jung, S.I. Lee, and S. Cho, "Ferromagnetic properties of $Zn_{1-x}Mn_xO$ epitaxial thin films." *Appl. Phys. Lett.* **80** (24), 4561 (2002).

40. P. Sharma, A. Gupta, K.V. Rao, F.J. Owens, R. Sharma, R. Ahuja, J.M. Osorio Guillen, B. Johansson, and G.A. Gehring, "Ferromagnetism above room temperature in bulk and transparent thin films of Mn-doped ZnO." *Nat. Mater.* **2** (10), 673 (2003).

41. K. Sato and H. Katayama-Yoshida, "Stabilization of ferromagnetic states by electron doping in Fe-, Co- or Ni-doped ZnO." *Jpn. J. Appl. Phys., Part 2: Lett.* **40** (4A), L334 (2001).

42. K. Ueda, H. Tabata, and K. Tomoji, "Magnetic and electric properties of transition-metal-doped ZnO films." *Appl. Phys. Lett.* **79** (7), 988 (2001).

43. Y. Matsumoto, M. Murakami, T. Shono, T. Hasegawa, T. Fukumura, M. Kawasaki, P. Ahmet, T. Chikyow, S. Koshihara, and H. Koinuma, "Room-temperature ferromagnetism in transparent transition metal-doped titanium dioxide." *Science* **291**, 854 (2001).

44. Y. Matsumoto, M. Murakami, T. Hasegawa, T. Fukumura, M. Kawasaki, P. Ahmet, K. Nakajima, T. Chikyow, and H. Koinuma, "Structural control and combinatorial doping of titanium dioxide thin films by laser molecular beam epitaxy." *App. Surf. Sci.* **189**, 344 (2002).

45. Y. Matsumoto, R. Takahashi, M. Murakami, T. Koida, X.J. Fan, T. Hasegawa, T. Fukumura, M. Kawasaki, S. Koshihara, and H. Koinuma, "Ferromagnetism in Co-doped TiO_2 rutile thin films grown by laser molecular beam epitaxy." *Jpn. J. Appl. Phys., Part 2: Lett.* **40** (11B), L1204 (2001).

46. W.K. Park, R.J. Ortega-Hertogs, J.S. Moodera, A. Punnoose, and M.S. Seehra,

"Semiconducting and ferromagnetic behavior of sputtered Co-doped TiO_2 thin films above room temperature." *J. Appl. Phys.* **91** (10), 8093 (2002).

47. V. Shutthanandan, S. Thevuthasan, S.M. Heald, T. Droubay, M.H. Engelhard, T.C. Kaspar, D.E. McCready, L. Saraf, S.A. Chambers, B.S. Mun, N. Hamdan, P. Nachimuthu, B. Taylor, R.P. Sears, and B. Sinkovic, "Room temperature ferromagnetism in ion-implanted Co-doped TiO_2(110) rutile." *Appl. Phys. Lett.* **84** (22) 4466 (2004).

48. T. Droubay, S.M. Heald, V. Shutthanandan, S. Thevuthasan, S.A. Chambers, and J. Osterwalder, "Room-temperature ferromagnetism in Cr-doped TiO_2 anatase." *Appl. Phys. Lett.* submitted (2004).

49. N.H. Hong, W. Prellier, J. Sakai, and A. Hassini, "Fe- and Ni-doped TiO_2 thin films grown on $LaAlO_3$ and $SrTiO_3$ substrates by laser ablation." *Appl. Phys. Lett.* **84** (15), 2850 (2004).

50. N.H. Hong, J. Sakai, and A. Hassini, "Ferromagnetism at room temperature with a large magnetic moment in anatase V-doped TiO_2 thin films."*Appl. Phys. Lett.* **84** (14), 2602 (2004).

51. Y. Matsumoto, H. Koinuma, T. Hasegawa, I. Takeuchi, F. Tsui, and Y.K. Yoo, "Combinatorial investigation of spintronic materials." *MRS Bull.* **28** (10), 734 (2003).

52. T. Dietl and H. Ohno, "Ferromagnetic III-V and II-IV semiconductors." *MRS Bull.* **28** (10), 714 (2003).

53. C. Palmstrom, "Epitaxial Heusler alloys: new materials for semiconductor spintronics." *MRS Bull.* **28** (10), 725 (2003).

54. T. Dietl, A. Haury, and Y. Merle d'Aubigne, "Free carrier-induced ferromagnetism in structures of diluted magnetic semiconductors." *Phys. Rev. B* **55** (6), R3347 (1997).

55. C. Zener, "Interaction between the *d* shells in the transition metals." *Phys. Rev.* **81** (4), 440 (1951).

56. C. Zener, "Interaction between the *d*-shells in the transition metals. II. Ferromagnetic compounds of manganese with perovskite structure." *Phys. Rev.* **82** (3), 403 (1951).

57. C. Zener, "Interaction between the *d*-shells of the transition metals. III.

Calculation of the Weiss factors in Fe, Co, and Ni." *Phys. Rev.* **83** (2), 299 (1951).

58. T. Dietl, "Ferromagnetic semiconductors." *Semicond. Sci. Technol.* **17**, 377 (2002).

59. J. Jaroszynski, T. Andrearczyk, G. Karczewski, J. Wrobel, T. Wojtowicz, E. Papis, E. Kaminska, A. Piotrowska, D. Popovic, and T. Dietl, "Ising quantum Hall ferromagnet in magnetically doped quantum wells." *Phys. Rev. Lett.* **89** (26), 266802 (2002).

60. S. Das Sarma, E.H. Hwang, and A. Kaminski, "How to make semiconductors ferromagnetic: a first course on spintronics." *Solid State Commun.* **127**, 99 (2003).

61. K. Sato and H. Katayama-Yoshida, "First principles materials design for semiconductor spintronics." *Semicond. Sci. Technol.* **17**, 367 (2002).

62. M.S. Park, S.K. Kwon, and B.I. Min, "Electronic structures of doped anatase TiO_2: $Ti_{1-x}M_xO_2$ (M = Co, Mn, Fe, Ni)." *Phys. Rev. B* **65**, 161201 (2002).

63. G. Schmidt and L.W. Molencamp, "Electrical spin injection: Spin-polarized transport from magnetic into non-magnetic semiconductors," in *Semiconductor Spintronics and Quantum Computation*, edited by D.D. Awschalom, D. Loss, and N. Samarth (Springer-Verlag, Berlin, 2002).

64. S.A. Chambers, S.M. Heald, and T. Droubay, "Local Co structure in epitaxial $Co_xTi_{1-x}O_{2-x}$ anatase." *Phys. Rev. B* **67**, 100401 (2003).

65. L. Forro, O. Chauvet, D. Emin, L. Zuppiroli, H. Berger, and F. Levy, "High mobility of *n*-type charge carriers in large single crystals of anatase (TiO_2)." *J. Appl. Phys.* **75** (1), 633 (1994).

66. U. Diebold, "The surface science of titanium dioxide." *Surf. Sci. Rep.* **48** (5-8), 53 (2003).

67. Sugiharto, S. Yamamoto, T. Sumita, and A. Miyashita, "Preparation of TiO_2-anatase film on Si(001) substrate with TiN and $SrTiO_3$ as buffer layers." *J. Phys. Condens. Matter* **13**, 2875 (2001).

68. D.R. Lide, ed. *CRC Handbook of Chemistry and Physics*, 84th ed. (CRC Press, 2003).

69. M. Hansen and K. Anderko, *Constitution of Binary Alloys*. (McGraw-Hill, New York, 1958).

70. G.V. Samsonov, ed. *The Oxide Handbook*. (IFI/Plenum, New York, 1973).

71. M. Catti and G. Sandrone, "Ab initio study of corundum-like Me_2O_3 oxides (Me = Ti, V, Cr, Fe, Co, Ni)." *Faraday Discuss.* **106**, 189 (1997).

72. D.H. Kim, J.S. Yang, K.W. Lee, S.D. Bu, D.-W. Kim, T.W. Noh, S.-J. Oh, Y.-W. Kim, J.-S. Chung, H. Tanaka, H.Y. Lee, T. Kawai, J.Y. Won, S.H. Park, and J.C. Lee, "Investigations on the nature of observed ferromagnetism and possible spin polarization in Co-doped anatase TiO_2 thin films."*J. Appl. Phys.* **93** (10), 6125 (2003).

73. R.J. Kennedy and P.A. Stampe, "The influence of lattice mismatch and film thickness on the growth of TiO_2 on $LaAlO_3$ and $SrTiO_3$ substrates." *J. Cryst. Growth* **252**, 333 (2003).

74. P.A. Stampe, R.J. Kennedy, Y. Xin, and J.S. Parker, "Investigation of the cobalt distribution in the room temperature ferromagnet TiO_2:Co." *J. Appl. Phys.* **93** (10), 7864 (2003).

75. J. Li, C.H. Sow, X.S. Rao, C.K. Ong, and D.N. Zheng, "Epitaxial growth and magnetic and electric properties of Co-doped TiO_2 thin films."*Eur. Phys. J. B* **32**, 471 (2003).

76. S.R. Shinde, S.B. Ogale, S. Das Sarma, J.R. Simpson, H.D. Drew, S.E. Lofland, C. Lanci, J.P. Buban, N.D. Browning, V.N. Kulharni, J. Higgins, R.P. Sharma, R.L. Greene, and T. Venkatesan, "Ferromagnetism in laser deposited anatase $Ti_{1-x}Co_xO_{2-\delta}$ films." *Phys. Rev. B.* **67**, 115211 (2003).

77. D.H. Kim, J.S. Yang, K.W. Lee, S.D. Bu, T.W. Noh, S.-J. Oh, Y.-W. Kim, J.-S. Chung, H. Tanaka, H.Y. Lee, and T. Kawai, "Formation of Co nanoclusters in epitaxial $Ti_{0.96}Co_{0.04}O_2$ thin films and their ferromagnetism." *Appl. Phys. Lett.* **81** (13), 2421 (2002).

78. J.-Y. Kim, J.-H. Park, B.-G. Park, H.-J. Noh, S.-J. Oh, J.S. Yang, D.H. Kim, S.D. Bu, T.-W. Noh, H.-J. Lin, H.-H. Hsieh, and C.T. Chen, "Ferromagnetism induced by clustered Co in Co-doped anatase TiO_2 thin films." *Phys. Rev. Lett.* **90** (1), 017401 (2003).

79. H.S. Yang, J. Choi, V. Craciun, and R.K. Singh, "Ferromagnetism of anatase $Ti_{1-x}Co_xO_{2-\delta}$ films grown by ultraviolet-assisted pulsed laser deposition." *J. Appl.*

Phys. **93** (10), 7873 (2003).

80. S.A. Chambers, S. Thevuthasan, R.F.C Farrow, R.F. Marks, J.U. Thiele, L. Folks, M.G. Samant, A.J. Kellock, N. Ruzycki, D.L. Ederer, and U. Diebold, "Epitaxial growth and properties of ferromagnetic Co-doped TiO_2 anatase." *Appl. Phys. Lett.* **79** (21), 3467 (2001).

81. S.A. Chambers, C.M. Wang, S. Thevuthasan, T. Droubay, D.E. McCready, A.S. Lea, V. Shutthanandan, and C.F. Windish Jr., "Epitaxial growth and properties of MBE-grown ferromagnetic Co-doped TiO_2 anatase films on $SrTiO_3(001)$ and $LaAlO_3(001)$." *Thin Solid Films* **418**, 197 (2002).

82. S.A. Chambers, T. Droubay, C.M. Wang, A.S. Lea, R.F.C. Farrow, L. Folks, V. Deline, and S. Anders, "Clusters and magnetism in epitaxial Co-doped TiO_2 anatase." *Appl. Phys. Lett.* **82** (8), 1257 (2003).

83. G.C. Han, Y.H. Wu, M. Tay, K.B. Li, Z.B. Guo, and T.C. Chong, "Epitaxial growth of ferromagnetic Co:TiO_2 thin films by co-sputtering." *J. Magn. Magn. Mater.* **268**, 159 (2004).

84. D.H. Kim, J.S. Yang, Y.S. Kim, D.-W. Kim, T.W. Noh, S.D. Bu, Y.-W. Kim, Y.D. Park, S.J. Pearton, Y. Jo, and J.-G. Park, "Superparamagnetism in Co-ion-implanted anatase TiO_2 thin films and effects of postannealing." *Appl. Phys. Lett.* **83** (22), 4574 (2003).

85. N.-J. Seong, S.-G. Yoon, and C-R. Cho, "Effects of Co-doping level on the microstructural and ferromagnetic properties of liquid-delivery metalorganic-chemical-vapor-deposited $Ti_{1-x}Co_xO_2$ thin films." *Appl. Phys. Lett.* **81** (22), 4209 (2002).

86. Y.L. Soo, G. Kioseoglou, S. Kim, Y.H. Kao, P. Sujatha Devi, J. Parise, R.J. Gambino, and P.I. Gouma, "Local environment surrounding magnetic impurity atoms in a structural phase transition of Co-doped TiO_2 nanocrystal ferromagnetic semiconductors." *Appl. Phys. Lett.* **81** (4), 655 (2002).

87. A. Manivannan, G. Glaspell, and M.S. Seehra, "Controlled transformation of paramagnetism to room-temperature ferromagnetism in cobalt-doped titanium dioxide." *J. Appl. Phys.* **94** (10), 6994 (2003).

88. I.-B. Shim, S.-Y. An, C.S. King, S.-Y. Choi, and Y.W. Park, "Growth of ferromagnetic semiconducting cobalt-doped anatase titanium thin films." *J. Appl. Phys.* **91** (10), 7914 (2002).

89. H.J.F. Jansen, "Electronic structure calculations for magnetically ordered systems." *Phys. Today* **April**, 50 (1995).

90. Z. Yang, G. Liu, and R. Wu, "Distribution and magnetization of Co impurities in anatase TiO_2." *Phys. Rev. B* **67**, 060402 (2003).

91. J.M. Sullivan and S.C. Erwin, "Theory of dopants and defects in Co-doped TiO_2 anatase." *Phys. Rev. B* **67**, 144415 (2003).

92. A.C. Tuan, T.C. Kaspar, T. Droubay, J.W. Rogers Jr., and S.A. Chambers, "Band offsets for the epitaxial $TiO_2/SrTiO_3/Si(001)$ system." *Appl. Phys. Lett.* **83** (18), 3734 (2003).

93. K. Szot, W. Speier, J. Herion, and Ch. Freiburg, "Restructuring of the surface region in $SrTiO_3$." *Appl. Phys. A* **64**, 55 (1997).

94. J.H. Haeni, C.D. Theis, D.G. Schlom, W. Tian, X.Q. Pan, H. Chang, I. Takeuchi, and X.-D. Xiang, "Epitaxial growth of the first five members of the $Sr_{n+1}Ti_nO_{3n+1}$ Ruddlesden-Popper homologous series." *Appl. Phys. Lett.* **78** (21), 3292 (2001).

95. T. Suzuki, Y. Nishi, and M. Fujimoto, "Defect structure in homoepitaxial non-stoichiometric strontium titanate thin films." *Philos. Mag. A* **80** (3), 621 (2000).

96. Y.G. Zhao, S.R. Shinde, S.B. Ogale, J. Higgins, R.J. Choudhary, V.N. Kulkarni, R.L. Greene, T. Venkatesan, S.E. Lofland, C. Lanci, J.P. Buban, N.D. Browning, S. Das Sarma, and A.J. Millis, "Co-doped $La_{0.5}Sr_{0.5}TiO_{3-\delta}$: diluted magnetic oxide system with high Curie temperature." *Appl. Phys. Lett.* **83** (11), 2199 (2003).

97. R. Meyer, K. Szot, and R. Waser, "Restructuring the surface region of donor doped $SrTiO_3$ single crystals under oxidizing conditions." *Ferroelectrics* **224**, 323 (1999).

98. A.P. Ramirez, "Colossal magnetoresistance." *J. Phys.-Condens. Mat.* **9**, 8171 (1997).

99. R.H. Potze, G.A. Sawatzky, and M. Abbate, "Possibility for an intermediate-spin ground state in the charge-transfer material $SrCoO_3$." *Phys. Rev. B* **51** (17), 11501 (1995).

100. H. Taguchi, M. Shimada, and M. Koizumi, "Magnetic properties in the system

$La_{1-x}Sr_xCoO_3$ ($0.5 \leq x \leq 1.0$)." *Mater. Res. Bull.* **13**, 1225 (1978).

101. M. Pouchard, A. Villesuzanne, and J.-P. Doumerc, "Spin state behavior in some cobaltites (III) and (IV) with perovskite or related structure." *J. Solid State Chem.* **162**, 282 (2001).

102. P.D. Battle, T.C. Gibb, and A.T. Steel, "A structural comparison of the two polymorphs of $Sr_2Co_2O_5$ by cobalt K-edge extended x-ray absorption fine structure spectroscopy." *J. Chem. Soc. Dalton Trans.*, 2359 (1987).

103. Y. Ito, R.F. Klie, and N.D. Browning, "Atomic resolution analysis of the defect chemistry and microdomain structure of brownmillerite-type strontium cobaltite." *J. Am. Ceram. Soc.* **85** (4), 969 (2002).

104. V.V. Kharton, L. Shuangbao, A.V. Kovalevsky, and E.N. Naumovich, "Oxygen permeability of perovskites in the system $SrCoO_{3-\delta}$ - $SrTiO_3$." *Solid state Ionics* **96**, 141 (1997).

105. H. Nakayama and H. Katayama-Yoshida, "Theoretical prediction of magnetic properties of $Ba(Ti_{1-x}M_x)O_3$ (M = Sc, V, Cr, Mn, Fe, Co, Ni, Cu)." *Jpn. J. Appl. Phys. Part 2* **40** (12B), L1355 (2001).

106. J.S. Lee, Z.G. Khim, Y.D. Park, D.P. Norton, N. Theodoropoulou, A.F. Hebard, J.D. Budai, L.A. Boatner, S.J. Pearton, and R.G. Wilson, "Magnetic properties of Co- and Mn-implanted $BaTiO_3$, $SrTiO_3$, and $KTaO_3$." *Solid State Electron.* **47**, 2225 (2003).

107. R.A. McKee, F.J. Walker, and M.F. Chisholm, "Crystalline oxides on silicon: the first five monolayers." *Phys. Rev. Lett.* **81** (14), 3014 (1998).

108. S. Jeon, F.J. Walker, C.A. Billman, R.A. McKee, and H. Hwang, "Electrical characteristics of epitaxially grown $SrTiO_3$ on silicon for metal-insulator-semiconductor gate dielectric applications." *IEEE Electr. Device L.* **24** (4), 218 (2003).

109. Z. Yu, J. Ramdani, J.A. Curless, C.D. Overgaard, J.M. Finder, R. Droopad, K.W. Eisenbeiser, J.A. Hallmark, and W.J. Ooms, "Epitaxial oxide thin films on Si(001)." *J. Vac. Sci. Technol. B* **18** (4), 2139 (2000).

110. G.Y. Yang, J.M. Finder, J. Wang, Z.L. Wang, Z. Yu, J. Ramdani, R. Droopad, K.W. Eisenbeiser, and R. Ramesh, "Study of microstructure in $SrTiO_3$/Si by high-resolution transmission electron microscopy." *J. Mater. Res.* **17** (1), 204 (2002).

111. X. Hu, H. Li, Y. Wei, Z. Yu, D. Marshall, J. Edwards, R. Droopad, X. Zhang, A.A. Demkov, and K. Moore, "The interface of epitaxial $SrTiO_3$ on silicon: *in situ* and *ex situ* studies." *Appl. Phys. Lett.* **82** (2), 203 (2003).

112. L. Hilt Tisinger, R. Liu, J. Kulik, X. Zhang, J. Ramdani, and A.A. Demkov, "Ultraviolet-Raman studies of $SrTiO_3$ ultrathin films on Si." *J. Vac. Sci. Technol. B* **21** (1), 53 (2003).

113. H. Li, X. Hu, Y. Wei, Z. Yu, X. Zhang, R. Droopad, A.A. Demkov, J. Edwards Jr., K. Moore, W. Ooms, J. Kulik, and P. Fejes, "Two-dimensional growth of high-quality strontium titanate thin films on Si." *J. Appl. Phys.* **93** (8), 4521 (2003).

114. X. Zhang, A.A. Demkov, H. Li, X. Hu, Y. Wei, and J. Kulik, "Atomic and electronic structure of the Si/$SrTiO_3$ interface." *Phys. Rev. B* **68**, 125323 (2003).

115. Y. Liang, S. Gan, and M. Engelhard, "First step towards the growth of single-crystal oxides on Si: Formation of a two-dimensional crystalline silicate on Si (001)." *Appl. Phys. Lett.* **79** (22), 3591 (2001).

116. J. Lettieri, J.H. Haeni, and D.G. Schlom, "Critical issues in the heteroepitaxial growth of alkaline-earth oxides on silicon." *J. Vac. Sci. Technol. A* **20** (4), 1332 (2002).

117. P.W. Peacock and J. Robertson, "Structure, bonding, and band offsets of (100) $SrTiO_3$-silicon interfaces." *Appl. Phys. Lett.* **83** (26), 5497 (2003).

118. C.J. Forst, C.R. Ashman, K. Schwarz, and P.E. Blochl, "The interface between silicon and a high-*k* oxide."*Nature* **427**, 53 (2004).

119. S.A. Chambers, Y. Liang, Z. Yu, R. Droopad, J. Ramdani, and K. Eisenbeiser, "Band discontinuities at epitaxial $SrTiO_3$/Si(001) heterojunctions." *Appl. Phys. Lett.* **77** (11), 1662 (2000).

120. S.A. Chambers, Y. Liang, Z. Yu, R. Droopad, and J. Ramdani, "Band offset and structure of $SrTiO_3$/Si(001) heterojunctions." *J. Vac. Sci. Technol. A* **19** (3), 934 (2001).

CHAPTER II: EXPERIMENTAL METHODS

Deposition chamber

Thin films were deposited in a custom-designed molecular beam epitaxy (MBE) chamber from DCA Instruments, as sketched in Figure 2.1(a). Pumping is provided by both a cryopump (CTI-Cryogenics) and an ion pump (Varian), with a separate gate valve between each pump and the chamber. A base pressure in the low 10^{-10} Torr range (as measured by an ion gauge) is achieved after baking; after repeated introduction of oxygen during depositions the base pressure is in the low 10^{-8} Torr range. A vertically oriented cryoshroud around the sides of the chamber can be filled with liquid nitrogen, allowing the inner chamber walls to be cooled and act as a sorption pump, reducing the base vacuum pressure from the low 10^{-8} Torr range to the low 10^{-9} Torr range before a deposition is initiated. A horizontal heat exchanger located above the chamber floor (at the level of the metal beam sources) is cooled by chilled water.

The chamber is equipped with a sample manipulator (Thermionics Northwest, Inc.) capable of 3-axis rotation as well as x, y, and z translation. Substrates 1 cm x 1 cm square and 1 mm thick are mounted on specialized Ta sample holders (Figure 2.2) which allow transfer between the MBE chamber and the appended x-ray photoelectron spectroscopy (XPS) chamber. Substrates are placed on the Mo backing plate of the holder, and held in position by a 1 mm thick Ta retainer ring with a 1 cm square opening (which fits around the substrate). A thin Ta foil shim ring with a 1 cm diameter circular opening is spot-welded to the top of the retainer ring to hold the corners of the substrate. Deposition occurs on the exposed 1 cm diameter circle in the center of the substrate. Once attached to the manipulator, the substrate faces down in the center of the chamber for deposition. Sample heating is accomplished by electron bombardment from a high voltage filament located on the

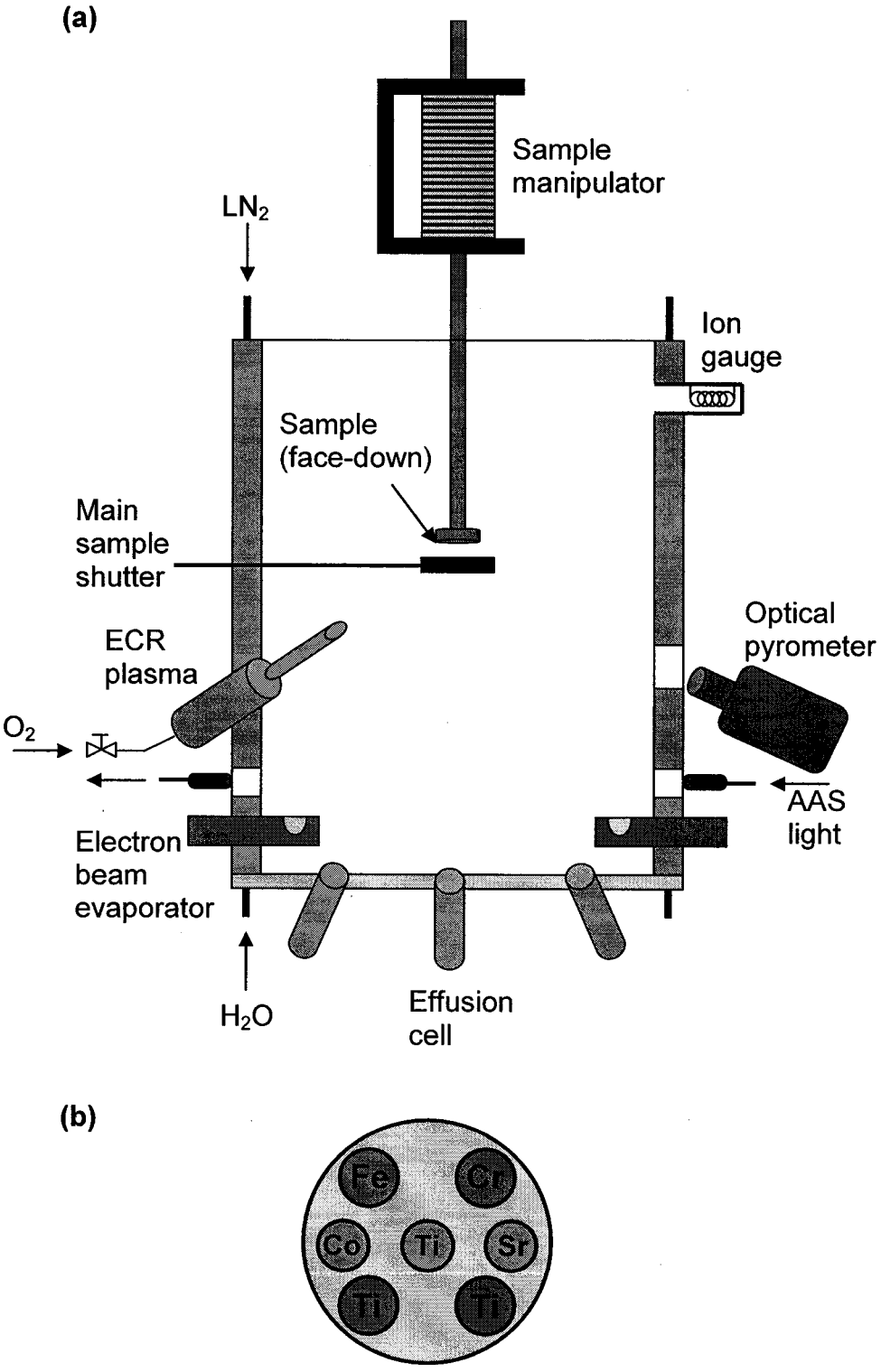

Figure 2.1. (a) Cross-section sketch of MBE deposition chamber utilized for thin film deposition. For clarity, RHEED apparatus and vacuum pumps are not shown. (b) Schematic of metal source locations in chamber if viewed from the top.

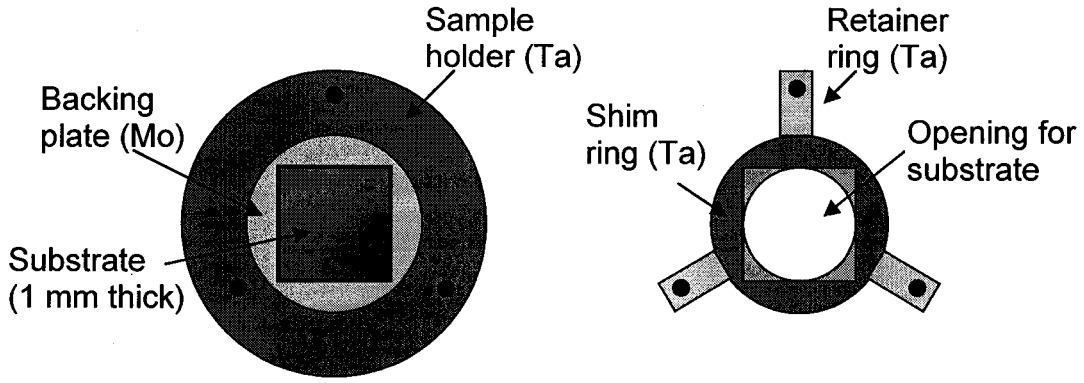

Figure 2.2. Sketch of substrate sample holder. The substrate sits on the backing plate, and is held in place with the retainer ring; the thin shim ring is spot-welded to the retainer ring and holds the corners of the substrate.

manipulator, which heats the Mo backing plate of the sample holder. The sample surface temperature is monitored by a dual-wavelength optical pyrometer (Ircon) mounted outside the chamber, which views the sample through a sapphire window. Since the pyrometer measures the infrared radiation emitted by the heated sample at two wavelengths (1.1 and 1.6 μm for temperature measurement in the range 550-1000°C), the emissivity of the surface does not need to be known. However, the difference in emissivity of the material at the two wavelengths does need to be known to produce an accurate temperature reading. For silicon, this value is known. The value for several other substrates commonly employed was determined *ex situ* by calibrating against a thermocouple. Difficulty in temperature measurement is encountered in substrates which are transparent at either of the measured infrared wavelengths (such as $SrTiO_3$). In this case the temperature reading more accurately reflects the temperature of the backing plate than the substrate surface.

The MBE chamber can accommodate seven metal deposition sources. The position of the seven sources is given in Figure 2.1(b). The floor of the chamber contains three Knudsen-style effusion cells, containing Sr, Co, and Ti, aimed at the sample growth position. Each cell has a crucible of approximately ½" diameter to hold the metal source; heating to evaporation temperatures is achieved by a resistance

filament coiled around the crucible. Cell temperature is monitored by a thermocouple and controlled by an external temperature controller (Eurotherm). Flux calibration is achieved by placing a quartz crystal oscillator (QCO) in the sample position. The metal flux is then calibrated against cell temperature. Each cell is equipped with a shutter to block the metal flux.

Four shuttered electron beam evaporator sources are arrayed just above the chamber floor, containing Ti (two sources), Cr, and Fe. Each e-beam evaporator source contains a crucible approximately 1" diameter to hold the metal source; the source is heated by electron bombardment from a high voltage filament. Sweep coils move the electron beam in a roughly circular motion on the surface of the source material to promote uniform heating and evaporation of the metal. Metal flux is monitored and controlled by atomic absorption spectroscopy (AAS). For each metal source, a lamp is utilized which produces a wavelength that is absorbed by the metal. This wavelength is brought to the chamber through a fiber optic cable, passed into the chamber through a quartz window after focusing and alignment optics, and directed through the metal atom beam, where some of the intensity is absorbed. A similar window and set of optics across the chamber collects the light. The intensity difference between the incident and collected light is proportional to the metal flux. Utilizing the QCO, the absorption can be calibrated to the absolute metal flux. Thus the absorption of the AAS light is monitored to measure the metal flux; control of the flux is accomplished by adjusting the e-beam filament current to maintain the desired absorption. Difficulties are encountered when a low flux of atoms with a small absorption cross-section is necessary for growth of high quality films, since the absorption signal may be reduced until it is on the same order as the noise of the AAS system. For example, to obtain the desired flux of Ti for $SrTiO_3$ deposition on silicon, 0.4% absorption is necessary; the typical noise of the system is ± 0.3%. In addition, the AAS absorption baseline has been observed to drift when the metal source begins evaporating, which can lead to a significant discrepancy between the

desired and actual metal flux.

Oxygen is utilized as the oxidant in oxide film deposition. Oxygen is introduced via a leak valve into an electron cyclotron resonance (ECR) plasma chamber (tectra GmbH). A microwave magnetron generates 2.45 GHz microwaves which excite the oxygen in the plasma tube, creating a plasma. The plasma density is significantly increased by a magnetic quadrupole arranged around the plasma chamber, which generates a static magnetic field. The combination of microwave frequency radiation and the static magnetic field induces free electrons in the plasma to undergo electron cyclotron resonance. The free electrons are accelerated in the ECR region, which significantly increases their path length in the plasma and results in more collisions with oxygen species. An ion trap removes ions from the plasma as the beam exits the plasma tube. The exit of the plasma tube is directed at the sample surface. Thus the oxygen pressure at the sample surface is approximately an order of magnitude greater than the pressure measured by the ion gauge. Typical plasma power settings are 70 mA and the ion trap set at approximately 1/3 of full scale. If the plasma unit is not powered, molecular oxygen can be introduced through the plasma unit into the chamber.

Reflection high energy electron diffraction (RHEED)

Real-time *in situ* analysis of the thin film surface during deposition is achieved with reflection high energy electron diffraction (RHEED).[1,2] The RHEED apparatus (Staib) consists of an electron gun producing high energy electrons (typically 15 keV) and a phosphor screen for electron detection, as illustrated in Figure 2.3(a). The electron beam crosses the sample at a very grazing angle of incidence (2.55° off the sample surface) such that the electrons only penetrate the first one or two atomic layers at the surface. The electron coherence length is approximately 1000 Å in RHEED; each surface atom illuminated by the incident electron wavepacket will

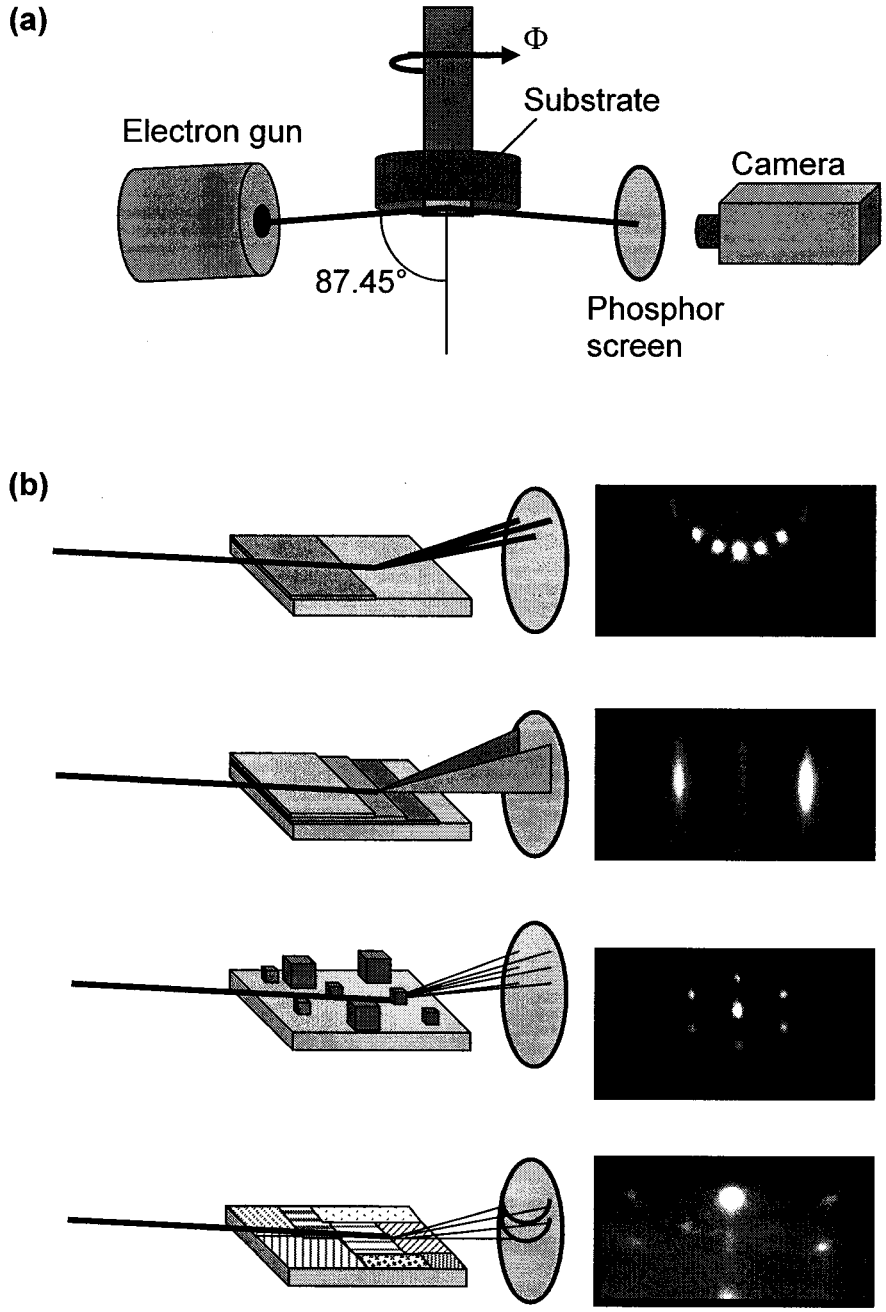

Figure 2.3. (a) Sketch of the experimental apparatus for RHEED. The substrate is mounted to the manipulator in the MBE chamber; the electron gun and phosphor screen are also in vacuum. (b) Schematic representation of various RHEED diffraction modes, as well as example RHEED diffraction images of each: diffraction arc from a smooth surface with broad terraces; streaky pattern from a smooth surface with small terraces; bulk diffraction through epitaxial surface roughness or surface particles; diffraction rings from a polycrystalline surface or surface particles.

coherently backscatter a portion of the incident wave. Constructive interference of the backscattered waves produces a diffraction pattern according to the Laue condition for diffraction,

$$\mathbf{R}\cdot(\mathbf{k}-\mathbf{k}') = 2\pi m \qquad (2.1)$$

where **R** is a real space lattice vector, **k** is the wave vector of the incident electron, **k'** is the wave vector of the scattered electron, and *m* is an integer. Aiming the incident electrons along densely-packed atomic rows results in high symmetry diffraction patterns collected by the phosphor screen at a grazing exit angle from the surface. The sample manipulator provides rotation of the azimuthal angle Φ, allowing RHEED images to be collected along these desired high-symmetry directions. The spacing of the diffraction features is inversely proportional to the periodicity of the surface. Surface reconstructions which affect the surface periodicity, such as the 2x1 reconstruction of Si(001), are observed as additional diffraction spots. Several possible diffraction images are presented in Figure 2.3(b). On surfaces in which the surface features are spaced further apart than the electron coherence length, such as steps between broad terraces on well-polished substrates, the surface appears atomically smooth and the resulting RHEED diffraction pattern consists of an arc (Laue circle) of spots. Small surface features spaced more closely than the coherence length, such as atomic steps, broaden the RHEED diffraction spots into streaks. An epitaxial film with a two-dimensional layer-by-layer growth mode will produce a streaky RHEED pattern. The electron beam will diffract through larger surface roughness features, such as three-dimensional islands, creating a spotty bulk transmission diffraction pattern. Polycrystallinity of either the smooth film surface or islands appears as diffraction rings. A charge-coupled device (CCD) camera and computer software are utilized to capture the RHEED diffraction patterns from the phosphor screen. In addition, the software allows real-time monitoring of the oscillating intensity of diffracted streaks during layer-by-layer growth mode depositions; the period of the intensity oscillation is (usually) the time required to deposit one monolayer.

Deposition procedures

In the following discussion one monolayer of Sr metal is defined as 6.78×10^{14} atoms/ cm^2 or one Sr atom at each Si site on the Si(001) surface, and one monolayer of $SrTiO_3$ is defined as one unit cell of $SrTiO_3$, consisting of one layer of SrO and one layer of TiO_2, strained to Si(001) such that the in-plane lattice parameter is 3.84 Å. One monolayer of anatase is defined to be ¼ of the unit cell height, or 2.38 Å, and the film is assumed to be strained to Si.

$SrTiO_3$ on Si

The deposition method utilized for $SrTiO_3$ (STO) on Si(001) is a modification of the methods developed by Li *et al.* at Motorola[3] and McKee *et al.* at Oak Ridge National Laboratory.[4] Silicon substrates with (001) orientation (Virginia Semiconductor) were carefully prepared to avoid metals contamination. Substrates were handled by plastic tweezers only and were not allowed to come into contact with stainless steel. Before deposition, the substrate was cleaned by placing in a Teflon beaker with buffered oxide etch (BOE) solution (4.5% HF and 36% NH_4F in water) for 1 minute. to etch off the native oxide. The substrate was then rinsed in a Teflon beaker containing distilled deionized (DI) water for approximately 1-2 minutes. The substrate was removed and dried with dry N_2. It was then placed on the sample holder without attaching the retainer ring, and placed in an ultraviolet / ozone (UV/O_3) cleaner, approximately 5 mm below the UV lamp. The sample holder, substrate, and retainer ring were exposed to the UV lamp for 3 minutes. to regrow a higher-density protective SiO_2 surface oxide, as well as to remove carbon contamination. Afterwards, the retainer ring was placed on the sample holder to secure the substrate. To prevent significant thermal contact between the retainer ring and the sample holder, the retainer ring screws were turned back approximately ¼ turn after tightening to allow a small amount of movement in the retainer ring. The substrate

surface was then blown with dry N_2 to remove any dust or particles, and immediately loaded into the vacuum load lock.

The substrate was placed in the MBE deposition chamber after achieving a base pressure in the 10^{-10} Torr range by cooling the cryoshroud. To prevent the formation of SiC, the substrate was not exposed to the RHEED electron beam until after *in situ* cleaning. The substrate was heated to approximately 750°C for a few minutes to degas. To desorb the UV/O_3-grown protective oxide, the substrate was flashed to 960°C for one minute, then cooled back to 750°C for one minute. This procedure was repeated twice more. The substrate was then cooled and RHEED images along the [100] and [110] azimuths were collected to ensure a smooth, well-ordered surface with a clear 2x1 reconstruction (observed along the [110] azimuth).

The first step in the deposition of STO on Si is the deposition of Sr metal at elevated temperature to form a strontium silicide layer. The substrate was heated to 675°C in vacuum and exposed to Sr metal at a deposition rate of 44 sec/ML (0.089 Å/s) until either ¼ or ½ ML Sr had been deposited. In the RHEED pattern along the [110] direction the 2x→3x→2x reconstruction was observed during the deposition. After cooling at least 10 minutes and collecting RHEED images, the sample was reheated to a low temperature (4.1 A / 0 V on heater power supply, estimated temperature 350-400°C) for deposition of $SrTiO_3$. Molecular oxygen was then introduced into the chamber. When the chamber pressure reached $8x10^{-8}$ Torr, the main sample shutter was opened to begin co-deposition of Sr and Ti at a deposition rate of 44 sec/ ML (0.089 Å/s), and the O_2 pressure was increased to $2x10^{-7}$ Torr. After deposition the main sample shutter and oxygen flow were closed simultaneously; the sample heater was then turned down. The sample cooled while residual oxygen was pumped from the chamber, until a base pressure of at least $5x10^{-9}$ Torr was achieved. The sample was then heated to approximately 550°C for 0.5 – 2 hours to recrystallize the STO film, as observed by the emergence and sharpening of a streaky RHEED

pattern. The sample was again cooled to collect final RHEED images of the STO buffer layer. The sample was moved to the XPS system to collect survey and high resolution photoemission spectra.

Co:TiO_2 on $SrTiO_3$ / Si

After successful deposition and recrystallization of the STO buffer layer on Si(001), the sample was heated to 550°C for deposition of Co-doped anatase TiO_2. Before deposition, the Co effusion cell was heated to 1000°C (just under the evaporation point) and the cell shutter was opened. With the ECR plasma unit powered, molecular oxygen was introduced into the chamber relatively quickly. When the plasma was observed to light (approximately $1x10^{-6}$ Torr), the main shutter was immediately opened to begin deposition of a pure TiO_2 buffer layer at a growth rate of 18 sec/ML (0.133 Å/sec) while the oxygen pressure was increased to $1.5x10^{-5}$ Torr. This method minimized exposure of the STO/Si substrate to the oxygen plasma. After 24 Å of TiO_2 buffer, the Co effusion cell was ramped to the desired evaporation temperature over two minutes with the cell shutter opened. Co doping was assumed to begin when the Co cell reached the target evaporation temperature. Pure anatase films without Co doping were deposited in a similar manner, with a deposition rate of 26 sec/ML (0.09 Å/s) and an oxygen pressure of $7x10^{-6}$ Torr. Deposition was stopped by simultaneously closing the main shutter and stopping the oxygen flow, which immediately extinguished the plasma. The sample heater was then turned down. The sample was allowed to cool before final RHEED images were collected. The sample was then moved to the XPS system to collect survey and high resolution spectra.

Co:$SrTiO_3$ on $SrTiO_3$

Deposition of Co-doped STO on STO(001) substrates is considerably less

complicated, since the deposition is essentially homoepitaxial and no care need be taken to avoid substrate oxidation. Before introduction into the chamber, STO(001) substrates (Princeton Scientific) were cleaned similarly to Si(001) substrates, since a dilute HF solution preferentially etches SrO and produces a single termination TiO_2 surface on STO.[5,6] The STO(001) substrate was etched in BOE for 1 minute, rinsed in DI water for approximately 1-2 minutes, and dried with dry N_2. The substrate was then set on the sample holder and placed in the UV/O_3 cleaner for 3 minutes to remove carbon contamination. After mounting to the sample holder, the substrate was blown off with dry N_2 and immediately loaded into the vacuum load lock.

The STO(001) substrate was cleaned *in situ* by exposure to the oxygen plasma at $2x10^{-5}$ Torr O_2 at room temperature for 30 minutes. to remove carbon contamination. RHEED images of the surface were then collected to confirm the presence of a well-ordered surface. The substrate was then heated to 800°C as measured by the pyrometer. Due to the difficulties discussed above regarding the transparency of STO to the infrared wavelengths measured by the pyrometer, this temperature reading is inaccurate. By eye, the substrate appeared to be glowing a dull orange color, and the true substrate temperature was estimated to be 650-700°C. However, since the substrate is also transparent in the visible spectrum, it is impossible to be sure the observed color originated from the substrate surface and not the backing plate. Initial depositions of Co:STO on STO(001) were accomplished utilizing the Ti e-beam evaporator as the Ti source. The Co effusion cell was brought to 1000°C with the cell shutter opened. The main shutter was then opened to initiate deposition of an STO buffer layer at a growth rate of approximately 10 sec/ML (0.39 Å/s). For Co doping, the Co effusion cell was ramped to the desired evaporation temperature in 3 minutes; deposition of Co:STO was assumed to begin when the Co cell reached evaporation temperature. Intensity of the RHEED (00) spot was monitored during growth to observe oscillations corresponding to layer-by-layer deposition. The main shutter was closed to end the deposition. The sample temperature was then lowered

relatively quickly to zero heater power; the oxygen flow was then stopped before the sample had completely cooled. The sample was allowed to cool at least 10 minutes. before final RHEED images were collected, then moved to the XPS system to collect survey and high resolution spectra.

Later depositions of Co:STO on STO(001) utilized Ti in an effusion cell as the Ti source to obtain better control over the Ti flux during deposition. After the STO(001) substrate was cleaned in the oxygen plasma for 30 minutes, the oxygen flow was stopped and the residual oxygen was pumped from the chamber. In a further effort to improve STO stoichiometry control, the sample was moved out of the way and the QCO was moved to the sample position. The flux of each metal source was adjusted to obtain the desired deposition rate as measured by the QCO. Once each source was producing the desired flux, its shutter was closed while it remained at the evaporation temperature. Once all three sources were at the desired evaporation temperature, the QCO was removed, the sample was brought to position, and the oxygen plasma was reintroduced. The sample was heated to 800°C (pyrometer reading) before closing the main shutter. The Sr and Ti effusion cell shutters were then opened for 3 minutes to allow for heating transients to stabilize; STO deposition was then initiated by opening the main shutter. After a buffer layer of pure STO had been deposited, the Co effusion cell shutter was opened to begin Co doping. Intensity of the RHEED (00) spot was monitored. The deposition was ended as described above.

Analysis techniques

X-ray photoelectron spectroscopy (XPS)

XPS[7-9] is available in an UHV analysis chamber appended to the MBE chamber for

in situ characterization of film composition. In XPS, x-ray photons are directed at the film surface. In laboratory-based XPS, Al K_α ($h\nu$ = 1486.6 eV) or Mg K_α (1253.6 eV) x-rays are commonly employed; XPS performed at a synchrotron facility can utilize a wide range of x-ray energies. Direct transfer of energy from the x-ray photon to a core-level electron in an atom near the surface results in emission of the electron, referred to as photoemission. A sketch of the atomic XPS process is given in Figure 2.4. The kinetic energy (KE) of the emitted core-level electron is characteristic of the chemical environment in which it originated, referred to as the binding energy (BE), plus the additional energy gained by the energy transfer from the x-ray photon ($h\nu$). The BE is determined primarily by the attractive force felt by the electron for the nucleus of the atom; thus there is a characteristic BE for each electron shell in an element, and these BEs vary from element to element. However, the exact BE of a core-level electron is also determined by the bonding state of the atom, which affects the atom's electron distribution and results in a chemical shift of the BE. By measuring the kinetic energy of photoemitted electrons, both elemental and chemical state information is obtained. An additional effect is observed for *p*, *d*, and *f* orbitals, where spin-orbit coupling lifts the orbital degeneracy such that a certain fraction of electrons in the orbital have a higher BE than the remainder. This results in a split of the photoemission peak into a doublet, referred to as spin-orbit splitting. The relaxation process to fill the core hole may be by an Auger emission process, so Auger electrons are also observed for some elements. Despite the low x-ray cross sections, photoemitted electrons from the valence band of the material can

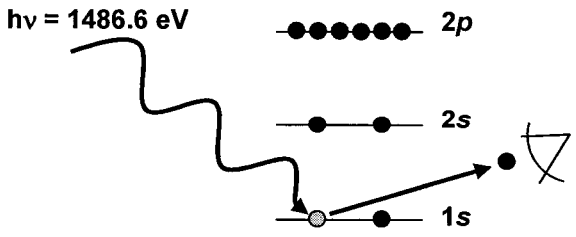

Figure 2.4. Schematic representation of core-level photoemission in XPS. Incident x-ray photon excites 1*s* electron, which is emitted and detected.

also be detected at very low binding energies. By comparing the core level and valence band energies, the level of the valence band maximum relative to the Fermi energy can be determined.[10,11] The surface sensitivity of XPS is determined primarily by the ability of photoemitted electrons to escape the material without undergoing inelastic collisions. For oxides such as STO and TiO_2, the inelastic mean free path (λ) of electrons is on the order of 20 - 30 Å, and since approximately 95% of the XPS signal originates from the first 3λ of the surface, the sampling depth is typically 40 - 80 Å.

XPS data was collected in a GammaData/Scienta SES-200 photoelectron spectrometer equipped with an Al K_α x-ray anode and monochromator providing an incident photon energy of 1486.6 eV. Photoemitted electrons were detected utilizing an electrostatic hemispherical energy analyzer placed along the sample normal (90° takeoff angle). After traversing the analyzer, energy-resolved electrons were amplified by microchannel plates and collected by a fluorescent screen. A CCD camera imaged the screen, and computer software was used to convert the data into an intensity versus energy plot. Survey scans were collected at a pass energy of 500 eV and detector slit width of 4 mm. High resolution scans were collected at a pass energy of 150 eV and detector slit width of 1.8 mm. A low energy electron flood gun was available to compensate electrical charging during measurements on insulating samples. Peak fitting was accomplished utilizing the Scienta ESCA300 analysis software. Peaks were fit as Gaussian functions, after fitting a Shirley background to the spectral region.

Auger electron spectroscopy (AES)

A related surface analysis technique is Auger electron spectroscopy (AES).[9,12] In AES, primary electrons with energies of 3-30 keV are directed at a sample surface. The primary electrons are of sufficient energy to cause the emission of core-level

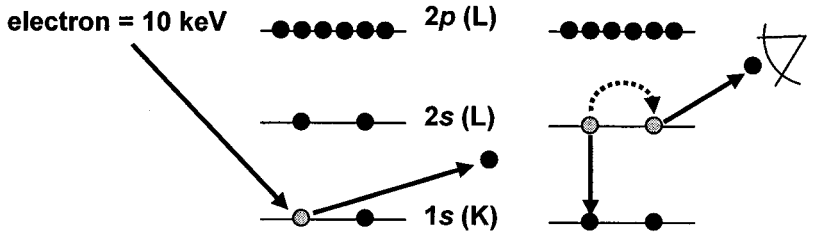

Figure 2.5. Schematic representation of KLL Auger electron emission in AES. Incident electron excites 1*s* (K) electron, which is emitted. 2*s* (L) electron loses energy to fill the core hole; its energy is absorbed by another 2*s* (K) electron, which is emitted and detected.

electrons in the sample. In the Auger process, an electron from a higher electron orbital will relax by transferring its excess energy to another electron in the same orbital, and fall to fill the core hole. The excited electron is then emitted as a secondary electron with an energy characteristic of the emitting element. If the ejected core-level electron is from the $n = 1$ core level (K), and an electron from the $n = 2$ level (L) relaxes to fill the core hole by transferring energy to another electron in the L level which is emitted as an Auger electron, the transition is referred to as a KLL Auger process, and is illustrated in Figure 2.5. The emitted electrons are typically collected in a hemispherical energy analyzer or in a cylindrical mirror analyzer (CMA). The low kinetic energy of the Auger electrons (< 2000 eV) makes this a very surface sensitive technique, with a sampling depth of less than 10 monolayers. In addition, AES offers the advantage of the ability to focus and raster the electron beam, allowing a very small area of the surface to be sampled as well as elemental mapping of the surface. However, chemical bonding information is very difficult to extract from AES data, since the Auger process involves multiple electrons and energy levels. Quantification of sample composition is accomplished by determining sensitivity factors from known standards, which to avoid matrix effects must be the same material as the sample of interest. Insulating samples cannot be measured by AES since in general surface charging cannot be compensated by the use of an electron flood gun.

The Auger data was collected on a scanning Auger microscope / Auger electron

spectrometer (Physical Electronics Model 680 Nanoprobe). The electron source was a Shottky field emission tip. Auger electrons were detected utilizing a single-pass cylindrical mirror analyzer (CMA) with a multichannel detector to amplify the signal. A fixed retard ratio (FRR) produced an energy resolution of approximately 0.4%, measured as the ratio of the full width at half maximum (FWHM) of the peak to the kinetic energy of the detected Auger electrons (e.g., for 1 keV Auger electrons the FWHM would be 4 eV). Spectra were collected utilizing a 10 nA / 10 kV electron beam, with an approximate beam size of 300 Å.

Rutherford backscattering spectrometry (RBS)

In a Rutherford backscattering spectrometry (RBS)[13-15] experiment, an energetic ion beam (generally He^+ ions of a few MeV) is directed at the sample surface. Since these ions are lighter than elements in the sample, a small fraction are backscattered by elastic collisions with atomic nuclei. The energy of a backscattered ion is dependent on the mass of the atom it collided with, as well as the energy lost penetrating through the sample before and after backscattering. The Rutherford scattering cross-section of a given element can be determined from the classical Coulomb potential. This allows absolute quantitative compositional information (i.e., the number of atoms of a given element within the sampling depth) to be extracted from RBS data without relying on sensitivity factors. Since the Coulomb potential increases with increasing nuclear charge Z, RBS is more sensitive to heavier elements. Depth profile information is also extracted from RBS data due to the energy loss experienced by the ions as they travel through the sample. The sampling depth of the He^+ ions is approximately 1 μm, with depth resolution of approximately 100 – 200 Å. The RBS spectrum is analyzed by calculating the simulated spectrum of a proposed layered structure and comparing to the experimental spectrum. By varying the composition and thickness of layers in the model structure, the experimental spectrum is fit. In channeling geometry RBS, the

energetic ions are incident on the sample parallel to a high-symmetry crystal direction. By comparing the backscattered ion yield from both random and channeling geometry measurements, a measure of the crystalline order in the sample is obtained; highly-ordered samples will backscatter fewer ions than poorly-ordered samples in the channeling geometry.

He^+ ions were produced with a radio frequency plasma source (Alphatross) and injected into a 3.4 MV tandem electrostatic accelerator (National Electrostatics Corporation 9SDH-2), where they were focused and accelerated to 2 MeV. For random geometry measurements, accelerated ions were incident on the sample at 7° off the sample normal to avoid ion channeling effects, as sketched in Figure 2.6(a). For channeling geometry measurements, the incident angle was adjusted to produce the minimum backscattering yield. The surface-barrier-type detector was placed at a scattering angle of 150° (37° off the sample normal) to collect backscattered ions. Data was collected for a total incident charge of 10-30 μC. Experimental spectra were fit utilizing the SimNRA software program.[16]

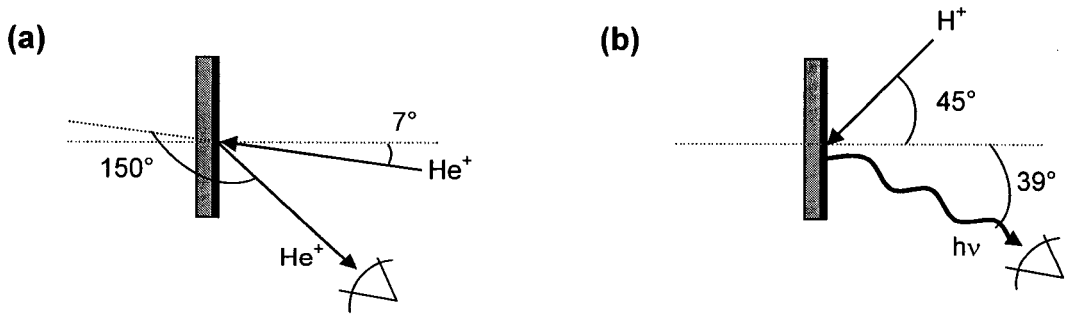

Figure 2.6. (a) Experimental setup for RBS measurements. He^+ ions are incident on the sample surface at 7° for random geometry or 0° for channeling geometry measurements. Backscattered ions are collected at a scattering angle of 150°. (b) Experimental setup for PIXE measurements. H^+ ions are incident on the sample at 45°, and x-rays are collected at 39°.

Proton-induced x-ray emission (PIXE)

Proton-induced (or particle-induced) x-ray emission spectrometry (PIXE)[17,18] is a surface analysis technique related to RBS. In PIXE, energetic light ions (generally H^+ or He^+ of a few MeV) are directed at the sample, analogous to RBS. Ions which come close to the atomic nucleus, but not close enough to be backscattered, can excite inner shell electrons in the atom which then relax by x-ray emission at characteristic energies in the range of 1-20 keV. Detection of the emitted x-rays provides elemental information with the advantage of a very low Bremsstrahlung radiation background. Due to the increasing Coulomb potential with increasing Z, PIXE is more sensitive to heavier elements. PIXE offers the advantages of higher sensitivity and better mass resolution over RBS. The sample composition can be quantified either by calculation from known cross section data, or by calibrating against a standard with a known concentration of the element of interest. Matrix effects do not interfere with the quantization since the emitted x-rays do not contain chemical state information. Since the emitted x-rays are able to escape from relatively deep within the sample, the sampling depth of PIXE is on the order of 1-2 μm, although without depth profile information.

H^+ ions of 2.5 MeV energy were generated by the plasma and accelerator described above for RBS. Accelerated ions were incident on the sample at 45° off the sample normal. The Si detector was placed 39° off the sample normal to collect the x-rays. The experimental geometry is illustrated in Figure 2.6(b). Data fitting was accomplished utilizing the GUIPIX version 2004 software program.

X-ray absorption near edge structure (XANES)

X-ray absorption near edge structure (XANES)[19,20] is one aspect of the broader analysis technique of x-ray absorption spectroscopy (XAS).[21] In XAS, x-rays are

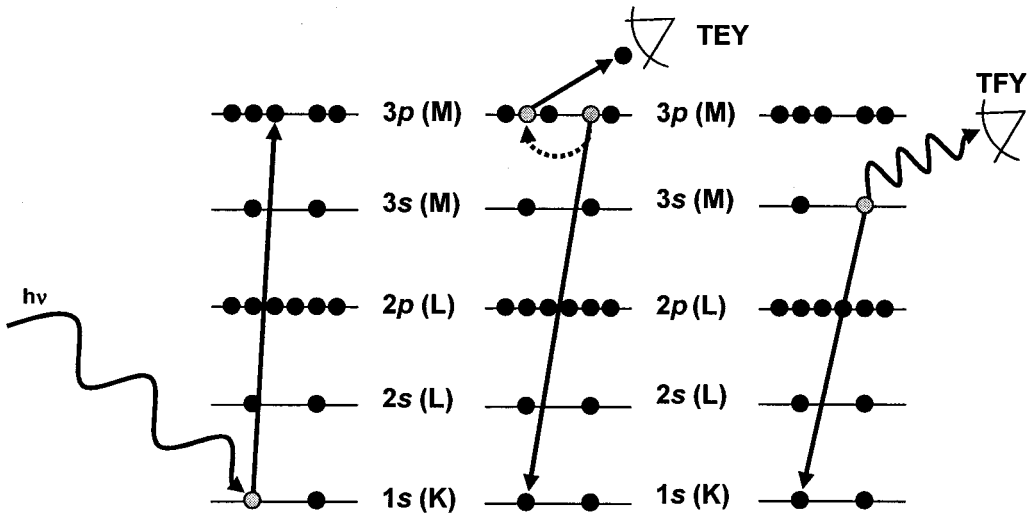

Figure 2.7. Schematic example of the atomic processes in XAS. Incident x-ray photon promotes a core-level electron to a higher unoccupied level. The core hole can be filled by an Auger process, and the emitted Auger electrons collected in TEY mode. Alternatively, the core hole can be filled by a radiative relaxation process, and the emitted photons collected in TFY mode.

directed at the sample surface. Each element in the sample will absorb x-rays of characteristic energy corresponding to the excitation of electrons from the core levels into higher unoccupied levels. The allowed electron excitations are determined by the dipole selection rule, which states that $\Delta L = \pm 1$, where L is the total orbital angular momentum. For first-row transition metals, excitation from the 1*s* core level (L = 0) to the 4*p* level (L = 1) is referred to as K-edge or K-shell absorption, excitation from the 2*p* (L = 1) core level to the 3*d* level (L = 2) is referred to as L-edge absorption, and so on. Relaxation processes of the excited atom emit both low-energy Auger electrons, which trigger a cascade of secondary electrons, and photons. The possible atomic absorption and emission processes are presented in Figure 2.7. Unlike XPS, which utilizes a single high photon energy x-ray source and sweeps the energy of detected photoelectrons, XAS sweeps the incident x-ray photon energy and detects, without energy discrimination, either emitted photons (total fluorescence yield or TFY) or emitted secondary electrons (total electron yield or TEY) at each incident photon energy. To obtain a bright source of variable photon energy, XAS is performed with a synchrotron x-ray source. The fluorescence or electron emission

spectrum obtained by XAS shows a sharp increase in intensity as the photon source reaches the energy of an absorption edge. For photon energies above the absorption edge, the absorption intensity falls off to a constant level. Superimposed on this tail is a significant amount of fine structure. In the first 50 eV above the absorption edge, the fine structure is considered "near edge," and analysis of this region is referred to as near edge x-ray absorption fine structure (NEXAFS) or XANES. The fine structure in this region is determined by a complex function of the final density of states, the transition probability, and resonance and many-body effects of the absorbing element. Development of the theoretical modeling of this region is being actively pursued. In the absence of theory, a simple comparison of lineshape to known standards yields considerable information. For a given element, the near edge structure can change appreciably depending on the charge state, as well as the local environment. For example, in Co K-edge XANES, the absorption spectrum for Co(0) is significantly different from that for Co(II), and the spectrum for Co(II) in CoO is distinguishable from Co(II) in $CoTiO_3$. Extending for several hundred eV past the near edge region is fine structure due to interference effects in the wavefunction of the excited electron as it is partially backscattered by neighboring atoms, known as extended x-ray absorption fine structure (EXAFS).[21,22] Analysis of this structure from theoretical calculations yields the local coordination number and nearest-neighbor bond distances for the element.

Co K-edge x-ray absorption measurements were made at the Advanced Photon Source at Argonne National Laboratory, on the PNC-CAT beamlines. The measurements were made in TFY mode in air. For both XANES and EXAFS measurements, the x-ray beam was incident on the sample at grazing angle (~1° off the sample surface). For XANES measurements, a bend magnet was utilized for parallel orientation (*s* polarization) of the electric field vector of the incident x-rays relative to the sample surface. For EXAFS measurements, an insertion device was utilized for perpendicular orientation (*p* polarization) of the electric field vector

relative to the sample surface. A focusing mirror was utilized for harmonic rejection, as well as to focus the beam to 50 μm if the bend magnet was used or 5 μm using the insertion device. The fluorescence signal was detected using a Ge detector with an energy resolution of approximately 1.1 eV. To eliminate spurious signals due to Bragg diffraction from the substrate, the samples were rotated at several hundred revolutions per minute (rpm). The energy calibration was monitored using Co foil, and the first peak in the derivative of the Co metal spectrum was set to E_o = 7708.8 eV. After data collection, spectra were normalized by fitting smooth curves (typically either linear or quadratic) to the data both above the absorption peak and below the onset of absorption, extrapolating both to E_o, and normalizing the data such that the difference between the fitted curves was unity. FEFF8 and iFEFFIT were utilized for EXAFS fitting.[21,23,24]

Atomic force microscopy (AFM)

Surface topography can be imaged with atomic force microscopy (AFM).[25-27] AFM utilizes a fine, sharp tip mounted on a cantilever and rastered over the sample surface, such that repulsive van der Waals interactions between the sample and tip cause deflections of the cantilever. AFM can be performed in two regimes: contact mode, in which the tip contacts the surface through the adsorbed surface fluid layer, and tapping mode, in which the cantilever oscillates near its resonant frequency, contacting the surface only at the lowest point of each oscillation. The lateral resolution of tapping mode AFM is on the order of 1-10 nm, depending on the radius of curvature of the tip. Cantilever deflections of < 1 Å can be detected; the height resolution is limited by thermal, electrical, mechanical, and acoustic noise. The observed topography is a convolution of the true surface topography and the tip shape. An ideal tip with a small radius of curvature and steep sidewalls will be capable of resolving small surface features without distortion. A dull tip will have poor resolution, and any uneven tip wear or accumulated debris on the tip will distort

the observed shape of surface features. Thus in AFM it is necessary to insure observed features are an accurate representation of the surface topography and free of tip effects.

Tapping mode AFM images were obtained in a Digital Instruments Nanoscope IIIa equipped with a piezoelectric scanner. Cantilever deflections were observed by reflecting a laser beam off the cantilever and monitoring the beam's deflection with a four-quadrant photodiode. Veeco TESP probes were utilized, consisting of a single crystal silicon substrate with an integral cantilever and tip produced by etching techniques. The cantilevers were 125 μm long with a resonant frequency in the range of 300-400 kHz and a spring constant of 20-100 N/m. The Si tips had a nominal radius of curvature of 5-10 nm. Scans were collected in 1-5 μm square regions of the sample surface, with 512 data points per line, at a scan rate of 0.25-1.00 Hz. After data collection, images were processed utilizing the *Flatten* procedure within the DI Nanoscope software. The third order *Flatten* procedure fits the scan line to a third order polynomial, which is then subtracted from the scan line. This removes Z offset between scan lines, as well as tilt and bow in each scan line.

Transmission electron microscopy (TEM)

Transmission electron microscopy (TEM)[28,29] is utilized to image thin samples of materials with very high spatial resolution, and is capable of atomic resolution in some cases. A well-focused energetic electron beam is directed at the sample; the elastic scattering, inelastic scattering, and phase shift of the transmitted electrons are used to produce direct images, high resolution (atomic-scale) images, and diffraction patterns. In addition, compositional information can be obtained by either collecting characteristic x-rays emitted by the sample due to electron-electron interactions with the primary electron beam (energy-dispersive x-ray spectroscopy or EDS), or by measuring the energy lost by the primary electron beam during the electron-electron

interactions (electron energy loss spectroscopy or EELS). Special specimen thinning techniques are employed to obtain electron-transparent specimens (usually < 200 nm thick).

Samples were prepared for TEM by standard thin film methods. The sample was first cut in half and epoxied film side to film side to protect the film during subsequent sample preparation. The sample was then cut to form cross-sections and thinned using tripod wedge polishing followed by Ar ion beam milling to obtain electron transparent specimens. High-resolution TEM analysis was carried out on a Jeol JEM 2010F microscope with a specified point-to-point resolution of 0.194 nm. The operating voltage on the microscope was 200 keV. All images were digitally recorded with a slow scan CCD camera (image size 1024 x 1024 pixels), and image processing was carried out using Digital Micrograph software by Gatan, Inc.

X-ray diffraction (XRD)

X-ray diffraction (XRD)[30-32] provides information about the crystal structure of a material. In XRD, x-rays of a given wavelength are directed at the crystalline sample at varying angles of incidence. At certain incident angles (θ, as measured from the sample surface), the x-ray path length of beams diffracted by successive atomic planes (parallel to the sample surface) will be an integer number of wavelengths, leading to constructive interference of the diffracted x-rays exiting the sample. This criterion is summarized by the Bragg diffraction equation,

$$n\lambda = 2d\sin(\theta) \qquad (2.2)$$

where n is an integer, λ is the x-ray wavelength, and d is the vertical spacing of the atomic planes. The diffracted x-rays are collected by a detector placed opposite the anode at an angle θ from the sample surface (2θ from the transmitted x-ray beam). At all incident angles which do not meet the Bragg criterion, the diffracted beams will destructively interfere. Through the Bragg equation, the θ-2θ values that

produce peaks in the intensity plot provide precise information on the atomic spacing of the diffracting planes in the crystal. From this data, the crystal structure, orientation, and strain state of the sample can be determined. In addition, the width of the x-ray intensity peak can reflect the crystalline quality of the sample, since well-ordered samples meet the Bragg criterion at precisely one incident angle, resulting in a sharp, narrow peak. In thin films of crystalline material the peak width is also influenced by the film thickness, since thinner films have fewer atomic planes to provide destructive interference at angles close to the Bragg angle, resulting in a wider peak. Reciprocal space mapping is utilized to obtain more information on a given diffraction peak. By tilting the sample slightly in all directions relative to the detector, a three-dimensional "map" of the diffraction peak in reciprocal space is obtained. The peak width provides information on the crystalline order in the sample. In addition, the exact location of the diffraction peak maximum can be located. This is especially useful for diffraction from planes which are not parallel to the substrate planes and allows the determination of the in-plane lattice parameter of the sample.

High resolution XRD patterns were obtained utilizing a Philips X'Pert Pro MRD System (PW3040/60 type) equipped with a four-circle goniometer which allowed both θ-2θ scans and reciprocal space mapping. Monochromatized Cu $K_{\alpha 1}$ radiation (1.5406 Å) was employed as the x-ray source; the anode was operated at 45 kV and 40 mA. Incident x-ray beam optics included a ½° fixed divergence slit and 10 mm axial beam mask. A ¼° receiving slit was placed in front of the detector.

Vibrating sample magnetometry (VSM)

Magnetic properties of a material can be measured by vibrating sample magnetometry (VSM).[33,34] In VSM, the sample is mounted to a long arm which is attached to a vibrating drive head. The sample is positioned between two large

electromagnets which produce a variable DC magnetic field. The sample is vibrated by the drive head with an up-and-down motion, such that the sample remains in a uniform magnetic field. Sensitive detection coils placed near the sample detect the change in magnetic flux emanating from the sample as the sample is vibrated relative to the coils. This provides a measure of the magnetic moment of the sample (M) at the given applied magnetic field (H). As the applied magnetic field is varied, the magnetic hysteresis loop of the sample is obtained. The magnetic response of the substrate is also included in the measurement, and can be subtracted out by either performing a measurement on a substrate with no film to determine the background signal, or, if the substrate response is diamagnetic, a linear background can be subtracted from the data. By placing the sample in either a cryostat or heating unit within the VSM, the temperature-dependent magnetic properties, such as the Curie transition temperature, can be measured.

VSM measurements were performed with a 7400 VSM system (Lakeshore Cryotronics, Inc.) equipped with a 4-inch electromagnet. For room temperature magnetic measurements of the in-plane magnetic moment, the sample was mounted to a glass rod with a small amount of vacuum grease; the glass rod was then mounted to the drive head. A sketch of the experimental setup is given in Figure 2.8. The drive head operates at a vibration frequency of 84 Hz and 3 mm vertical amplitude. For maximum sensitivity, the gap between detector coils was set to be just large enough to accommodate the sample without touching. The applied magnetic field in the gap was measured by a Gaussmeter probe placed at the detector coils. After data collection, the diamagnetic response of the substrate (either Si or STO) was removed by subtracting a linear background from the data.

Four-point probe

Four-point probe measurements were made to determine the sheet resistivity of

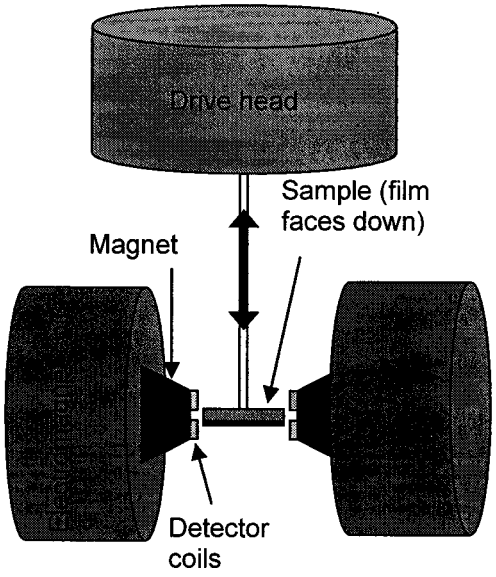

Figure 2.8. Experimental setup for VSM measurements. The sample is attached to the glass rod with a small amount of vacuum grease applied to the back side of the substrate. The drive head then vibrates the glass rod vertically; detector coils measure the change in magnetic flux caused by the sample as it moves past the coils.

semiconducting oxides deposited on insulating oxide substrates. The four point probe apparatus consists of four equally spaced metal tips which are contacted to the film surface, as illustrated in Figure 2.9. Current and voltage are supplied and monitored by a Keithley 2400 SourceMeter. To determine the resistivity of a thin film sample, a set current (0.025 – 10 μA) is applied between the outer two metal probes. The voltage drop arising from the resistance of the thin film is measured across the inner two metal probes. The sample resistivity can then be calculated from:

$$R = \Delta V / I = (\rho / A)\, dr \qquad (2.3)$$

where R is the sample resistance in Ω, ρ is the resistivity of the sample in Ω·cm, V is the measured voltage drop, I is the applied current, and A is the area across which current is flowing. Assuming uniform current flux across the depth of the thin film such that $A = 2\pi r t$, where t is the film thickness (in cm), Equation 2.3 can be integrated between probes V_1 and V_2 to give:

$$\rho = (\pi / \ln 2)\, (\Delta V / I)\, t \qquad (2.4)$$

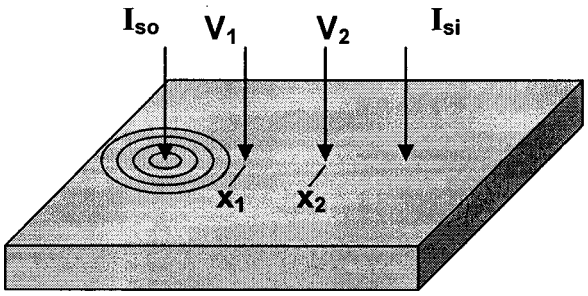

Figure 2.9. Experimental setup for four-point probe resistivity measurements. Four equally spaced metal probes are represented by arrows in the sketch. Current is applied across the outer probes, and the voltage drop due to resistance in the film is measured across the two inner probes. Rings of constant current flux flowing from I_{source} are included in the sketch.

A factor of 2 has been removed by assuming only half the current flowing from the source probe reaches the sink probe. The maximum allowed voltage drop is set to 21 V; if necessary the current is reduced from the set value to maintain a voltage drop of 21 V or less. Resistivity measurements cannot be made accurately for thin films deposited on semiconducting substrates such as Si, since the technique would measure the resistive properties of both the film and the substrate.

Notes to Chapter II

1. W.R. Flavell, "Surface Structure Determination by Interference Techniques," in *Surface Analysis: The Principal Techniques*, edited by J.C. Vickerman (John Wiley and Sons, New York, 1997).

2. J.E. Mahan, K.M. Geib, G.Y. Robinson, and R.G. Long, "A review of the geometrical fundamentals of reflection high-energy electron diffraction with application to silicon surfaces." *J. Vac. Sci. Technol. B* **8** (5), 3692 (1990).

3. H. Li, X. Hu, Y. Wei, Z. Yu, X. Zhang, R. Droopad, A.A. Demkov, J. Edwards Jr., K. Moore, W. Ooms, J. Kulik, and P. Fejes, "Two-dimensional growth of high-quality strontium titanate thin films on Si." *J. Appl. Phys.* **93** (8), 4521 (2003).

4. R.A. McKee, F.J. Walker, and M.F. Chisholm, "Crystalline oxides on silicon: the first five monolayers." *Phys. Rev. Lett.* **81** (14), 3014 (1998).

5. G. Koster, B.L. Kropman, G.J.H.M. Rijnders, D.H.A. Blank, and H. Rogalla, "Quasi-ideal strontium titanate crystal surfaces through formation of strontium hydroxide." *Appl. Phys. Lett.* **73** (20), 2920 (1998).

6. M. Kawasaki, K Takahashi, T. Maeda, R. Tsuchiya, M. Shinohara, O. Ishiyama, T. Yonezawa, M. Yoshimoto, and H. Koinuma, "Atomic control of the $SrTiO_3$ crystal surface." *Science* **266**, 1540 (1994).

7. B.D. Ratner and D.G. Castner, "Electron Spectroscopy for Chemical Analysis," in *Surface Analysis: The Principal Techniques*, edited by J.C. Vickerman (John Wiley and Sons, New York, 1997).

8. C.S. Fadley, "Basic concepts of x-ray photoelectron spectroscopy," in *Electron Spectroscopy Theory, Techniques, and Applications*, edited by C.R. Brundle and A.D. Baker (Pergamon Press, 1978), Vol. II.

9. D. Briggs and M.P. Seah, *Practical Surface Analysis by Auger and X-ray Photoelectron Spectroscopy*. (John Wiley and Sons, New York, 1984).

10. E.A. Kraut, R.W. Grant, J.R. Waldrop, and S.P. Kowalczyk, "Precise determination of the valence-band edge in x-ray photoemission spectra: Application to measurements of semiconductor interface potentials." *Phys. Rev. Lett.* **44** (24), 1620 (1980).

11. E.A. Kraut, R.W. Grant, J.R. Waldrop, and S.P. Kowalczyk, "Semiconductor core-level to valence-band maximum binding-energy differences: Precise determination by x-ray photoelectron spectroscopy." *Phys. Rev. B* **28** (4), 1965 (1983).

12. H.J. Mathieu, "Auger Electron Spectroscopy," in *Surface Analysis: The Principal Techniques*, edited by J.C. Vickerman (John Wiley and Sons, New York, 1997).

13. E. Taglauer, "Low-energy Ion Scattering and Rutherford Backscattering," in *Surface Analysis: The Principal Techniques*, edited by J.C. Vickerman (John Wiley and Sons, New York, 1997).

14. S.M. Baumann, "Rutherford Backscattering Spectrometry," in *Encyclopedia of Materials Characterization*, edited by C.R. Brundle, C.A. Evans Jr., and S. Wilson (Butterworth-Heinemann, Boston, 1992).

15. J.R. Tesmer and M. Nastasi, ed. *Handbook of Modern Ion Beam Materials Analysis*. (Materials Research Society, Pittsburgh, 1995).

16. M. Mayer, ed. *SIMNRA User's Guide*. (Max-Planck-Institut fur Plasmaphysik, Germany).

17. R.G. Musket, "Particle-Induced X-ray Emission," in *Encyclopedia of Materials Characterization*, edited by C.R. Brundle, C.A. Evans Jr., and S. Wilson (Butterworth-Heinemann, Boston, 1992).

18. S.A.E. Johansson, J.L. Campbell, and K.G. Malmqvist, ed. *Particle Induced X-ray Emission Spectrometry (PIXE)*. (John Wiley and Sons, New York, 1995).

19. J. Stohr, *NEXAFS Spectroscopy*. (Springer-Verlag, New York, 1992).

20. D. Norman, "Surface Extended X-ray Absorption Fine Structure and Near Edge X-ray Absorption Fine Structure," in *Encyclopedia of Materials Characterization*, edited by C.R. Brundle, C.A. Evans Jr., and S. Wilson (Butterworth-Heinemann, Boston, 1992).

21. J.J. Rehr and R.C. Albers, "Theoretical approaches to x-ray absorption fine structure." *Rev. Mod. Phys.* **72** (3), 621 (2000).

22. M.R. Antonio, "Extended X-ray Absorption Fine Structure," in *Encyclopedia of Materials Characterization*, edited by C.R. Brundle, C.A. Evans Jr., and S. Wilson (Butterworth-Heinemann, Boston, 1992).

23. M. Newville, Ravel. B., D. Haskel, J.J. Rehr, E.A. Stern, and Y. Yacoby, "Analysis of multple-scattering XAFS data using theoretical standards." *Physica B* **208&209**, 154 (1995).

24. M. Newville, "IFEFFIT: interactive XAFS analysis and FEFF fitting." *J. Synchrotron Radiat.* **8**, 322 (2001).

25. G.J. Leggett, "Scanning Tunneling Microscopy and Atomic Force Microscopy," in *Surface Analysis: The Principal Techniques*, edited by J.C. Vickerman (John Wiley and Sons, New York, 1997).

26. R.S. Howland and M.D. Kirk, "Scanning Tunneling Microscopy and Scanning Force Microscopy," in *Encyclopedia of Materials Characterization*, edited by C.R. Brundle, C.A. Evans Jr., and S. Wilson (Butterworth-Heinemann, Boston, 1992).

27. *Scanning Probe Microscopy Training Notebook.* (Digital Instruments).

28. L. Reimer, *Transmission Electron Microscopy Physics of Image Formation and Microanalysis*. (Springer-Verlag, New York, 1984).

29. K.E. Sickafus, "Transmission Electron Microscopy," in *Encyclopedia of Materials Characterization*, edited by C.R. Brundle, C.A. Evans Jr., and S. Wilson (Butterworth-Heinemann, Boston, 1992).

30. M.F. Toney, "X-ray Diffraction," in *Encyclopedia of Materials Characterization*, edited by C.R. Brundle, C.A. Evans Jr., and S. Wilson (Butterworth-Heinemann, Boston, 1992).

31. D.K. Bowen and B.K. Tanner, *High Resolution X-ray Diffractometry and Topography*. (Taylor and Francis, Philadelphia, 1998).

32. B.D. Cullity, *Elements of X-ray Diffraction*, Second ed. (Addison-Wesley, Menlo Park, 1978).

33. D. Speliotis, "Getting the most from your vibrating sample magnetometer." (ADE Technologies, Inc).

34. J.A. Gerber, W.L. Burmester, and D.J. Sellmeyer, "Simple vibrating sample magnetometer." *Rev. Sci. Instrum.* **53** (8), 691 (1982).

CHAPTER III: ANATASE TiO_2 / $SrTiO_3$ / Si(001)

To deposit epitaxial anatase TiO_2 on Si(001), it is necessary to utilize a buffer layer to prevent interfacial reactions resulting in Ti silicide and SiO_2 formation, which would destroy the Si surface template for epitaxy. In this work, a buffer layer consisting of ¼ or ½ ML Sr deposited on the clean Si(001) surface to form a silicide, followed by epitaxial $SrTiO_3$ (STO), was employed. Epitaxy of STO on Si(001) is possible since the lattice mismatch between STO(001) and Si(001) is only 1.5% if the *a-b* plane of STO is rotated 45° relative to Si such that (001)STO // (001)Si and [100]STO // [110]Si. For thin STO layers, the small lattice mismatch is expected to cause the STO layer to grow with compressive strain to more closely match the Si lattice. The lattice mismatch between anatase TiO_2 and Si(001) is -1.5%, and the mismatch between anatase TiO_2 and unstrained STO is -3%. The actual lattice mismatch between anatase TiO_2 and 10 ML STO deposited on Si is expected to be between -1.5% and -3%, depending on the strain in the STO layer.

Silicon

For successful epitaxial deposition, it is necessary to begin with a clean, well-ordered Si(001) surface. After substrate preparation as described in Chapter II, RHEED images of the cleaned Si(001) surface were obtained to evaluate the surface order. The top layer of atoms on the Si(001) surface form dimers to reduce the number of surface dangling bonds, resulting in a 2x1 surface reconstruction that can be observed in RHEED. Figure 3.1 shows a sketch of the Si(001) surface and the 2x1 surface reconstruction (Figure 3.1(a)), as well as example RHEED images taken along the [110] and [100] azimuths of clean Si, showing a clean, well-ordered surface with broad terraces and a clear 2x1 reconstruction (Figure 3.1(b)), a relatively poor surface with smaller terraces (Figure 3.1(c)), and a surface exhibiting a crystalline impurity

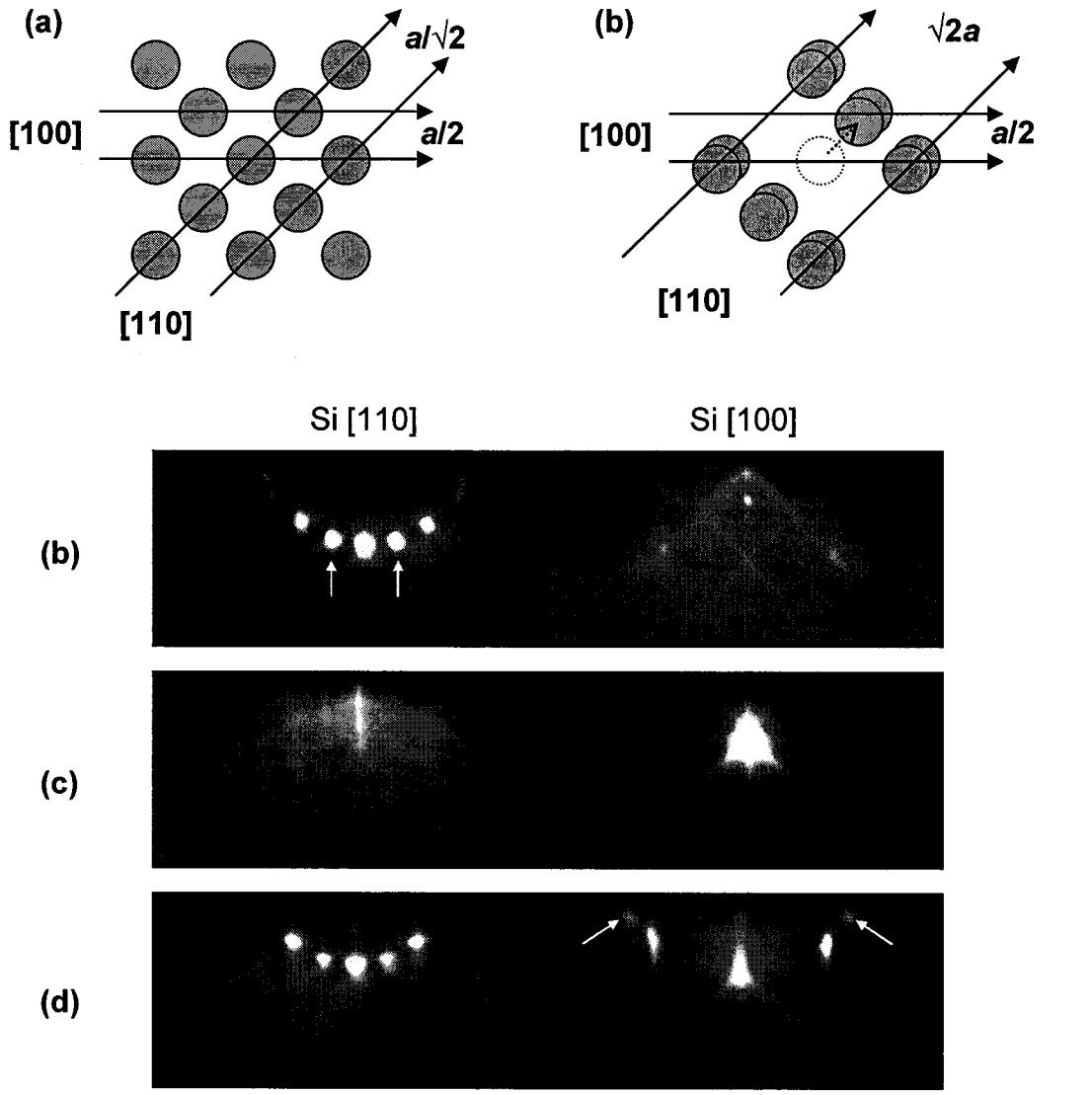

Figure 3.1. (a) Sketch of Si(001) surface before and after 2x1 surface reconstruction. Arrows indicate direction of electron beam and atomic spacing for RHEED measurements. Dotted circle indicates original position of Si atom before reconstruction. (b) RHEED images along Si[110] and Si[100] azimuths of cleaned Si. Arrows indicate the extra spots produced by the 2x reconstruction. (c) RHEED images of cleaned Si surface with terrace size less than the electron coherence length. (d) RHEED images of cleaned Si with crystalline β-SiC contamination. Arrows indicate spots produced by SiC.

(Figure 3.1(d)). The crystalline impurity spots have been identified[1] as transmission diffraction through epitaxial β-SiC, which has the zinc-blende structure with $a = 4.36$ Å. For most samples the Si surface was strongly ordered without crystalline SiC, although a strong correlation between the quality of the clean Si(001) surface and the

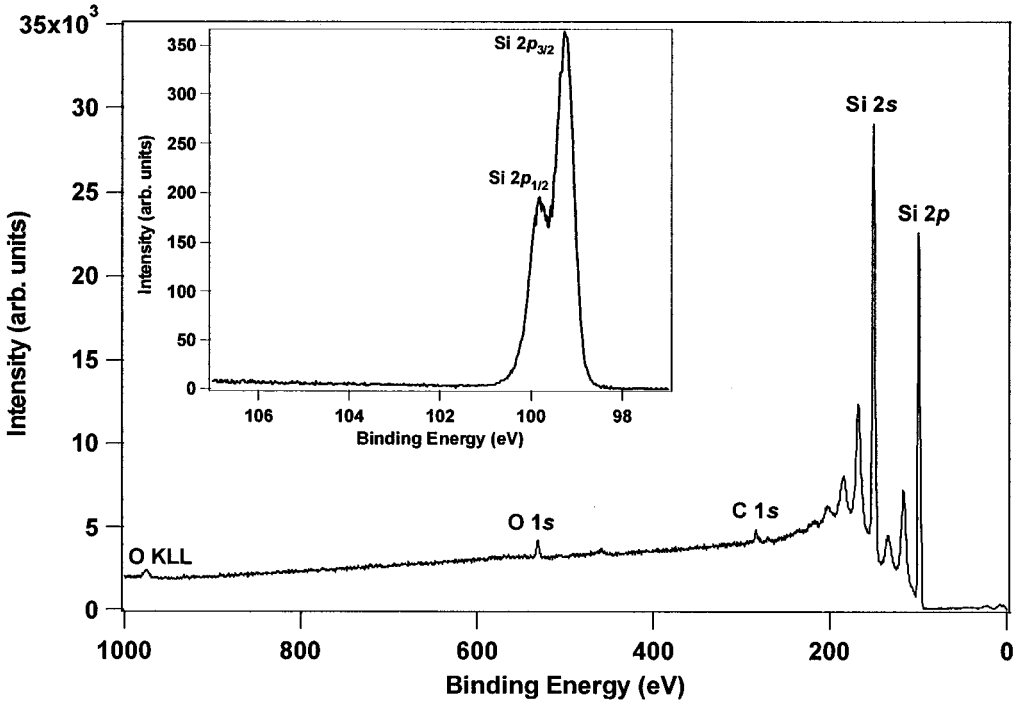

Figure 3.2. XPS survey spectrum of Si(001) substrate after *ex situ* cleaning and *in situ* oxide desorption. Surface contamination by oxygen and carbon is present. High resolution Si 2*p* spectrum in inset shows no evidence of oxidized Si species.

quality of subsequent layers could not be made. An XPS survey spectrum of clean Si is shown in Figure 3.2. The small carbon and oxygen peaks are the result of surface contamination accumulated during UHV transfer to the XPS chamber. The lack of Si-O bonding is evidenced by the high resolution spectrum of Si 2*p* shown in the inset, in which no oxidized Si is observed. Fully stoichiometric SiO_2 shifts the Si 2*p* binding energy approximately 4 eV above the bulk value; substoichiometric SiO_x falls between the bulk and fully oxidized binding energies, depending on the degree of oxidation. On cleaned Si, no detectable SiO_x is present, and the surface contamination observed in XPS is most likely desorbed as the substrate is heated to 675°C for Sr silicide deposition.

Strontium silicide

Deposition of Sr metal onto clean Si(001) at elevated temperature (675°C) results in

the formation of Sr silicide (nominally $SrSi_2$). The deposition can be monitored in real time by RHEED. At approximately 1/6 ML Sr,[2] the Si surface undergoes a reconstruction observed in the [110] azimuth as a transition from the 2x to a 3x reconstruction. As the Sr coverage is increased to ¼ ML, the 3x reconstruction transitions back to a 2x pattern. The 2x pattern remains up to ½ ML Sr coverage. Between ½ and 1 ML Sr, several higher order reconstructions (5x, 7x, 8x) are observed.[3] Previous groups have claimed both ¼ and ½ ML Sr coverages are effective in protecting the Si surface from oxidation during subsequent oxide deposition.[2,4]

Figure 3.3 shows the Si [110] RHEED evolution during ¼ ML Sr deposition. At

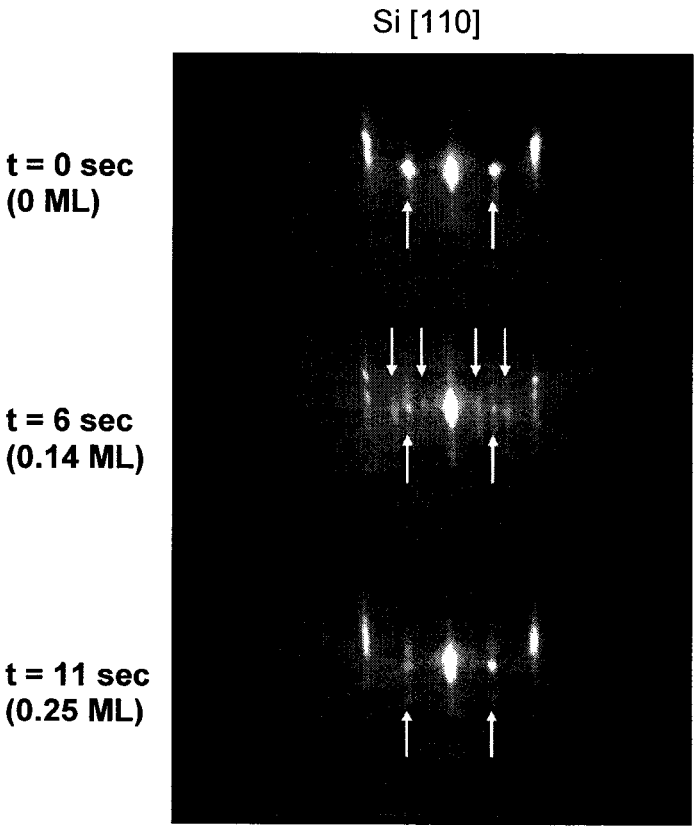

Figure 3.3. Series of RHEED images as Sr metal is deposited on clean Si(001) at 675°C. Up arrows indicate spots from the 2x reconstruction of Si(001); down arrows indicate spots from the 3x reconstruction induced by Sr deposition.

approximately 1/6 ML coverage, a clear 3x reconstruction is observed, although a portion of the surface retains the 2x reconstruction of clean Si. The 3x reconstruction transitions back to a 2x reconstruction by ¼ ML coverage. The transition 2x→3x→2x was not always clearly observed during Sr deposition, but no correlation between the observation of a clear 3x transition during Sr deposition and the quality of the subsequent STO layer could be made. Likewise, the deposition of ¼ or ½ ML Sr did not significantly affect the crystalline quality of the STO layer, as observed by RHEED. However, the use of ¼ or ½ ML Sr was found to affect the oxidation resistance of the Si surface during deposition of STO. Shown in Figure 3.4 are both final RHEED images and high resolution Si 2*p* XPS spectra of 10 ML STO deposited on Si(001) utilizing either ¼ ML (Figure 3.4(a)) or ½ ML (Figure 3.4(b)) Sr at the interface. The final quality of the STO film (after annealing to recrystallize) was similar for both coverages, although the ¼ ML Sr sample exhibited slight modulation of the RHEED streaks, which indicates some surface roughness. The ½ ML Sr sample did not exhibit modulation, indicating a smooth STO surface. The XPS spectra indicate that the Si interface protected by ¼ ML Sr was partially oxidized during STO deposition, as evidenced by the increased intensity centered around 102-103 eV. No evidence of SiO_x was observed for the Si interface protected by ½ ML

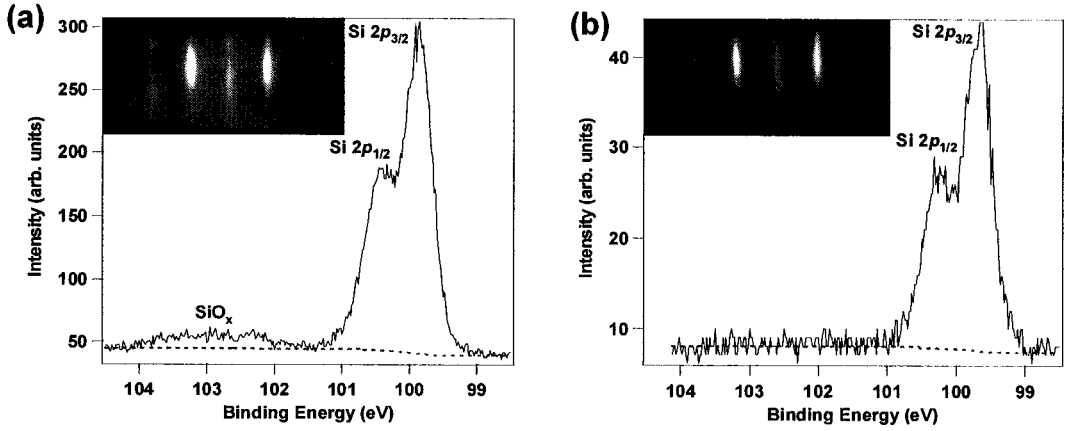

Figure 3.4. Final RHEED images along th STO[001] azimuth and high resolution XPS Si 2*p* spectra of 10 ML STO deposited on Sr / Si(001), along with a fitted Shirley background (dotted line). (a) 10 ML STO / ¼ ML Sr / Si(001). (b) 10 ML STO / ½ ML Sr / Si(001). Crystalline quality of the STO surface is comparable, but no oxidation of the Si surface is observed with ½ ML Sr.

Sr, which is clearly seen in comparing the XPS intensity to the fitted Shirley background. This indicates the use of ½ ML Sr significantly improves the oxidation resistance of the Si interface compared to ¼ ML Sr. In the initial studies of pure anatase deposited on STO / Si(001), ¼ ML Sr was utilized. In subsequent work on Co-doped anatase, the STO buffer layer was prepared with ½ ML Sr.

$SrTiO_3$ buffer layer

It is necessary to deposit the STO buffer layer under carefully controlled conditions to prevent oxidation of the Si interface. As described in detail in Chapter II, this is accomplished by depositing the thin STO film (usually 10 ML) under sufficient oxygen pressure ($2x10^{-7}$ Torr) to oxidize the metals but at low temperature (350-400°C) to reduce oxygen diffusion to and reactivity at the Si interface. This is facilitated by the catalytic oxidation properties of Sr, which allows full oxidation of Sr and Ti to STO at lower temperature and oxygen pressure than, for example, TiO_2. With this high oxygen pressure / low temperature method, 10 ML STO could be deposited without significant oxidation of the Si interface, as illustrated above in Figure 3.4(b). The crystallinity of the as-deposited STO film was found to range from fully amorphous to well-crystallized, as judged by RHEED. The film crystallinity was often improved by annealing under oxygen-free conditions to relatively high temperature (550°C). The success of this deposition method on the crystalline quality of the final STO film was found to vary significantly, as presented in Figure 3.5 for four samples of 10 ML STO / ½ ML Sr / Si(001) deposited and annealed under nominally the same conditions. In some cases an as-deposited amorphous film could be recrystallized to obtain a well-ordered STO(001) surface (as shown in Figure 3.5(b)), while in other cases annealing produced no visible change in the amorphous film (Figure 3.5(a)). Likewise, the degree of improvement in film crystallinity after annealing was found to vary in films which were at least

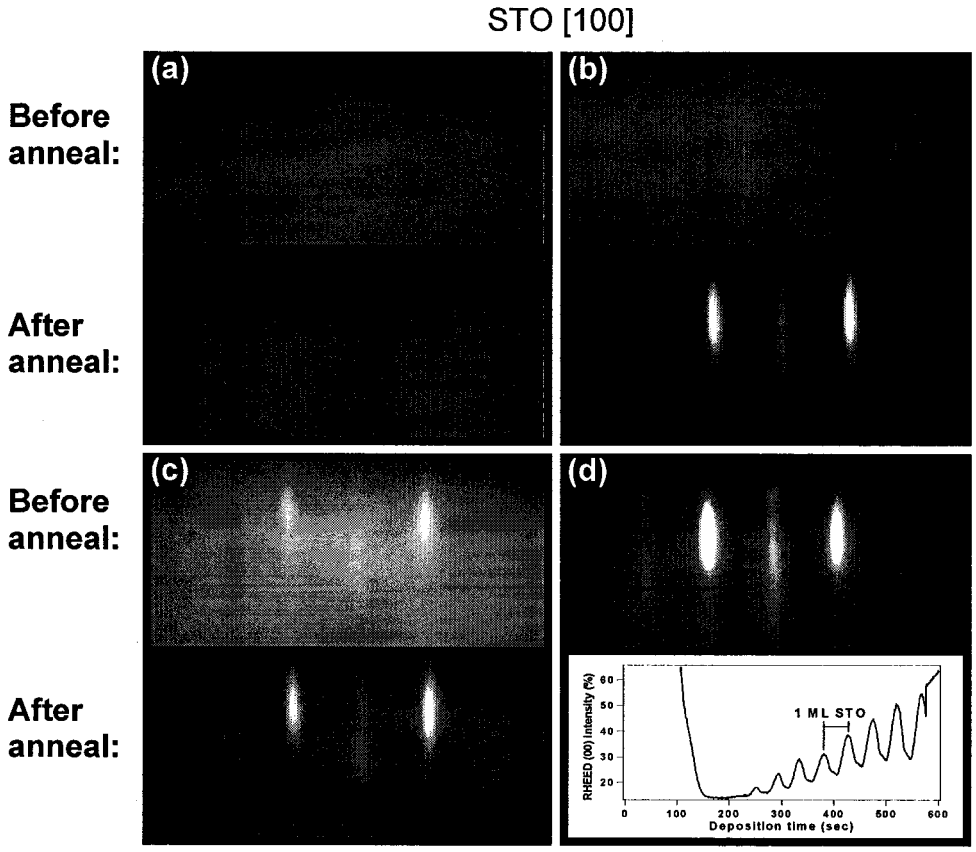

Figure 3.5. RHEED images of four different samples of 10 ML STO / ½ ML Sr / Si(001) deposited and annealed under the same nominal conditions. (a) STO was amorphous as deposited, with no crystallinity change after annealing. (b) Amorphous STO recrystallized during annealing. (c) Partially crystalline STO was significantly improved by annealing. (d) STO was deposited well-crystallized, and no anneal was necessary. RHEED oscillations were observed during deposition, indicating two-dimensional layer-by-layer growth.

partially crystalline as deposited (such as Figure 3.5(c), in which significant crystalline improvement was observed after annealing). Under some circumstances, the STO film was deposited such that RHEED oscillations were observed, indicating well-ordered two-dimensional growth, and no recrystallizing anneal was necessary (Figure 3.5(d)).

The observed variation in STO deposition behavior is attributed to two factors: the cation stoichiometry of the STO film and the oxidation of the Si interface. The cation stoichiometry varied from run to run under the same nominal deposition

conditions due to variation in the source metal fluxes, especially drift in the atomic absorption spectroscopy (AAS) baseline used to control the Ti flux. The stoichiometry was determined by comparison of the XPS survey spectrum for the STO film to a reference spectrum taken for a clean, bulk single crystal *n*-$SrTiO_3$ doped with 0.2 at% Nb. As shown in Figure 3.6 for this reference standard, the areas under both the Sr 3*p* and the Ti 2*p* peaks were determined, after subtracting a Shirley background, and their ratio (Sr / Ti) was found to be 1.06. Since this ratio is nearly unity (by coincidence), determination of the Sr 3*p* / Ti 2*p* ratio for the STO thin films provides the approximate cation stoichiometry. The excess ¼ or ½ ML Sr deposited at the STO / Si interface is not accounted for with this method and thus introduces error into the area ratio for STO thin films, although the error decreases as the STO thickness increases and XPS signal from the interface is attenuated. By application

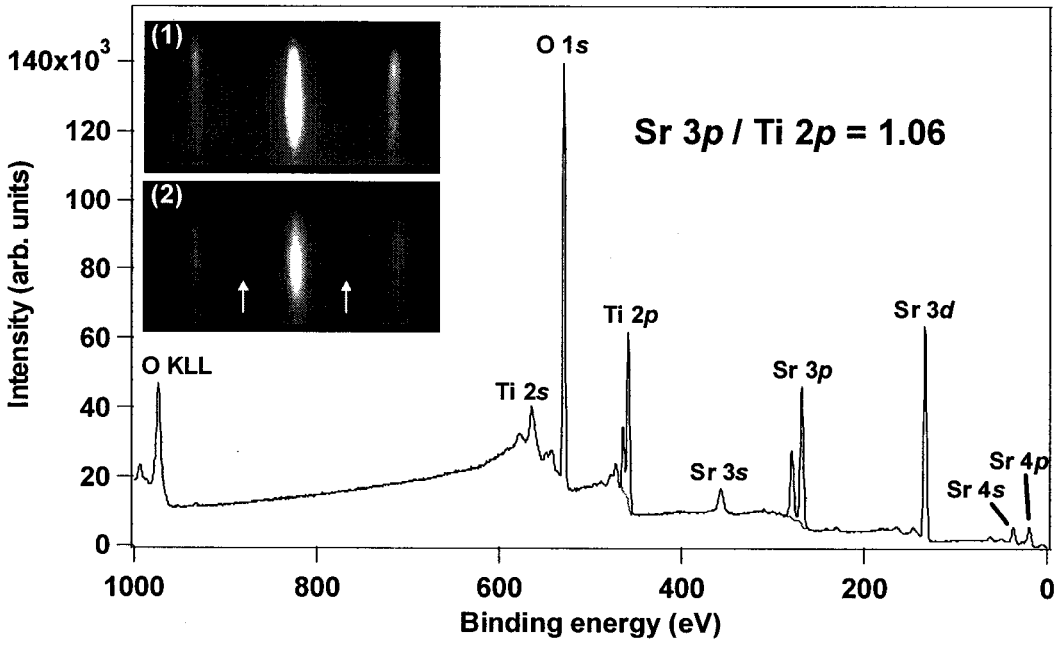

Figure 3.6. XPS survey spectrum of a clean *n*-STO(001) bulk single crystal. The area ratio of the Sr 3*p* peak to the Ti 2*p* peak, after subtracting a Shirley background from each region, was determined to be 1.06 for this stoichiometric sample. Comparison of the same area ratio for STO thin films provides an approximate measure of the film cation stoichiometry. Inset: (1) Final RHEED image of STO[110] azimuth for 10 ML STO / ½ ML Sr / Si(001). Film was stoichiometric, with Sr 3*p* / Ti 2*p* = 1.03. (2) STO [110] RHEED image of 10 ML STO / ½ ML Sr / Si(001) for non-stoichiometric film with Sr 3*p* / Ti 2*p* = 1.64. Arrows indicate faint 2x reconstruction.

of Beer's law with a photoelectron inelastic mean free path of 20-30 Å, the XPS Sr 3*p* intensity from ½ ML Sr under 10 ML STO is estimated to be < 3% of the total Sr 3*p* intensity. Strongly Sr-rich films also exhibited a faint 2x reconstruction in RHEED images of the STO [110] azimuth, as seen in the inset to Figure 3.6, possibly due to the formation of Ruddlesden-Popper SrO-rich phases with the rock salt structure.

The extent of oxidation of the Si interface was determined by the Sr silicide coverage, as illustrated above in Figure 3.4, as well as subtle variations in deposition conditions. The extent of SiO_x formation was quantified by fitting the high resolution Si 2*p* spectrum, as shown in Figure 3.7, and determining the area fraction of the oxidized contribution. The effect of the cation stoichiometry and Si interface oxidation on the crystallinity of the STO thin film is summarized in the phase diagram presented in Figure 3.8, for 10 ML STO deposited on Si(001) with either ¼ or ½ ML Sr silicide. A general trend is observed that reducing Sr relative to Ti increases the amount of SiO_x formed during deposition. This is explained by the

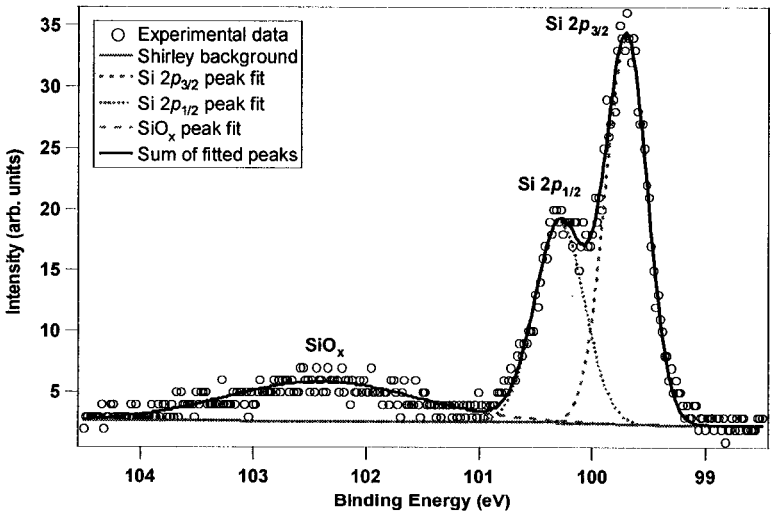

Figure 3.7. High resolution XPS Si 2*p* spectrum of 10 ML STO / ½ ML Sr / Si(001). Solid gray line is the fitted Shirley background. Dotted lines are best fit Gaussian peaks (as determined by the ESCA300 software) for the Si $2p_{3/2}$, Si $2p_{1/2}$, and SiO_x peaks. All three peaks were allowed to vary independently (neither the $2p_{3/2}$ to $2p_{1/2}$ spacing nor area ratio were fixed.) The SiO_x contribution was determined as the area fraction of the fitted SiO_x peak relative to the area of all three fitted peaks.

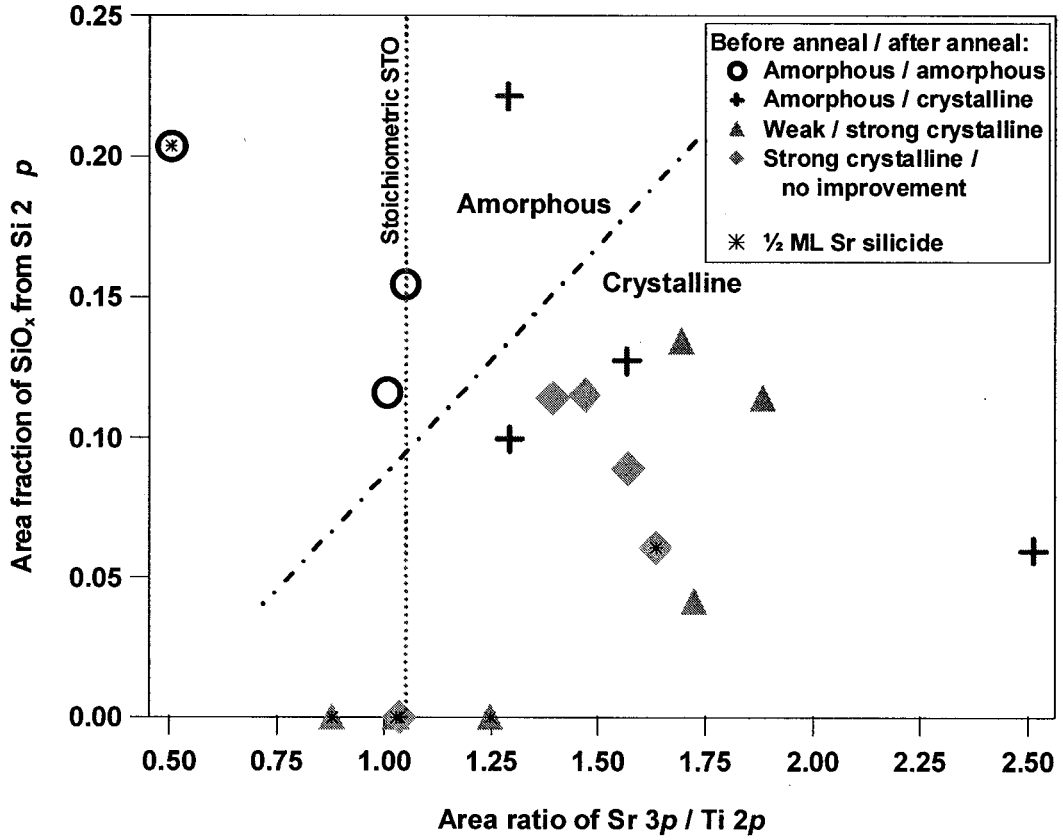

Figure 3.8. Crystallinity dependence of 10 ML STO / (¼ or ½) ML Sr / Si(001) on STO cation stoichiometry and SiO_x formation, as measured by XPS. The approximate transition from amorphous to crystalline STO (after annealing) is indicated by the dash-dotted line.

higher oxidation rate and catalytic oxidation properties of Sr; less Sr means slower oxidation and more opportunity for oxygen diffusion to the Si interface. The exceptions to this trend are four nearly stoichiometric STO films deposited on ½ ML Sr silicide, in which no SiO_x was observed. A delineation has been made on the phase diagram indicating the approximate transition from amorphous to crystalline STO (after annealing) as a function of STO stoichiometry and SiO_x formation.

In high resolution XPS Ti 2*p* scans of STO films after annealing, a small amount of Ti(III) was observed in addition to the expected Ti(IV). Figure 3.9(a) illustrates that some Ti(III) was present in the as-deposited film, and increased during the STO anneal due to oxygen loss under the oxygen-free annealing conditions. While the

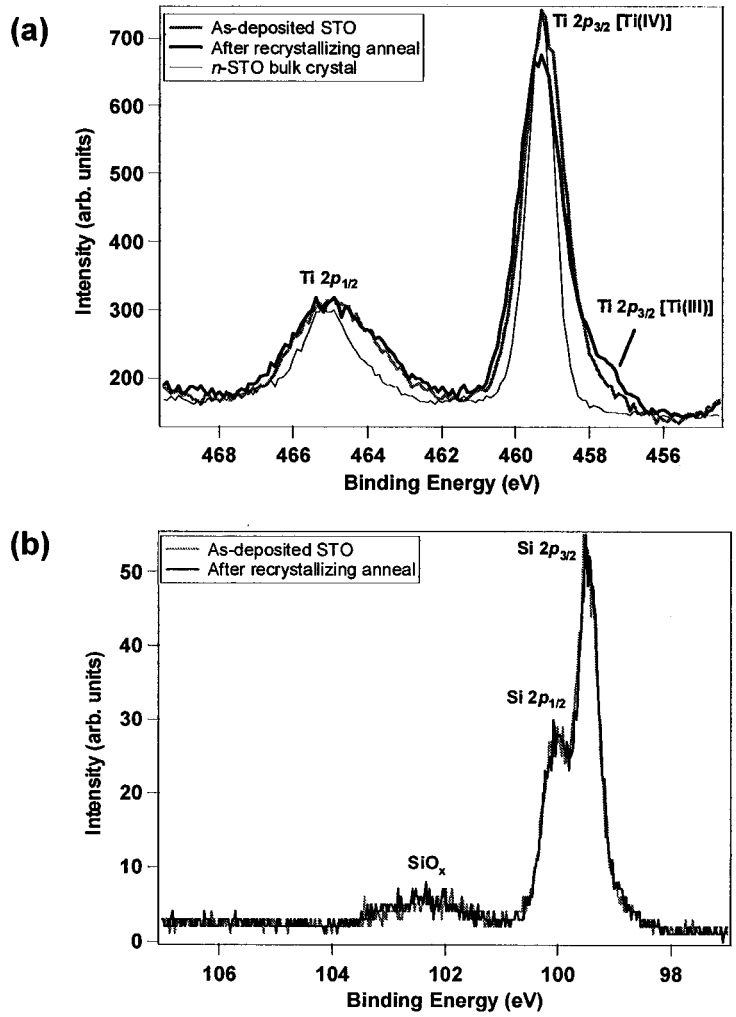

Figure 3.9. High resolution XPS spectra of 5 ML STO / ¼ ML Sr / Si(001) before and after recrystallizing anneal. (a) Ti 2*p* region: some Ti(III) is observed before annealing, and increases after annealing. For comparison, the Ti 2*p* spectrum of an *n*-STO bulk single crystal is also presented, which is free of Ti(III). Spectra were overlayed without normalization; *n*-STO was shifted in intensity to match the pre-edge background. (b) Si 2*p* region: no increase in SiO_x is observed after recrystallizing anneal in vacuum.

presence of Ti(III) would generally be detrimental, it was considered acceptable in this case since the oxidation of Ti(III) to Ti(IV) during the subsequent anatase deposition would eliminate reduced Ti as well as act as an oxygen sink, allowing less oxygen to diffuse to the Si interface. The high resolution Si 2*p* spectra presented in Figure 3.9(b) indicate that further oxidation of the Si interface does not occur during the recrystallizing anneal. Likewise, no change was observed in the oxidation state

of Sr as measured by high resolution XPS scans of the Sr 3*d* region before and after annealing (not shown).

True epitaxy of the STO film with respect to the Si(001) surface would result in a compressively strained STO film whose *a-b* plane lattice parameter matched that of the Si surface (3.84 Å). Compressive strain in the *a-b* plane results in a tetragonal distortion of the STO unit cell, with a proportional increase in the *c*-axis lattice parameter, as expressed by the Poisson's ratio for the material. As a critical STO thickness is reached, relaxation of the film to the bulk STO lattice parameter (3.905 Å) occurs through the formation of defects such as dislocations. Lattice parameters, and thus film strain, can be determined by both θ-2θ XRD and cross sectional TEM diffraction patterns. Since diffraction peaks are only observed for lattice planes parallel to the sample surface in θ-2θ XRD, this technique is limited to determining the *c* lattice parameter of STO. Due to the deep penetration of x-rays, XRD provides a macroscopic lattice parameter averaged over the film depth and a significant area. Reduced intensity and peak broadening of thin STO films significantly increases the uncertainty in the lattice parameter measurement; no measurement could be made for 5 ML (20 Å) STO. Transmission electron diffraction through a small area of the cross-sectional TEM sample can provide the *c* lattice parameter of STO from careful measurement of (00*l*) diffraction spots. Due to the relatively large error associated with this measurement (~3%), the *a* and *c* lattice parameters of STO could not be distinguished for samples which were not highly strained. In contrast to XRD, electron diffraction provides a microscopic lattice parameter from a very small section of the sample. Figure 3.10 presents the STO *c* lattice parameter, as measured by both XRD and TEM, as a function of the STO film thickness for 100 Å anatase / STO / ¼ ML Sr / Si(001) with 5, 10, 20, or 50 ML STO. For the thinnest STO layer (5 ML or 20 Å), the lattice parameter as measured by TEM was found to be significantly greater than the expected bulk value. This is due to compressive strain in the*a-b* plane of STO as a result of epitaxy with the Si substrate, which reduces the

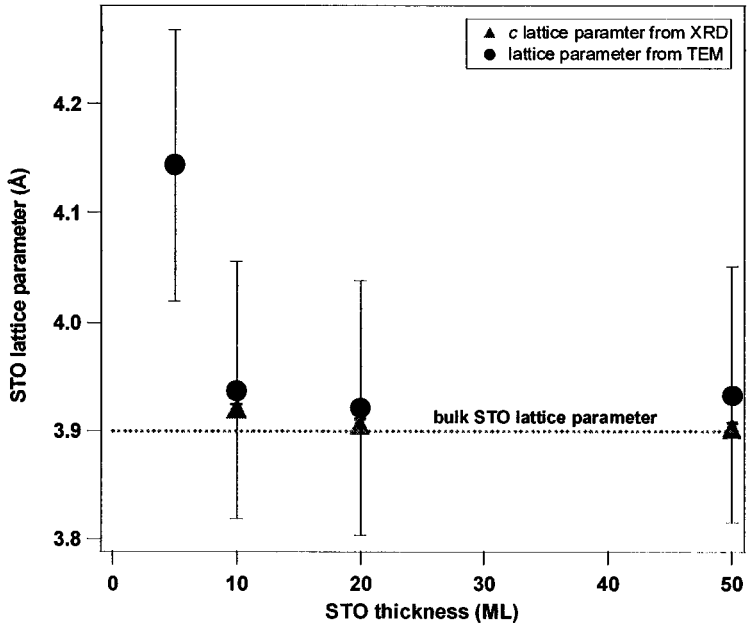

Figure 3.10. Plot of STO lattice parameter, as measured by both XRD and TEM, versus nominal STO film thickness. XRD measures the c lattice parameter of STO; TEM measures The critical thickness for STO to grow strained to Si appears to be between 5 and 10 ML (20-39 Å). (5 ML STO was too thin to obtain an accurate lattice parameter from XRD.) 10 ML or thicker STO films relax to nearly the bulk STO lattice parameter. Error bars are the estimated error associated with each measurement technique.

STO *a* lattice parameter and correspondingly increases the *c* parameter. However, it appears that even at 10 ML (39 Å) of STO the critical thickness for true epitaxy to Si has been exceeded, and the STO lattice parameter has relaxed to nearly the bulk value. Increasing the STO thickness past 10 ML does not appear to affect the lattice parameter. Although the strain exhibited by the 5 ML STO is favorable for subsequent anatase deposition, recrystallization of such a thin STO layer generally does not result in a strongly ordered surface. For this reason, 10 ML STO buffer layers were utilized for subsequent anatase deposition.

Anatase TiO_2

Pure anatase was deposited utilizing the oxygen plasma. It is expected that activated oxygen from the oxygen plasma will be necessary to fully oxidize Co during the

deposition of Co-doped anatase; thus, its use was first explored for deposition of pure anatase. As would be expected, the successful deposition of anatase depended strongly on the crystalline quality of the STO buffer layer providing the epitaxial template, as seen in Figure 3.11. Well-crystallized anatase deposition was never realized on a poorly-crystallized STO buffer layer. The surface of smooth, well-ordered anatase exhibits a 4x1 reconstruction, as observed as a 4x pattern in the RHEED images along the [100] azimuth. Figure 3.11(a) illustrates an example of well-ordered anatase with a 4x1 surface reconstruction deposited on a well-ordered 9 ML STO buffer layer on ¼ ML Sr / Si(001). As shown in Figure 3.11(b), deposition

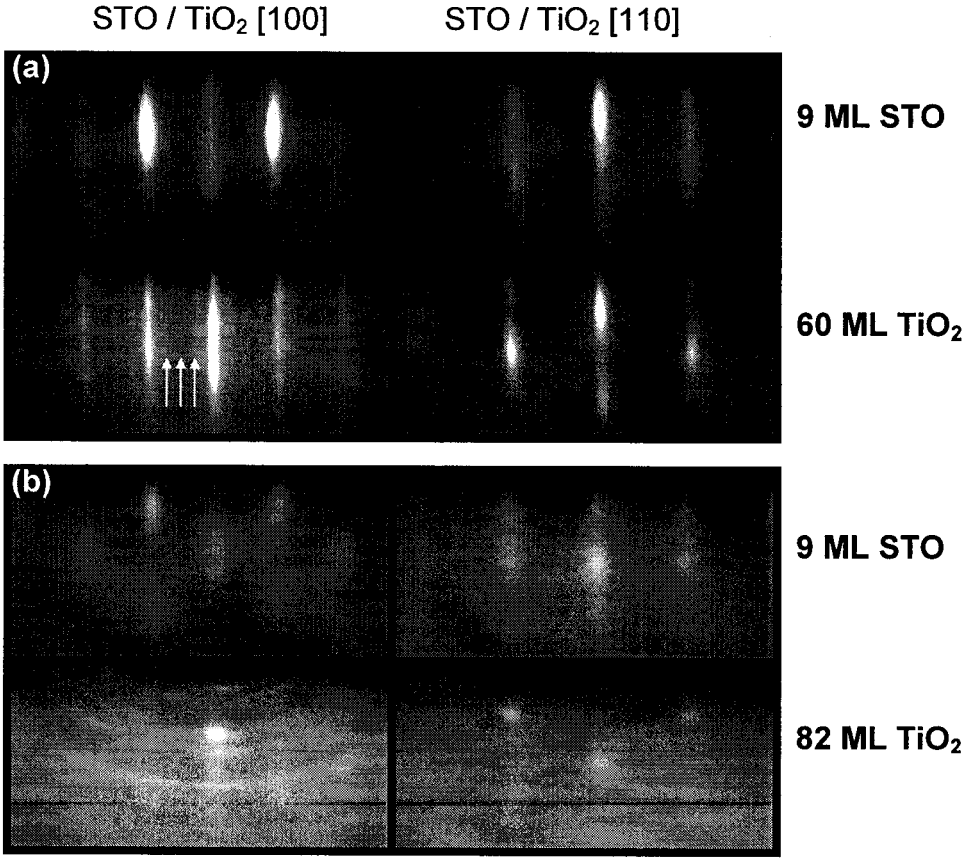

Figure 3.11. RHEED images of 9 ML STO / ¼ ML Sr / Si(001) after recrystallizing anneal, and after deposition of anatase TiO_2. (a) A high quality STO surface allows the deposition of high quality anatase TiO_2. Arrows in the TiO_2 [110] azimuth indicate the 4x reconstruction of the anatase surface. (b) STO with poor crystalline quality results in poor anatase TiO_2 deposition, with significant polycrystalline and amorphous regions.

of anatase on poor quality STO results in a very poor film consisting primarily of polycrystalline and amorphous regions. For this reason samples with poor STO crystalline quality after annealing, as determined by RHEED, were discarded.

In an attempt to protect the Si interface from the strongly oxidizing plasma species present during anatase deposition, the Ti flux was initiated as soon as the plasma lit. Despite this precaution, after deposition of 5 ML (12 Å) anatase under these conditions the Si interface showed significant oxidation, as seen in the high resolution XPS Si 2*p* spectra presented in Figure 3.12. After deposition of 5 ML TiO_2, the XPS intensity of SiO_x increased and shifted to higher BE, indicating a higher oxidation state of Si (closer to SiO_2). To determine the role of STO buffer layer thickness in the oxidation of the Si interface, 100 Å of anatase was deposited on ¼ ML Sr / Si(001) utilizing 5 ML, 10 ML, 20 ML, and 50 ML STO buffer layers. Since the Si interface could not be observed by XPS after deposition of 100 Å of anatase, TEM was employed to quantify the extent of Si oxidation, as shown in

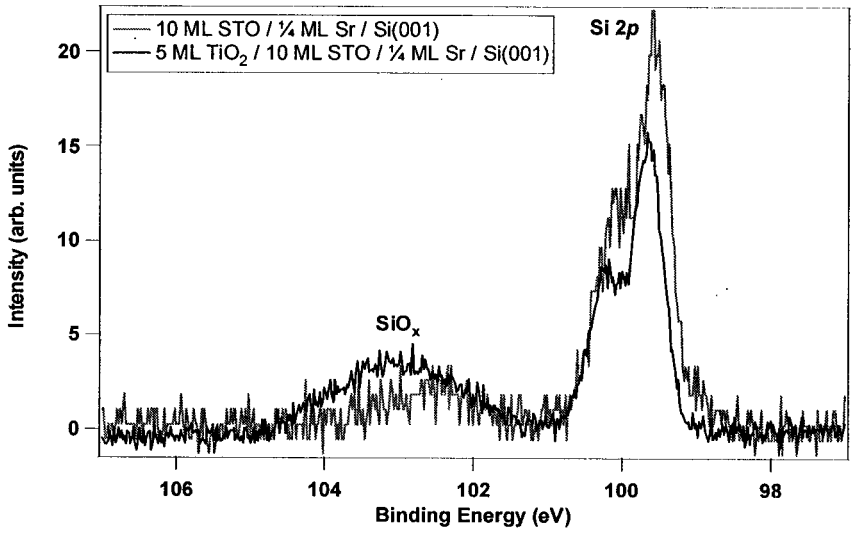

Figure 3.12. High resolution XPS Si 2*p* spectra of 10 ML STO / ¼ ML Sr / Si(001) and the same sample after 5 ML anatase TiO_2 utilizing the oxygen plasma. The SiO_x peak increases and shifts to higher binding energy (closer to SiO_2), indicating significant interfacial oxidation during anatase deposition. Each spectrum was normalized by its total integrated intensity (Si and SiO_x), and the pre-edge background was subtracted.

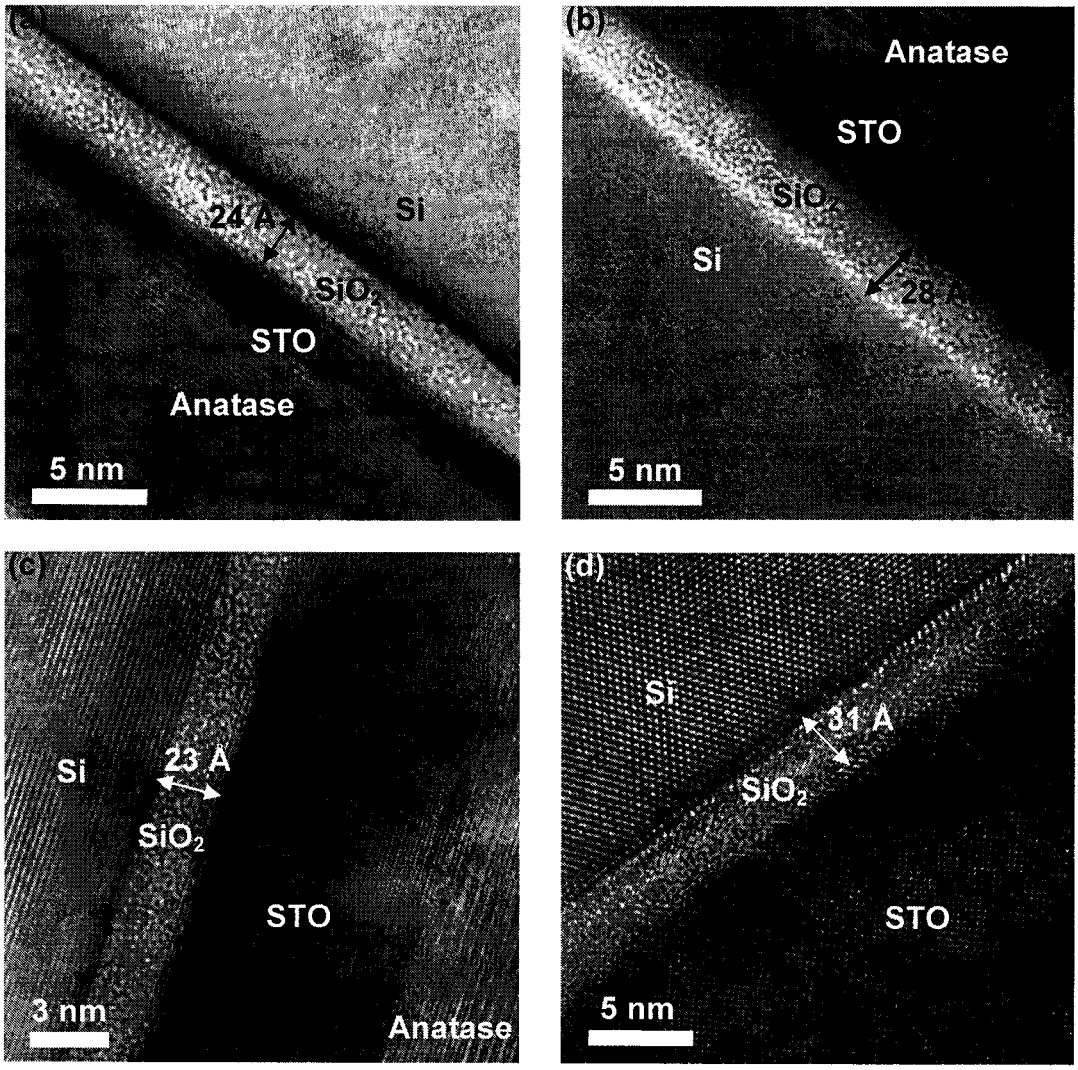

Figure 3.13. High resolution TEM images of 100 Å anatase / STO / ¼ ML Sr / Si(001). SiO_2 formed primarily during deposition of anatase TiO_2. (a) 5 ML STO. (b) 10 ML STO. (c) Nominally 20 ML STO, TEM image indicates STO thickness is 25 ML. (d) Nominally 50 ML STO, TEM image indicates STO thickness is 65 ML.

Figure 3.13. A thick amorphous oxide layer was observed for all STO buffer layer thicknesses. In the high resolution images, the STO layer was observed to "float" above the SiO_2 layer, and epitaxial registry of the STO to the Si substrate was preserved, as observed in both high resolution and electron diffraction images. This is further confirmation that the SiO_2 layer formed during anatase deposition, not during STO deposition. The SiO_2 layer thicknesses, averaged over several

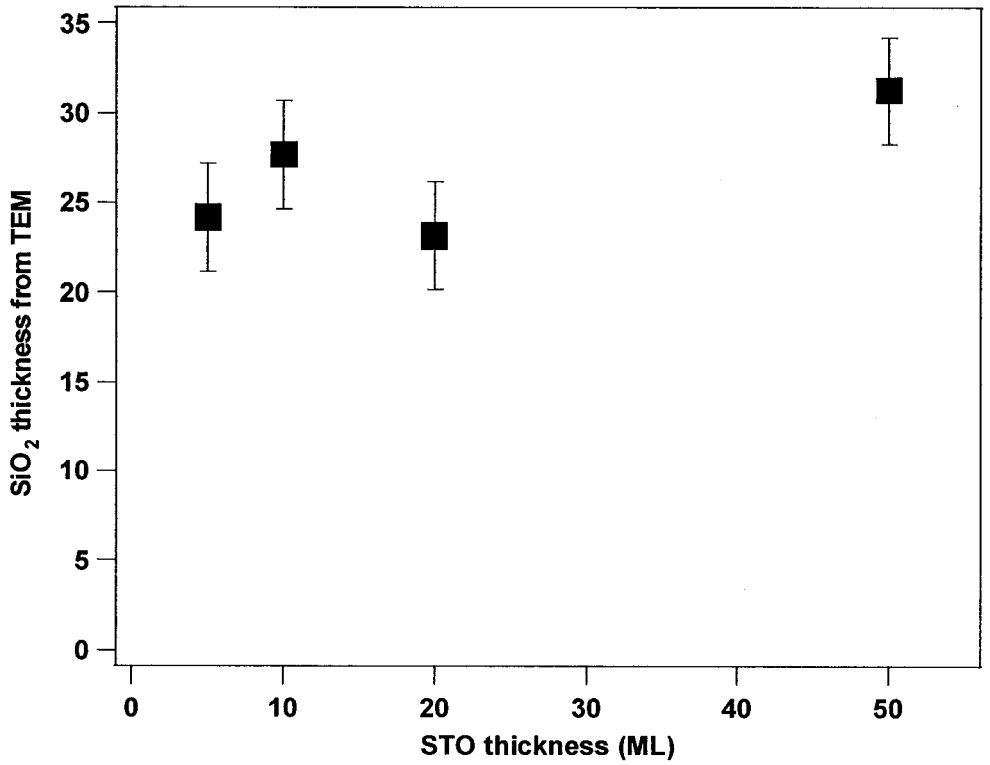

Figure 3.14. Plot of average SiO_2 thickness, as determined by high resolution TEM images, versus nominal STO thickness for 100 Å TiO_2 / STO / ¼ ML Sr / Si(001). Error bars are one standard deviation of several SiO_2 thickness measurements for each sample. Within measurement error, the SiO_2 thickness is constant at all STO thicknesses.

measurements for each sample, are plotted in Figure 3.14. It was found that approximately 25-30 Å of SiO_2 was observed for each sample; the SiO_2 thickness did not depend on the STO buffer layer thickness. Thus, STO does not act as an oxygen barrier, and increasing the STO buffer layer thickness is not an effective mechanism for eliminating oxidation of the Si interface. Oxidation of the Si interface appears to be only a function of anatase deposition time, which for these samples was equal (approximately 26 minutes), resulting in a similar SiO_2 thickness for each sample.

Analogous to the data presented above for STO, the strain in the anatase TiO_2 layer can be determined by XRD and TEM diffraction images. To accurately determine the anatase *a* lattice parameter from XRD, asymmetric reciprocal space mapping of the anatase (116) peak was utilized to obtain the position of the maximum diffraction

peak intensity. Results for the anatase lattice parameters determined by both XRD and TEM are presented in Figure 3.15 for the samples discussed above (100 Å of anatase deposited on 5, 10, 20, or 50 ML STO on ¼ ML Sr / Si(001)). For anatase deposited on 5, 10, or 20 ML STO, little dependence of lattice strain on STO thickness was observed. For anatase on 10 and 20 ML STO, this is consistent with the strain results obtained for STO above (see Figure 3.10), in which 10 and 20 ML STO were observed to have relaxed to approximately the bulk STO lattice parameter. However, 5 ML STO was observed to exhibit significant strain due to epitaxy with

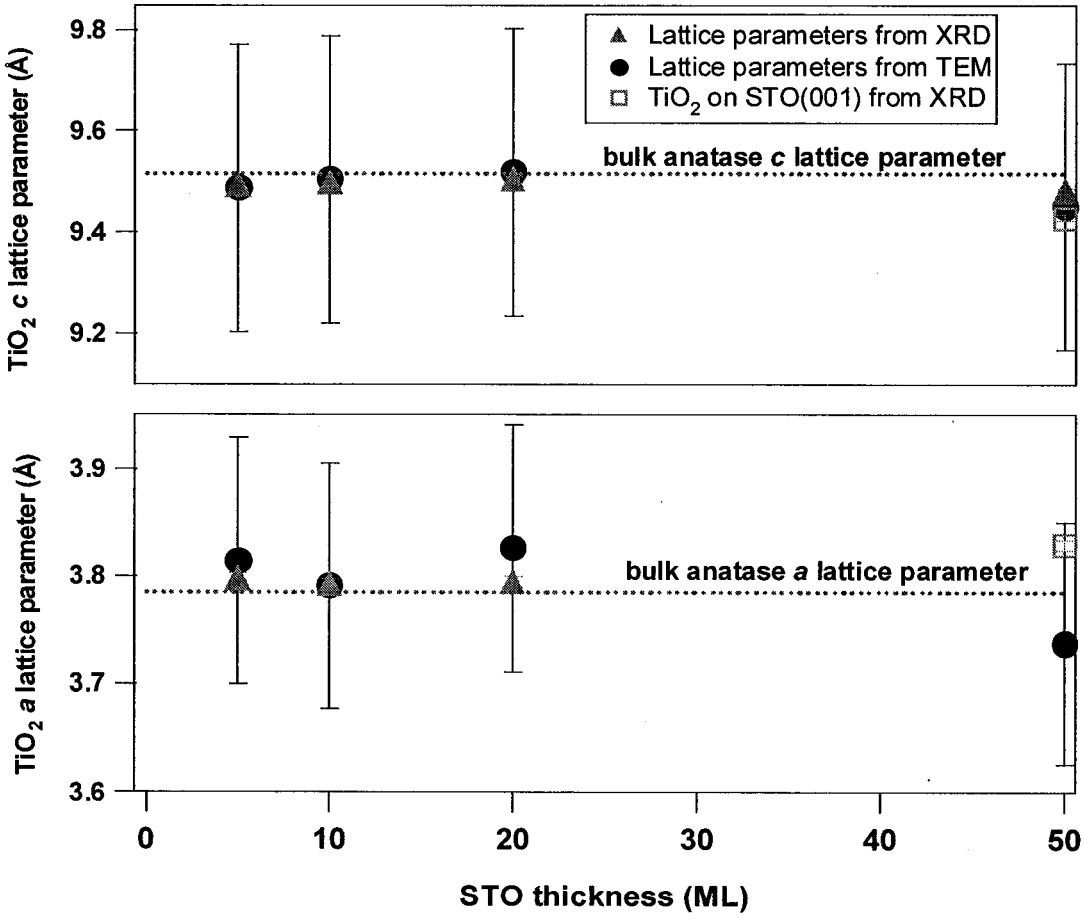

Figure 3.15. Anatase TiO_2 lattice parameters, as measured by θ-2θ XRD (*c* parameter), XRD reciprocal space mapping (*a* parameter), and high resolution TEM images, versus nominal STO thickness for 100 Å TiO_2 / STO / ¼ ML Sr / Si(001). Neither the *a* nor *c* lattice parameters appear to depend on the STO thickness. Error bars are the estimated error associated with each measurement technique. For comparison, the lattice parameters determined by XRD for 100 Å TiO_2 deposited on an STO(001) substrate are included.

Si, which should reduce the lattice mismatch between STO and anatase and result in an anatase layer exhibiting less strain. Instead, the anatase film on 5 ML STO exhibits a similar magnitude of strain as the films on 10 and 20 ML STO. For anatase deposited on 50 ML STO, unusual results were obtained. While it is expected that expansion in one lattice parameter, such as the anatase *a* parameter as it is strained to STO, would result in compression of the perpendicular parameter, the anatase film deposited on 50 ML STO exhibited significant compression of both lattice parameters, as measured by TEM. This is a physically unreasonable result that represents a violation of Poisson's ratio, and thus must be attributed to the inherent measurement error associated with lattice parameter determination by TEM. In contrast, deposition of anatase on a bulk STO(001) substrate under the same conditions resulted in expansion of *a* and compression of *c*, as expected.

It is known from previous work on Co-doped anatase deposited on oxide substrates that Co prefers to segregate to surface particles of epitaxial anatase.[5] The formation of surface particles is not induced solely by the presence of Co, and can be observed on pure undoped anatase films. Surface particle formation on pure anatase films was investigated to determine the effect of deposition conditions and strain. Figure 3.16 shows 5 x 5 μm AFM images of the anatase films discussed above (100 Å anatase on 5, 10, 20, or 50 ML STO on ¼ ML Sr / Si(001)), as well as the surface of 100 Å of anatase deposited on a single crystal STO(001) substrate. Surface particle formation is evident on all samples. No secondary phases or polycrystalline rings were observed in final RHEED images of these films, indicating the particles are epitaxially oriented anatase. To quantify the particle coverage, the AFM image analysis software was employed, as illustrated in Figure 3.16(f). The threshold height for each sample was chosen such that the maximum number of particles was included, without a significant contribution from the surface roughness of the film. The error in surface coverage determination introduced by this qualitative judgment is estimated to be roughly ± 0.5% surface coverage. Table 3.1 summarizes the

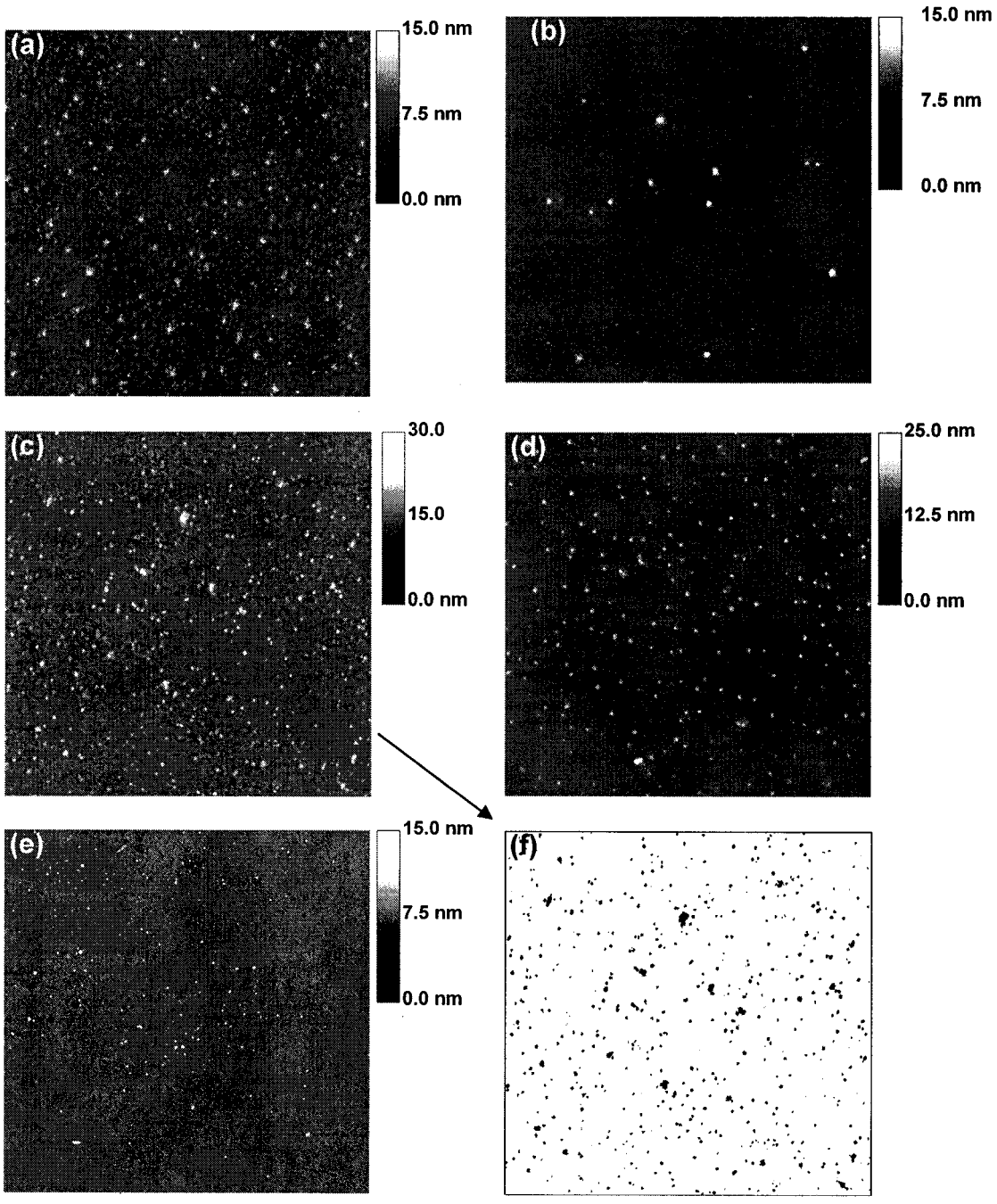

Figure 3.16. Tapping-mode AFM images of 100 Å TiO_2 / STO / ¼ ML Sr / Si(001). Images are 5 x 5 μm. (a) 5 ML STO. (b) 10 ML STO. (c) 20 ML STO. (d) 50 ML STO. (e) 100 Å TiO_2 / STO (001). (f) Example of surface particle coverage determination for (c). Dark areas in image are counted as "particles," and white areas are "film." The threshold height was chosen to include as many particles as possible without including surface roughness from the film.

Table 3.1. Surface particle data for 100 Å TiO_2 / STO / ¼ ML Sr / Si(001). Data are from image analysis of tapping-mode AFM images. For comparison, 100 Å TiO_2 on STO(001) is also presented.

100 Å TiO_2 / STO / ¼ ML Sr / Si(001)	Average height (nm)	Average diameter (nm)	Surface coverage (%)
5 ML STO	6.1	23.0	0.44
10 ML STO	5.8	56.0	0.36
20 ML STO	5.8	34.5	2.70
50 ML STO	7.6	42.2	3.97
STO(001) substrate	3.9	16.0	1.89

surface particle analysis results for the samples shown in Figure 3.16. Figure 3.17(a) presents the surface coverage of particles as a function of strain in the anatase *c* lattice parameter. From this plot, it is evident that no clear correlation can be made between strain in the anatase lattice and the number or size of surface particles. Thus strain in the anatase film is not directly responsible for surface particle formation. However, a correlation between increasing particle coverage and increasing STO film thickness is observed in Figure 3.17(b). This dependence on STO thickness, without a corresponding dependence on STO or anatase film strain, indicates the particle formation is influenced most strongly by the surface quality of the STO film. Although significant surface morphology changes are not observed in RHEED images of the STO film with increasing thickness, it can be assumed that thicker STO films have more surface defects due to strain relaxation, as well as defects such as stacking faults introduced during film deposition. It is speculated that these surface defects provide nucleation sites for anatase film defects, some of which may persist through the film and result in surface particle formation. It is unlikely that the surface features are hillocks formed to relieve compressive stress in the film, as occurs in strained metal films,[6] since the surface particles are also observed on anatase films deposited on closely lattice matched $LaAlO_3$ substrates (0.13% lattice mismatch). However, $LaAlO_3$ is known to form twins, and the epi-polished surface of an $LaAlO_3$(001) single crystal substrate exhibits significant surface corrugation due to twinning, which may provide nucleation sites for anatase particles.

Anatase films were deposited under varying deposition conditions to evaluate the effect of growth parameters on surface particle formation. Figure 3.18(a) shows 100 Å anatase deposited on 10 ML STO / ¼ ML Sr / Si(001) at a growth rate of 26 sec/ML (0.09 Å/sec) and an oxygen pressure of $7x10^{-6}$ Torr. As discussed above, this film exhibits small surface particles of epitaxial anatase. For comparison, Figure 3.18(b) shows 250 Å anatase deposited on 10 ML STO / ½ ML Sr / Si(001) at a growth rate of 18 sec/ML (0.133 Å/sec) and an oxygen pressure of $1.5x10^{-5}$ Torr.

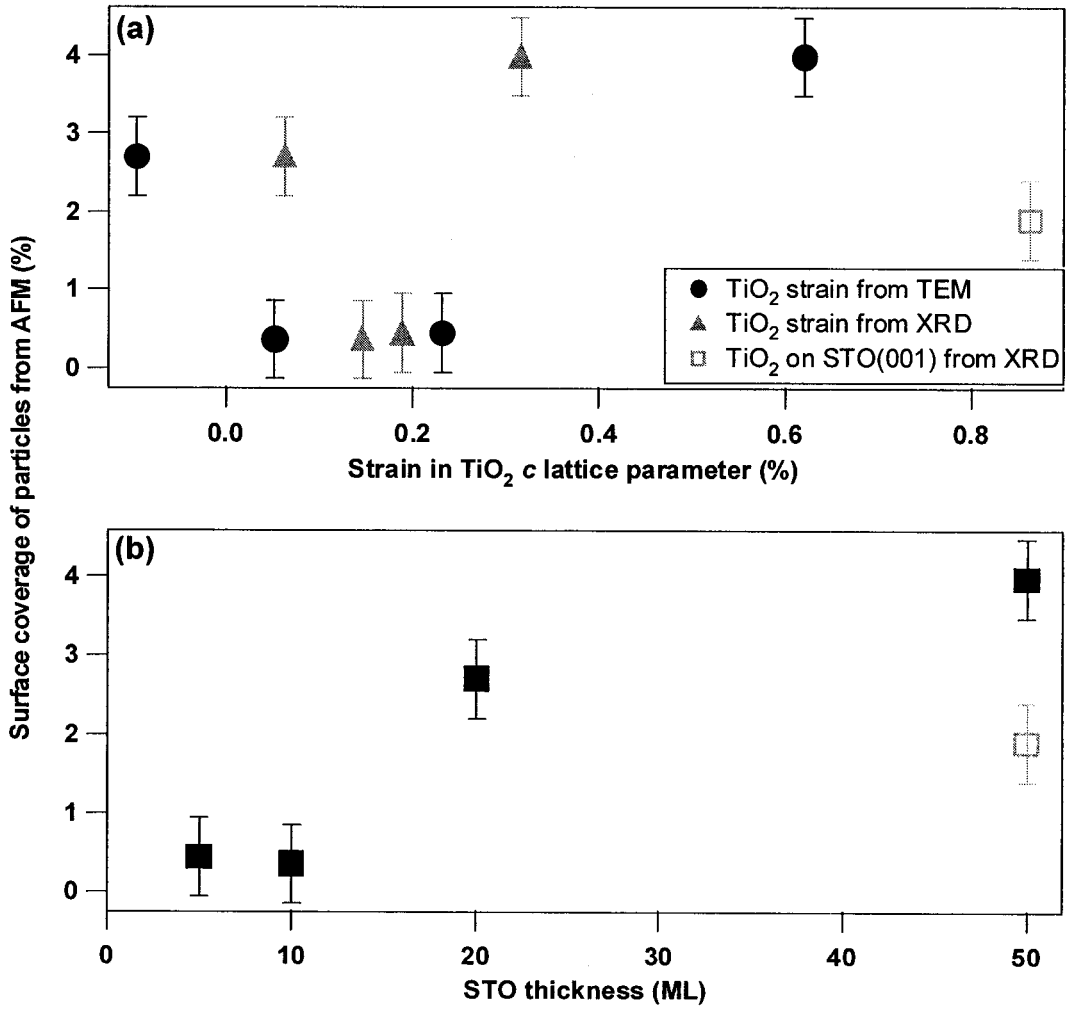

Figure 3.17. (a) Surface coverage of particles, as observed by AFM, versus % strain in TiO_2 *c* lattice parameter as measured by TEM and θ-2θ XRD. No dependence of particle formation on anatase strain is observed. (b) Surface coverage of particles versus nominal STO film thickness. An increase in particle coverage with increasing STO film thickness is observed. Error bars are estimated error in surface particle analysis due to qualitative determination of threshold height.

The increase in oxygen pressure for this film more than compensates the increased anatase deposition rate, such that oxygen deficiency during deposition should not be an issue, and the only significant differences between the two films are film thickness and anatase deposition rate. It is clear from Figure 3.18(b) that particle formation on 250 Å anatase deposited relatively quickly results in a significantly different surface morphology than that observed in Figure 3.18(a), with larger diameter, much taller surface particles. In addition, the particles exhibit a distinct square or rectangular

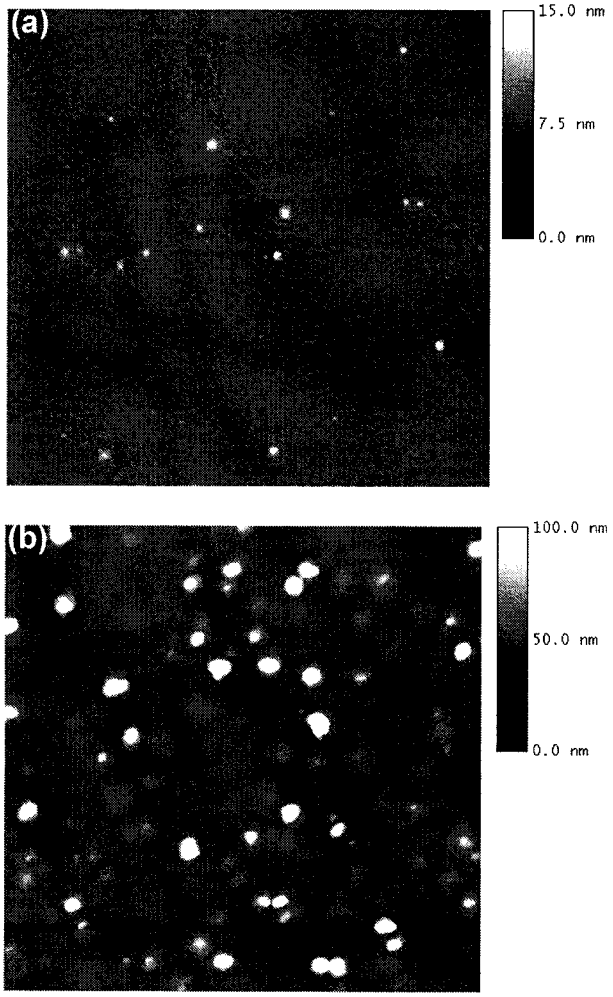

Figure 3.18. 5 x 5 μm tapping-mode AFM images. (a) 100 Å TiO_2 / 10 ML STO / ¼ ML Sr / Si (001). Anatase deposition rate was 26 sec/ML (0.09 Å/sec). Surface particles are round and dispersed. (b) 250 Å TiO_2 / 10 ML STO / ½ ML Sr / Si(001). Anatase deposition rate was 18 sec/ ML (0.13 Å/sec). Surface particles are numerous, and exhibit a distinct square shape due to faceting.

shape, indicative of faceting. Since faceted particles have been observed on several anatase films, utilizing several different AFM tips for imaging, it is unlikely that the square particle shape is the result of AFM tip shape effects. Larger, more closely spaced particles are expected as the deposition rate is increased, since nucleation increases with increasing flux to the surface, favoring an island growth mode over a layer-by-layer growth mode. However, it is unclear why a faster deposition rate would result in faceting of the particles.

Summary

It was found that utilizing ½ ML Sr on clean Si(001) as a protective silicide layer reduced or eliminated interfacial oxide formation during the subsequent deposition of 10 ML STO, in contrast to ¼ ML Sr, which did not completely inhibit Si oxidation. The deposition of STO was found to fall into several regimes depending on subtle variations in deposition conditions. In general, it was found that deposition under Sr-rich conditions reduced oxidation of the Si interface and thus resulted in crystalline STO. With ¼ ML Sr at the interface, deposition under stoichiometric or Ti-rich conditions resulted in more Si oxidation, preventing the crystallization of STO even during post-growth annealing. Utilizing ½ ML Sr to eliminate interfacial oxidation allowed stoichiometric or Ti-rich STO films to crystallize. The critical thickness for STO films to deposit strained to Si was observed to be between 5 and 10 ML (20 – 39 Å); films 10 ML or thicker relaxed to nearly the bulk STO lattice parameter.

Deposition of anatase on the STO buffer layer resulted in significant interfacial oxidation due to use of the oxygen plasma. The SiO_x thickness was not affected by the STO buffer layer thickness, indicating that STO is not an effective oxygen barrier. Strain in the anatase layer was not observed to depend on STO thickness or strain. Significant surface particle formation was observed on the anatase film, and

was found to depend only on STO layer thickness, indicating the primary influence of particle formation may be the surface quality of the STO film. Deposition of anatase at higher growth rate resulted in much larger particles exhibiting a square shape due to faceting.

Notes to Chapter III

1. J.P. Becker, R.G. Long, and J.E. Mahan, "Reflection high-energy electron diffraction patterns of carbide-contaminated silicon surfaces." *J. Vac. Sci. Technol. A* **12** (1), 174 (1994).

2. J. Lettieri, J.H. Haeni, and D.G. Schlom, "Critical issues in the heteroepitaxial growth of alkaline-earth oxides on silicon." *J. Vac. Sci. Technol. A* **20** (4), 1332 (2002).

3. Y. Liang, S. Gan, and M. Engelhard, "First step towards the growth of single-crystal oxides on Si: Formation of a two-dimensional crystalline silicate on Si(001)." *Appl. Phys. Lett.* **79** (22), 3591 (2001).

4. R.A. McKee, F.J. Walker, and M.F. Chisholm, "Crystalline oxides on silicon: the first five monolayers." *Phys. Rev. Lett.* **81** (14), 3014 (1998).

5. S.A. Chambers, T. Droubay, C.M. Wang, A.S. Lea, R.F.C. Farrow, L. Folks, V. Deline, and S. Anders, "Clusters and magnetism in epitaxial Co-doped TiO_2 anatase." *Appl. Phys. Lett.* **82** (8), 1257 (2003).

6. K.-N. Tu, J.W. Mayer, and L.C. Feldman, *Electronic Thin Film Science*. (Macmillan Publishing Company, New York, 1992).

CHAPTER IV: COBALT-DOPED ANATASE TiO_2 / $SrTiO_3$ / Si(001)

Utilizing the insights gained during deposition of pure anatase on STO / Sr / Si(001), several Co-doped anatase films were deposited. For evaluation as a true dilute magnetic semiconductor (DMS) material with a spin-polarized carrier concentration, Co-doped anatase must consist solely of Co atoms substituted for Ti in the anatase lattice. Ferromagnetic secondary phases such as Co oxide or Co metal inclusions would make a determination of the DMS properties of this material impossible, since any magnetic signal from the DMS spin-polarized carriers would be superimposed on the magnetic signal from the secondary phases. The oxidation of Co to Co(II) is particularly important since the Co metal clusters observed in previous reports on Co-doped anatase[1-3] contribute a significant ferromagnetic component to the overall magnetism of the sample. From a thermodynamic viewpoint, Co is more difficult to oxidize than Ti. Table 4.1 tabulates the heat of formation ($\Delta_f H°$) of representative oxide compounds from the elements.[4] It is apparent that the oxidation of Ti to TiO_2 ($\Delta_f H° = -944$ kJ/mol) is significantly more thermodynamically favorable than the oxidation of Co to CoO (-237.9 kJ/mol). These values provide only a rough estimate of the situation during non-equilibrium MBE deposition of Co-doped anatase, but serve to illustrate the challenges inherent in doping anatase with Co. In Co-doped anatase deposition on oxide substrates, the substrate temperature and oxygen partial pressure can be increased to insure all Co is oxidized to Co(II). When depositing on Si substrates, however, an increase in the oxidative environment during Co-doped

Table 4.1. Thermodynamic heat of formation ($\Delta_f H°$) of various oxides from their respective elements. Data from [4].

Material	$\Delta_f H°$ at room temperature (kJ/mol)
TiO_2	-944.0
CoO	-237.9
Co_3O_4	-891.0
SiO_2 (α-quartz)	-910.7

anatase deposition must be balanced by the desire to prevent oxidation of the Si interface.

Deposition conditions

As described in Chapter II, Co-doped anatase was deposited in a similar manner to pure anatase films on STO / Sr / Si(001); all Co-doped films utilized ½ ML Sr deposited on Si(001). A higher activated oxygen partial pressure ($1.5x10^{-5}$ Torr) was chosen in an effort to ensure full oxidation of the Co dopant to Co(II). Deposition at $1.5x10^{-5}$ Torr activated oxygen and substrate temperature of 600-700°C is known to fully oxidize Co to Co(II) when deposited on $LaAlO_3$ (LAO) substrates.[5,6] To protect the Si interface from oxidation, as well as to preserve the quality of the STO buffer layer, a lower deposition temperature of 550°C was chosen. As discussed in the previous section, these deposition conditions are still expected to result in some interfacial Si oxidation; however, it was considered more important initially to attempt to fully oxidize the Co dopant than to minimize oxidation of the Si interface.

Surface morphology and composition

After deposition of a pure anatase buffer layer (approximately 40 Å) on 10 ML STO / ½ ML Sr / Si(001), Co was introduced and 200 Å of $Co_xTi_{1-x}O_2$ was deposited. The Co flux was varied to achieve 1%, 2%, or 4% Co doping (calculated on a cation basis). Final RHEED images of the three films are shown in Figure 4.1. The RHEED images consist of a streaky pattern with a 4x1 reconstruction observed along the TiO_2[100] azimuth, indicating a smooth epitaxial anatase film surface. No crystalline secondary phases are observed, although some polycrystallinity is observed in the [110] azimuth of 1% Co:TiO_2. Modulation of the anatase streaks

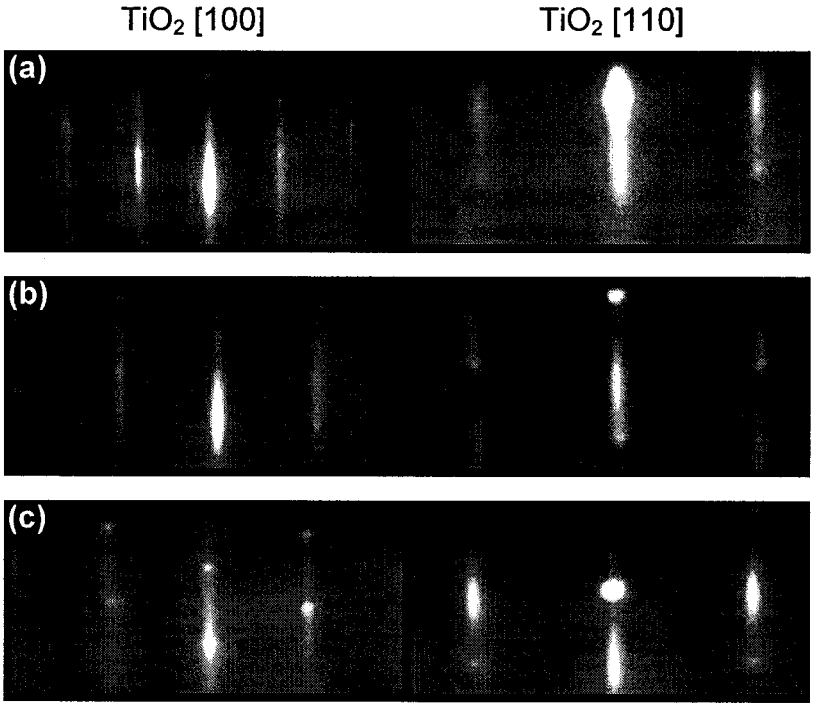

Figure 4.1. RHEED images of 200 Å Co:TiO_2 / 10 ML STO / ½ ML Sr / Si(001). (a) 1% Co:TiO_2. (b) 2% Co:TiO_2. (c) 4% Co:TiO_2.

indicate roughness of the surface; the modulation appears to become more pronounced with increasing Co concentration. This modulation is revealed to be due to anatase particles on the film surface, as observed by tapping-mode AFM (Figure 4.2). For 1% Co-doped anatase (Figure 4.2(a)), the surface particles have a distinct square shape. It is believed that this square shape is due to faceting of the particles. As the Co concentration is increased, the faceted surface particles become less numerous in favor of much larger particles with a less well defined, rounded shape. However, even for 4% Co doping, small faceted particles are still observed along with many large rounded particles (Figure 4.2(c)).

Segregation of Co to surface particles of epitaxial anatase has been observed for Co-doped anatase deposited on oxide substrates.[7] Auger electron spectroscopy (AES) was used to determine the surface Co distribution for Co-doped anatase films deposited on Si. Results for 4% Co-doped anatase are shown in Figure 4.3. In the

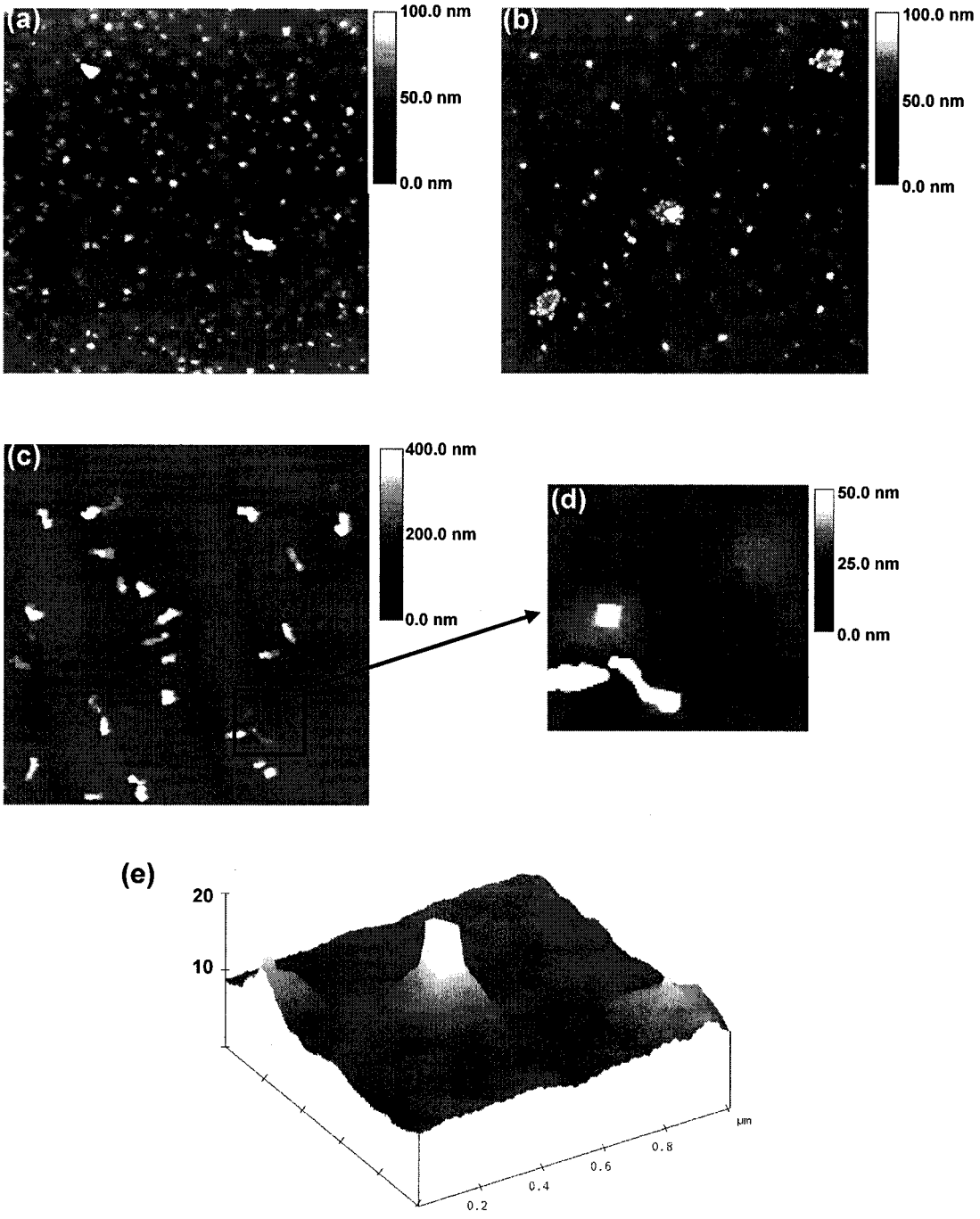

Figure 4.2. 5x5 µm AFM images of 200 Å Co:TiO_2 / 10 ML STO / ½ ML Sr / Si(001). (a) 1% Co:TiO_2. Numerous faceted particles are observed. (b) 2% Co:TiO_2. Larger clustered particles also present. (c) 4% Co:TiO_2. Primarily large particles with amorphous shape. (d) 2x2 µm AFM image of 4% Co:TiO_2. Small faceted particles are still observed. (e) Enlarged view of faceted particle on 2% Co:TiO_2. The top 15 nm of the particle is not shown.

scanning electron microscopy (SEM) image of the film surface, the large rounded and small faceted particles protrude from the smooth continuous anatase film, in agreement with the AFM image of the same film (Figure 4.2(c)). Numbers on the SEM image indicate the position of the electron beam for AES compositional analysis, and representative AES data are presented for Co, Ti and O. Table 4.2 summarizes the results of the AES compositional analysis. Due to matrix effects that affect the known sensitivity factors necessary for accurate AES compositional analysis, the peak-to-valley intensity of each AES peak was utilized to determine the compositional data presented in Table 4.2. Large Co signals are observed on the

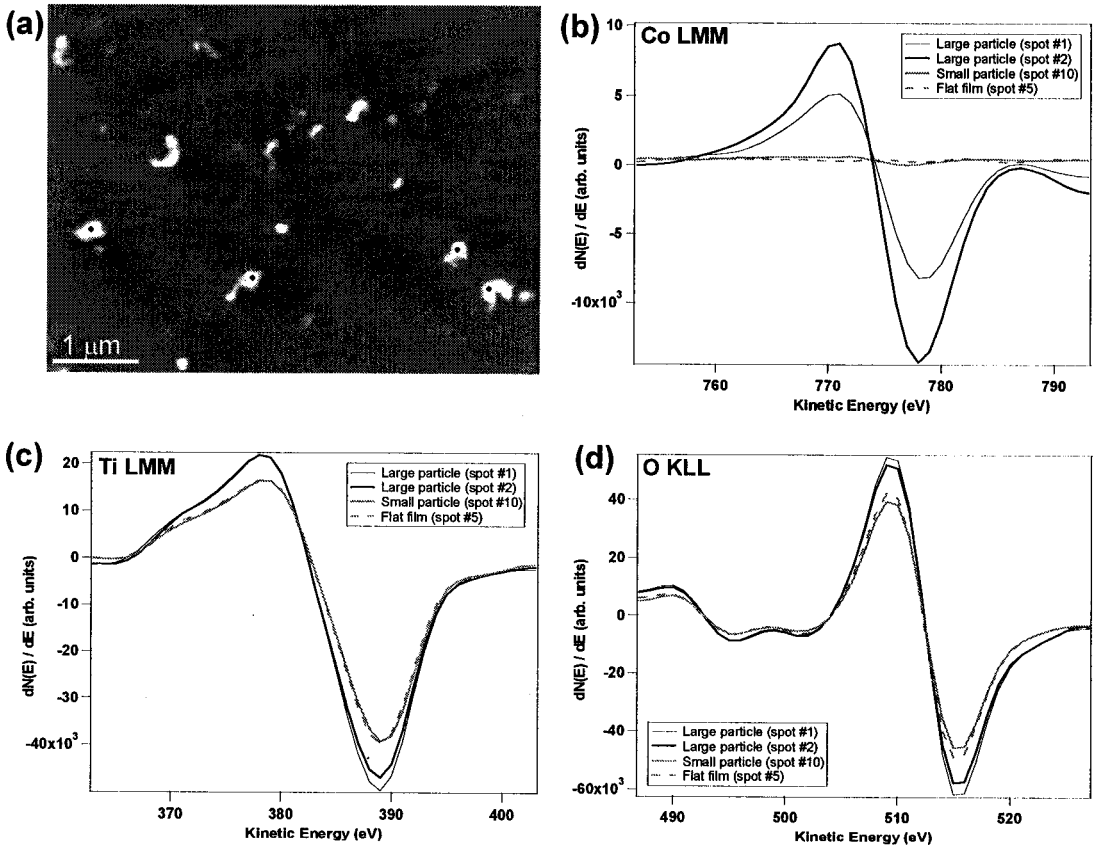

Figure 4.3. AES of 4% Co:TiO_2 / STO / Sr / Si(001). (a) SEM image of region investigated. Numbers indicate points at which AES data were collected. (b) Co LMM peak for four representative regions of film surface. A significant amount of Co is observed in the large particles, while essentially no Co is observed in the flat anatase film. (c) Ti LMM peak. Ti is observed in the large particles as well as the flat film. (d) O KLL peak. Oxygen is observed in both the anatase film and the particles.

Table 4.2. Summary of AES data for 4% Co:TiO_2 / STO / Sr / Si(001). Region numbers correspond to the SEM image in Figure 4.3. Atomic fractions were calculated from comparison of the peak-to-valley AES peak intensities.

Region	Description	Co/(Ti+Co)	O/(Ti+Co)	O_{2-x} expected*
1	large particle	0.16	1.37	1.84
2	large particle	0.25	1.19	1.75
3	large particle	0.13	1.43	1.87
4	large particle	0.28	1.21	1.72
5	flat film	0.006	1.62	1.99
6	flat film	0.005	1.60	1.99
7	flat film	0.004	1.60	2.00
8	flat film	0.004	1.59	2.00
9	small particle	0.004	1.51	2.00
10	small particle	0.010	1.51	1.99

*Expected from Co stoichiometry ($Co_xTi_{1-x}O_{2-x}$)

large rounded particles, while very little Co is observed in the small faceted particles and no Co is detected in the smooth film. This indicates that Co has segregated to large particles on the sample surface, with a Co concentration on the order of 15 - 25%. Since no secondary phases were observed in RHEED images of this surface, and Ti was also detected in the particles, it is believed that these particles are Co-enriched anatase similar to those observed on Co:TiO_2 / LAO.[7] The flat anatase film contains virtually no Co. All areas of the surface appear to be oxygen-poor compared to the expected stoichiometry expressed as $Co_xTi_{1-x}O_{2-x}$, although this reduction may be due to strong matrix effects for oxygen which have not been accounted for. However, the measured oxygen concentration follows the trend based on the expected stoichiometry as shown in Figure 4.4, with a significant reduction in oxygen content in the large particles relative to the continuous film. To maintain charge neutrality, the substitution of Co(II) for Ti(IV) is expected to require the formation of an associated oxygen vacancy. The reduction in oxygen concentration in the large particles strongly implies that Co is substitutional for Ti in the anatase lattice in the particles, and oxygen vacancies have been created to maintain charge neutrality.

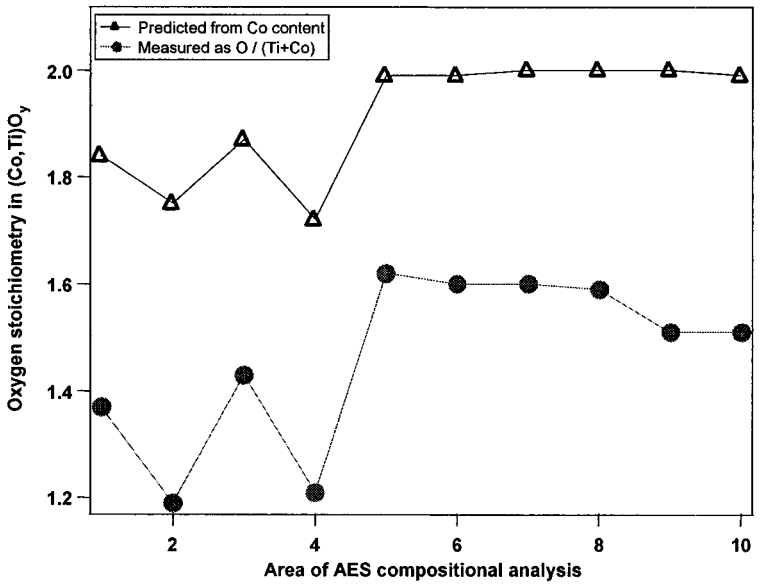

Figure 4.4. Predicted and actual oxygen stoichiometry for each point in the AES compositional analysis of 4% Co:TiO_2 / STO / Sr / Si(001). Predicted stoichiometry calculated based on the Co content as $Co_{1-x}Ti_xO_{2-x}$. Actual stoichiometry determined as the ratio of the oxygen AES peak to the Co and Ti peaks.

The formation of large, Co-enriched anatase clusters may be detrimental to the integration of Co-doped anatase films as spin injector materials in proposed spintronic devices. The segregation of Co to discrete clusters precludes the formation of a true DMS material. If the mechanism of Co-enriched cluster formation were understood, it may be possible to eliminate their formation. However, many of the conventional mechanisms of cluster formation do not readily apply in the case of Co-doped anatase. For example, the formation of clusters can be induced or prevented by varying the substrate temperature and incident metal flux during deposition; only in a certain range will two-dimensional layer-by-layer film growth occur. If the substrate temperature is too low, incident atoms do not possess enough thermal energy to move to a step edge and incorporate into two-dimensional islands; instead, they incorporate into the lattice where they land, resulting in surface roughness. If the substrate temperature is too high, the incident atoms possess sufficient thermal energy to reach their true equilibrium position, which may be clusters instead of a smooth film, depending on the interfacial energy and lattice

mismatch of the system. Likewise, if the incident metal flux is low, arriving atoms have time to move and incorporate into step edges, resulting in layer-by-layer growth, whereas if the flux is high incident atoms will meet on terraces before reaching step edges, creating nucleation sites and resulting in three-dimensional island growth. Stranski-Krastanov growth mode results in an intermediate growth mode, where a few monolayers of the film are able to grow layer-by-layer, before strain causes the formation of clusters. While these mechanisms may play a role in the cluster formation of Co-doped anatase, they do not explain the significant Co enrichment in the clusters.

Phase segregation or spinodal decomposition may explain the separation of a Co-rich phase (the clusters) from a Ti-rich phase (the anatase film). For phase segregation to occur, highly Co-doped anatase must be a thermodynamically distinct phase from pure anatase. If phase segregation were occurring, it is likely that clusters of the Co-rich phase would be found throughout the film thickness, not segregated at the anatase surface. However, density functional theory calculations by Yang *et al.*[8] predict greater energetic stability for substitutional Co in anatase when the Co – Co distances are reduced. This theoretical result implies that Co-rich anatase regions are thermodynamically favored over the uniform distribution of Co in the lattice.

In conjunction with this thermodynamic driving force for non-uniform Co distribution, a likely mechanism for the formation of surface clusters is modification of the film growth kinetics by the presence of Co. The influence of a surface segregating species on the thin film growth mode has been observed previously; both enhancement and reduction of surface nucleation is possible depending on coverage of the surface segregating species.[9] Co is known to be very mobile in anatase, especially in an oxidizing environment.[5] If Co segregates to the film surface during deposition, it may act to reduce nucleation of two-dimensional islands (i.e., layer-by-layer growth), resulting in the formation and growth of a few large three-dimensional

clusters. Although the Co may be temporarily incorporated into the anatase lattice at the film (or cluster) surface, it continues to diffuse out of the lattice and to the surface as the growth front moves, leaving behind nearly pure anatase. In this way, large clusters of significantly Co-enriched anatase are formed on a smooth, nearly pure anatase film.

Another clue to the mechanism of cluster formation may be the observed faceting of the surface particles. Faceting is often observed in deposition of strained films, such as epitaxial Ge on Si(001), which has a lattice mismatch of -4.2%.[10] Lattice mismatch strain is unlikely to be the cause of faceting of Co-doped anatase clusters on anatase, since the substitution of Co(II) for Ti(IV) in the anatase lattice is not expected to result in a lattice expansion of the magnitude necessary to induce faceting. Recently, large faceted clusters were observed in homoepitaxy of Al (110).[11] The proposed mechanism for faceted cluster formation in this system, which is strain-free, was upward adatom diffusion of surface atoms which possessed sufficient energy to overcome the kinetic barrier to climb the base of the cluster. A similar mechanism of upward adatom diffusion may be occurring on Co-doped anatase, resulting in faceted surface particles. In addition, if Co adatoms were able to more easily overcome the kinetic barrier to upward diffusion than Ti adatoms, Co enrichment of the clusters would result.

Film morphology

Epitaxial Co-doped anatase films with a high degree of crystalline order were inferred from the RHEED images during growth, in which the streaky diffraction pattern attributed to anatase was present throughout the deposition. Rutherford backscattering spectrometry (RBS) in the channeling geometry can provide confirmation of crystalline order in a thin film sample. Reduction in the

backscattered ion yield in the channeling geometry relative to the yield in the random geometry was observed for all Co-doped anatase films, as shown in Figure 4.5 for 2% Co:TiO_2 / STO / Sr / Si(001). For Ti, the minimum yield in the channeling geometry, defined as $I_{max,\ channeling} / I_{max,\ random}$, was found to be 45% for 1% Co:TiO_2, 37% for 2% Co:TiO_2, and 44% for 4% Co:TiO_2, indicating all three films possess approximately equal crystalline order. For Ti, the yield in the channeling geometry is a superposition of disorder in the surface particles, anatase film, and STO buffer layer. The depth resolution of RBS is insufficient to precisely determine the sample region in which most backscattering is occurring, although from comparison of the Ti peak position in both random and channeling geometries it appears to originate mainly from the film surface, implying the surface particles may possess the most

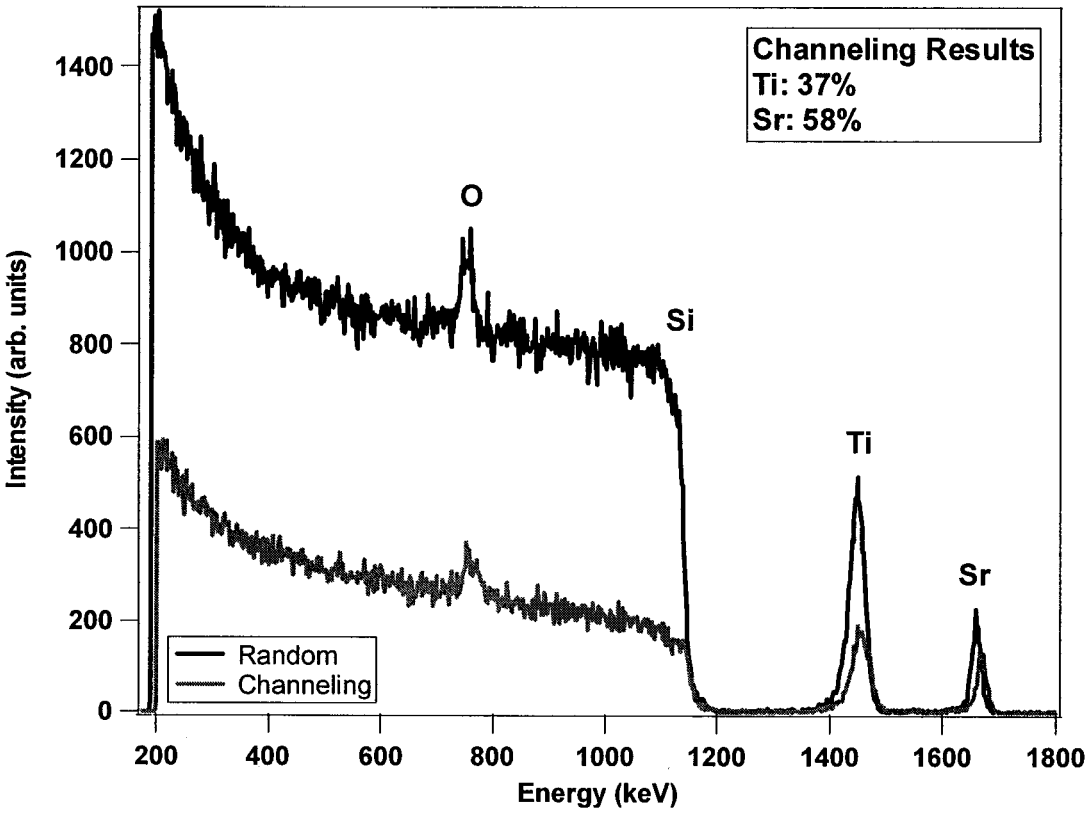

Figure 4.5. RBS data for 2% Co:TiO_2 / STO / Sr / Si(001) for both random and channeling (aligned) geometry. Reduction of the ion yield for the channeling geometry is a measure of the crystalline order in the film.

crystalline disorder. Disorder in the 10 ML STO buffer layer can be quantified by determining the minimum yield for Sr, which was found to be 83% for 1% Co:TiO_2, 58% for 2% Co:TiO_2, and 72% for 4% Co:TiO_2. These high minimum yields imply significant crystalline disorder in the STO buffer layer. From comparison of the Sr peak position for both the random and channeling geometries, it appears that the backscattering in the channeling geometry occurs primarily at the STO / anatase interface, indicating a significant amount of disordering occurs when the deposition of anatase is initiated on the STO buffer layer.

To determine the presence of secondary phases, XRD is commonly employed. However, based on the low Co concentration in these films, secondary phase crystallites would likely be too small to be observed by XRD. Grazing incidence XRD (GIXRD) was utilized to confirm that no secondary phases large enough to be observed were present. GIXRD of 2% Co:TiO_2 did not reveal any secondary phases.

High resolution transmission electron microscopy (TEM) is a much more sensitive technique for the identification of inclusions and secondary phases, as well as providing detailed information on the crystal structure and crystalline quality of the thin film. A cross-sectional TEM image of 2% Co:TiO_2 / STO / Sr / Si(001) is presented in Figure 4.6. As expected, an amorphous SiO_2 layer approximately 35 Å thick has formed at the STO / Si interface during anatase deposition. This SiO_2 layer is thicker than the 25 – 30 Å SiO_2 observed when pure anatase is deposited on STO / Si, as presented in Chapter III. Although both sets of films were deposited for approximately the same growth time, an increase in SiO_2 thickness is expected since the Co-doped TiO_2 samples were deposited under 1.5×10^{-5} Torr oxygen while the pure anatase films discussed in Chapter III were deposited under an oxygen pressure of only 7×10^{-6} Torr. The epitaxial STO buffer layer (10 ML thick) is observed to float above the SiO_2 layer, implying that Si oxidation occurred during the deposition of Co:TiO_2, not STO. The Co:TiO_2 film and STO buffer layer possess high

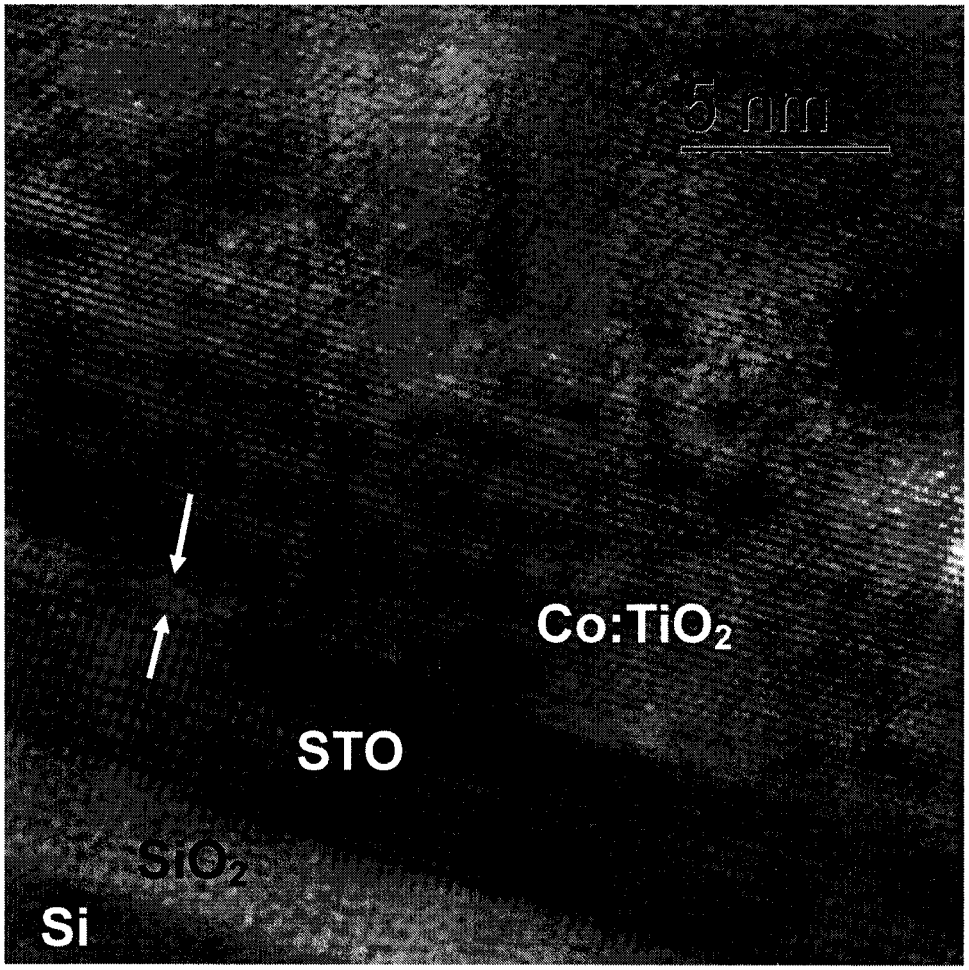

Figure 4.6. High resolution TEM image of 2% Co:TiO_2 / STO / Sr / Si(001). The epitaxial relationship and crystalline quality of the STO and Co:TiO_2 films can be seen. Arrows indicate disorder at the Co:TiO_2 / STO interface. In addition, the amorphous SiO_2 layer that formed during Co:TiO_2 deposition is observed.

crystalline order, although some disorder is observed at the Co:TiO_2 / STO interface. This is consistent with the RBS channeling results presented above and suggests that disordering occurs when the deposition of TiO_2 is initiated.

The surface particles observed by AFM (see Figure 4.2(b)) were also imaged by TEM, as shown in Figure 4.7. The surface particles sit on top of a continuous anatase film. From investigation of several particles similar to Figure 4.7(a), it is concluded that the surface particles retain anatase crystallinity. Energy dispersive x-

ray spectroscopy (EDS) of several regions of the continuous anatase film, as well as several particles, was able to detect small amounts of Co only in the surface particles; no Co was detected in the continuous anatase film. However, the Co concentration in the particles was consistently measured as less than 2.5%, considerably less than the 15 – 25% concentration obtained by AES for large surface particles on 4% Co:TiO_2. In contrast to the majority of the particles observed for this film, the particle shown in Figure 4.7(b) originates at the STO surface and propogates through the film with a distinct inverted V shape. This "particle" appears to be a rutile inclusion, as observed previously for Co:TiO_2 deposited on LAO.[5] In contrast to previous reports,[5,12] however, no Co was detected in the rutile inclusion.

No Co metal inclusions or other secondary phases were observed in either the continuous anatase film or the surface particles after careful inspection. However, the Co did not appear to be uniformly distributed, even within a single anatase surface particle. As an example, the electron beam location and resulting Co concentration determined by EDS for three locations on one Co-doped anatase

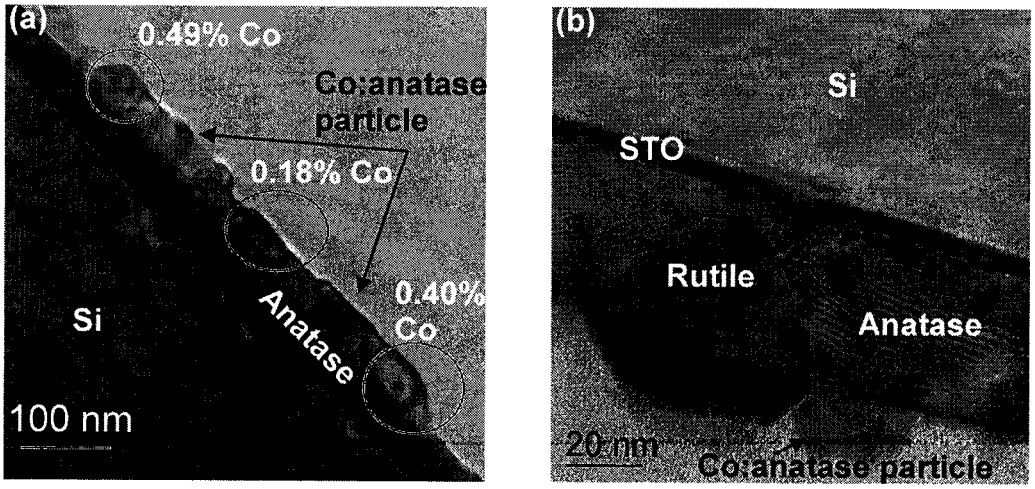

Figure 4.7. High resolution TEM images of surface particles on 2% Co:TiO_2 / STO / Sr / Si(001). (a) Surface particle of Co-enriched anatase sitting on continuous anatase film. Circles indicate electron beam position for EDS composition measurements; resulting Co concentrations are shown. (b) Rutile inclusion originating at STO surface and propogating through film to form surface particle. Anatase surface particle containing Co is also indicated.

particle is shown in Figure 4.7(a). Significantly more Co is present at the edges of the particle than in the center.

Quantification of Co concentration

It is necessary to accurately determine the total concentration of Co in the Co-doped anatase film in order to calculate the magnetic moment on a Co atom basis. RBS is commonly employed for compositional quantification, since it does not rely on sensitivity factors, and can provide depth profiling information. An RBS spectrum for 2% Co-doped anatase is shown in Figure 4.8. To quantify the spectrum, the SimNRA software program was utilized to develop a model film structure that reproduces the experimental data. Due to the fact that Ti and Co have similar atomic mass, they appear near each other in the backscattering spectrum. At a film thickness of 200 Å, the Co peak may partially overlap the Ti peak. Several issues make quantification of this spectrum difficult. The low Co signal, which is barely detectable above the noise level, makes it difficult to determine what constitutes a good simulated fit for the Co region. The width of the Co peak, which is related to the sample thickness in which Co is present, is especially difficult to determine from the experimental RBS spectrum, due to the low signal and interference from the Ti peak. This could be overcome by assuming the Co and Ti are in the same film, whose thickness is determined by fitting the Ti peak. The Co content of the simulated layer would then be adjusted to reproduce the height of the experimental Co peak. However, it is known from AES data on similar films that Co preferentially segregates to surface particles such as those observed on this film by AFM. Thus, the thickness of the region containing Co (the surface particles) is not equal to the thickness of the region containing Ti (both the surface particles and the anatase film). The simulation software does not allow the creation of a film containing voids, which would be necessary to accurately model the surface particles. For these reasons, an

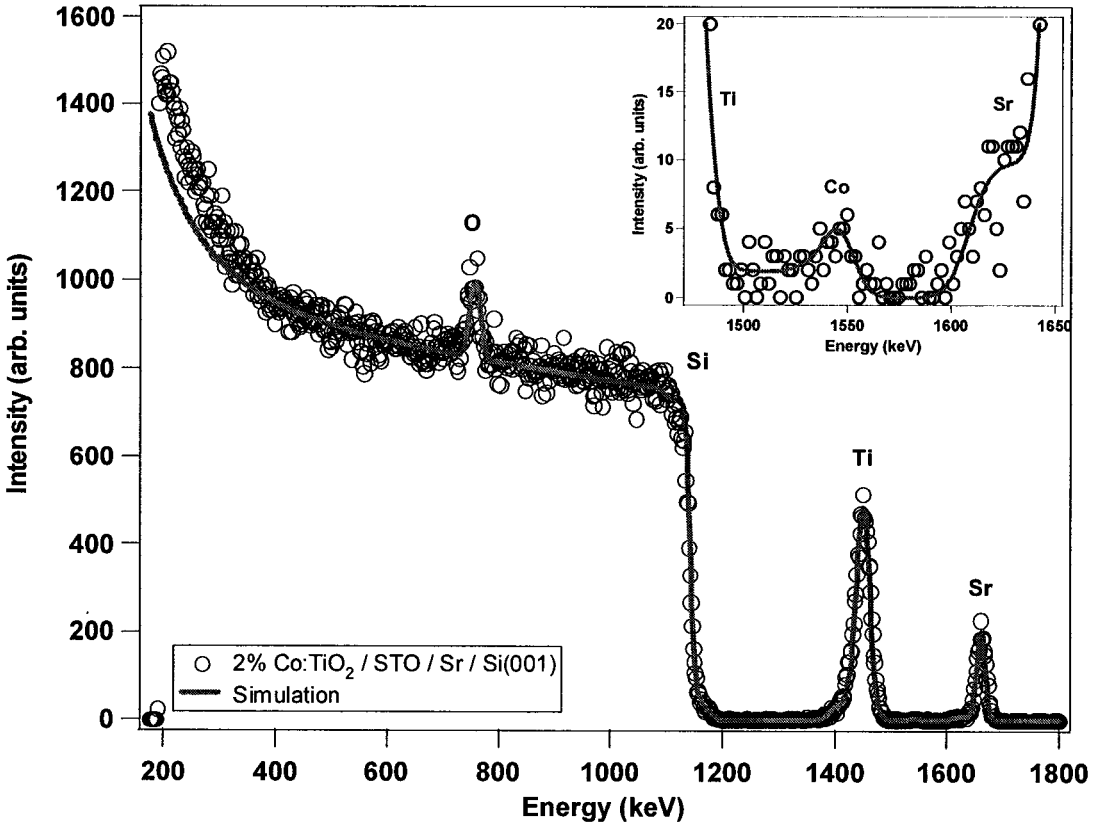

Figure 4.8. RBS data and simulation for 2% Co:TiO_2 / STO / Sr / Si(001) in the random geometry. Inset shows Co peak and simulated fit.

accurate determination of Co content cannot be made by RBS.

Proton-induced x-ray emission (PIXE) offers several advantages over RBS for Co determination. The atomic peak separation in PIXE is a function of the x-ray emission energy, not the atomic mass, so the Co K_α and K_β peaks appear without interference from Ti, Sr, or Si. By comparing the Co peak area to that of a known standard, the Co content can be accurately determined. As a standard, a thin film of 150 Å γ-Co_2O_3 / MgO(001) was used, and the Co content was calibrated by RBS. Figure 4.9 shows the PIXE spectrum and simulated fit as calculated by the GUIPIX program for 2% Co-doped anatase. The x-ray background present in the experimental data was subtracted before the simulation was performed. While the simulation appears to fit the intense Si and Ti peaks well, the simulation does a poor

job of fitting the small Co K_α and K_β peaks This is most likely a consequence of the low intensity and poor signal-to-noise ratio of the Co peak. Table 4.3 gives the compositional results from PIXE, RBS, and the Co concentration estimated from the Co flux during deposition. From these results, it is clear that both RBS and PIXE significantly underestimate the number of Co atoms in the film relative to the expected Co content determined from the Co flux. The discrepancy in the Co content determined by RBS is expected, as discussed above. However, the PIXE measurement was expected to provide a more accurate value for the Co concentration than determination from the Co flux. The error in the Co flux determination, which arises from changes in source flux during deposition from the anticipated value based on the flux calibration, is not expected to be large enough to account for the discrepancy between the flux and PIXE values. Thus it appears there is an error in

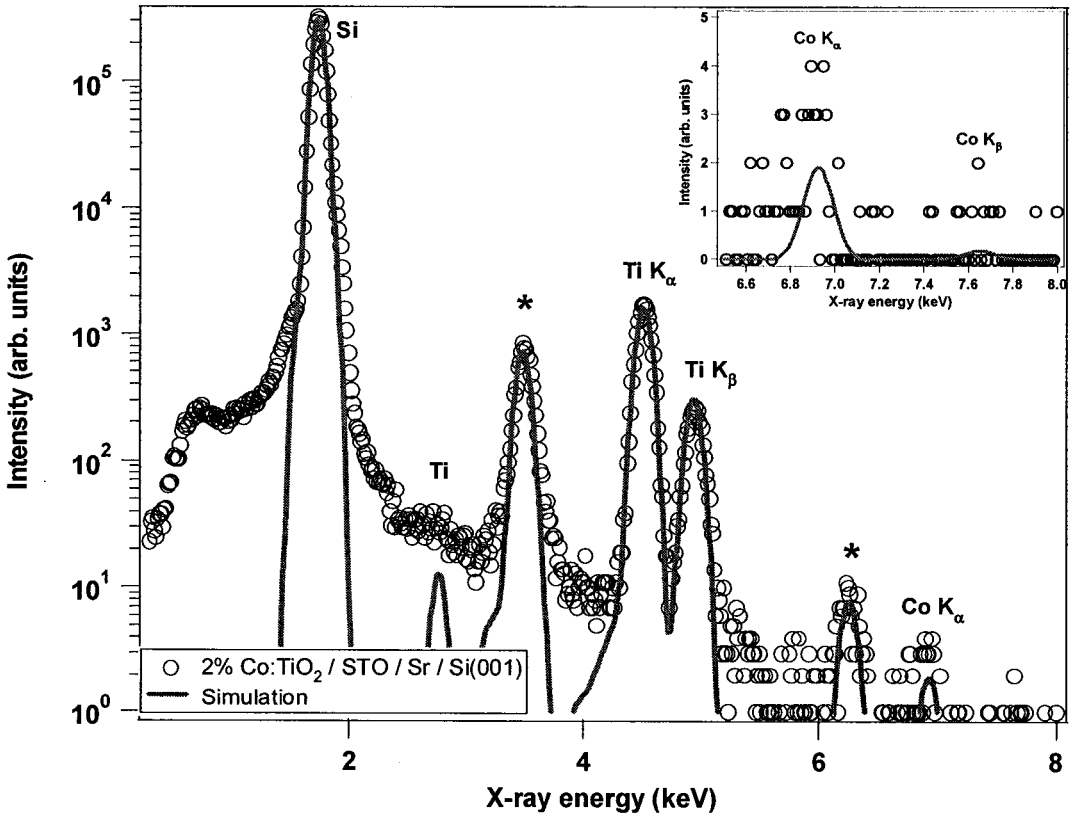

Figure 4.9. PIXE data and simulation for 2% Co:TiO_2 / STO / Sr / Si(001). Inset shows simulated fit for Co K_α and K_β peaks. The low intensity and poor statistics make it difficult to fit the Co peaks accurately. Asterisks (*) indicate pile-up peaks arising from detector overload.

Table 4.3. Summary of Co content in Co:TiO_2 determined by calculation based on the assumed Co flux during deposition, simulation of the RBS spectrum, and simulation of the PIXE spectrum for each sample. RBS and PIXE consistently underestimate the Co content relative to the expected value.

Nominal Co concentration	Co atoms in film (x 10^{15})		
	Co flux	RBS	PIXE
1% Co	0.49	0.36	0.00
2% Co	1.09	0.62	0.26
4% Co	2.16	0.39	0.23

the PIXE measurement or data analysis which results in a severe underestimation of the Co content for these films. A likely source of error is the underestimation of the Co peak in the PIXE simulation. For this reason, the Co content determined from the Co flux during deposition will be utilized for quantification of the magnetic measurements for these films.

Magnetic measurements

The magnetic properties of Co-doped anatase / STO / Sr / Si(001) were measured by vibrating sample magnetometry (VSM) at room temperature. The raw magnetic loop for 4% Co-doped anatase is presented in Figure 4.10(a). Since VSM measures the properties of the entire sample, the weak signal from the Co-doped anatase film is superimposed on the strong diamagnetic signal from the Si substrate. To remove the diamagnetic signal, a linear background was fit and subtracted from the raw data. The resultant magnetic signal attributed to the 4% Co-doped anatase thin film is shown in Figure 4.10(b). Similar data for 2% and 1% Co-doped anatase are shown in Figures 4.10(c) and 4.10(d), respectively. The characteristic "S" shape of the magnetization curves and the observed hysteresis at low field indicate these films are ferromagnetic at room temperature. The magnetization properties measured for the 1% and 2% Co-doped anatase films were similar, with a remanence (M_r) of 9% of the saturation moment (M_s) and a coercive field (H_c) of 100 G. These values correlate

well to the magnetic properties measured for Co-doped anatase films deposited on LAO substrates (M_r = 20% and H_c = 125 G).[7] In contrast, the square loop with high remanence (M_r = 56%) and high coercive field (H_c = 410 G) observed for 4% Co-doped anatase is consistent with a significant magnetic contribution from ferromagnetic Co metal.

To quantify the magnetic moment per Co atom for these samples, the measured total

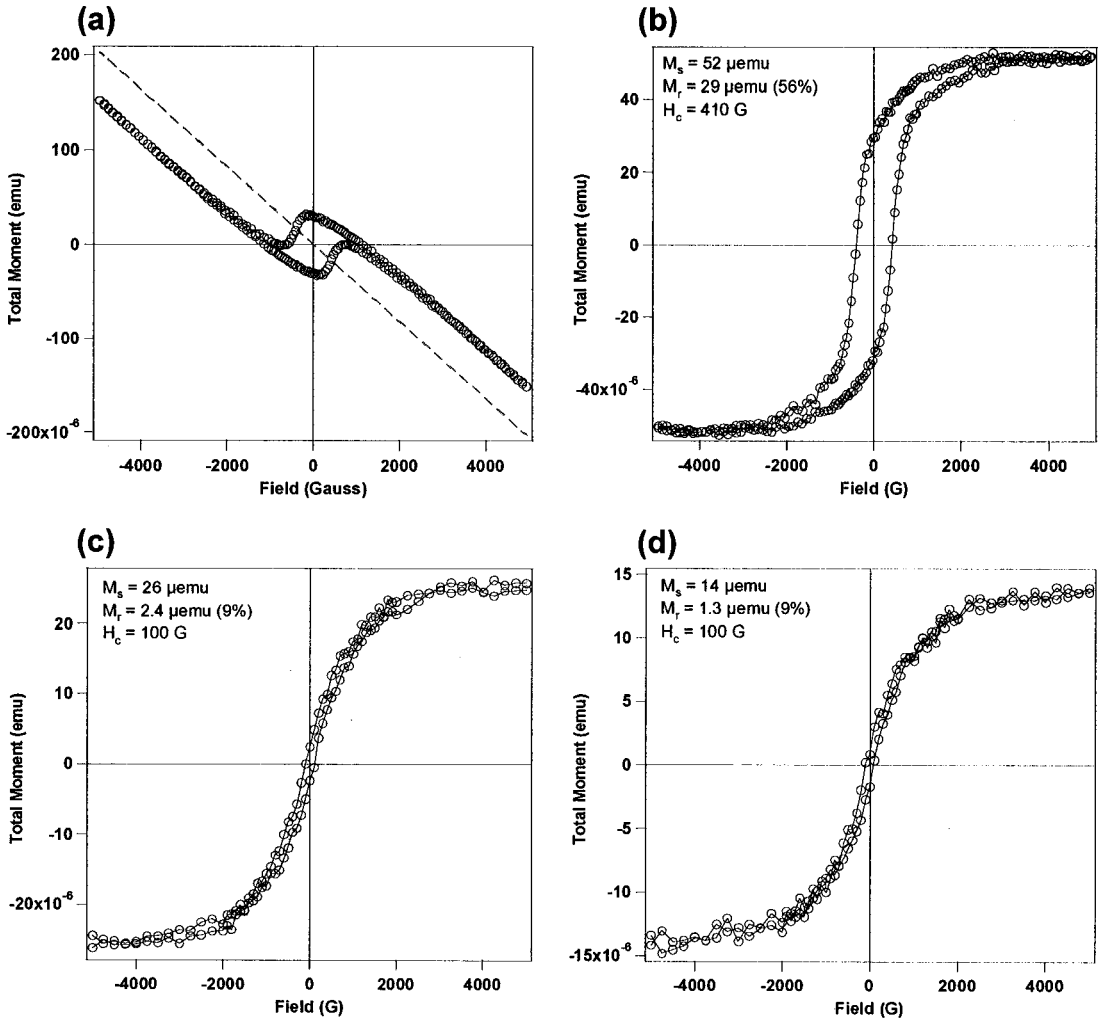

Figure 4.10. Magnetic hysteresis loops measured by VSM at room temperature for 200 Å Co:TiO_2 / STO / Sr / Si(001). (a) Raw magnetic loop for 4% Co:TiO_2. Diamagnetic response from Si substrate dominates measurement. Dotted line is linear background due to diamagnetic signal. (b) Magnetic loop for 4% Co:TiO_2 after subtraction of linear background to remove the diamagnetic signal. The saturation magnetization (M_s), remanence (M_r), and coercive field (H_c) are given. (c) Magnetic loop for 2% Co:TiO_2 after subtraction of linear background. (d) Magnetic loop for 1% Co:TiO_2 after subtraction of linear background.

saturation moment was converted to Bohr magnetons (μ_B) and divided by the total number of Co atoms in the film, as calculated from the Co flux during deposition. Since the number of Co atoms in the film was not independently quantified, an unknown amount of error (which could be as high as 50 – 100%) is introduced into determination of the magnetic moment per Co atom by estimating the Co content based on the flux. Figure 4.11 presents the results of this conversion of the magnetic hysteresis loops shown in Figure 4.10. It is expected that the saturation magnetic moment per Co atom would be the same for all Co-doped anatase films if all the Co incorporated into the anatase lattice and participated equally in the ferromagnetic

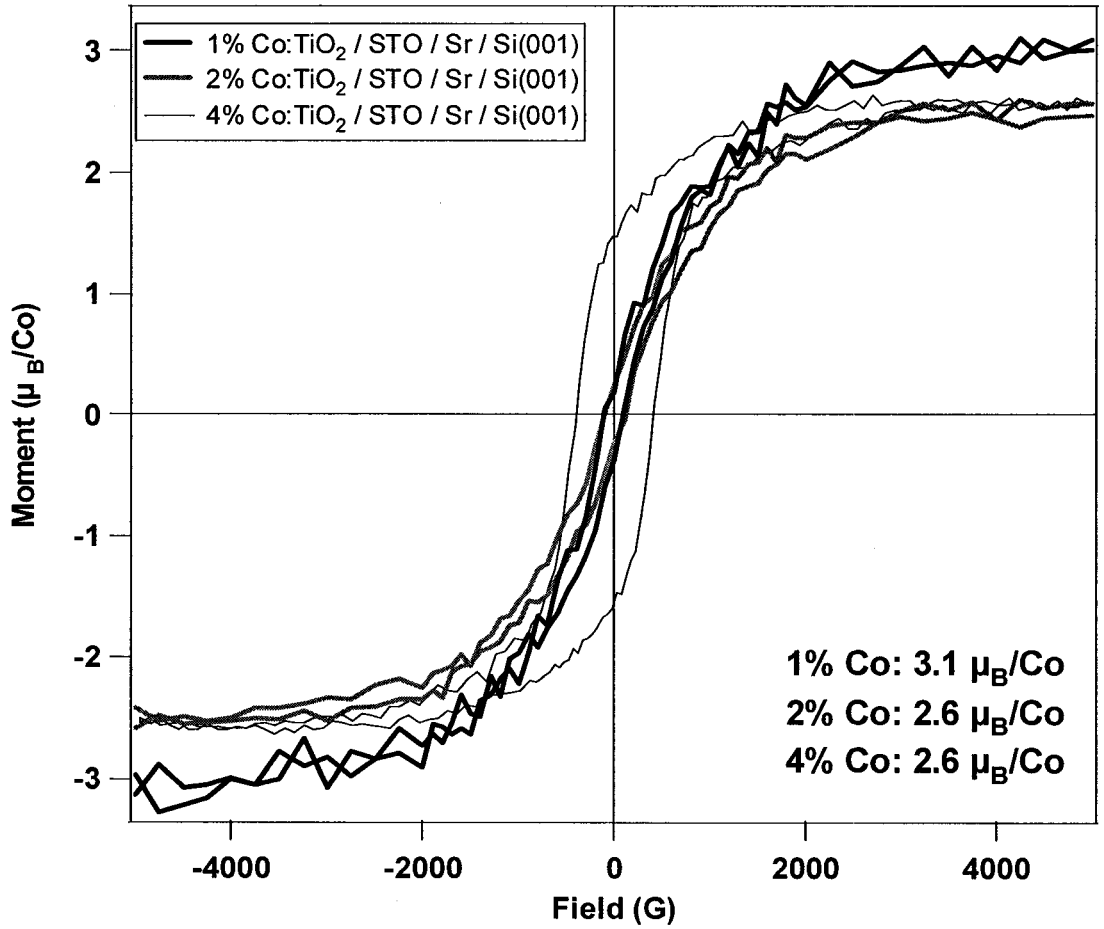

Figure 4.11. Magnetic hysteresis loops normalized to total Co content for 200 Å Co:TiO_2 / STO / Sr / Si(001) with 1%, 2%, or 4% nominal Co doping. The Co content of each film was determined from the expected flux during deposition. The average saturation magnetization for each film is given in the inset. Samples were measured by VSM at room temperature.

ordering. From previous work on Co:TiO_2 / LAO, the magnetic moment per Co atom is predicted to be 1.1 – 1.2 μ_B/Co. From Figure 4.11, it is apparent that this is not the case, and the moment per Co atom ranges from 2.6 to 3.1 μ_B/Co. This is an unexpected result, since the measured moment is significantly higher than both the moment measured previously for Co:TiO_2 / LAO and the known magnetic moment for Co metal (1.72 μ_B/Co). In addition, there appears to be some variation in hysteresis and saturation magnetization between the samples. To determine the source of these variations, the charge state and local environment of the Co dopant needs to be investigated.

Cobalt charge state

The charge state of Co, as well as information about its local environment, can be determined by x-ray absorption near edge structure (XANES). Since the films measured were only 200 Å thick with low Co concentration (< 5%), the Co K-edge XANES sampling depth is expected to be greater than the film thickness; thus, XANES is probing all the Co in the film. Due to the difficulty of modeling the XANES region theoretically, a simple lineshape analysis was performed by comparing the experimental absorption spectrum to known standards. Table 4.4 lists the Co standards utilized. The normalized Co K-edge absorption spectra (E_o = 7708.8 eV) for the Co standards are presented in Figure 4.12. Lineshape differences and shifts in the leading absorption edge are clearly observed between standards with

Table 4.4. Materials used as Co standards for Co K-edge XANES measurements.

Sample	Crystal structure	Form for XANES	Co charge state
Co metal	hcp	foil	Co(0)
CoO	rock salt	epi film on MgO	Co(II)
$CoTiO_3$	ilmenite	powder	Co(II)
$Co_{0.06}Ti_{0.94}O_2$	anatase	220 Å film on LAO	Co(II)
γ-Co_2O_3	spinel	150 Å film on MgO	Co(III)

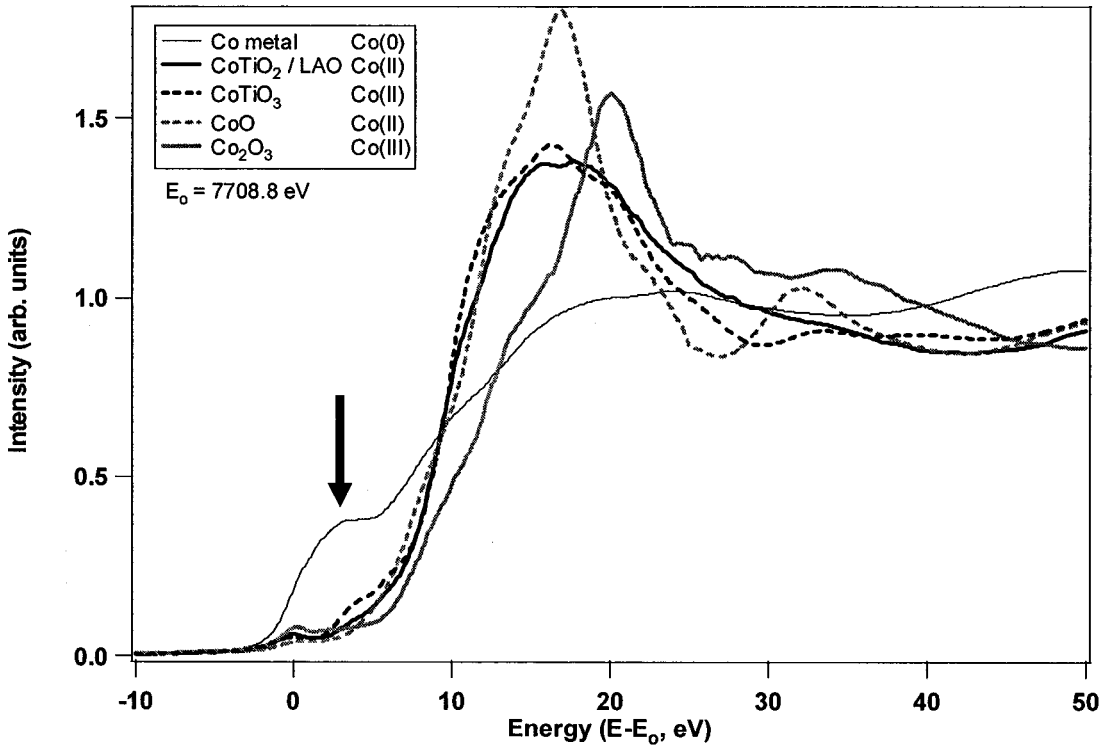

Figure 4.12. Co K-edge XANES reference spectra of Co standards. Lineshape differences are easily observed for Co in various charge states. A distinct shoulder in the absorption spectrum for Co metal, indicated by an arrow, can be utilized as a characteristic feature of Co(0) present in Co-doped films.

different Co charge states. Most importantly, a distinct shoulder is apparent in the Co metal absorption spectrum along the leading edge (indicated by an arrow in Figure 4.12); since this shoulder does not appear in the spectra for oxidized Co compounds, it can be used as a signature of Co(0) present in the film. In addition, differences are observed between CoO and $CoTiO_3$, which both consist of Co(II). This is due to differences in the local Co environment, which is an undistorted octahedron for CoO (rock salt structure) and a distorted octahedron for $CoTiO_3$ (spinel structure). The spectrum for 200 Å $Co_{0.06}Ti_{0.94}O_2$ anatase on LAO is very similar to $CoTiO_3$, indicating the local Co environment is a distorted octahedral cage in the Co:TiO_2 film. This result is consistent with Co substitution for Ti in the anatase lattice.

In Figure 4.13(a), the experimental absorption spectrum for 1% Co:TiO_2 / STO / Sr /

Si(001) is presented, along with the Co reference standards. In contrast to Co:TiO_2 deposited on LAO, the film does not closely match any of the reference standards. The absorption leading edge appears to have a slight shoulder, indicating the presence of Co(0), and the shift in the absorption peak indicates the oxidized Co occurs primarily as Co(III). To quantify the presence of various charge states of Co,

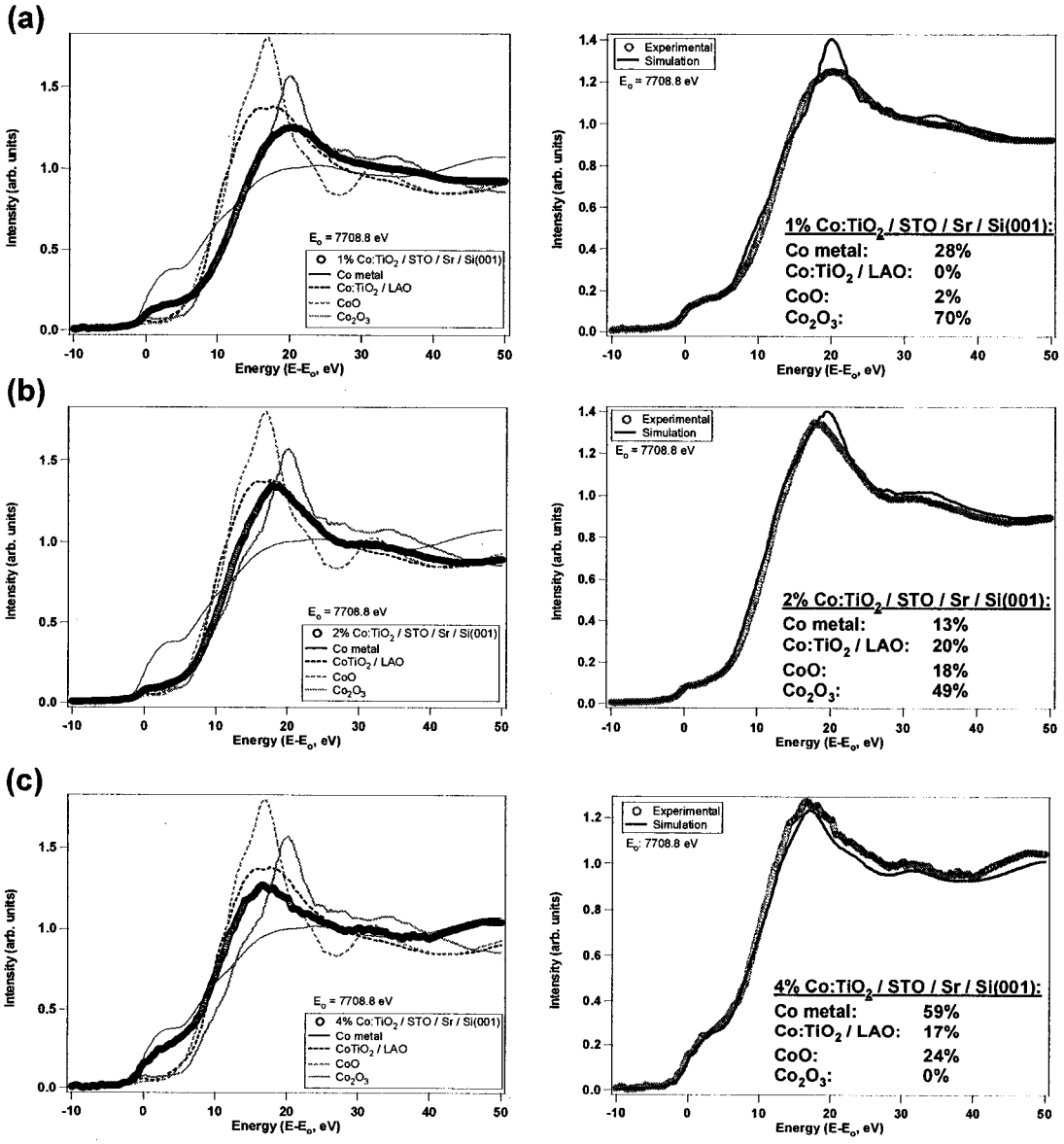

Figure 4.13. Co K-edge XANES spectra for 200 Å Co:TiO_2 / STO / Sr / Si(001), as well as Co reference spectra for comparison. Simulations were obtained by a linear combination of the Co reference spectra. (a) 1% Co:TiO_2. (b) 2% Co:TiO_2. (c) 4% Co:TiO_2.

a linear combination of reference spectra was determined which best simulated the experimental spectrum. The difference between the experimental (I_{exp}) and simulated (I_{sim}) intensity was quantified as $\chi^2 = (I_{exp}-I_{sim})^2 / I_{sim}$ for each experimental data point, and the sum of χ^2 was minimized to obtain the best fit of the simulated spectrum. The best fit results, as presented in Figure 4.13(a), are 28% Co metal, 0% Co:TiO_2, 2% CoO, and 70% Co_2O_3. From this, it is concluded that the film consists primarily of Co(0) and Co(III), with little or no Co(II). However, the simulation does not fit the data well at the absorption peak, indicating a portion of Co may be in a charge state or local environment not represented by the reference standards.

The absorption spectrum for 2% Co:TiO_2 / STO / Sr / Si(001) and the best fit simulation are presented in Figure 4.13(b). From the simulation, it appears this film consists of 13% Co metal, 20% Co:TiO_2, 18% CoO, and 49% Co_2O_3. Despite the higher Co concentration in this film, it appears to have less Co metal and more Co(II) than the 1% Co-doped anatase film, which may indicate better substitutional incorporation of Co into the anatase lattice. In addition, the simulation is able to fit the experimental data, including the absorption peak, indicating the various Co environments in the film are well represented by the reference standards.

The results for 4% Co:TiO_2 / STO / Sr / Si(001) were quite different, as shown in Figure 4.13(c). The experimental absorption spectrum could be fit well, and indicated the film consists of 59% Co metal, 17% Co:TiO_2, 24% CoO, and 0% Co_2O_3. In contrast to 1% and 2% Co:TiO_2, this film contains a significant amount of Co metal and no Co(III). The presence of Co(II) may indicate that at least some Co has substituted for Ti in the anatase lattice.

It is clear from these results that, in contrast to Co:TiO_2 deposited on LAO, Co:TiO_2 films deposited on STO / Sr / Si(001) do not exclusively contain Co(II) substituted for Ti(IV) in the anatase lattice. Deposition on Si appears to result in a mixture of

Co(0), Co(II), and Co(III). As presented in Figure 4.14, the proportion of atoms with the Co(0), Co(II), and Co(III) charge state varies with total Co concentration. The observed increase in Co(0) and corresponding decrease in Co(III) as the total Co concentration is increased is attributed to the increased competition for oxygen by Co atoms in the more highly doped films. This implies a significant quantity of excess oxygen was not present under these deposition conditions, such that sufficient oxygen was not available to oxidize all the incident Co. The situation for Co(II) is more complicated. As plotted in Figure 4.14, the total number of Co atoms with the +2 charge state is a combination of the fractions of Co:TiO_2 / LAO and CoO utilized in the XANES fitting. From Figure 4.14 it is evident that Co oxidation to Co(II), and thus possible incorporation into the anatase lattice, increases with increasing Co concentration. This is unexpected in light of the situation for Co(0) and Co(III); with

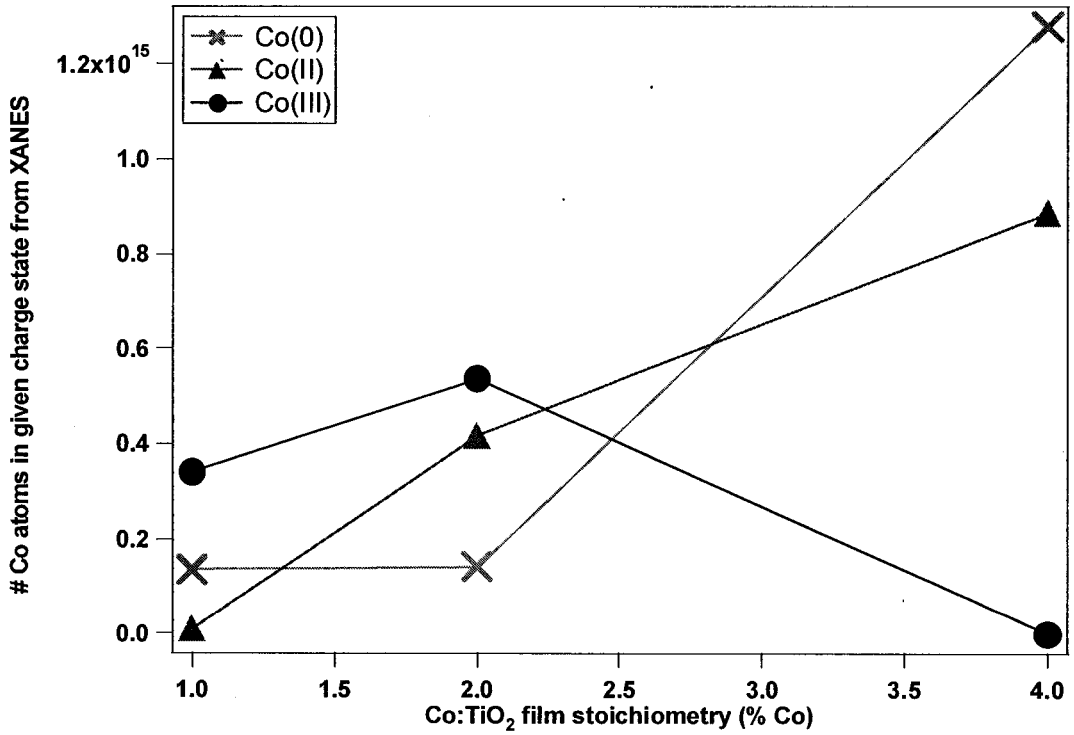

Figure 4.14. Co charge state in 200 Å Co:TiO_2 / STO / Sr / Si(001) samples, as determined by simulating the Co K-edge XANES spectra with a linear combination of the Co reference spectra. The Co(II) charge state is a combination of Co:TiO_2 / LAO and CoO. With increasing Co doping concentration, Co(0) and Co(II) increase as Co(III) decreases.

decreasing excess oxygen the oxidation of Co to Co(II) should decrease. Likewise, if the solid solubility of Co in anatase was exceeded for higher doping concentrations, the proportion of substitutional Co, represented by Co:TiO_2 / LAO in the XANES simulation, should plateau with increasing Co concentration. Instead, it is observed to increase along with CoO.

XANES is a much more sensitive technique than either XRD or TEM to identify Co that has not incorporated as Co(II) into the anatase lattice. In particular, XANES is much more effective at identifying the presence of Co(0). For example, 2% Co:TiO_2 / STO / Sr / Si(001) was measured by both grazing incidence XRD and high resolution TEM, and no secondary phases were identified; in contrast, the XANES data indicates the film contains a significant portion of Co as Co(0) (13%) and Co_2O_3 (49%). However, while the XANES data provides information about the charge states and local environments felt by Co atoms in the film, it cannot distinguish the form these local environments take. The difference between secondary phases which have precipitated out of the anatase lattice and distorted, interstitial, or grain boundary sites in anatase whose local environment is similar to a bulk secondary phase cannot be determined from XANES. In samples with primarily one local environment, extended x-ray absorption fine structure (EXAFS) can be utilized to obtain information on the specific geometry of the local environment, such that bulk secondary phases could be distinguished from interstitial sites, for example. However, in these Co:TiO_2 films the mixture of Co charge states and local environments make interpretation of EXAFS spectra impossible.

Magnetic measurements, revisited

In light of the various Co charge states present in each film, as determined by XANES, it should be possible to reinterpret the saturation magnetic moment per Co

atom discussed above. For example, 4% Co:TiO_2 was found to consist of 59% Co metal; thus, 59% of the Co atoms should ferromagnetically order with the known magnetic moment of Co metal (1.72 μ_B/Co). Assigning the oxidized Co species is more difficult. If the "CoO" and "Co_2O_3" fractions observed in XANES are separate phases precipitated out of the anatase lattice, the Co atoms will be antiferromagnetically coupled and will not contribute to the observed saturation magnetization. However, if the Co atoms are in CoO-like or Co_2O_3-like environments distributed throughout the anatase lattice (i.e., Co(III) substituting for Ti(IV) in the anatase lattice), such that antiferromagnetic coupling is not possible, the magnetic moment on each Co will contribute to the overall measured magnetism. Assuming the orbital magnetic moment is fully quenched, Co(II) will have a magnetic moment of 1 μ_B/Co in the low spin state and 3 μ_B/Co in the high spin state. Likewise, the spin magnetic moment of Co(III) is 0 μ_B/Co in the low spin state and 4 μ_B/Co in the high spin state. In first row transition metal salts, the orbital magnetic moment of the transition metal cation is quenched.[13] However, in work on Co:TiO_2 / LAO, the magnetic moment has been found to be 1.1 – 1.2 μ_B/Co in films with exclusively Co(II), which was attributed to low spin Co(II) with some contribution from the orbital magnetic moment.[14] Incomplete quenching of the orbital magnetic moment in this case may arise from distortion of the octahedral environment in anatase. Prediction of the expected orbital magnetic moment arising from incomplete quenching by the crystal lattice would require detailed knowledge of the local environment of each Co atom, which cannot be extracted from Co K-edge XANES spectra. Due to this, the contribution of an unquenched orbital magnetic moment to the total saturation moment cannot be quantified.

Measurement of the magnetic moment of Co:TiO_2 / LAO suggests that Co(II) is in a low spin state;[14] however, Co L-edge x-ray absorption spectroscopy (XAS) of Co:TiO_2 / LAO deposited by pulsed laser deposition suggests that Co(II) is in a high spin state.[15] Since it is difficult to know *a priori* the spin state and ferromagnetic or

antiferromagnetic coupling of Co in various environments in the samples, some assumptions must be made before attempting to quantify the magnetic measurements. Co(0) present in the film is assumed to be in ferromagnetic clusters with a moment of 1.72 μ_B/Co. In addition, all Co(II) and Co(III) present in the film is assumed to participate in the ferromagnetic ordering. This assumption is reasonable based on the high overall moment per Co atom measured for these films; if a significant fraction of Co atoms were antiferromagnetically coupled, the overall magnetic moment would be lower than expected (i.e., less than 1 μ_B/Co). The orbital magnetic moment is assumed to be fully quenched for both Co(II) and Co(III). With these assumptions, the predicted magnetic moment per Co atom can then be calculated from the following equations:

Co(II) low spin / Co(III) low spin:

$$M_{s,\,low/low} = X_{Co(0)}*1.72 + Y_{Co(II)}*1 + Z_{Co(III)}*0 \quad (4.1)$$

Co(II) low spin / Co(III) high spin:

$$M_{s,\,low/high} = X_{Co(0)}*1.72 + Y_{Co(II)}*1 + Z_{Co(III)}*4 \quad (4.2)$$

Co(II) high spin / Co(III) low spin:

$$M_{s,\,high/low} = X_{Co(0)}*1.72 + Y_{Co(II)}*3 + Z_{Co(III)}*0 \quad (4.3)$$

Co(II) high spin / Co(III) high spin:

$$M_{s,\,high/high} = X_{Co(0)}*1.72 + Y_{Co(II)}*3 + Z_{Co(III)}*4 \quad (4.4)$$

where M_s is the predicted saturation magnetic moment (μ_B/Co) and $X_{Co(0)}$, $Y_{Co(II)}$, and $Z_{Co(III)}$ are the atomic fractions of Co in the respective charge states as determined by XANES simulation. Table 4.5 presents the results of these calculations for 1%, 2%, and 4% Co:TiO_2. For comparison, the measured saturation moments for the films are also tabulated. Overall, it appears that the measured magnetic moment can be reproduced reasonably well assuming both Co(II) and Co(III) are in high spin states. The difference between the measured value and the predicted value, defined as $(M_{s,\,measured} - M_{s,\,predicted}) / M_{s,\,measured}$, is -8% for 1% Co:$TiO_2$, -30% for 2% Co:$TiO_2$, and 13% for 4% Co:$TiO_2$. The measured magnetic moment for 2% Co:TiO_2 is better reproduced by assuming Co(II) is in a low spin state and Co(III) is in a high spin

Table 4.5. Measured saturation moment for 200 Å Co:TiO_2 / STO / Sr / Si(001), on a per Co basis (as determined by the flux during deposition). Predicted moment calculation is based on the fraction of Co in each charge state, as determined by simulation of the Co K-edge XANES spectra.

Nominal Co content	Measured moment (μ_B/Co)	Predicted moment with Co(II) / Co(III) spin state (μ_B/Co)			
		Low / low	Low / high	High / low	High / high
1% Co	3.1	0.5	3.3	0.5	3.3
2% Co	2.6	0.6	2.6	1.4	3.3
4% Co	2.6	1.4	1.4	2.2	2.2

state (0% difference between measured and predicted values); this implies the local crystal field splitting for Co(II) is sufficiently different from that for Co(III) that low spin is favored for Co(II) and high spin is favored for Co(III). This situation would only be possible if the Co(II) participating in ferromagnetic ordering were in a distinct crystal phase from Co(III).

Utilizing the XANES results to predict the saturation magnetization for each Co:TiO_2 film, it appears that essentially all the Co in the film participates in ferromagnetic ordering, and the oxidized Co species are in a high spin arrangement. Unfortunately, this analysis cannot determine if the Co atoms are substitutional in the anatase lattice or forming secondary phases which are ferromagnetic. Error may also be introduced in calculating the number of Co atoms in the film from the Co source flux during deposition; this calculation sensitively affects the measured saturation magnetization per Co atom.

Investigation of Si oxidation influence

The Co oxidation state in a Co:TiO_2 film deposited on STO / Sr / Si(001) is very different from Co:TiO_2 deposited on LAO, even though the deposition conditions were very similar. While Co:TiO_2 / LAO consists entirely of Co(II) in distorted octahedral sites ($CoTiO_3$-like), consistent with substitution for Ti(IV) in the anatase

lattice, Co:TiO_2 / STO / Sr / Si(001) consists of Co(0), Co(II), and Co(III), with the proportion of each charge state dependent in a complex manner on the Co doping concentration.

The variation in Co oxidation state when deposited on STO / Sr / Si(001) might be attributed to the Si substrate. One possibility is that the strong thermodynamic driving force for oxidation of Si to SiO_2 at the interface during the deposition of Co:TiO_2 may act as an oxygen sink, pulling oxygen through the STO buffer layer and thus reducing the concentration of oxygen available for reaction with Co and Ti at the film surface. The STO buffer layer does not act as an effective barrier to oxygen diffusion during anatase deposition, and a 35 Å thick SiO_2 layer has been observed after deposition of 200 Å Co:TiO_2. Since oxidation of Ti is more thermodynamically favorable than oxidation of Co (see Table 4.1), the reduced oxygen concentration at the film surface primarily affects Co oxidation.

To eliminate the influence of Si oxidation on the oxidation of Ti and Co, with the goal of reducing the Co(0) content in the film, two approaches were considered. The first was to eliminate the formation of SiO_2 by reducing the amount of oxygen supplied to the film during deposition, such that all oxygen is consumed by Ti and Co with no excess to diffuse to the Si interface. However, this method would still result in a reduced oxygen concentration at the film surface, which would negatively impact oxidation of Co. Alternatively, a thick SiO_2 layer was purposefully grown at the Si interface after deposition of 10 ML STO / ½ ML Sr by exposing the heated STO / Sr / Si(001) film to the oxygen plasma for 45 minutes before deposition of Co:TiO_2 was initiated. This plasma treatment should result in a thick SiO_2 film at the Si interface, significantly reducing the thermodynamic driving force for oxygen diffusion through the STO buffer layer. Thus, deposition at the same oxygen partial pressure should result in a higher oxygen concentration at the film surface during Co:TiO_2 deposition.

Figure 4.15 shows the RHEED images of 10 ML STO / Sr / Si(001) as-deposited, after plasma treatment for 45 minutes, and after deposition of 200 Å 4% Co-doped anatase. From these RHEED images, it is apparent that the STO buffer layer surface became slightly rougher after the plasma treatment, but retained its epitaxial relationship with the underlying Si(001) substrate. The effect of the degraded surface quality of the STO buffer layer is observed in the Co:TiO_2 film, which contains significant polycrystallinity along with epitaxial regions and surface roughness. The low quality crystallinity of the Co:TiO_2 film is not expected to significantly affect the oxidation of Co and Ti.

From the XANES spectrum, shown in Figure 4.16, the film appears to contain primarily Co(0) and Co(III); the simulated fit indicates the film consists of 50% Co(0), 0% Co:TiO_2 / LAO, 4% CoO, and 46% Co_2O_3. This is in contrast to the 4% Co:TiO_2 / STO / Sr / Si(001) sample deposited without plasma treatment, which

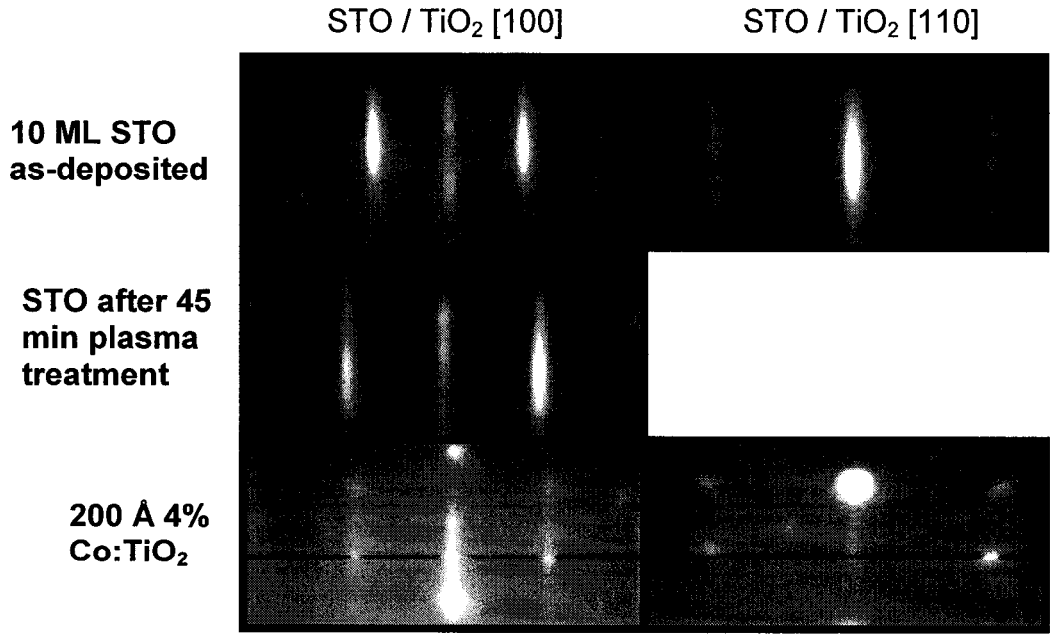

Figure 4.15. RHEED images of 10 ML STO as-deposited on ½ ML Sr /Si(001); the same film after exposure to the oxygen plasma at elevated temperature (550-575°C) for 45 minutes; and after deposition of 200 Å 4% Co:TiO_2. STO surface roughness after plasma treatment resulted in significant polycrystallinity and amorphous regions in Co:TiO_2 film.

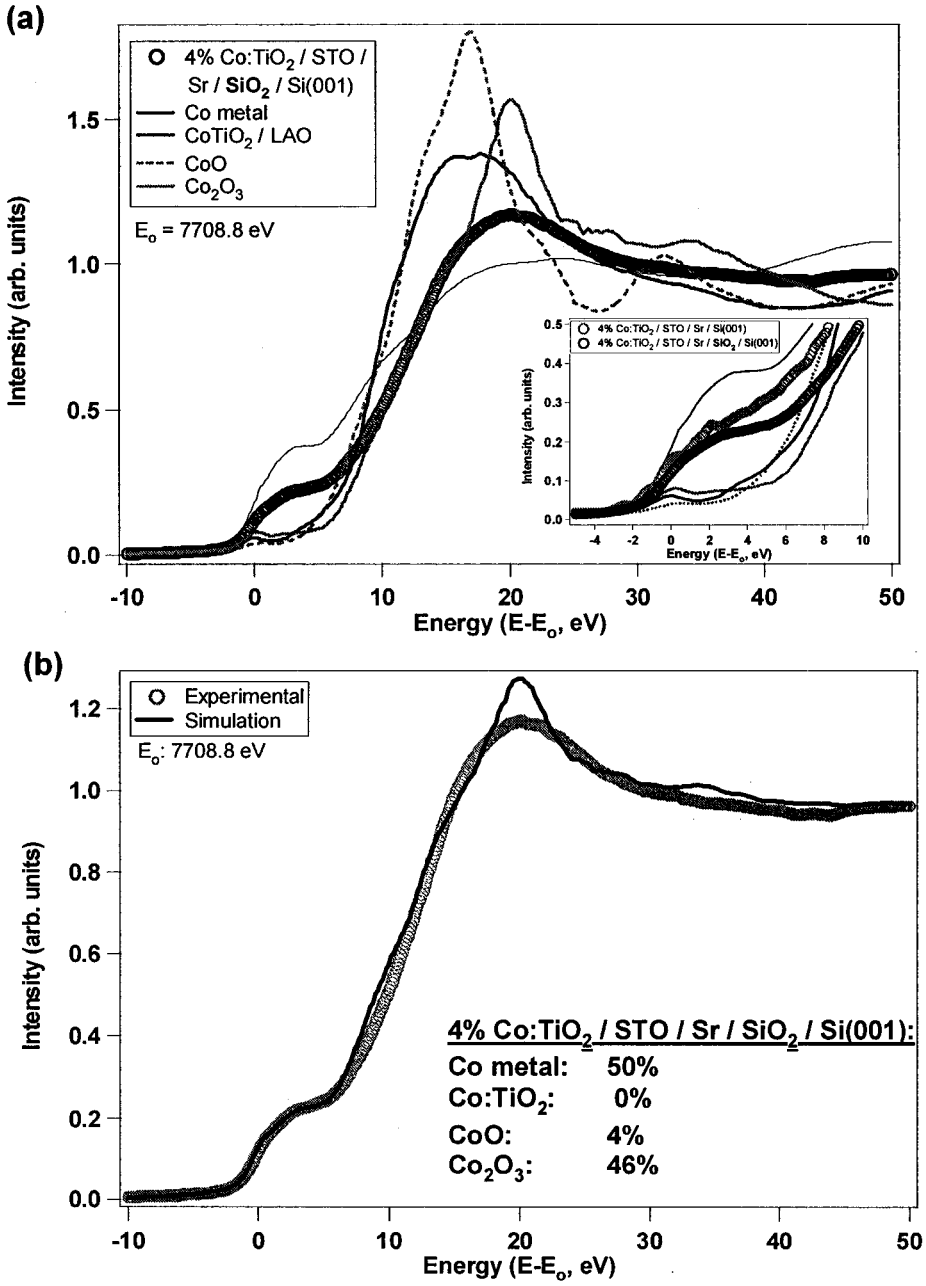

Figure 4.16. (a) Co K-edge XANES of 200 Å 4% Co:TiO_2 / STO / Sr / SiO_2 / Si(001). Co reference standard spectra are included for comparison. Inset shows the Co(0) shoulder region; compared to 4% Co:TiO_2 deposited without prior plasma treatment to grow SiO_2, the amount of Co (0) in the plasma treated film is not significantly reduced. (b) Simulated spectrum obtained by linear combination of the Co reference spectra. Film consists primarily of Co(0) and Co(III).

consisted of Co(0) and Co(II) (see Figure 4.13(c)). The increased proportion of Co(III) in the plasma-treated film may result from an increased concentration of oxygen at the film surface during deposition. This indicates that oxidation of the Si

interface during anatase deposition has at least some effect on the oxygen concentration at the anatase film surface. However, from the inset to Figure 4.16(a), it is evident that no significant reduction in Co(0) content was achieved by deliberately growing a SiO_2 layer before anatase deposition.

Summary

Co-doped anatase films were deposited on STO / Sr / Si(001) with the goal of obtaining single-phase anatase films containing Co substituted for Ti and distributed throughout the anatase lattice. From the AFM and AES results, it is clear that large particles or clusters form on the surface of Co-doped anatase films, and that most, if not all, Co segregates to these particles. Determining the true mechanism of Co-enriched cluster formation would require a significant experimental and theoretical effort. It is unlikely that the resulting mechanistic understanding of cluster formation would lead to a deposition scheme that produces flat anatase films with uniform Co incorporation while simultaneously oxidizing Co to Co(II) and preserving the STO / Si(001) interface.

Analysis by XANES indicates that the Co atoms in the sample are present in a mixture of charge states and local environments. Co(III) and Co(II) in the form of CoO are not desired since they indicate Co may not have substituted for Ti in the anatase lattice. Particularly detrimental is Co(0), which is likely in the form of ferromagnetic Co metal clusters. The presence of Co(0) under oxidative conditions which are known to oxidize the Si interface strongly suggests that no regime exists in which Co is fully oxidized to Co(II) while simultaneously preventing oxidation of the Si interface. Based on these results, it is concluded that Co-doped anatase on Si is a poor candidate as a DMS material for spintronic devices.

Notes to Chapter IV:

1. P.A. Stampe, R.J. Kennedy, Y. Xin, and J.S. Parker, "Investigation of the cobalt distribution in the room temperature ferromagnet TiO_2:Co." *J. Appl. Phys.* **93** (10), 7864 (2003).

2. S.R. Shinde, S.B. Ogale, S. Das Sarma, J.R. Simpson, H.D. Drew, S.E. Lofland, C. Lanci, J.P. Buban, N.D. Browning, V.N. Kulharni, J. Higgins, R.P. Sharma, R.L. Greene, and T. Venkatesan, "Ferromagnetism in laser deposited anatase $Ti_{1-x}Co_xO_{2-\delta}$ films." *Phys. Rev. B.* **67**, 115211 (2003).

3. D.H. Kim, J.S. Yang, K.W. Lee, S.D. Bu, D.-W. Kim, T.W. Noh, S.-J. Oh, Y.-W. Kim, J.-S. Chung, H. Tanaka, H.Y. Lee, T. Kawai, J.Y. Won, S.H. Park, and J.C. Lee, "Investigations on the nature of observed ferromagnetism and possible spin polarization in Co-doped anatase TiO_2 thin films."*J. Appl. Phys.* **93** (10), 6125 (2003).

4. D.R. Lide, ed. *CRC Handbook of Chemistry and Physics*, 84th ed. (CRC Press, 2003).

5. S.A. Chambers, C.M. Wang, S. Thevuthasan, T. Droubay, D.E. McCready, A.S. Lea, V. Shutthanandan, and C.F. Windish Jr., "Epitaxial growth and properties of MBE-grown ferromagnetic Co-doped TiO_2 anatase films on $SrTiO_3$(001) and $LaAlO_3$(001)." *Thin Solid Films* **418**, 197 (2002).

6. S.A. Chambers, S.M. Heald, and T. Droubay, "Local Co structure in epitaxial $Co_xTi_{1-x}O_{2-x}$ anatase." *Phys. Rev. B* **67**, 100401 (2003).

7. S.A. Chambers, T. Droubay, C.M. Wang, A.S. Lea, R.F.C. Farrow, L. Folks, V. Deline, and S. Anders, "Clusters and magnetism in epitaxial Co-doped TiO_2 anatase." *Appl. Phys. Lett.* **82** (8), 1257 (2003).

8. Z. Yang, G. Liu, and R. Wu, "Distribution and magnetization of Co impurities in anatase TiO_2." *Phys. Rev. B* **67**, 060402 (2003).

9. A.M. Dabiran, S.M. Seutter, and P.I. Cohen, "Direct observations of the strain-limited island growth of Sn-doped GaAs(100)." *Surf. Rev. Lett.* **5** (3), 783 (1998).

10. R.S. Williams, G. Medeiros-Ribeiro, T.I. Kamins, and D.A.A. Ohlberg, "Thermodynamics of the size and shape of nanocrystals: epitaxial Ge on Si(001)." *Annu. Rev. Phys. Chem.* **51**, 527 (2000).

11. F.B. de Mongeot, W. Zhu, A. Molle, R. Buzio, C. Boragno, U. Valbusa, E.G. Wang, and Z. Zhang, "Nanocrystal formation and faceting instability in Al(110) homoepitaxy: true upward adatom diffusion at step edges and island corners." *Phys. Rev. Lett.* **91** (1), 016102 (2003).

12. J. Li, C.H. Sow, X.S. Rao, C.K. Ong, and D.N. Zheng, "Epitaxial growth and magnetic and electric properties of Co-doped TiO_2 thin films."*Eur. Phys. J. B* **32**, 471 (2003).

13. C. Kittel, *Introduction to Solid State Physics*, Seventh ed. (John Wiley and Sons, New York, 1996).

14. S.A. Chambers, S. Thevuthasan, R.F.C Farrow, R.F. Marks, J.U. Thiele, L. Folks, M.G. Samant, A.J. Kellock, N. Ruzycki, D.L. Ederer, and U. Diebold, "Epitaxial growth and properties of ferromagnetic Co-doped TiO_2 anatase." *Appl. Phys. Lett.* **79** (21), 3467 (2001).

15. J.-Y. Kim, J.-H. Park, B.-G. Park, H.-J. Noh, S.-J. Oh, J.S. Yang, D.H. Kim, S.D. Bu, T.-W. Noh, H.-J. Lin, H.-H. Hsieh, and C.T. Chen, "Ferromagnetism induced by clustered Co in Co-doped anatase TiO_2 thin films." *Phys. Rev. Lett.* **90** (1), 017401 (2003).

CHAPTER V: COBALT-DOPED $SrTiO_3$ / $SrTiO_3$(001)

As discussed in Chapter IV, Co-doped anatase TiO_2 on STO / Sr / Si(001) is ferromagnetic at room temperature, an essential criterion for a dilute magnetic semiconductor (DMS) material in practical spintronic devices. However, the deposition results in segregation of Co to surface clusters, with essentially no Co incorporation in the underlying anatase film. In addition, the Co occurs in a mixture of Co(0), Co(II), and Co(III) charge states, depending in a complex way on the Co doping concentration and deposition conditions. Both of these materials issues are detrimental to the utilization of Co-doped anatase as a DMS material. As an alternative, Co-doped perovskite $SrTiO_3$ (STO) was considered. Very little work[1-3] has been attempted previously on STO as a host lattice for DMS materials, since undoped STO is generally an insulating rather than semiconducting oxide. However, STO can be made semiconducting by donor doping or the introduction of oxygen vacancies. STO is an appealing oxide for integration with Si; STO can be deposited epitaxially on Si without the formation of an interfacial SiO_x layer, as demonstrated in Chapter III. The deposition of STO on Si is facilitated by the catalytic effect of Sr on the oxidation of Ti, allowing stoichiometric STO to be formed at lower temperature and/or oxygen pressure than would be required for TiO_2. This property is also expected to aid in the oxidation of Co. To evaluate the materials and magnetic properties of Co-doped STO as a potential DMS material, Co-doped STO films were deposited on STO(001) substrates.

Deposition conditions

As described in Chapter II, 300 – 450 Å Co-doped STO / STO(001) was deposited under similar conditions to Co-doped anatase / LAO.[4] In an attempt to fully oxidize the Co dopant to Co(II) and avoid Co(0), the oxygen plasma at an oxygen partial

pressure of $2x10^{-5}$ Torr was utilized, and a substrate temperature of 650-700°C (800°C pyrometer reading) was chosen. These growth conditions would most likely have to be modified for deposition on Si; they were selected to produce high quality Co-doped STO for materials and magnetic evaluation, not for compatibility with Si. Initial depositions utilized electron beam evaporation of Ti; however, difficulty in stoichiometry control of the multicomponent STO film prompted a change to Ti evaporation from an effusion cell.

Stoichiometry of $SrTiO_3$

Stoichiometry control is vital to the successful deposition of STO. Unlike TiO_2, where Ti is the only metal cation and flux variations can be accommodated under excess oxygen conditions, in STO the Sr and Ti fluxes must be equal to achieve stoichiometric films. Slight variations in the flux of either Sr or Ti result in stoichiometry variations in the film. For this reason, the Ti source was changed from electron beam evaporation to an effusion cell, which is expected to provide a more stable and reproducible flux. To further improve stoichiometry control, the metal fluxes were checked by the quartz crystal oscillator (QCO) prior to deposition. Since the QCO is placed in the sample position, geometric factors (such as a tooling factor) do not need to be used to correct the measured flux to determine flux reaching the sample during deposition. However, other issues reduce the accuracy of the flux values measured by the QCO relative to film deposition.[5] QCO measurements are performed in vacuum with a minimal background pressure of oxygen, while film deposition occurs in $2x10^{-5}$ Torr of oxygen. This partial pressure of oxygen may form a thin oxide layer on the heated metal sources, reducing their flux during film deposition relative to that during QCO measurement. In addition, the QCO is held at ambient temperature with the aid of cooling water during flux measurements. However, the substrate surface during film deposition is held at approximately 650-

700°C. Thus, the sticking coefficients of the metal atoms may be significantly higher on the cooled QCO crystal than on the heated substrate, reducing the apparent flux to the substrate. This is expected to be a concern especially for Sr, which is relatively volatile in both Sr metal and SrO forms.[5] Due to these issues, matching the absolute flux as measured by the QCO for Sr and Ti will not result in a stoichiometric STO film. In most cases, the film will be rich in Ti, which indicates there may be a significant desorption of Sr from the heated substrate surface. As an alternative method, the metal fluxes were measured prior to deposition and compared to the STO film stoichiometry as determined by x-ray photoemission spectroscopy (XPS), as discussed in detail below. The metal fluxes measured by the QCO were then adjusted to compensate for observed non-stoichiometry in the film. In this way, target fluxes measured by the QCO were developed which produced nearly stoichiometric STO films. For example, a measured deposition rate of 11.3 sec / ML STO for Ti and 8.25 sec / ML STO for Sr was found to produce stoichiometric or slightly Ti-rich films, despite the increased Sr rate relative to Ti. Despite these attempts, a certain amount of STO stoichiometry variation was observed, attributable to slight variations in deposition conditions during each growth.

As expected for homoepitaxy of STO on STO(001), oscillations of the RHEED (00) spot intensity were observed for nearly all depositions, regardless of stoichiometry. A particularly clear example is shown in Figure 5.1 for 340 Å Co:STO / STO(001) doped with nominally 6% Co. The oscillation spacing corresponds to the time to deposit one monolayer of STO. As discussed above, the expected deposition rate, based on the metal fluxes, was 8.25 – 11.3 sec / ML STO. However, the deposition rate calculated from the RHEED oscillations was 16 sec / ML, indicating the overall flux from each metal source was significantly reduced during deposition. This may be attributed to the formation of an oxide skin on the metal sources during deposition. The changes in overall RHEED spot intensity over the course of the deposition may be due to subtle changes in the metal fluxes or oxygen partial

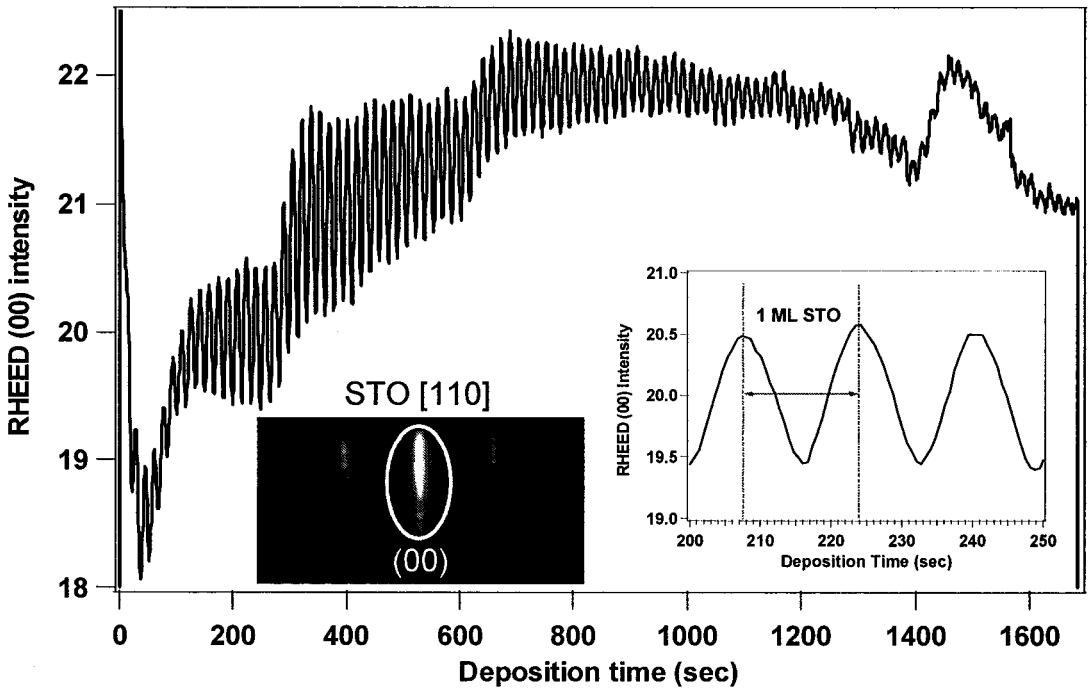

Figure 5.1. Intensity oscillations of the RHEED (00) streak during deposition of 340 Å nominally 6% Co:STO / STO(001). As indicated in the inset, the oscillation spacing corresponds to the time required to deposit one monolayer of STO.

pressure in the chamber.

In situ x-ray photoelectron spectroscopy (XPS) was employed to quantify the STO composition after deposition. As discussed in Chapter III, the ratio of the area under the Sr 3*p* peak to the area under the Ti 2*p* peak, after subtracting a Shirley background for each region, was compared to the same ratio for a bulk single crystal of *n*-STO. For this reference standard, the ratio of Sr $3p_{reference}$ / Ti $2p_{reference}$ was found to be 1.06. For thick (300 - 500 Å), pure STO films, the experimentally determined ratio is directly comparable to the reference standard. However, for Co-doped films, the occupation of Ti sites by Co must be considered when calculating stoichiometry. To account for this, assuming all Co substitutes for Ti, the expected ratio for $Sr(Ti_{1-x}Co_x)O_3$ is corrected as Sr $3p_{reference}$ / [Ti $2p_{reference}$ * (1-x)] or 1.06 / (1-x). To normalize the stoichiometry of films with varying concentrations of Co, the

experimental Sr 3*p* / Ti 2*p* ratio was divided by the corrected reference standard ratio, such that an exactly stoichiometric film exhibiting the expected Sr / Ti ratio will have a corrected stoichiometric ratio of 1.0. Deviations from this value indicate excess Sr (ratio > 1) or excess Ti (ratio < 1). All Sr / Ti ratios given below have been corrected in this way for Co incorporation. For the purposes of the discussion below, "nearly stoichiometric" STO films are defined as those with Sr / Ti > ~ 0.85.

Due to the insulating properties of the STO films, it was necessary to utilize the low energy electron flood gun during XPS measurements to compensate for surface charging. Imperfect charge compensation by the flood gun results in some peak asymmetry. However, the peak asymmetry will not affect the area under the peak provided the background subtraction is accurate; the slight asymmetry observed in these STO films does not alter the background subtraction, such that the peak area is unaffected.

Quantification of Co concentration

Quantification of Co content in Co:STO presents the same challenges as quantification in Co:TiO_2, as discussed in Chapter IV. For Co:STO, Co is only observed in XPS in some cases for higher doping concentrations; thus, XPS cannot be utilized to quantify the Co content in the films. Instead, quantification was attempted with both Rutherford backscattering spectrometry (RBS) and proton-induced x-ray emission (PIXE). Interpretation of RBS data is made more difficult by the presence of both Sr and Ti throughout the film and substrate, such that the Co signal rides on the Sr background, and interference from Ti may occur. The RBS spectrum and simulated fit as determined utilizing the SimNRA computer program for nominally 6% Co:STO / STO(001) are shown in Figure 5.2. Although the Co peak is small relative to the background level, the simulation appears to fit it

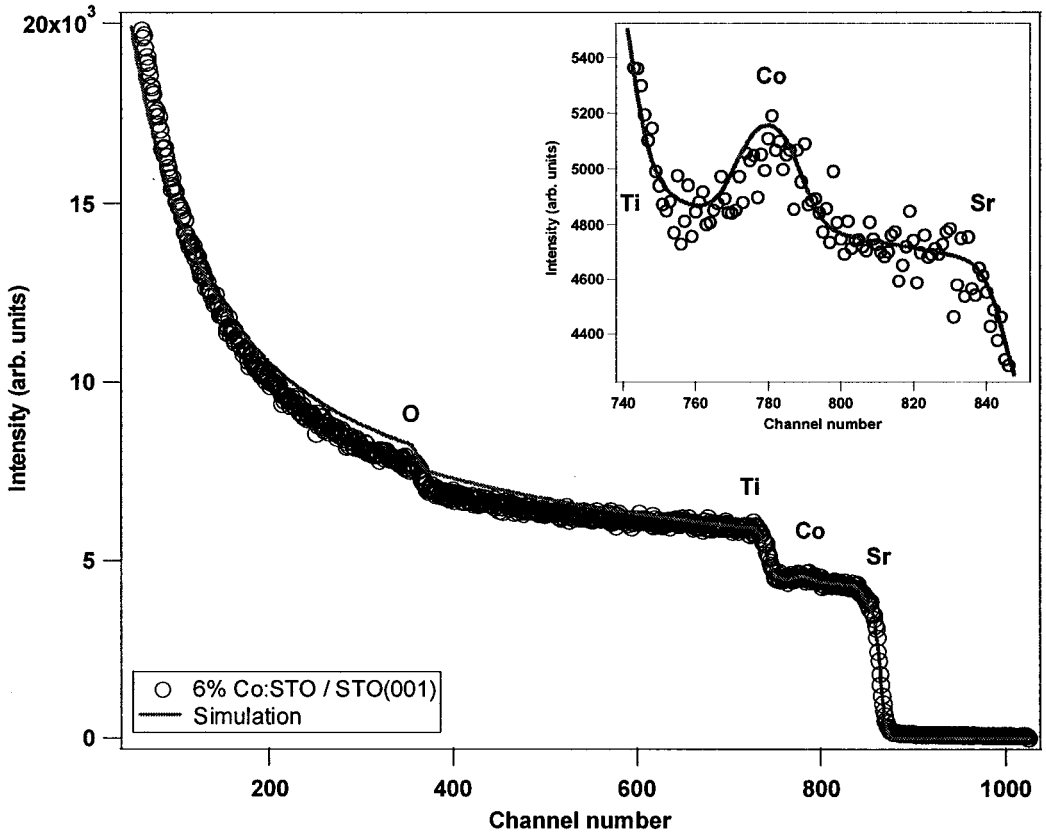

Figure 5.2. RBS spectrum and simulated fit for nominally 6% Co:STO / STO(001). The inset shows the simulated fit in the Co region.

reasonably well. The Co content extracted from the simulation is 4.20×10^{15} Co atoms/cm^2. Using the film thickness calculated from the deposition rate as measured by RHEED oscillations (342 Å), this corresponds to a doping concentration of 7.3%. This value is in reasonable agreement with the nominal Co concentration of 6%.

PIXE is expected to provide a more sensitive measurement of Co content than RBS. Although PIXE spectra can be fit by theoretical models in much the same way RBS data is simulated, to eliminate errors in this method the PIXE simulation by the GUIPIX software was only utilized to obtain the area under the Co K_α peak. This peak area was then compared to the peak area for a reference standard of approximately 144 Å epitaxial γ-Co_2O_3 / MgO(001), whose Co content has been determined independently from both RBS and x-ray reflectivity (XRR) to be (5.0 ±

0.2) x10^{16} Co atoms/cm^2. Due to the high Co concentration, the Co K_α peak area in the PIXE spectrum for this standard was obtained with significantly better statistics than can be obtained in a reasonable amount of time from the Co:STO films. To determine the accuracy of both PIXE and RBS at lower Co concentrations, another γ-Co_2O_3 / MgO(001) standard was grown, with a thickness of only 31 Å as measured by XRR. As presented in Table 5.1, both RBS and PIXE (utilizing the thick γ-Co_2O_3 film as a standard) significantly underestimate the Co content of the thin reference film as compared to the Co content calculated from the known film thickness. The source of this discrepancy is currently under investigation. To reduce the error in quantifying smaller amounts of Co, the 31 Å film was chosen as the PIXE reference standard for Co:STO.

Figure 5.3 shows the PIXE spectrum and simulated fit for the same film as discussed above for RBS (nominally 6% Co:STO / STO(001)). The film contains sufficient Co to produce clear Co K_α and K_β peaks, which are fit well by the simulation. From comparison of the Co peak area to that for the reference standard of 31 Å γ-Co_2O_3 / MgO(001), the Co content of this film is estimated to be 4.64x10^{15} Co atoms/cm^2, slightly higher than the value obtained from RBS (4.20x10^{15} Co atoms/cm^2). The Co concentration calculated from PIXE is 8.1%. Similar results are presented in Table 5.2 for several other Co:STO / STO(001) samples. From these results, it is evident that the expected Co content was not always obtained, and in some cases the

Table 5.1. γ-Co_2O_3 / MgO(001) reference standards utilized for quantification of PIXE spectra. The actual film thickness was measured by x-ray reflectivity and used to calculate the expected Co content. The Co content determined by RBS for 144 Å Co_2O_3 was used to calibrate the data from PIXE. The Co content by PIXE for the thin Co_2O_3 film was determined using the thick Co_2O_3 film as reference.

γ–Co_2O_3 thickness (XRR)	Calculated Co content (x 10^{15} atoms/cm^2)		
	Expected	RBS	PIXE
144 Å	52.0	50.0	----
31 Å	11.3	3.0	6.97

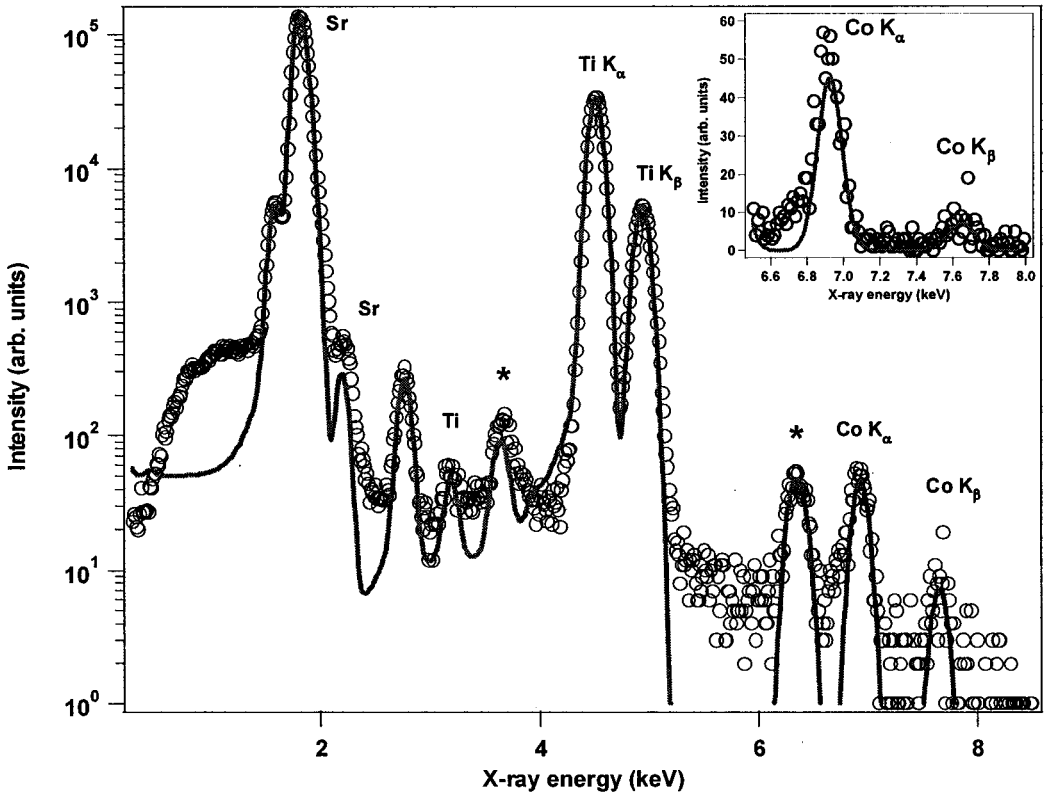

Figure 5.3. PIXE spectrum and theoretical simulation for nominally 6% Co:STO / STO(001). The simulation appears to fit the Co K_a and K_b peaks well, as shown in the inset. Asterisks (*) indicate pile-up peaks arising from detector overload.

discrepancy appears to be too great to be accounted for by the observed error in PIXE quantification. The difference is especially apparent in the nominally 12% Co:STO sample, which by both RBS and PIXE is only doped with 4.1 - 4.7% Co. From this, it appears that Co flux variations occurred during deposition relative to the flux values obtained by measurement with the QCO. Thus, despite the inaccuracy in determining the absolute Co concentration values from PIXE, it is expected to provide a better relative measure of the Co content of Co:STO / STO(001) than calculations based on the Co flux.

The underestimation of Co content by RBS and PIXE may also result if a significant concentration of Co diffused deep into the STO substrate during deposition. Co diffusion into STO during deposition has been inferred previously.[6] If Co resides

Table 5.2. Co content of several Co:STO / STO(001) films, as determined by calculation based on the expected Co flux during deposition, RBS spectra, and PIXE spectra. Values in parenthesis are the Co doping concentrations based on the Co content and the film thickness.

Nominal Co concentration	Co atoms in film (x 10^{15})		
	Co flux	RBS	PIXE
1% Co	0.94		0.62 (1.3%)
1% Co	0.82	0.00	0.00
3% Co	2.80		0.46 (1.0%)
3% Co	2.26	0.00	0.00
6% Co	5.44	3.30 (7.3%)	3.65 (8.1%)
6% Co	5.04		3.07 (6.3%)
9% Co	8.26	8.25 (15.3%)	13.24 (24.5%)
12% Co	9.76	2.36 (4.1%)	2.68 (4.7%)

deeper than the approximately 1 μm probe depth of RBS and PIXE, it will not be detected, lowering the measured Co concentration relative to the actual content. This may be the reason no Co signal was detected by either RBS or PIXE for two Co:STO samples (1% and 3%); since these films exhibited ferromagnetism, it is believed that they do contain Co. However, currently there is no independent verification of Co diffusion into the STO substrate in these samples.

To distinguish Co concentrations calculated with various methods, the following notation will be utilized: Co concentrations determined from the expected flux during deposition will be expressed as $\%_{Flux}$; Co concentrations determined by RBS will be expressed as $\%_{RBS}$, and Co concentrations determined by PIXE will be expressed as $\%_{PIXE}$.

Surface morphology

Regardless of STO stoichiometry or Co content, all Co:STO films exhibited a smooth surface morphology free of large clusters or particles. As illustrated in Figure 5.4(a)

for a $6\%_{Flux}$ Co:STO film with the corrected stoichiometric ratio from XPS of Sr / Ti = 0.63, poor quality "spotty" final RHEED images are associated with atomic-scale roughness as observed by tapping-mode AFM, not the formation of large surface particles. Only a few small surface protrusions are observed. Streaky RHEED images of the final film correspond to a smoother film, as shown in Figure 5.4(b) for a nearly stoichiometric $1\%_{Flux}$ Co:STO film, with Sr / Ti = 0.90. Faint atomic-scale terraces are observed as nearly vertical lines in the AFM image. Figure 5.4(c) shows the RHEED and AFM images of a very high quality surface with broad atomic terraces, from $8\%_{PIXE}$ Co:STO with Sr / Ti = 0.89. Although the RHEED images contain spots, they arise from diffraction of single atomically flat planes, characteristic of a smooth surface with terraces larger than the electron coherence length. The streaks in the image indicate that some areas of the surface possess terraces which are smaller than the coherence length. In general an improvement in both RHEED (00) oscillations and final RHEED diffraction images was observed with increasing Sr content in the STO film, regardless of Co doping. This may be due to the ease with which STO can incorporate excess Sr into lattice-matched Ruddlesden-Popper phases which do not significantly disrupt the epitaxial lattice. Incorporation of excess Ti cannot be accommodated as easily, and Ti-rich secondary phases are expected to disrupt the STO lattice to some extent.

For Co:STO films which are nearly stoichiometric ($0.85 < Sr / Ti / < 1.02$), the effect of Co content on the surface morphology as observed by RHEED is presented in Figure 5.5. Increasing the Co doping level in the film does not appear to be detrimental to the surface morphology or crystallinity. Instead, the opposite effect of a slight improvement in surface crystallinity with increasing Co content is observed. This is surprising since the addition of Co to STO is expected to expand the lattice, creating strain in the film. As the Co content is increased, the film strain is expected to increase as well, and surface roughness is often associated with film strain.

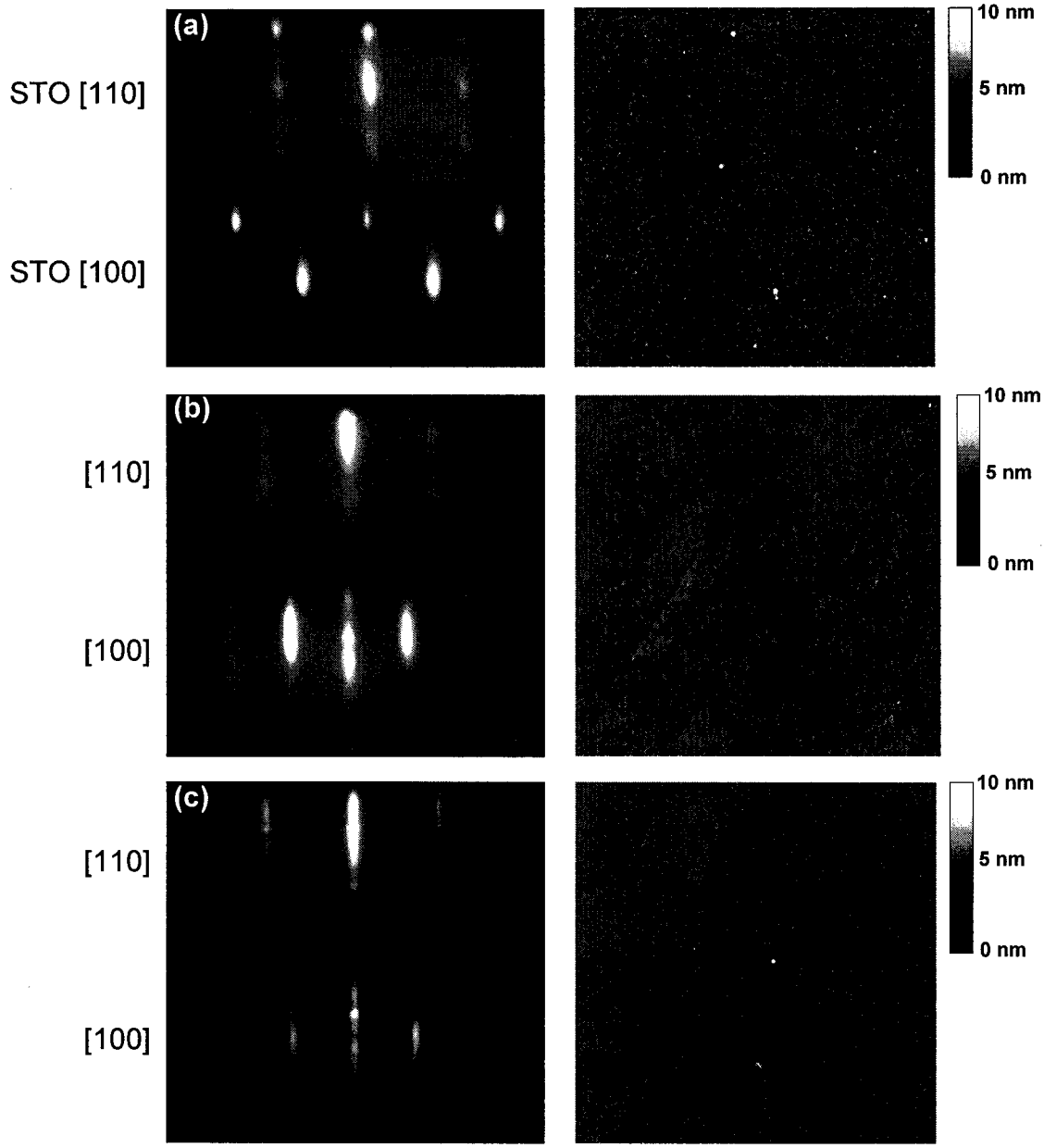

Figure 5.4. Final RHEED images and 5 x 5 μm tapping mode AFM images of representative Co:STO / STO(001) film surfaces. (a) 400 Å $6\%_{Flux}$ Co:STO / STO(001); Sr / Ti = 0.63. RHEED images are spotty, corresponding to atomic-scale roughness obsreved by AFM. (b) Streaky RHEED images of 330 Å $1\%_{Flux}$ Co:STO / STO(001) correspond to smooth film in which closely-spaced atomic terraces are observed. Sr / Ti = 0.90 for this film. (c) 340 Å $8\%_{PIXE}$ Co:STO / STO(001); Sr / Ti = 0.89. Modulation in the RHEED images is the result of an atomically smooth film, as observed in the AFM image of a smooth film with widely-spaced atomic terraces.

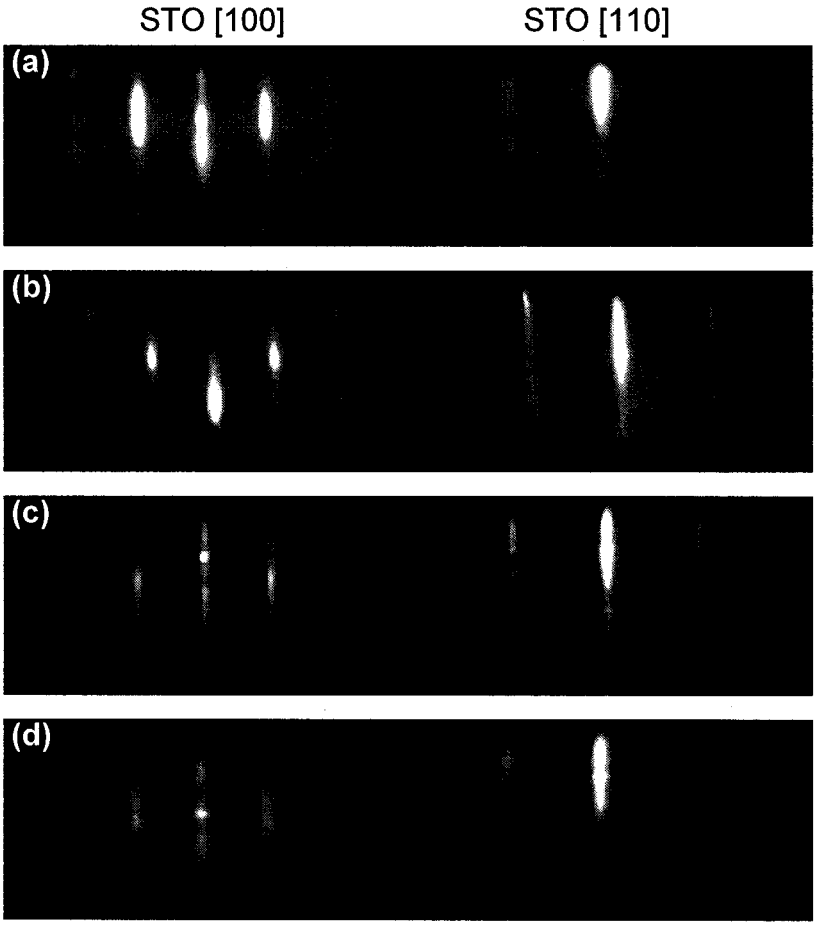

Figure 5.5. Final RHEED images of nearly stoichiometric Co:STO / STO(001). (a) 330 Å $1\%_{Flux}$ Co:STO / STO(001). (b) 340 Å $1\%_{PIXE}$ Co:STO / STO(001). (c) 340 Å $8\%_{PIXE}$ Co:STO / STO (001). (d) 400 Å $15\%_{RBS}$ Co:STO / STO(001). A slight improvement in the RHEED images is observed with increasing Co content.

Film morphology

Incorporation of Co into the STO lattice can be inferred from a change in deposition rate when Co is introduced; if Co incorporates into STO, the deposition rate should increase, whereas if Co forms secondary phases the STO deposition rate will not be affected. The RHEED oscillations observed during deposition provide a monolayer-by-monolayer measure of the STO deposition rate; a change in deposition rate is observed as a change in the oscillation frequency. Figure 5.1 above shows the RHEED (00) oscillations for $8\%_{PIXE}$ ($6\%_{Flux}$) Co:STO / STO(001); in Figure 5.6 the

time at which each peak minimum and maximum occurred is plotted for the first 600 seconds of deposition. A change in oscillation frequency would appear as a slope change in this plot. Least squares linear regressions of both the peak minima and maxima indicate a slight decrease in slope of approximately 0.27 sec / oscillation after Co was introduced. This corresponds to a slightly increased deposition rate, as expected for Co incorporation into the lattice. Although this change in slope is within the measurement error of approximately ± 0.4 seconds, it is believed to be a real effect since it is observed for both the oscillation minima and maxima. The change in deposition rate is approximately 2% after the introduction of Co. For 8% Co doping, a change in deposition rate of 8% would be expected.

More convincing evidence of Co incorporation into the STO lattice is obtained by

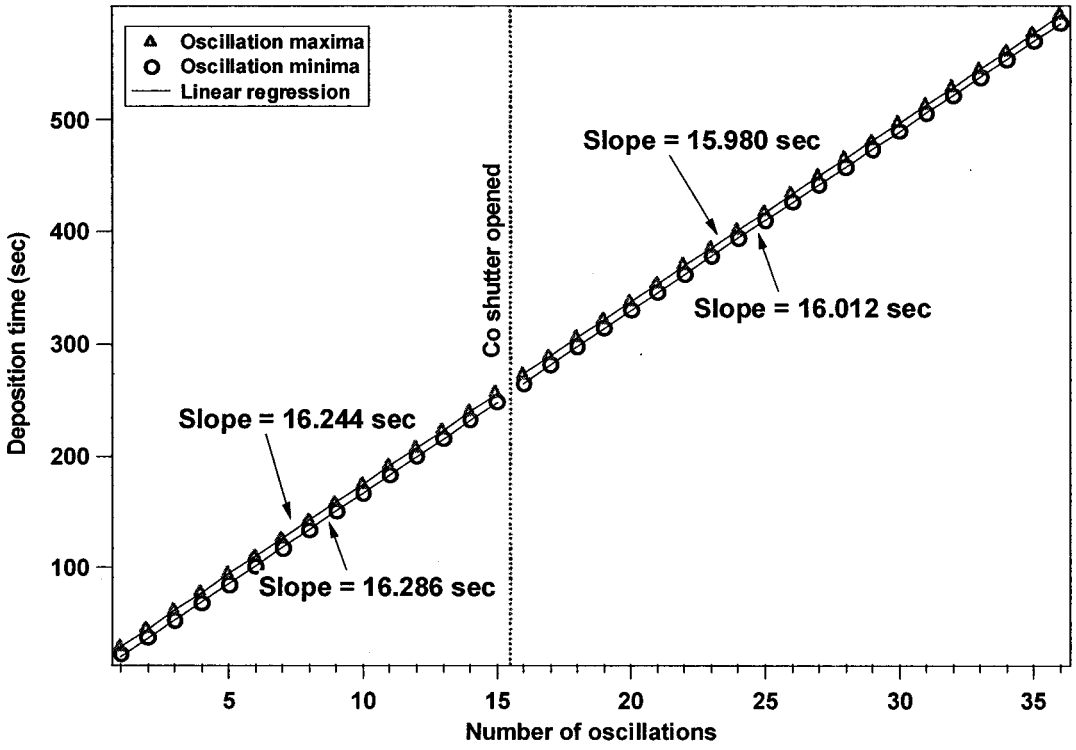

Figure 5.6. Plot of deposition time for RHEED (00) intensity oscillation minima and maxima versus number of clearly observed oscillations for $8\%_{PIXE}$ Co:STO deposited on STO(001). The slope of least squares linear regressions of each set of data are indicated. For both the minima and maxima, a clear change in slope is observed after the Co shutter was opened. The faster deposition rate after opening the Co shutter is evidence of Co incorporation into the STO lattice.

high resolution XRD rocking curves. Figure 5.7 shows STO(002) rocking curves for 300-500 Å nominally stoichiometric STO / STO(001) doped with $1\%_{Flux}$, $1\%_{PIXE}$, $8\%_{PIXE}$, and $15\%_{RBS}$ Co. The multiple peaks observed for the STO substrate are due to defects such as twinning. The small oscillations observed in the background are thickness fringes arising from diffraction interference of the film and the substrate. Due to strain in the lattice, the Co:STO film has a different lattice spacing than the STO substrate and thus appears as a distinct peak in the diffraction pattern. Film strain can arise from two primary sources: substitution of Co for Ti and lattice

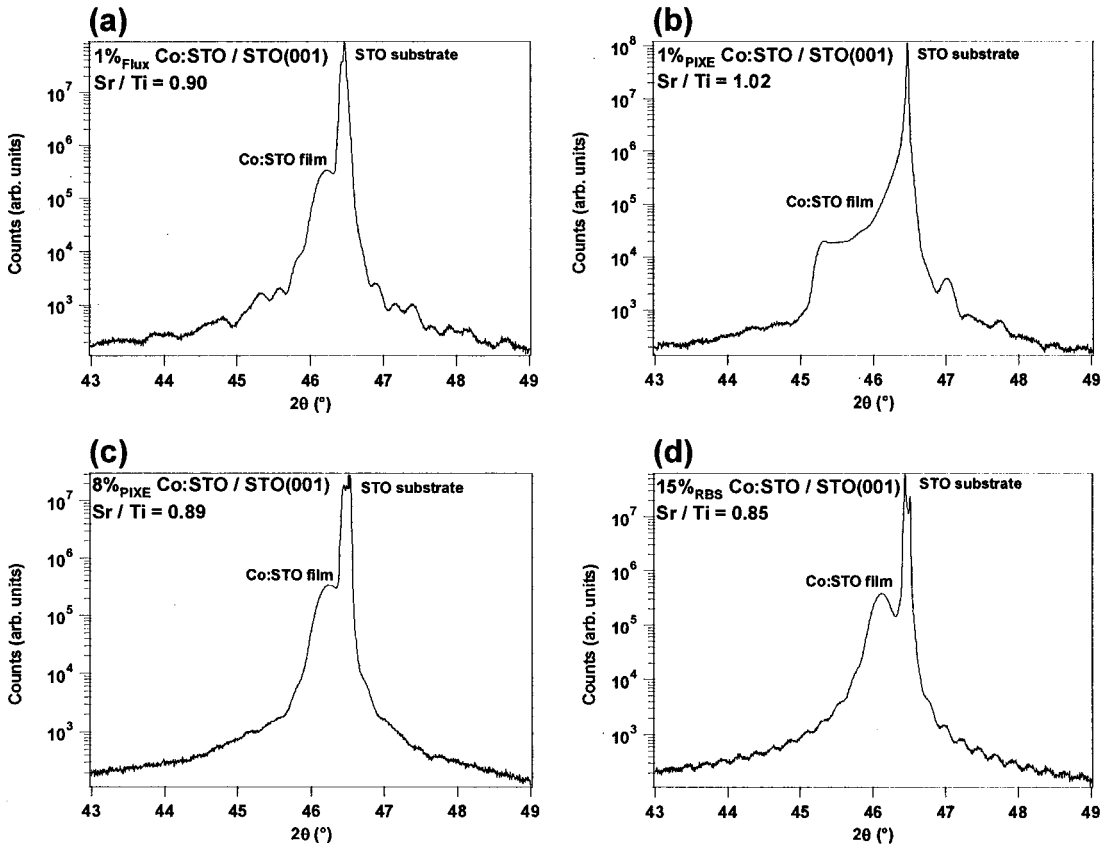

Figure 5.7. High resolution XRD rocking curve patterns of the STO(002) reflection for Co:STO / STO(001) films. Strained Co:STO film is observed as a distinct diffraction peak occurring at lower angle than the STO substrate peak. (a) 330 Å $1\%_{Flux}$ Co:STO / STO(001). (b) 340 Å $1\%_{PIXE}$ Co:STO / STO(001). Unusual film peak shape may be due strain gradients resulting from Ruddlesden-Popper phases incorporated into the film. (c) 330 Å $8\%_{PIXE}$ Co:STO / STO(001). (d) 400 Å $15\%_{RBS}$ Co:STO / STO(001). Clearly resolved thickness interference fringes indicate film is uniform and of high crystalline quality.

Table 5.3. Co:STO film strain, relative to bulk STO, as measured by high resolution XRD rocking curves of the STO(002) reflection. For $1\%_{PIXE}$ Co:STO, the tabulated lattice parameter is from the highest-strained portion of the film diffraction peak. For reference, the lattice parameter of bulk STO is also presented.

Film	Thickness	Lattice parameter	Strain
$1\%_{Flux}$ Co:STO	330 Å	3.925 Å	0.64%
$1\%_{PIXE}$ Co:STO	340 Å	3.999 Å	2.54%
$8\%_{PIXE}$ Co:STO	330 Å	3.923 Å	0.59%
$15\%_{RBS}$ Co:STO	400 Å	3.933 Å	0.85%
Bulk STO	----	3.905 Å	0

matching of this film to the STO substrate. As presented in Table 5.3 for the films shown in Figure 5.7, the Co:STO peak appears at lower 2θ angle (larger *c* plane spacing) relative to the STO substrate peak, indicating the Co:STO film has an expanded lattice compared to bulk STO. This implies that Co has substituted into the STO lattice, and possesses a larger ionic radius than the atom it is substituting for. Using this result, the various possibilities of Co substitution can be evaluated. If Co acts in a similar manner to Co-doped anatase TiO_2, it will substitute as Co(II) for Ti(IV), creating an associated oxygen vacancy to maintain charge neutrality. However, Co in perovskite $SrCoO_3$ processed under highly oxidizing conditions is present as Co(IV),[7] thus Co in Co:STO may take the higher oxidation states of Co(III) or Co(IV). In addition, Co(II) may substitute for Sr(II) as an isovalent dopant. To determine the effect of these possible substitutions on the STO lattice, the effective ionic radii[8,9] of Co(II), Co(III), Ti(IV), and Sr(II) are given in Table 5.4. For substitution of Co for Ti in an octahedral site (coordination number of 6), only Co(II) possesses a larger ionic radius than Ti(IV), so a lattice expansion would only be observed for Co(II) substitution. If Co were to take a higher oxidation state, a lattice contraction would result. This trend is observed for $SrCoO_3$, which has a lattice parameter of 3.84 Å,[10,11] a significant contraction from $SrTiO_3$ (3.905 Å). Although data is not readily available for the ionic radius of Co(II) with a coordination number of 12, it is likely that if Co(II) were to substitute for Sr(II), it would possess a significantly smaller ionic radius and result in a lattice contraction.

From the observed expansion of the Co:STO film lattice, it is concluded that Co substitutes as Co(II) for Ti(IV).

The film strain in the *c* axis direction is included above in Table 5.3 for the samples shown in Figure 5.7. In some cases, the film strain can be used to calculate the doping concentration by comparing to bulk undoped specimens and applying Vegard's law, which states that the lattice parameter changes linearly with composition between two known endpoint compositions. Unfortunately, Vegard's law cannot be applied to Co:STO / STO(001) due to lattice matching to the STO substrate. In films which are truly epitaxial, the in-plane lattice parameter is constrained to be 3.905 Å to match the STO(001) substrate; the observed expansion in the *c* lattice parameter thus results from both inherent lattice expansion due to Co doping and expansion due to the in-plane compressive stress. Since these two effects cannot be separated by STO(002) rocking curves alone, the reported film strain will contain both effects. Thus, lower Co-doped films may actually exhibit more strain than higher doped films, since the lower doped film is able to epitaxially match the STO substrate while the higher doped film relaxes in-plane. This is likely why $1\%_{Flux}$ Co:STO exhibits more strain than $8\%_{PIXE}$ Co:STO.

Table 5.4. Effective ionic radius for various charge states and coordinations of Co. For octahedral coordination, the radius for both low spin (LS) and high spin (HS) electronic configurations are given. For comparison, the ionic radii expected for Ti(IV) and Sr(II) in STO are also given. Values from [9].

	Charge state	Coordination number	Effective ionic radius
Co	(II)	6	0.65 Å (LS) 0.745 Å (HS)
	(II)	8	0.90 Å
	(III)	6	0.545 Å (LS) 0.61 Å (HS)
	(IV)	6	0.53 Å (HS)
Ti	(IV)	6	0.605 Å
Sr	(II)	12	1.44 Å

It is clear from Figure 5.7 that $1\%_{PIXE}$ Co:STO / STO(001) does not exhibit the same film strain characteristics as the other samples. Rocking curve measurements of this sample in various orientations, as well as a triple-axis scan, confirm that the observed diffraction pattern is not an artifact. This unusual peak shape can be interpreted as arising from a heterogeneous strain profile in the *c* direction of the film. The significant strain observed in this film may be due to the formation of Ruddlesden-Popper (RP) phases. RP phases consist of single layers of rock salt SrO periodically interspersed in the STO lattice in the {100} directions, and form to accommodate excess Sr. SrO, with a lattice parameter of 5.16 Å, is reasonably well lattice-matched to the "SrO" layer of STO(001) with an in-plane rotation of 45°. As measured by the XPS Sr / Ti ratio, this film contains more Sr than the other films shown in Figure 5.7. Suzuki *et al.*[12] found epitaxial $Sr_{1.25}TiO_{3.25}$ thin films formed RP planar faults; the measured lattice parameter in the *c* direction was significantly expanded (4.087 Å), while the in-plane lattice parameter was measured to be 3.905 Å indicating an epitaxial relationship to the STO(001) substrate. This magnitude of *c* lattice expansion is observed in $1\%_{PIXE}$ Co:STO (c = 3.999 Å), although the significant strain gradient observed in Co:STO was not seen in the $Sr_{1.25}TiO_{3.25}$ film.[12] The large heterogeneous strain gradient, indicating the *c* lattice parameter in the Co:STO film ranges from 3.999 Å to nearly the bulk STO parameter of 3.905 Å, may result from non-periodicity of the inserted SrO layers in the STO lattice.

The semiconducting properties of Co:STO films on STO(001) were evaluated by measuring the film resistivity with a four point probe apparatus. All films, regardless of STO stoichiometry or Co content, were found to exhibit $\rho > 5x10^3$ Ω·cm. For most films the resistivity was too high to be measured with the four point probe apparatus, indicating the resistivity was greater than approximately $15x10^3$ Ω·cm. These resistivity values place the Co:STO films in the range of semiconductors (generally defined as $10^{-2} < \rho < 10^9$ Ω·cm).[13] However, the measured resistivities are significantly higher than previously reported for semiconducting Co:TiO_2 / LAO ($\rho \sim$

100 Ω·cm)[4,6] and ferromagnetic Co-doped $La_{0.5}Sr_{0.5}O_3$ ($\rho \sim 10^{-4}$ - 10^{-2} Ω·cm);[3] in comparison, the Co:STO films can be considered insulating.

Cobalt charge state and local environment

The charge state of Co in Co:STO was investigated by Co K-edge x-ray absorption near edge structure (XANES), as shown in Figure 5.8 for stoichiometric $1\%_{PIXE}$ Co:STO / STO(001). The experimental spectrum was fit by a linear combination of the Co reference standards by minimization of χ^2, as described in Chapter IV. The resulting best fit simulation is shown in Figure 5.8(b). The data is best fit with 5% Co metal, 11% $CoTiO_3$, 33% CoO, and 51% Co_2O_3. However, the simulation does not fit the data well in either the absorption edge or absorption peak regions. Although the best fit model includes 5% Co(0), the lack of intensity in the pre-edge region implies little or no Co(0) present. As shown in the inset to Figure 5.8(b), performing the fit with the Co(0) contribution set to zero slightly improves the fit to the experimental data in the region of the Co(0) shoulder. From this, it is concluded that the Co:STO film does not contain Co(0). This is a significant result, since it indicates Co is fully incorporated into oxide phases. The experimental data exhibits a double peak shape which the simulation is unable to reproduce, indicating the local environment of Co in STO is not well represented by the Co reference standards. The absorption edge for Co:STO appears at approximately the same energy as the Co(II) reference standards, indicating most or all the Co in the film is Co(II). No significant differences were observed in spectra for several other Co:STO films, regardless of Co content (approximately 1% to 5% Co) or STO stoichiometry (Sr / Ti = 0.63 to 1.02). As an example, Figure 5.9 shows two Co:STO / STO films with similar Co content but different STO stoichiometry (Sr / Ti = 0.76 and Sr / Ti = 1.02). Despite these variations, the two spectra are nearly identical.

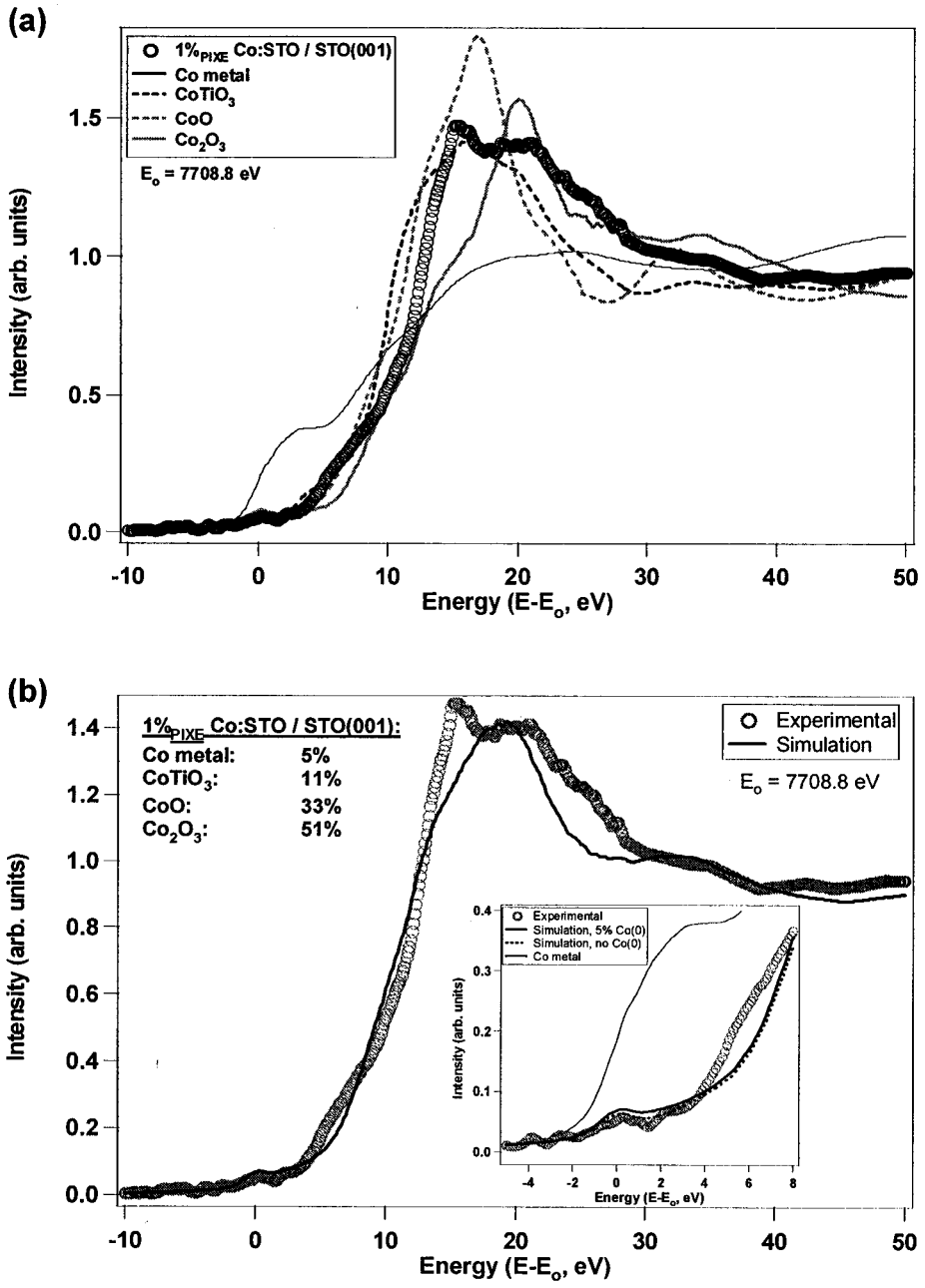

Figure 5.8. (a) Co K-edge XANES of 1%$_{PIXE}$ Co:STO / STO(001); Sr / Ti = 1.02. Co reference standards are shown for comparison. The experimental lineshape does not appear to match any of the Co standards. (b) Simulated fit to the experimental data. The data cannot be fit well along the leading edge or at the peak. Shown in the inset is the pre-edge region of the experimental spectrum, as well as a comparison of the simulated fit including Co(0) to a simulated fit with no Co(0). The fit in this region is slightly improved assuming no Co(0), indicating there is no Co(0) in the film. For reference, the Co metal spectrum is also included.

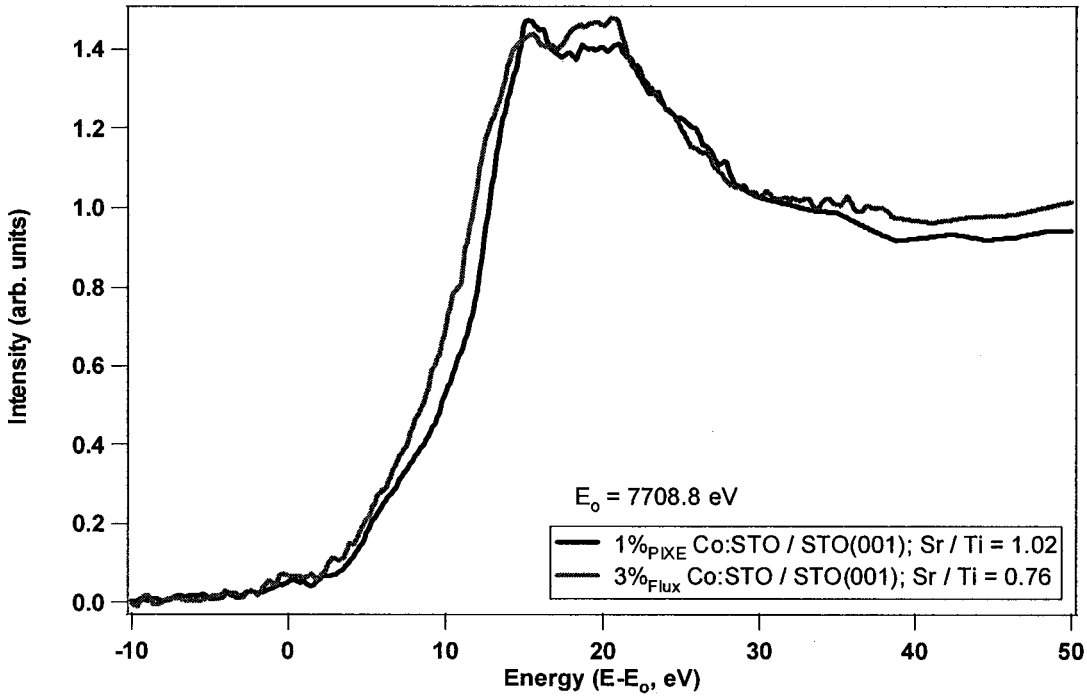

Figure 5.9. Co K-edge XANES of Co:STO / STO(001) samples. A nearly stoichiometric 1%$_{PIXE}$ Co:STO film with Sr / Ti = 1.02 has an almost identical lineshape to a Ti-rich 3%$_{Flux}$ Co:STO film with Sr / Ti = 0.76, indicating the Co is in a similar local environment in both samples regardless of Co concentration or STO stoichiometry.

From the XANES spectra the presence of secondary phases cannot be ruled out, although they are unlikely since the lineshape does not change with Co content or STO stoichiometry. The experimental lineshape may arise from Co(II) substitution for Ti(IV), in which the local Co environment is sufficiently different from Co(II) in either CoO or $CoTiO_3$ that these reference standards do not reproduce the lineshape. Alternatively, the lineshape may arise from some Co(II) substitution for Sr(II), and the charge state and 12-coordinate symmetry of this site is not represented by the reference standards. Although no experimental XANES spectrum of Co:STO or $SrCoO_3$ is available, comparison of the lineshape with the XANES spectrum[14] for brownmillerite structure $Sr_2Co_2O_5$, reproduced in Figure 5.10, shows qualitative agreement. Brownmillerite $Sr_2Co_2O_5$ has a defected perovskite structure with an ordered array of oxygen vacancies, containing Co(III) in both distorted octahedral and distorted tetrahedral sites. In XANES, the influence of charge state in an

otherwise identical structural environment is to shift the absorption edge to higher energy without signficantly affecting the lineshape. Thus, the similarity in the XANES spectra lineshape for Co:STO and $Sr_2Co_2O_5$ implies that Co(II) in Co:STO is primarily incorporated into the STO lattice at Ti sites. A mixture of octahedral and tetrahedral coordinations is not expected in Co:STO; however, octahedral versus tetrahedral coordination should not have a significant effect on the K-edge XANES lineshape[15] since K shell excitation does not probe the 3*d* shells. In addition, oxygen vacancies which form near the Co cations in Co:STO to maintain charge neutrality may distort the local coordination and structural environment of the Co cations.

To elucidate the local Co environment in Co:STO, EXAFS was utilized. Figure 5.11(a) shows the raw EXAFS data for stoichiometric $1\%_{PIXE}$ Co:STO / STO(001); Sr / Ti = 1.02. The observed oscillations are due to interference of the propagating wavefunction generated by the excited (absorbing) electron and backscattered waves

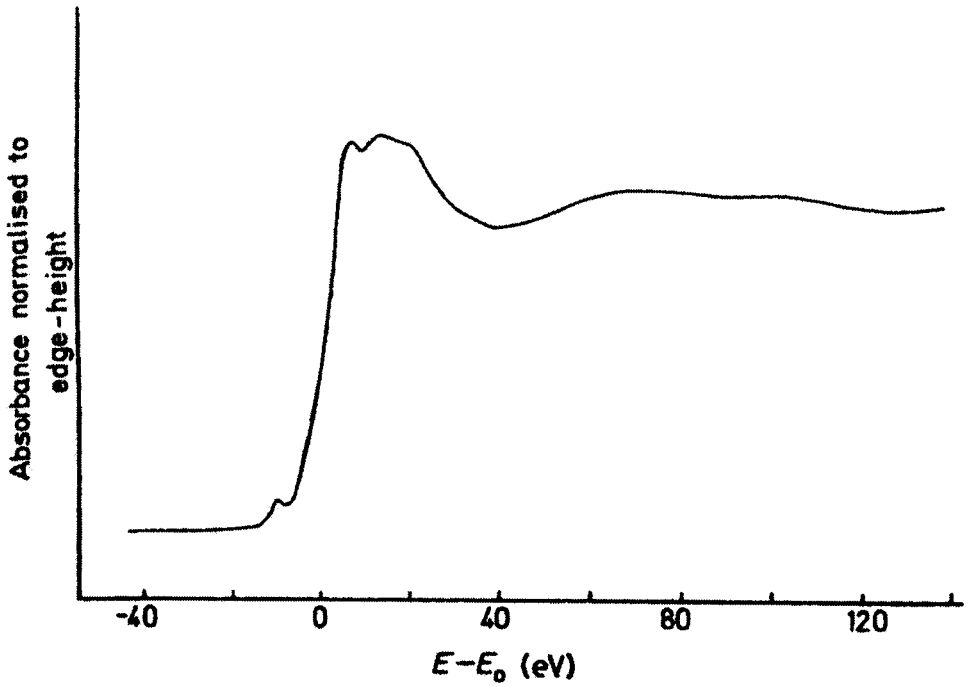

Figure 5.10. Reproduced from [14]. Co K-edge XANES spectrum of brownmillerite $Sr_2Co_2O_5$. $E-E_o = 0$ was defined as the inflection point of the absorption edge.

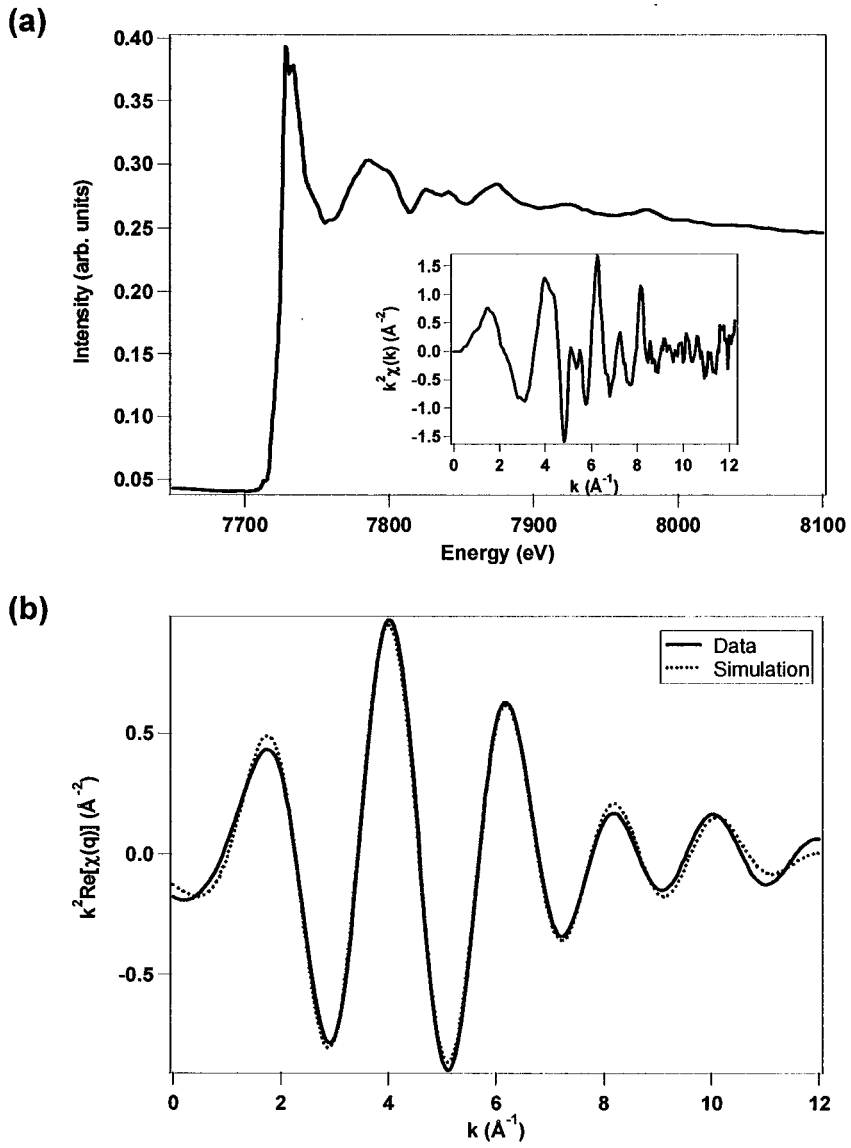

Figure 5.11. Co K-edge EXAFS spectrum and theoretical fit to the data for stoichiometric $1\%_{PIXE}$ Co:STO / STO(001). (a) Raw EXAFS spectrum. Oscillations arise from electron wave interference with neighboring atoms. Inset shows extracted data. (b) First shell theoretical fit to the data assuming all Co substitutes for Ti in the STO lattice.

generated when the propagating wave encounters neighboring atoms. Thus, information regarding the number and distance of neighboring atoms can be extracted from EXAFS data, providing a clear picture of the local environment of the absorbing atom. After subtraction of a smooth background function from the raw EXAFS data presented in Figure 5.11(a) and multiplication by $\mathbf{k}^2$ (where **k** is the

photoelectron wave vector in $Å^{-1}$) to compensate for amplitude attenuation as a function of **k**, the extracted EXAFS data shown in the inset to Figure 5.11(a) is obtained. Figure 5.11(b) shows the extracted EXAFS spectrum after Fourier-filtering, as well as a first shell theoretical calculation fit to the data, assuming all Co substituted for Ti in STO. From this best fit calculation, Co was found to have approximately 6 nearest neighbors with a Co-O bond length of 2.00 Å. This corresponds well to Co substitution for Ti in STO, in which Ti has six nearest oxygen neighbors with a bond length of 1.95 Å. A slight lattice expansion is expected when Co(II) is substituted for Ti(IV), since Co(II) is slightly larger (Table 5.4).

Shown in Figure 5.12 is a comparison of the theoretical first shell fits for two 350 Å thick films with the same STO stoichiometry as measured by XPS (Sr / Ti = 0.9). Although both films were nominally doped with $1\%_{Flux}$ Co, intensity differences in the x-ray absorption spectra indicate the film in Figure 5.12(b) contains 2-3 times as much Co as the film shown in Figure 5.12(a); since ferromagnetism was not observed in this film (as discussed below), it is assumed to have $> 5\%_{Nominal}$ Co doping. Assuming Co substitution for Ti only, the quality of theoretical fit to both data sets appears to be similar, although slightly different parameters are necessary to fit the data for each sample. As a comparison of the effect of increasing Co concentration on the local Co environment in Co:STO, Figure 5.13 shows the Fourier transformed EXAFS data for all three samples. Since this data includes higher shells it is more sensitive to differences in Co environment than the first shell data shown in Figures 5.11 and 5.12. It is evident from this plot that the local environment in each of the three samples is not equivalent. Instead, each sample appears to contain differing admixtures of Co in several local environments.

To determine the exact local environment for Co in Co:STO, the theoretical fits shown in Figures 5.11 and 5.12 could be improved by both expanding the calculation to include further shells of neighboring atoms, as well as by including the effects of a

portion of Co in another lattice site. For example, the fit shown in Figure 5.11(b) can be improved by allowing approximately 20% of the Co atoms to occupy Sr sites in the STO lattice. Although Sr is much larger than Co, substitution may be favored since Co(II) would be an isovalent dopant; no oxygen vacancies would be necessary to maintain charge neutrality. However, a full analysis considering all the possible Co sites, including Co substitution at various points in the lattice, interstitials, and

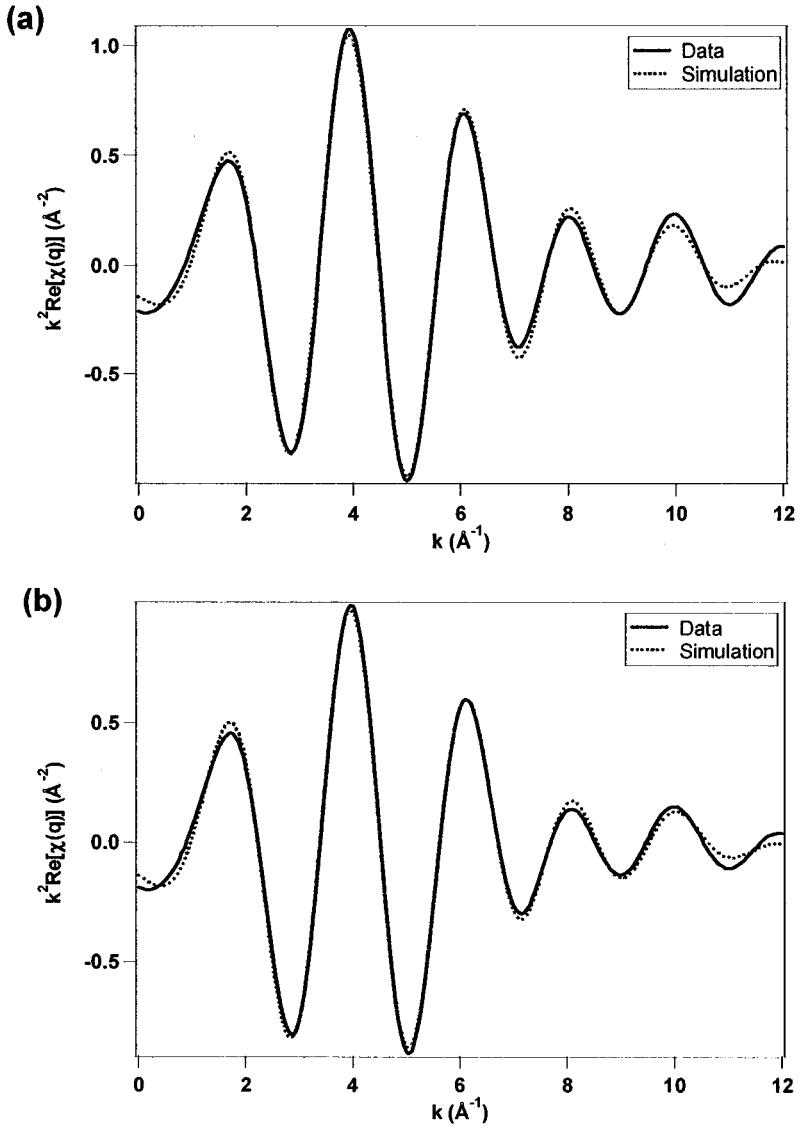

Figure 5.12. (a) Theoretical fit to the Co K-edge EXAFS spectra for $1\%_{Flux}$ Co:STO / STO(001); Sr / Ti = 0.90. (b) Theoretical fit for > $5\%_{Nominal}$ Co:STO with similar STO stoichiometry (Sr / Ti = 0.89).

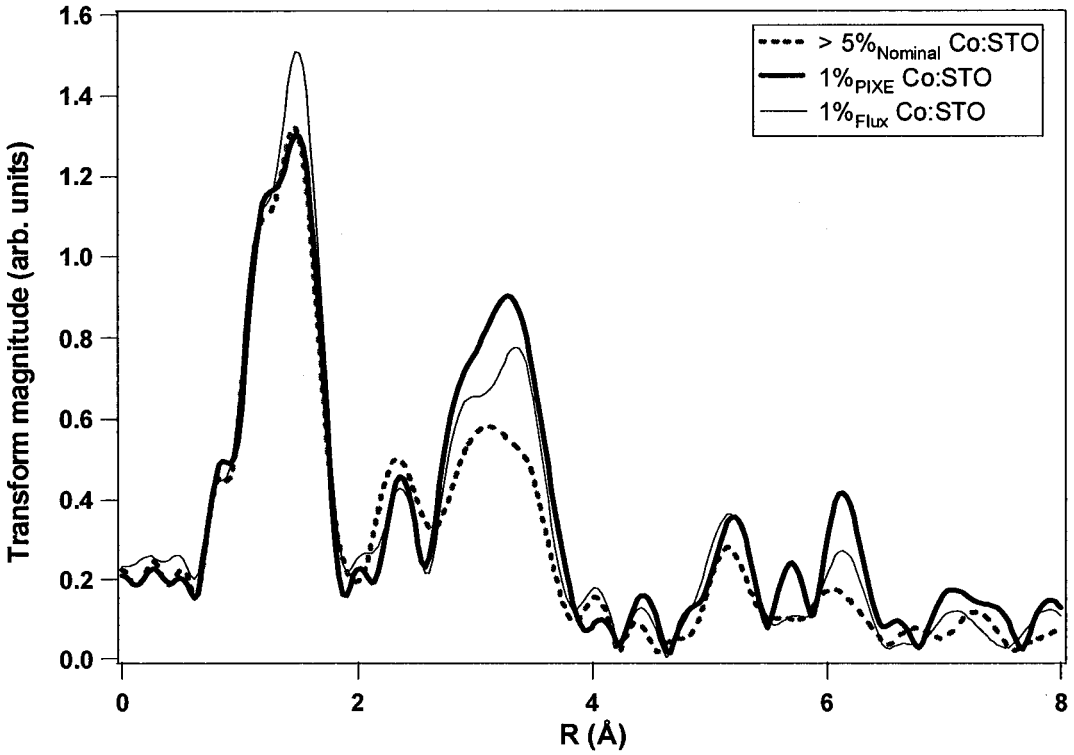

Figure 5.13. Fourier-transformed EXAFS data for three nearly stoichiometric Co:STO samples with varying Co concentration. Clear differences are observed in the Co environment for the three samples.

secondary phases, is required before any proposed model can be considered definitive. Despite this, the initial fits presented here strongly indicate that most if not all Co substitutes for Ti in the STO lattice.

Magnetic measurements

Several of the Co:STO / STO(001) films were ferromagnetic at room temperature. From the XANES data presented above, a ferromagnetic response due to the presence of Co(0) precipitates can be ruled out. Likewise, since no secondary phases were observed by XRD or XANES, the magnetic signal appears to originate from substitutional Co in the STO lattice. Figure 5.14 presents the room temperature hysteresis loops, after subtraction of a linear background to eliminate the diamagnetic

signal from the substrate, obtained by vibrating sample magnetometry (VSM) for two representative films: $5\%_{PIXE}$ Co:STO and $8\%_{PIXE}$ Co:STO. The film with less Co exhibits clear ferromagnetic hysteresis, with a coercive field of 84 G and 17.5% remanence. In contrast, the sample with higher Co content appears to exhibit no ferromagnetic hysteresis, although the faint "S" shape of the loop may indicate the film is superparamagnetic. From comparison of the ferromagnetic properties of these two films, there appears to be a dependence of the ferromagnetism on Co content. This dependence is clearly observed in Figure 5.15, which plots the ferromagnetic saturation magnetization per Co atom versus the Co content as determined by PIXE in several Co:STO films. At Co doping concentrations less than $5\%_{PIXE}$, ferromagnetism is observed, while at concentrations greater than $5\%_{PIXE}$, consistently non-ferromagnetic films are obtained. The ferromagnetic moment per Co atom appears to be high ($2 - 7\ \mu_B$/Co). High spin Co(II) is expected to have a magnetic

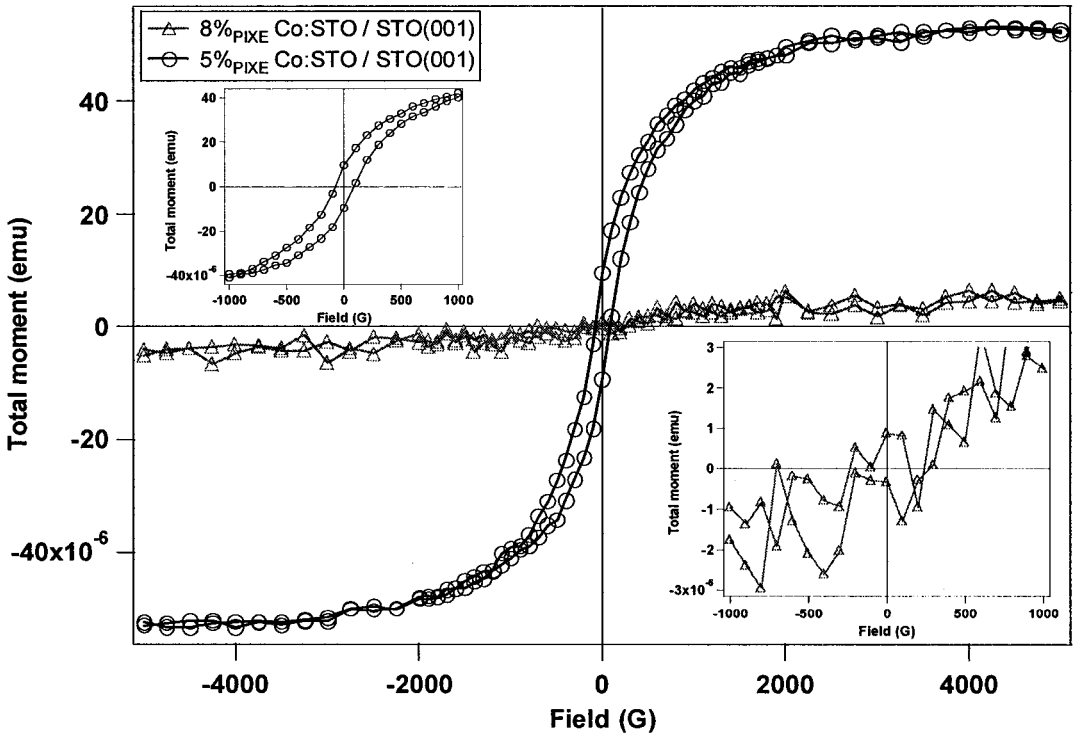

Figure 5.14. Magnetic hysteresis loops obtained at room temperature by VSM for Co:STO / STO (001) with varying Co dopant concentration (as calculated from PIXE data). $5\%_{PIXE}$ Co:STO exhibits clear ferromagnetic hysteresis, while $8\%_{PIXE}$ Co:STO is non-ferromagnetic.

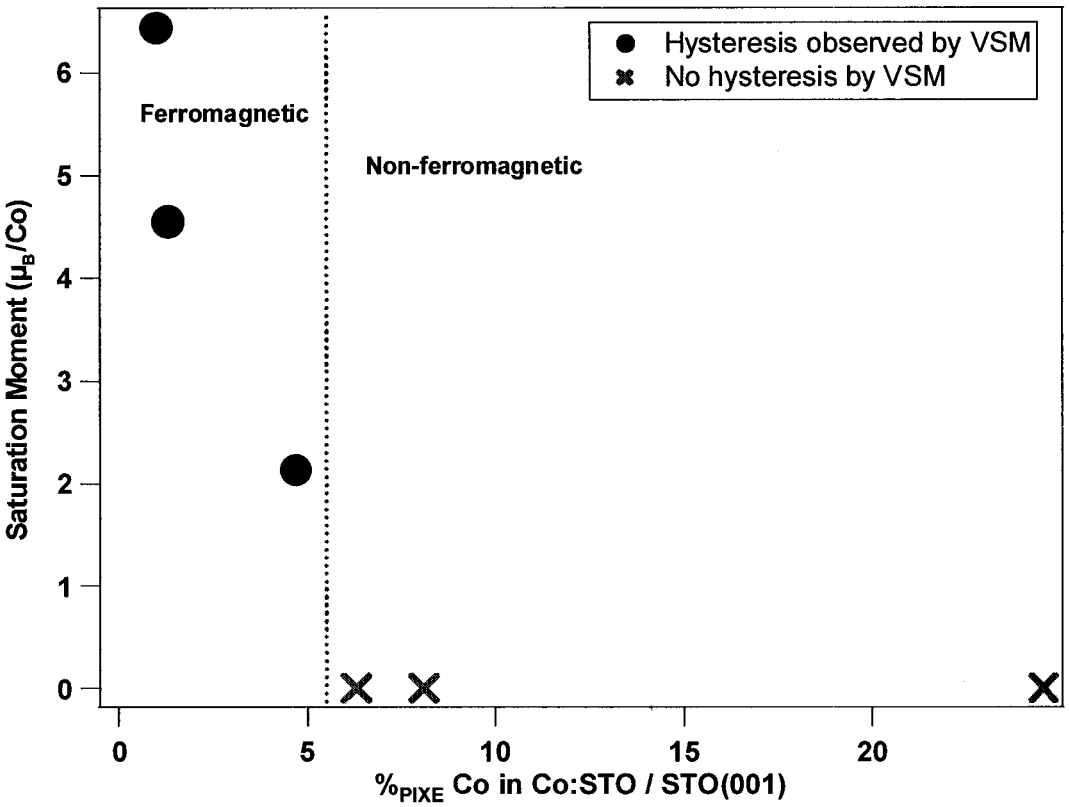

Figure 5.15. Plot of ferromagnetic moment per Co atom versus the Co dopant concentration in Co:STO / STO(001). Data points were determined using the Co concentration obtained by PIXE; inherent error in quantification makes the magnetic moments representative, not absolute values. At low Co concentrations, ferromagnetism is observed. As the Co content is increased, the ferromagnetic moment decreases until approximately 5.5%$_{PIXE}$ Co, when ferromagnetism disappears.

moment of 3 μ_B/Co if the orbital magnetic moment is fully quenched; the moment will be higher with contributions from an unquenched orbital moment. However, the orbital magnetic moment of Co(II) is approximately 1 μ_B in CoO and has been estimated as 0.9 μ_B in Co:TiO_2,[16] so the highest physically reasonable magnetic moment for Co(II) is approximately 4 μ_B. Values higher than this, such as those plotted in Figure 5.15, must result from measurement inaccuracy. Most likely, this inaccuracy arises in the determination of the number of Co atoms present in the film. A higher than expected magnetic moment per (measured) Co atom could be explained by significant Co diffusion into the STO substrate, where it remains ferromagnetic but resides too deep (> 1 μm) to be detected by RBS or PIXE.

Mechanism of magnetism in Co-doped $SrTiO_3$

Carrier-mediated mechanisms of ferromagnetism, such as the RKKY / Zener model and double exchange, rely on the presence of a significant quantity of free carriers to induce long-range ordering in dilute magnetic alloys (see Chapter I for a complete discussion). In Co:TiO_2 / LAO, ferromagnetic ordering was only observed for samples with a resistivity less than approximately $5x10^3$ Ω·cm; more insulating samples did not exhibit ferromagnetic hysteresis.[4,6] Carriers appeared to play an even more important role in Co-doped $La_{0.5}Sr_{0.5}TiO_3$, in which ferromagnetism with a high moment was only observed in samples with resistivity in the range of 10^{-4} - 10^{-2} Ω·cm.[3] In contrast, ferromagnetic hysteresis is clearly observed for < $5\%_{PIXE}$ Co:STO / STO(001) samples, all of which are insulating with resistivities of at least $5 - 15\ x10^3$ Ω·cm. At these high resistivities, it is likely that the free carrier concentration is too low to effectively mediate ferromagnetic ordering of the dopant either through the RKKY / Zener interaction or through double exchange.

Recently, Coey *et al.*[17] proposed another mechanism of magnetism, referred to as *F*-center exchange (FCE), as an explanation for the observed room temperature ferromagnetism in insulating Fe-doped SnO_2. In FCE, the oxygen vacancy site that forms near the transition metal dopant to maintain charge neutrality acts to mediate the ferromagnetic ordering of neighboring dopant cations. An electron trapped by the vacancy creates an *F* center, and the electron occupies an orbital which overlaps the *d* orbitals of neighboring dopant cations. This orbital overlap results in spin ordering of the dopant cations relative to the *F* center electron. In this way the mechanism is similar to the bound magnetic polaron model proposed by Das Sarma *et al.*[18] To approximate the *F* center electron orbital radius, *r*, the Bohr model is utilized:

$$r = \frac{4\pi\varepsilon_r\varepsilon_0\hbar^2}{Zm^*e^2}$$

where ε_r is the relative dielectric permittivity of the host lattice ($\varepsilon_r = \kappa = \varepsilon/\varepsilon_0$), ε_0 is the permittivity of free space, $\hbar$ is Planck's constant, Z is the charge on the F center, m^* is the effective mass of electrons in the host lattice, and e is the electron charge. In F centers with one trapped electron, the resultant magnetic ordering of the neighboring transition metal dopants is ferromagnetic, with all dopant cations within the electron radius aligned antiparallel to the trapped electron. In order for ferromagnetic ordering to be favored over antiferromagnetic ordering in F centers with two trapped electrons, the two electrons must have their spins aligned parallel. The ground state configuration of two tightly bound electrons is a singlet state (spins aligned antiparallel), which would result in antiferromagnetic ordering of the neighboring transition metal dopants. However, the large electron radius may allow the creation of an "excited" state, in which one electron is tightly bound to the vacancy and the other is not as tightly bound. In this configuration a triplet state (spins aligned parallel) could occur, resulting in ferromagnetic ordering of the neighboring transition metal dopants.

The mechanism of FCE may explain the ferromagnetic ordering observed for insulating Co:STO films with < $5\%_{PIXE}$ Co doping. To maintain charge neutrality, substitution of Co(II) for Ti(IV) creates one oxygen vacancy with two bound electrons, which becomes an F center. Assuming the dielectric permittivity of the STO film is the same as for bulk STO at room temperature ($\varepsilon_r = 332$)[19] and using the known electron effective mass in STO ($m^* = 5m_0$),[20] the electron orbital radius is approximately 18 Å. Thus, even a low concentration of Co atoms within the STO lattice may order ferromagnetically through interaction with their associated F centers. As shown in Table 5.5, for a uniform distribution of approximately 1% substitutional Co the Co cations are separated by approximately 41 Å or 15 M_{Ti} –O – M_{Ti} bonds, where M represents a transition metal cation on a Ti site. At this distance, neither direct magnetic exchange nor superexchange is possible. However, it is approximately the same distance as the estimated diameter of an F center electron

Table 5.5. Theoretical Co-Co distance in Co:STO, assuming Co substitutes for Ti, for various Co doping concentrations. The number of M_{Ti}-O-M_{Ti} bonds, where M is a transition metal cation on a Ti site, gives an estimate of the distance over which superexchange would have to operate to induce antiferromagnetic ordering.

Doping concentration	Nearest Co – Co distance	# M_{Ti}-O-M_{Ti} bonds
0.9%	40.6 Å	15
4.0%	13.5 Å	6
11.2%	9.6 Å	4

(36 Å), such that one *F* center may overlap two or more Co cations and induce ferromagnetic ordering. At higher Co concentrations (> 5%), ferromagnetic ordering vanishes and Co:STO becomes nominally non-magnetic. As the Co doping concentration increases, the proximity of neighboring Co atoms increases as illustrated in Table 5.5; as Co atoms become second-nearest-neighbors separated by oxygen anions, strong local antiferromagnetic coupling of Co-O-Co can overcome the long-range ferromagnetic ordering induced by *F* centers, resulting in a reduction in the overall ferromagnetic ordering. This decrease in the apparent ferromagnetic moment per Co atom as the Co concentration is increased is observed in Figure 5.15. At a critical doping concentration, which appears to be approximately $5\%_{PIXE}$ for Co:STO, antiferromagnetic coupling of neighboring Co atoms overcomes the long-range ferromagnetic ordering, and the films appear non-magnetic. Thus, only for very low Co doping concentrations will strong ferromagnetism be observed, and increasing the Co concentration is detrimental to the ferromagnetic properties.

Summary

To evaluate the potential DMS properties of Co-doped STO for integration into future Si-based spintronic devices, homoepitaxial Co:STO was deposited on STO(001) substrates. Smooth epitaxial films were obtained which were free of large

surface particles or clusters. Although obtaining the desired stoichiometry control in the host STO lattice was difficult, variations in Sr / Ti did not significantly affect the measured film properties. XANES and EXAFS results indicate Co(II) substitutes for Ti in the STO lattice without evidence of Co(0), although the detailed local environment for Co appears to change with increasing Co concentration. Co:STO films with a Co concentration < $5\%_{PIXE}$ are ferromagnetic at room temperature. To fully understand the magnetic results, accurate quantification of the Co content in Co:STO is necessary. PIXE was utilized to determine the relative Co concentration, although the observed errors in the measurement technique prevented the determination of the absolute Co content. Due to this, the magnetic moment per Co atom could not be calculated with confidence, although it appears to be large, indicating Co(II) may be in a high spin configuration. *F*-center mediated exchange (FCE) was proposed as the mechanism of magnetism in these insulating films. To maintain charge neutrality, an oxygen vacancy with two trapped electrons forms for each Co(II) substituted for Ti(IV); these trapped electrons act as an *F* center with an estimated electron radius of 18 Å. Interaction of these electrons with neighboring Co cations can induce magnetic ordering. As the Co content was increased, antiferromagnetic ordering acted to reduce the observed moment per Co atom, and ferromagnetic ordering vanished in favor of antiferromagnetic ordering at approximately $5\%_{PIXE}$ Co. Based on these results, STO doped with less than 5% Co is a promising candidate as a potential DMS material for utilization in future spintronic devices.

Notes to Chapter V

1. J.S. Lee, Z.G. Khim, Y.D. Park, D.P. Norton, N. Theodoropoulou, A.F. Hebard, J.D. Budai, L.A. Boatner, S.J. Pearton, and R.G. Wilson, "Magnetic properties of Co- and Mn-implanted $BaTiO_3$, $SrTiO_3$, and $KTaO_3$." *Solid State Electron.* **47**, 2225 (2003).

2. H. Nakayama and H. Katayama-Yoshida, "Theoretical prediction of magnetic properties of $Ba(Ti_{1-x}M_x)O_3$ (M = Sc, V, Cr, Mn, Fe, Co, Ni, Cu)." *Jpn. J. Appl. Phys. Part 2* **40** (12B), L1355 (2001).

3. Y.G. Zhao, S.R. Shinde, S.B. Ogale, J. Higgins, R.J. Choudhary, V.N. Kulkarni, R.L. Greene, T. Venkatesan, S.E. Lofland, C. Lanci, J.P. Buban, N.D. Browning, S. Das Sarma, and A.J. Millis, "Co-doped $La_{0.5}Sr_{0.5}TiO_{3-\delta}$: diluted magnetic oxide system with high Curie temperature." *Appl. Phys. Lett.* **83** (11), 2199 (2003).

4. S.A. Chambers, S.M. Heald, and T. Droubay, "Local Co structure in epitaxial $Co_xTi_{1-x}O_{2-x}$ anatase." *Phys. Rev. B* **67**, 100401 (2003).

5. J.H. Haeni, C.D. Theis, and D.G. Schlom, "RHEED intensity oscillations for the stoichiometric growth of $SrTiO_3$ thin films by reactive molecular beam epitaxy." *J. Electroceram.* **4** (2/3), 385 (2000).

6. S.A. Chambers, S. Thevuthasan, R.F.C Farrow, R.F. Marks, J.U. Thiele, L. Folks, M.G. Samant, A.J. Kellock, N. Ruzycki, D.L. Ederer, and U. Diebold, "Epitaxial growth and properties of ferromagnetic Co-doped TiO_2 anatase." *Appl. Phys. Lett.* **79** (21), 3467 (2001).

7. M. Pouchard, A. Villesuzanne, and J.-P. Doumerc, "Spin state behavior in some cobaltites (III) and (IV) with perovskite or related structure." *J. Solid State Chem.* **162**, 282 (2001).

8. R.D. Shannon and C.T. Prewitt, "Effective ionic radii in oxides and fluorides." *Acta Cryst.* **B25**, 925 (1969).

9. R.D. Shannon, "Revised effective ionic radii and systematic studies of interatomic distances in halides and chalcogenides." *Acta Cryst.* **A32**, 751 (1976).

10. H. Taguchi, M. Shimada, and M. Koizumi, "Magnetic properties in the system $La_{1-x}Sr_xCoO_3$ ($0.5<x<1.0$)." *Mater. Res. Bull.* **13**, 1225 (1978).

11. R.H. Potze, G.A. Sawatzky, and M. Abbate, "Possibility for an intermediate-spin ground state in the charge-transfer material $SrCoO_3$." *Phys. Rev. B* **51** (17), 11501 (1995).

12. T. Suzuki, Y. Nishi, and M. Fujimoto, "Defect structure in homoepitaxial non-stoichiometric strontium titanate thin films." *Philos. Mag. A* **80** (3), 621 (2000).

13. C. Kittel, *Introduction to Solid State Physics*, Seventh ed. (John Wiley and Sons, New York, 1996).

14. P.D. Battle, T.C. Gibb, and A.T. Steel, "A structural comparison of the two polymorphs of $Sr_2Co_2O_5$ by cobalt K-edge extended x-ray absorption fine structure spectroscopy." *J. Chem. Soc. Dalton Trans.*, 2359 (1987).

15. T. Jiang and D.E. Ellis, "X-ray absorption near edge structure in cobalt oxides." *J. Mater. Res.* **11** (9), 2242 (1996).

16. M.S. Park, S.K. Kwon, and B.I. Min, "Electronic structures of doped anatase TiO_2: $Ti_{1-x}M_xO_2$ (M = Co, Mn, Fe, Ni)." *Phys. Rev. B* **65**, 161201 (2002).

17. J.M.D Coey, A.P. Douvalis, C.B. Fitzgerald, and M. Venkatesan, "Ferromagnetism in Fe-doped SnO_2 thin films."*Appl. Phys. Lett.* **84** (8), 1332 (2004).

18. S. Das Sarma, E.H. Hwang, and A. Kaminski, "How to make semiconductors ferromagnetic: a first course on spintronics." *Solid State Commun.* **127**, 99 (2003).

19. D.R. Lide, ed. *CRC Handbook of Chemistry and Physics*, 84th ed. (CRC Press, 2003).

20. J.H. Haeni, A.M. Ellis, D.G. Schlom, S.A. Chambers, J. Schottenfeld, T.E. Mallouk, J. Robertson, W. Tian, and X.Q. Pan, "Band structure of Sr_2TiO_4 / $SrTiO_3$ heterojunctions." *Appl. Phys. Lett.* submitted (2004).

CHAPTER VI: CONCLUSIONS

Deposition of the semiconducting oxides anatase TiO_2 and perovskite $SrTiO_3$ (STO) doped with the magnetic transition metal dopant Co was explored utilizing molecular beam epitaxy (MBE) in an effort to achieve a dilute magnetic semiconductor (DMS) system with desirable materials and magnetic properties for application in future spintronic devices. DMS materials would find wide application in future spintronic devices, in which the electron spin would be utilized to carry and store information. For successful integration into proposed spintronic devices, a prospective DMS material must have a uniform dopant distribution within the semiconductor lattice without the presence of secondary phases, and the dopant must ferromagnetically order such that the semiconductor carriers are spin-polarized. Compatibility with Si requires the DMS material to be deposited under mildly oxidizing conditions to protect the Si interface from oxidation.

Anatase TiO_2 doped with Co and deposited on oxide substrates such as $LaAlO_3$ has received significant attention as a ferromagnetic semiconductor, although it has not been definitively shown to be a true DMS possessing spin-polarized carriers. In this work, epitaxial Co-doped anatase TiO_2 was deposited on Si(001) substrates. To protect the Si interface from SiO_x and Ti silicide formation which would destroy the epitaxial template, a buffer layer of epitaxial STO was employed. Oxidation resistance of the interface during the buffer layer deposition was achieved with a ¼ or ½ ML Sr metal deposited on the clean Si surface at elevated temperature to form a Sr silicide layer. With this method, 10 ML (39 Å) of STO could be deposited without oxidation of the Si interface. Deposition of Co-doped anatase TiO_2 was explored on this heterostructure utilizing the oxygen plasma. While use of the oxygen plasma was expected (and later confirmed) to result in significant oxidation of the Si interface during deposition, it was pursued in an effort to fully oxidize the Co dopant. Despite this, the charge state of Co in the doped anatase films was found

to be a mixture of Co(0), Co(II), and Co(III). The distribution of Co in the three oxidation states appears to depend on the Co dopant concentration and deposition conditions in a complex way. Although secondary phases were not observed by XRD or TEM, Co-enriched surface particles were observed on all films. For low Co concentrations, the particles were found to have a square shape indicative of faceting. Although the Co:TiO_2 films were found to be ferromagnetic at room temperature, ferromagnetism of a true Co-doped anatase DMS phase could not be conclusively identified amid the contributions from Co(0) and other possible secondary phases. The inability to fully oxidize Co to Co(II) and incorporate it uniformly into the anatase lattice, even under oxidizing conditions known to be detrimental to the Si interface, preclude the use of Co-doped anatase TiO_2 as a DMS material in future spintronic devices based on Si technology.

As an alternative, Co-doped $SrTiO_3$ (STO) was investigated and was found to be significantly more promising as a potential DMS material. Epitaxial STO can be deposited on Si without oxidation of the Si interface, making STO-based DMS materials an ideal candidate for integration with future Si-based spintronic devices. As an initial evaluation of Co:STO, epitaxial films were deposited on single crystal STO(001) substrates by MBE. Smooth films free of particles or clusters were obtained for all Co doping concentrations. Evidence from XRD, XANES, and preliminary EXAFS fitting corroborated the substitution of Co(II) for Ti(IV) in the STO lattice, with no evidence of Co(0). Co-doped STO films were found to be ferromagnetic at room temperature for doping concentrations less than approximately $5\%_{PIXE}$ Co. The magnetic moment per Co atom appears to be high, although difficulty in quantifying the Co content of the films prevented the determination of the exact magnetic moment values. In the absence of a significant quantity of free carriers in these insulating films ($\rho > 5$ kΩ·cm), *F*-center mediated exchange was proposed as the mechanism of ferromagnetic ordering. The ferromagnetic moment per Co atom appeared to decrease with increasing Co concentration, and

ferromagnetic hysteresis was not observed for Co:STO films doped with > $5\%_{PIXE}$ Co. This was speculated to be due to short-range antiferromagnetic ordering which is favored over long-range ferromagnetic ordering as the Co-Co distance decreases. From these preliminary results, Co:STO is considered a promising candidate as a DMS material integrated with Si.

There are several further avenues of interest to explore in the Co:STO system. Elucidation of the unusual mechanism of room temperature ferromagnetism in insulating Co:STO films, as well as the function of both Co doping and free carrier concentration, is of both scientific and practical interest. Further evaluation of Co:STO is necessary to establish it as a true DMS with a spin-polarized free carrier population. Finally, the successful deposition of Co:STO on Si must be demonstrated before it can be considered for integration into future Si-based spintronic devices. The integration of ferromagnetic oxide materials on Si presents many challenges due to the dual requirements of complete oxidation of the film while simultaneously avoiding oxidation of the Si interface. These challenges were demonstrated by Co:TiO_2, which showed promising properties when deposited on oxide substrates but proved impossible to successfully integrate onto Si. The demonstrated procedure to deposit STO on Si without oxidation of the interface implies that Co:STO has a significantly better chance of overcoming these challenges.

LIST OF REFERENCES

P. Ahmet, T. Koida, M. Takakura, K. Nakajima, M. Yoshimoto, H. Koinuma, M. Tanaka, M. Takeguchi, and T. Chikyow, "Diffusion induced amorphization in the crystalline $SrTiO_3$ thin films grown on Si(100) investigated by combinatorial method." *Appl. Surf. Sci.* **189**, 307 (2002).

N.W. Ashcroft and N.D. Mermin, *Solid State Physics*. (Saunders College, Philadelphia, 1976).

J. Asmussen, "Electron cyclotron resonance microwave discharges for etching and thin film deposition," in *Handbook of Plasma Processing Technology*, edited by S.M. Rossnagel, J.J. Cuomo, and W.D. Westwood (Noyes Publications, Park Ridge, NJ, 1990).

D.D. Awschalom, M.E. Flatte, and N. Samarth, "Spintronics." *Sci. Am.* **286** (6), 66 (2002).

D.D. Awschalom, D. Loss, and N. Samarth, ed. *Semiconductor Spintronics and Quantum Computation*. (Springer-Verlag, New York, 2002).

M.N. Baibich, J.M. Broto, A. Fert, F. Nguyen Van Dau, F. Petroff, P. Eitenne, G. Creuzet, A. Friederich, and J. Chazelas, "Giant magnetoresistance of (001)Fe/(001)Cr magnetic superlattices." *Phys. Rev. Lett.* **61** (21), 2472 (1988).

P.D. Battle, T.C. Gibb, and A.T. Steel, "A structural comparison of the two polymorphs of $Sr_2Co_2O_5$ by cobalt K-edge extended x-ray absorption fine structure spectroscopy." *J. Chem. Soc. Dalton Trans.*, 2359 (1987).

J.P. Becker, R.G. Long, and J.E. Mahan, "Reflection high-energy electron diffraction patterns of carbide-contaminated silicon surfaces." *J. Vac. Sci. Technol. A* **12** (1), 174 (1994).

D.K. Bowen and B.K. Tanner, *High Resolution X-ray Diffractometry and Topography*. (Taylor and Francis, Philadelphia, 1998).

D. Briggs and M.P. Seah, *Practical Surface Analysis by Auger and X-ray Photoelectron Spectroscopy*. (John Wiley and Sons, New York, 1984).

C.R. Brundle, C.A. Evans Jr., S. Wilson, and L.E. Fitzpatrick, ed. *Encyclopedia of Materials Characterization*. (Butterworth-Heinemann, Boston, 1992).

M. Catti and G. Sandrone, "Ab initio study of corundum-like Me_2O_3 oxides (Me = Ti, V, Cr, Fe, Co, Ni)." *Faraday Discuss.* **106**, 189 (1997).

S.A. Chambers, Y. Liang, Z. Yu, R. Droopad, J. Ramdani, and K. Eisenbeiser, "Band discontinuities at epitaxial $SrTiO_3$/Si(001) heterojunctions." *Appl. Phys. Lett.* **77** (11), 1662 (2000).

S.A. Chambers, S. Thevuthasan, R.F.C Farrow, R.F. Marks, J.U. Thiele, L. Folks, M.G. Samant, A.J. Kellock, N. Ruzycki, D.L. Ederer, and U. Diebold, "Epitaxial growth and properties of ferromagnetic Co-doped TiO_2 anatase." *Appl. Phys. Lett.* **79** (21), 3467 (2001).

S.A. Chambers, Y. Liang, Z. Yu, R. Droopad, and J. Ramdani, "Band offset and structure of $SrTiO_3$/Si(001) heterojunctions." *J. Vac. Sci. Technol. A* **19** (3), 934 (2001).

S.A. Chambers, C.M. Wang, S. Thevuthasan, T. Droubay, D.E. McCready, A.S. Lea, V. Shutthanandan, and C.F. Windish Jr., "Epitaxial growth and properties of MBE-grown ferromagnetic Co-doped TiO_2 anatase films on $SrTiO_3$(001) and $LaAlO_3$(001)." *Thin Solid Films* **418**, 197 (2002).

S.A. Chambers, "A potential role in spintronics." *Materials Today*, 34 (2002).

S.A. Chambers, T. Droubay, C.M. Wang, A.S. Lea, R.F.C. Farrow, L. Folks, V. Deline, and S. Anders, "Clusters and magnetism in epitaxial Co-doped TiO_2 anatase." *Appl. Phys. Lett.* **82** (8), 1257 (2003).

S.A. Chambers and R.F.C. Farrow, "New possibilities for ferromagnetic semiconductors." *MRS Bull.* **28** (10), 729 (2003).

S.A. Chambers, S.M. Heald, and T. Droubay, "Local Co structure in epitaxial $Co_xTi_{1-x}O_{2-x}$ anatase." *Phys. Rev. B* **67**, 100401 (2003).

C.-W. Chen, *Magnetism and Metallurgy of Soft Magnetic Materials*. (Dover Publications, Inc., New York, 1986).

J.M.D Coey and C.L. Chien, "Half-metallic ferromagnetic oxides." *MRS Bull.* **28** (10), 720 (2003).

J.M.D Coey, A.P. Douvalis, C.B. Fitzgerald, and M. Venkatesan, "Ferromagnetism in Fe-doped SnO_2 thin films." *Appl. Phys. Lett.* **84** (8), 1332 (2004).

B.D. Cullity, *Elements of X-ray Diffraction*, Second ed. (Addison-Wesley, Menlo

Park, 1978).

A.M. Dabiran, S.M. Seutter, and P.I. Cohen, "Direct observations of the strain-limited island growth of Sn-doped GaAs(100)." *Surf. Rev. Lett.* **5** (3), 783 (1998).

S. Das Sarma, "Spintronics." *Am. Sci.* **89** (6), 516 (2001).

S. Das Sarma, E.H. Hwang, and A. Kaminski, "How to make semiconductors ferromagnetic: a first course on spintronics." *Solid State Commun.* **127**, 99 (2003).

S. Datta and B. Das, "Electronic analog of the electro-optic modulator." *Appl. Phys. Lett.* **56** (7), 665 (1990).

J. Daughton, "Spin-dependent sensors." *Proc. IEEE* **91** (5), 681 (2003).

F.B. de Mongeot, W. Zhu, A. Molle, R. Buzio, C. Boragno, U. Valbusa, E.G. Wang, and Z. Zhang, "Nanocrystal formation and faceting instability in Al(110) homoepitaxy: true upward adatom diffusion at step edges and island corners." *Phys. Rev. Lett.* **91** (1), 016102 (2003).

U. Diebold, "The surface science of titanium dioxide." *Surf. Sci. Rep.* **48** (5-8), 53 (2003).

T. Dietl, A. Haury, and Y. Merle d'Aubigne, "Free carrier-induced ferromagnetism in structures of diluted magnetic semiconductors." *Phys. Rev. B* **55** (6), R3347 (1997).

T. Dietl, H. Ohno, F. Matsukura, J. Cibert, and D. Ferrand, "Zener model description of ferromagnetism in zinc-blende magnetic semiconductors." *Science* **287**, 1019 (2000).

T. Dietl, "Ferromagnetic semiconductors." *Semicond. Sci. Technol.* **17**, 377 (2002).

T. Dietl and H. Ohno, "Ferromagnetic III-V and II-IV semiconductors." *MRS Bull.* **28** (10), 714 (2003).

T. Dietl, "Functional ferromagnets." *Nat. Mater.* **2**, 646 (2003).

T. Droubay, S.M. Heald, V. Shutthanandan, S. Thevuthasan, S.A. Chambers, and J. Osterwalder, "Room-temperature ferromagnetism in Cr-doped TiO_2 anatase." *Appl. Phys. Lett.* submitted (2004).

K.W. Edmonds, K.Y. Wang, R.P. Campion, A.C. Neumann, N.R.S. Farley, B.L. Gallagher, and C.T. Foxon, "High-Curie-temperature $Ga_{1-x}Mn_xAs$ obtained by resistance-monitored annealing." *Appl. Phys. Lett.* **81** (26), 4991 (2002).

C.S. Fadley, "Basic concepts of x-ray photoelectron spectroscopy," in *Electron Spectroscopy Theory, Techniques, and Applications*, edited by C.R. Brundle and A.D. Baker (Pergamon Press, 1978), Vol. II.

L. Forro, O. Chauvet, D. Emin, L. Zuppiroli, H. Berger, and F. Levy, "High mobility of *n*-type charge carriers in large single crystals of anatase (TiO_2)." *J. Appl. Phys.* **75** (1), 633 (1994).

C.J. Forst, C.R. Ashman, K. Schwarz, and P.E. Blochl, "The interface between silicon and a high-*k* oxide."*Nature* **427**, 53 (2004).

T. Fukumura, Z. Jin, M. Kawasaki, T. Shono, T. Hasegawa, S. Koshihara, and H. Koinuma, "Magnetic properties of Mn-doped ZnO." *Appl. Phys. Lett.* **78** (7), 958 (2001).

J.A. Gerber, W.L. Burmester, and D.J. Sellmeyer, "Simple vibrating sample magnetometer." *Rev. Sci. Instrum.* **53** (8), 691 (1982).

W. Giriat and J.K. Furdyna, in *Diluted Magnetic Semiconductors*, edited by J.K. Furdyna and J. Kossut (Academic Press, Inc., San Diego, 1988), Vol. 25.

J.H. Haeni, C.D. Theis, and D.G. Schlom, "RHEED intensity oscillations for the stoichiometric growth of $SrTiO_3$ thin films by reactive molecular beam epitaxy." *J. Electroceram.* **4** (2/3), 385 (2000).

J.H. Haeni, C.D. Theis, D.G. Schlom, W. Tian, X.Q. Pan, H. Chang, I. Takeuchi, and X.-D. Xiang, "Epitaxial growth of the first five members of the $Sr_{n+1}Ti_nO_{3n+1}$ Ruddlesden-Popper homologous series." *Appl. Phys. Lett.* **78** (21), 3292 (2001).

J.H. Haeni, A.M. Ellis, D.G. Schlom, S.A. Chambers, J. Schottenfeld, T.E. Mallouk, J. Robertson, W. Tian, and X.Q. Pan, "Band structure of Sr_2TiO_4 / $SrTiO_3$ heterojunctions." *Appl. Phys. Lett.* submitted (2004).

D. Hagele, M. Oestreich, W.W. Ruhle, Nestle. N., and K. Eberl, "Spin transport in GaAs." *Appl. Phys. Lett.* **73** (11), 1580 (1998).

P.R. Hammar and M. Johnson, "Detection of spin-polarized electrons injected into a two-dimensional electron gas." *Phys. Rev. Lett.* **88** (6), 066806 (2002).

G.C. Han, Y.H. Wu, M. Tay, K.B. Li, Z.B. Guo, and T.C. Chong, "Epitaxial growth of ferromagnetic Co:TiO_2 thin films by co-sputtering." *J. Magn. Magn. Mater.* **268**, 159 (2004).

A.T. Hanbicki, B.T. Jonker, G. Itskos, G. Kioseoglou, and A. Petrou, "Efficient electrical spin injection from a magnetic metal/tunnel barrier contact into a semiconductor." *Appl. Phys. Lett.* **80** (7), 1240 (2002).

M. Hansen and K. Anderko, *Constitution of Binary Alloys*. (McGraw-Hill, New York, 1958).

L. Hilt Tisinger, R. Liu, J. Kulik, X. Zhang, J. Ramdani, and A.A. Demkov, "Ultraviolet-Raman studies of $SrTiO_3$ ultrathin films on Si." *J. Vac. Sci. Technol. B* **21** (1), 53 (2003).

N.H. Hong, W. Prellier, J. Sakai, and A. Hassini, "Fe- and Ni-doped TiO_2 thin films grown on $LaAlO_3$ and $SrTiO_3$ substrates by laser ablation." *Appl. Phys. Lett.* **84** (15), 2850 (2004).

N.H. Hong, J. Sakai, and A. Hassini, "Ferromagnetism at room temperature with a large magnetic moment in anatase V-doped TiO_2 thin films." *Appl. Phys. Lett.* **84** (14), 2602 (2004).

X. Hu, H. Li, Y. Wei, Z. Yu, D. Marshall, J. Edwards, R. Droopad, X. Zhang, A.A. Demkov, and K. Moore, "The interface of epitaxial $SrTiO_3$ on silicon: *in situ* and *ex situ* studies." *Appl. Phys. Lett.* **82** (2), 203 (2003).

Y. Ito, R.F. Klie, and N.D. Browning, "Atomic resolution analysis of the defect chemistry and microdomain structure of brownmillerite-type strontium cobaltite." *J. Am. Ceram. Soc.* **85** (4), 969 (2002).

H.J.F. Jansen, "Electronic structure calculations for magnetically ordered systems." *Phys. Today* **48** (4), 50 (1995).

J. Jaroszynski, T. Andrearczyk, G. Karczewski, J. Wrobel, T. Wojtowicz, E. Papis, E. Kaminska, A. Piotrowska, D. Popovic, and T. Dietl, "Ising quantum Hall ferromagnet in magnetically doped quantum wells." *Phys. Rev. Lett.* **89** (26), 266802 (2002).

S. Jeon, F.J. Walker, C.A. Billman, R.A. McKee, and H. Hwang, "Electrical characteristics of epitaxially grown $SrTiO_3$ on silicon for metal-insulator-semiconductor gate dielectric applications." *IEEE Electr. Device L.* **24** (4), 218 (2003).

T. Jiang and D.E. Ellis, "X-ray absorption near edge structure in cobalt oxides." *J. Mater. Res.* **11** (9), 2242 (1996).

S.A.E. Johansson, J.L. Campbell, and K.G. Malmqvist, ed. *Particle Induced X-ray Emission Spectrometry (PIXE)*. (John Wiley and Sons, New York, 1995).

B.T. Jonker, S.C. Erwin, A. Petrou, and A.G. Petukhov, "Electrical spin injection and transport in semiconductor spintronic devices." *MRS Bull.* **28** (10), 740 (2003).

B.T. Jonker, "Progress toward electrical spin injection of spin-polarized electrons into semiconductors." *Proc. IEEE* **91** (5), 727 (2003).

S.W. Jung, S.-J. An, G.-C. Yi, C.U. Jung, S.I. Lee, and S. Cho, "Ferromagnetic properties of $Zn_{1-x}Mn_xO$ epitaxial thin films." *Appl. Phys. Lett.* **80** (24), 4561 (2002).

M. Kawasaki, K Takahashi, T. Maeda, R. Tsuchiya, M. Shinohara, O. Ishiyama, T. Yonezawa, M. Yoshimoto, and H. Koinuma, "Atomic control of the $SrTiO_3$ crystal surface." *Science* **266**, 1540 (1994).

M. Kawasaki, A. Ohtomo, T. Arakane, K Takahashi, M. Yoshimoto, and H. Koinuma, "Atomic control of $SrTiO_3$ surface for perfect epitaxy of perovskite oxides." *App. Surf. Sci.* **107**, 102 (1996).

R.J. Kennedy and P.A. Stampe, "The influence of lattice mismatch and film thickness on the growth of TiO_2 on $LaAlO_3$ and $SrTiO_3$ substrates." *J. Cryst. Growth* **252**, 333 (2003).

V.V. Kharton, L. Shuangbao, A.V. Kovalevsky, and E.N. Naumovich, "Oxygen permeability of perovskites in the system $SrCoO_{3-\delta}$- $SrTiO_3$." *Solid State Ionics* **96**, 141 (1997).

J.M. Kikkawa and D.D. Awschalom, "Resonant spin amplification in *n*-type GaAs." *Phys. Rev. Lett.* **80** (19), 4313 (1998).

J.M. Kikkawa and D.D. Awschalom, "Lateral drag of spin coherence in gallium arsenide." *Nature* **397**, 139 (1999).

D.H. Kim, J.S. Yang, K.W. Lee, S.D. Bu, T.W. Noh, S.-J. Oh, Y.-W. Kim, J.-S. Chung, H. Tanaka, H.Y. Lee, and T. Kawai, "Formation of Co nanoclusters in epitaxial $Ti_{0.96}Co_{0.04}O_2$ thin films and their ferromagnetism." *Appl. Phys. Lett.* **81** (13), 2421 (2002).

D.H. Kim, J.S. Yang, Y.S. Kim, D.-W. Kim, T.W. Noh, S.D. Bu, Y.-W. Kim, Y.D. Park, S.J. Pearton, Y. Jo, and J.-G. Park, "Superparamagnetism in Co-ion-implanted anatase TiO_2 thin films and effects of postannealing." *Appl. Phys. Lett.* **83** (22), 4574 (2003).

D.H. Kim, J.S. Yang, K.W. Lee, S.D. Bu, D.-W. Kim, T.W. Noh, S.-J. Oh, Y.-W. Kim, J.-S. Chung, H. Tanaka, H.Y. Lee, T. Kawai, J.Y. Won, S.H. Park, and J.C. Lee, "Investigations on the nature of observed ferromagnetism and possible spin polarization in Co-doped anatase TiO_2 thin films."*J. Appl. Phys.* **93** (10), 6125 (2003).

J.-Y. Kim, J.-H. Park, B.-G. Park, H.-J. Noh, S.-J. Oh, J.S. Yang, D.H. Kim, S.D. Bu, T.-W. Noh, H.-J. Lin, H.-H. Hsieh, and C.T. Chen, "Ferromagnetism induced by clustered Co in Co-doped anatase TiO_2 thin films."*Phys. Rev. Lett.* **90** (1), 017401 (2003).

C. Kittel, *Introduction to Solid State Physics*, Seventh ed. (John Wiley and Sons, New York, 1996).

G. Koster, B.L. Kropman, G.J.H.M. Rijnders, D.H.A. Blank, and H. Rogalla, "Quasi-ideal strontium titanate crystal surfaces through formation of strontium hydroxide." *Appl. Phys. Lett.* **73** (20), 2920 (1998).

E.A. Kraut, R.W. Grant, J.R. Waldrop, and S.P. Kowalczyk, "Precise determination of the valence-band edge in x-ray photoemission spectra: Application to measurements of semiconductor interface potentials." *Phys. Rev. Lett.* **44** (24), 1620 (1980).

E.A. Kraut, R.W. Grant, J.R. Waldrop, and S.P. Kowalczyk, "Semiconductor core-level to valence-band maximum binding-energy differences: Precise determination by x-ray photoelectron spectroscopy." *Phys. Rev. B* **28** (4), 1965 (1983).

K.C. Ku, J. Potashnik, R.F. Wang, S.H. Chun, P. Schiffer, N. Samarth, M.J. Seong, A. Mascarenhas, E. Johnston-Halperin, R.C. Myers, A.C. Gossard, and D.D. Awschalom, "Highly enhanced Curie temperature in low-temperature annealed [Ga,Mn]As epilayers." *Appl. Phys. Lett.* **82** (14), 2302 (2003).

J.S. Lee, Z.G. Khim, Y.D. Park, D.P. Norton, N. Theodoropoulou, A.F. Hebard, J.D. Budai, L.A. Boatner, S.J. Pearton, and R.G. Wilson, "Magnetic properties of Co- and Mn-implanted $BaTiO_3$, $SrTiO_3$, and $KTaO_3$." *Solid State Electron.* **47**, 2225 (2003).

J. Lettieri, J.H. Haeni, and D.G. Schlom, "Critical issues in the heteroepitaxial growth of alkaline-earth oxides on silicon." *J. Vac. Sci. Technol. A* **20** (4), 1332 (2002).

J. Li, C.H. Sow, X.S. Rao, C.K. Ong, and D.N. Zheng, "Epitaxial growth and magnetic and electric properties of Co-doped TiO_2 thin films."*Eur. Phys. J. B* **32**, 471 (2003).

H. Li, X. Hu, Y. Wei, Z. Yu, X. Zhang, R. Droopad, A.A. Demkov, J. Edwards Jr., K. Moore, W. Ooms, J. Kulik, and P. Fejes, "Two-dimensional growth of high-quality strontium titanate thin films on Si." *J. Appl. Phys.* **93** (8), 4521 (2003).

Y. Liang, S. Gan, and M. Engelhard, "First step towards the growth of single-crystal oxides on Si: Formation of a two-dimensional crystalline silicate on Si(001)." *Appl. Phys. Lett.* **79** (22), 3591 (2001).

D.R. Lide, ed. *CRC Handbook of Chemistry and Physics*, 84th ed. (CRC Press, 2003).

F. Liu, S.E. Davenport, H.M. Evans, and M.G. Lagally, "Self-organized replication of 3D coherent island size and shape in multilayer heteroepitaxial films." *Phys. Rev. Lett.* **82** (2), 2528 (1999).

J.E. Mahan, K.M. Geib, G.Y. Robinson, and R.G. Long, "A review of the geometrical fundamentals of reflection high-energy electron diffraction with application to silicon surfaces." *J. Vac. Sci. Technol. B* **8** (5), 3692 (1990).

A. Manivannan, G. Glaspell, and M.S. Seehra, "Controlled transformation of paramagnetism to room-temperature ferromagnetism in cobalt-doped titanium dioxide." *J. Appl. Phys.* **94** (10), 6994 (2003).

A. Manivannan, M.S. Seehra, S.B. Majumder, and R.S. Katiyar, "Magnetism of Co-doped titania thin films prepared by spray pyrolysis." *Appl. Phys. Lett.* **83** (1), 111 (2003).

Y. Matsumoto, M. Murakami, T. Shono, T. Hasegawa, T. Fukumura, M. Kawasaki, P. Ahmet, T. Chikyow, S. Koshihara, and H. Koinuma, "Room-temperature ferromagnetism in transparent transition metal-doped titanium dioxide." *Science* **291**, 854 (2001).

Y. Matsumoto, R. Takahashi, M. Murakami, T. Koida, X.J. Fan, T. Hasegawa, T. Fukumura, M. Kawasaki, S. Koshihara, and H. Koinuma, "Ferromagnetism in

Co-doped TiO_2 rutile thin films grown by laser molecular beam epitaxy." *Jpn. J. Appl. Phys., Part 2: Lett.* **40** (11B), L1204 (2001).

Y. Matsumoto, M. Murakami, T. Hasegawa, T. Fukumura, M. Kawasaki, P. Ahmet, K. Nakajima, T. Chikyow, and H. Koinuma, "Structural control and combinatorial doping of titanium dioxide thin films by laser molecular beam epitaxy." *App. Surf. Sci.* **189**, 344 (2002).

Y. Matsumoto, H. Koinuma, T. Hasegawa, I. Takeuchi, F. Tsui, and Y.K. Yoo, "Combinatorial investigation of spintronic materials." *MRS Bull.* **28** (10), 734 (2003).

M. Mayer, ed. *SIMNRA User's Guide*. (Max-Planck-Institut fur Plasmaphysik, Germany).

R.A. McKee, F.J. Walker, and M.F. Chisholm, "Crystalline oxides on silicon: the first five monolayers." *Phys. Rev. Lett.* **81** (14), 3014 (1998).

R. Meyer, K. Szot, and R. Waser, "Restructuring the surface region of donor doped $SrTiO_3$ single crystals under oxidizing conditions." *Ferroelectrics* **224**, 323 (1999).

G.E. Moore, "Cramming more components onto integrated circuits." *Electronics* **38**, 114 (1965).

A.F. Morpurgo, J.P. Heida, T.M. Klapwijk, B.J. van Wees, and G. Borghs, "Ensemble-average spectrum of Aharonov-Bohm conductance oscillations: evidence for spin-orbit-induced Berry's phase." *Phys. Rev. Lett.* **80** (5), 1050 (1998).

Motorola Press Release, "Motorola produces world's first 4 MBit MRAM chip." *http://www.motorola.com/mediacenter/news/detail/0,,3158_2591_23,00.html* (Oct. 27, 2003).

V.F. Motsnyi, J. De Boeck, J. Das, W. Van Roy, G. Borghs, E. Goovaerts, and V.I. Safarov, "Electrical spin injection in a ferromagnet/tunnel barrier/ semiconductor heterostructure." *Appl. Phys. Lett.* **81** (2), 265 (2002).

H. Munekata, H. Ohno, S. von Molnar, A. Segmuller, L.L. Chang, and L. Esaki, "Diluted magnetic III-V semiconductors." *Phys. Rev. Lett.* **63** (17), 1849 (1989).

E.L. Nagaev, "Colossal-magnetoresistance materials: manganites and conventional

ferromagnetic semiconductors." *Phys. Rep.* **346**, 387 (2001).

H. Nakayama and H. Katayama-Yoshida, "Theoretical prediction of magnetic properties of $Ba(Ti_{1-x}M_x)O_3$ (M = Sc, V, Cr, Mn, Fe, Co, Ni, Cu)." *Jpn. J. Appl. Phys. Part 2* **40** (12B), L1355 (2001).

A. Nazmul, S. Sugahara, and M. Tanaka, "Ferromagnetism and high Curie temperature in semiconductor heterostructures with Mn δ-doped GaAs and *p*-type selective doping." *Phys. Rev. B* **67**, 241308 (2003).

M. Newville, Ravel. B., D. Haskel, J.J. Rehr, E.A. Stern, and Y. Yacoby, "Analysis of multple-scattering XAFS data using theoretical standards." *Physica B* **208&209**, 154 (1995).

M. Newville, "IFEFFIT: interactive XAFS analysis and FEFF fitting." *J. Synchrotron Radiat.* **8**, 322 (2001).

J. Nitta, F. Meijer, Y. Narita, and H. Takayanagi, "Gate voltage-dependent Aharanov-Bohm experiment in the presence of Rashba spin-orbit interaction." *Physica E* **6**, 318 (2000).

M. Oestreich, J. Hubner, D. Hagele, P.J. Klar, W. Heimbrodt, W.W. Ruhle, D.E. Ashenford, and B. Lunn, "Spin injection into semiconductors." *Appl. Phys. Lett.* **74** (9), 1251 (1999).

C. Ohly, S. Hoffmann, K. Szot, and R. Waser, "High temperature conductivity behavior of doped $SrTiO_3$ thin films."*Integr. Ferroelectr.* **33**, 363 (2001).

H. Ohno, A. Shen, F Matsukura, A. Oiwa, A. Endo, S. Katsumoto, and Y. Iye, "(Ga,Mn)As: A new diluted magnetic semiconductor based on GaAs." *Appl. Phys. Lett.* **69** (3), 363 (1996).

H. Ohno, "Making nonmagnetic semiconductors ferromagnetic." *Science* **281**, 951 (1998).

Y. Ohno, D.K. Young, B. Beschoten, F Matsukura, H. Ohno, and D.D. Awschalom, "Electrical spin injection in a ferromagnetic semiconductor heterostructure." *Nature* **402** (6763), 790 (1999).

P.A. Packan, "Pushing the limits." *Science* **285** (5436), 2079 (1999).

C. Palmstrom, "Epitaxial Heusler alloys: new materials for semiconductor spintronics." *MRS Bull.* **28** (10), 725 (2003).

W.K. Park, R.J. Ortega-Hertogs, J.S. Moodera, A. Punnoose, and M.S. Seehra, "Semiconducting and ferromagnetic behavior of sputtered Co-doped TiO_2 thin films above room temperature." *J. Appl. Phys.* **91** (10), 8093 (2002).

M.S. Park, S.K. Kwon, and B.I. Min, "Electronic structures of doped anatase TiO_2: $Ti_{1-x}M_xO_2$ (M = Co, Mn, Fe, Ni)." *Phys. Rev. B* **65**, 161201 (2002).

P.W. Peacock and J. Robertson, "Structure, bonding, and band offsets of (100) $SrTiO_3$-silicon interfaces." *Appl. Phys. Lett.* **83** (26), 5497 (2003).

S.J. Pearton, C.R. Abernathy, M.E. Overberg, G.T. Thaler, D.P. Norton, N. Theodoropoulou, A.F. Hebard, Y.D. Park, F. Ren, J. Kim, and L.A. Boatner, "Wide band gap ferromagnetic semiconductors and oxides." *J. Appl. Phys.* **93** (1), 1 (2003).

S.J. Pearton, M.E. Overberg, G.T. Thaler, C.R. Abernathy, J. Kim, F. Ren, N. Theodoropoulou, A.F. Hebard, and Y.D. Park, "Room temperature ferromagnetism in GaMnN and GaMnP." *Phys. Stat. Sol. (a)* **195** (1), 222 (2003).

R.H. Potze, G.A. Sawatzky, and M. Abbate, "Possibility for an intermediate-spin ground state in the charge-transfer material $SrCoO_3$." *Phys. Rev. B* **51** (17), 11501 (1995).

M. Pouchard, A. Villesuzanne, and J.-P. Doumerc, "Spin state behavior in some cobaltites (III) and (IV) with perovskite or related structure." *J. Solid State Chem.* **162**, 282 (2001).

W. Prellier, A. Fouchet, and B. Mercey, "Oxide-diluted magnetic semiconductors: a review of the experimental status." *J. Phys.-Condens. Mat.* **15**, R1583 (2003).

G.A. Prinz, "Magnetoelectronics." *Science* **282**, 1660 (1998).

A.P. Ramirez, "Colossal magnetoresistance." *J. Phys.-Condens. Mat.* **9**, 8171 (1997).

C.N.R. Rao and B. Raveau, *Transition Metal Oxides Structure, Properties, and Synthesis of Ceramic Oxides*, 2nd ed. (Wiley-VCH, New York, 1998).

E.I. Rashba, "Theory of electrical spin injection: Tunnel contacts as a solution of the conductivity mismatch problem." *Phys. Rev. B* **62** (24), R16267 (2000).

M.L. Reed, N.A. El-Masry, H.H. Stadelmaier, M.K. Ritums, M.J. Reed, C.A. Parker, J.C. Roberts, and S.M. Bedair, "Room temperature ferromagnetic properties

of (Ga,Mn)N." *Appl. Phys. Lett.* **79** (21), 3473 (2001).

J.J. Rehr and R.C. Albers, "Theoretical approaches to x-ray absorption fine structure." *Rev. Mod. Phys.* **72** (3), 621 (2000).

L. Reimer, *Transmission Electron Microscopy Physics of Image Formation and Microanalysis.* (Springer-Verlag, New York, 1984).

G.V. Samsonov, ed. *The Oxide Handbook.* (IFI/Plenum, New York, 1973).

K. Sato and H. Katayama-Yoshida, "Stabilization of ferromagnetic states by electron doping in Fe-, Co- or Ni-doped ZnO." *Jpn. J. Appl. Phys., Part 2: Lett.* **40** (4A), L334 (2001).

K. Sato and H. Katayama-Yoshida, "First principles materials design for semiconductor spintronics." *Semicond. Sci. Technol.* **17**, 367 (2002).

Scanning Probe Microscopy Training Notebook. (Digital Instruments).

G. Schmidt, D. Ferrand, L.W. Molencamp, A.T. Filip, and B.J. van Wees, "Fundamental obstacle for electrical spin injection from a ferromagnetic metal into a diffusive semiconductor." *Phys. Rev. B* **62** (8), R4790 (2000).

L.M.R. Scolfaro, "Phase separation in cubic Group-III nitride alloys." *Phys. Stat. Sol. (a)* **190** (1), 15 (2002).

N.-J. Seong, S.-G. Yoon, and C-R. Cho, "Effects of Co-doping level on the microstructural and ferromagnetic properties of liquid-delivery metalorganic-chemical-vapor-deposited $Ti_{1-x}Co_xO_2$ thin films." *Appl. Phys. Lett.* **81** (22), 4209 (2002).

R.D. Shannon and C.T. Prewitt, "Effective ionic radii in oxides and fluorides." *Acta Cryst.* **B25**, 925 (1969).

R.D. Shannon, "Revised effective ionic radii and systematic studies of interatomic distances in halides and chalcogenides." *Acta Cryst.* **A32**, 751 (1976).

P. Sharma, A. Gupta, K.V. Rao, F.J. Owens, R. Sharma, R. Ahuja, J.M. Osorio Guillen, B. Johansson, and G.A. Gehring, "Ferromagnetism above room temperature in bulk and transparent thin films of Mn-doped ZnO." *Nat. Mater.* **2** (10), 673 (2003).

I.-B. Shim, S.-Y. An, C.S. King, S.-Y. Choi, and Y.W. Park, "Growth of

ferromagnetic semiconducting cobalt-doped anatase titanium thin films." *J. Appl. Phys.* **91** (10), 7914 (2002).

S.R. Shinde, S.B. Ogale, S. Das Sarma, J.R. Simpson, H.D. Drew, S.E. Lofland, C. Lanci, J.P. Buban, N.D. Browning, V.N. Kulharni, J. Higgins, R.P. Sharma, R.L. Greene, and T. Venkatesan, "Ferromagnetism in laser deposited anatase $Ti_{1-x}Co_xO_{2-\delta}$ films." *Phys. Rev. B.* **67**, 115211 (2003).

V. Shutthanandan, S. Thevuthasan, S.M. Heald, T. Droubay, M.H. Engelhard, T.C. Kaspar, D.E. McCready, L. Saraf, S.A. Chambers, B.S. Mun, N. Hamdan, P. Nachimuthu, B. Taylor, R.P. Sears, and B. Sinkovic, "Room temperature ferromagnetism in ion-implanted Co-doped TiO_2(110) rutile." *Appl. Phys. Lett.* **84** (22) 4466 (2004).

R. Singh, D. Doppalapudi, T.D. Moustakas, and L.T. Romano, "Phase separation in InGaN thick films and formation of InGaN/GaN double heterostructures in the entire alloy composition." *Appl. Phys. Lett.* **70** (9), 1089 (1997).

Y.L. Soo, G. Kioseoglou, S. Kim, Y.H. Kao, P. Sujatha Devi, J. Parise, R.J. Gambino, and P.I. Gouma, "Local environment surrounding magnetic impurity atoms in a structural phase transition of Co-doped TiO_2 nanocrystal ferromagnetic semiconductors." *Appl. Phys. Lett.* **81** (4), 655 (2002).

N. Spaldin, *Magnetic Materials: Fundamentals and Device Applications*. (University Press, Cambridge, 2003).

D. Speliotis, "Getting the most from your vibrating sample magnetometer." (ADE Technologies, Inc.).

P.A. Stampe, R.J. Kennedy, Y. Xin, and J.S. Parker, "Investigation of the cobalt distribution in the room temperature ferromagnet TiO_2:Co." *J. Appl. Phys.* **93** (10), 7864 (2003).

J. Stohr, *NEXAFS Spectroscopy*. (Springer-Verlag, New York, 1992).

R.M. Stroud, A.T. Hanbicki, Y.D. Park, G. Kioseoglou, A.G. Petukhov, B.T. Jonker, G. Itskos, and A. Petrou, "Reduction of spin injection efficiency by interface defect spin scattering in ZnMnSe / AlGaAs-GaAs spin-polarized light-emitting diodes." *Phys. Rev. Lett.* **89** (16), 166602 (2002).

Sugiharto, S. Yamamoto, T. Sumita, and A. Miyashita, "Preparation of TiO_2-anatase film on Si(001) substrate with TiN and $SrTiO_3$ as buffer layers." *J. Phys. Condens. Matter* **13**, 2875 (2001).

J.M. Sullivan and S.C. Erwin, "Theory of dopants and defects in Co-doped TiO_2 anatase." *Phys. Rev. B* **67**, 144415 (2003).

T. Suzuki, Y. Nishi, and M. Fujimoto, "Defect structure in homoepitaxial non-stoichiometric strontium titanate thin films." *Philos. Mag. A* **80** (3), 621 (2000).

K. Szot, W. Speier, J. Herion, and Ch. Freiburg, "Restructuring of the surface region in $SrTiO_3$." *Appl.Phys. A* **64**, 55 (1997).

A. Tabata, L.K. Teles, L.M.R. Scolfaro, J.R. Leite, A. Kharchenko, T. Frey, D.J. As, D. Schikora, K. Lischka, J. Furthmuller, and F. Bechstedt, "Phase separation suppression in InGaN epitaxial layers due to biaxial strain." *Appl. Phys. Lett.* **80** (5), 769 (2002).

H. Taguchi, M. Shimada, and M. Koizumi, "Magnetic properties in the system $La_{1-x}Sr_xCoO_3$ ($0.5 \leq x \leq 1.0$)." *Mater. Res. Bull.* **13**, 1225 (1978).

J.R. Tesmer and M. Nastasi, ed. *Handbook of Modern Ion Beam Materials Analysis*. (Materials Research Society, Pittsburgh, 1995).

G.T. Thaler, M.E. Overberg, B. Gila, R. Frazier, C.R. Abernathy, S.J. Pearton, J.S. Lee, S.Y. Lee, Y.D. Park, and Z.G. Khim, "Magnetic properties of *n*-GaMnN thin films." *Appl. Phys. Lett.* **80** (21), 3964 (2002).

Y. Tokura, "Correlated-electron physics in transition-metal oxides." *Phys. Today* **56** (7), 50 (2003).

K.-N. Tu, J.W. Mayer, and L.C. Feldman, *Electronic Thin Film Science*. (Macmillan Publishing Company, New York, 1992).

A.C. Tuan, T.C. Kaspar, T. Droubay, J.W. Rogers Jr., and S.A. Chambers, "Band offsets for the epitaxial TiO2/SrTiO3/Si(001) system." *Appl. Phys. Lett.* **83** (18), 3734 (2003).

K. Ueda, H. Tabata, and K. Tomoji, "Magnetic and electric properties of transition-metal-doped ZnO films." *Appl. Phys. Lett.* **79** (7), 988 (2001).

J.C. Vickerman, ed. *Surface Analysis: The Principal Techniques*. (John Wiley and Sons, New York, 1997).

R.S. Williams, G. Medeiros-Ribeiro, T.I. Kamins, and D.A.A. Ohlberg, "Thermodynamics of the size and shape of nanocrystals: epitaxial Ge on

Si(001)." *Annu. Rev. Phys. Chem.* **51**, 527 (2000).

S.A. Wolf, D.D. Awschalom, R.A. Buhrman, J. Daughton, S. von Molnar, M.L. Roukes, A.Y. Chtchelkanova, and D.M. Treger, "Spintronics: a spin-based electronics vision for the future." *Science* **294**, 1488 (2001).

G.Y. Yang, J.M. Finder, J. Wang, Z.L. Wang, Z. Yu, J. Ramdani, R. Droopad, K.W. Eisenbeiser, and R. Ramesh, "Study of microstructure in $SrTiO_3$/Si by high-resolution transmission electron microscopy." *J. Mater. Res.* **17** (1), 204 (2002).

H.S. Yang, J. Choi, V. Craciun, and R.K. Singh, "Ferromagnetism of anatase $Ti_{1-x}Co_xO_{2-\delta}$ films grown by ultraviolet-assisted pulsed laser deposition." *J. Appl. Phys.* **93** (10), 7873 (2003).

Z. Yang, G. Liu, and R. Wu, "Distribution and magnetization of Co impurities in anatase TiO_2." *Phys. Rev. B* **67**, 060402 (2003).

H.S. Yang, J. Choi, S.-J. Song, and R.K. Singh, "Enhanced crystalline and magnetic properties of Co-doped TiO_2 films grown by ultraviolet-assisted pulsed laser deposition." *Electrochem. Solid St.* **7** (1), C4 (2004).

Z. Yu, J. Ramdani, J.A. Curless, C.D. Overgaard, J.M. Finder, R. Droopad, K.W. Eisenbeiser, J.A. Hallmark, and W.J. Ooms, "Epitaxial oxide thin films on Si(001)." *J. Vac. Sci. Technol. B* **18** (4), 2139 (2000).

M. Zajac, J. Gosk, E. Grzanda, M. Kaminska, A. Twardowski, B. Strojek, T. Szyszko, and S. Podsiadlo, "Possible origin of ferromagnetism in (Ga,Mn)N." *J. Appl. Phys.* **93** (8), 4715 (2003).

C. Zener, "Interaction between the *d* shells in the transition metals." *Phys. Rev.* **81** (4), 440 (1951).

C. Zener, "Interaction between the *d*-shells in the transition metals. II. Ferromagnetic compounds of manganese with perovskite structure." *Phys. Rev.* **82** (3), 403 (1951).

C. Zener, "Interaction between the *d*-shells of the transition metals. III. Calculation of the Weiss factors in Fe, Co, and Ni." *Phys. Rev.* **83** (2), 299 (1951).

Z. Zhang and M.G. Lagally, "Atomic scale mechanisms for surfactant-mediated layer-by-layer growth in homoepitaxy." *Phys. Rev. Lett.* **72** (5), 693 (1994).

Z. Zhang and M.G. Lagally, "Atomistic processes in the early stages of thin-film growth." *Science* **276**, 377 (1997).

X. Zhang, A.A. Demkov, H. Li, X. Hu, Y. Wei, and J. Kulik, "Atomic and electronic structure of the Si/$SrTiO_3$ interface." *Phys. Rev. B* **68**, 125323 (2003).

Y.G. Zhao, S.R. Shinde, S.B. Ogale, J. Higgins, R.J. Choudhary, V.N. Kulkarni, R.L. Greene, T. Venkatesan, S.E. Lofland, C. Lanci, J.P. Buban, N.D. Browning, S. Das Sarma, and A.J. Millis, "Co-doped $La_{0.5}Sr_{0.5}TiO_{3-\delta}$: diluted magnetic oxide system with high Curie temperature." *Appl. Phys. Lett.* **83** (11), 2199 (2003).

VITA

Tiffany Kaspar

Maiden name: Coulter

Education

University of Washington Seattle, WA
Doctor of Philosophy (Chemical Engineering), May 2004.

Fellowships
Joint Institute for Nanoscience Fellowship (2002-2004), National Science Foundation Fellowship (1999-2002), Achievement Rewards for College Scientists Fellowship (1998-2001), Henry L. Gray Memorial Fellowship (2000), Shell Oil Foundation Fellowship (1999)

University of Colorado Boulder, CO
Bachelor of Science with Honors, Chemical Engineering, May 1998.

Professional Societies

American Vacuum Society (1999-present)
American Institute of Chemical Engineers (2001-present)

Publications

V. Shutthanandan, S. Thevuthasan, S.M. Heald, T. Droubay, M.H. Engelhard, T.C. Kaspar, D.E. McCready, L. Saraf, S.A. Chambers, B.S. Mun, N. Hamdan, P. Nachimuthu, B.Taylor, R.P. Sears, B. Sinkovic. "Room temperature ferromagnetism in ion-implanted Co-doped TiO_2(110) rutile." *Applied Physics Letters* **84** (22) May 2004.

S.A. Chambers, T. Droubay, T.C. Kaspar, M. Gutowski. "Accurate valence band maximum determination for $SrTiO_3$(001)." *Surface Science Letters* **554** (2-3) 2004.

T.C. Kaspar, C.L. Aardahl, D.E. McCready, A.S. Lea, B.R. Johnson, D.W. Matson, T.S. Dory, J.W. Rogers, Jr. "Investigation of Cr as an alternative adhesion layer in Pt / Si electrodes for ferroelectric perovskites." Submitted to *Thin Solid Films* January 2004.

S.A. Chambers, T. Droubay, T.C. Kaspar, M. Gutowski. "Experimental determination of valence band maxima for $SrTiO_3$, TiO_2, and SrO and the associated valence band offsets with Si(001)." Submitted to *Journal of Vacuum Science and Technology B* January 2004.

A.C. Tuan, T.C. Kaspar, T. Droubay, J.W. Rogers, Jr., S.A. Chambers. "Band offsets for the epitaxial TiO_2 / $SrTiO_3$ / Si(001) system." *Applied Physics Letters* **83** (19) November 2003.

T. Kaspar, A. Tuan, R. Tonkyn, W. Hess, J.W. Rogers, Jr., Y. Ono. "The role of $O(^1D)$ in the oxidation of Si(100)." *Journal of Vacuum Science and Technology B* **21** (2) Mar/April 2003.

Tiffany Kaspar

Presentations

T.C. Kaspar, *et al.* "Materials characterization and magnetic studies of epitaxial $Co_xTi_{1-x}O_{2-x}$ deposited on Si(001) by molecular beam epitaxy." AVS 50th International Symposium in Baltimore, Maryland, November 2003. *Received the Leo M. Falicov Student Award from the Magnetic Interfaces and Nanostructures Division.*

T.C. Kaspar, *et al.*"Materials characterization of epitaxial TiO_2 and $Co_xTi_{1-x}O_{2-x}$ deposited on Si(001) by molecular beam epitaxy." Third Annual Nanoscale Science and Technology Workshop in Seattle, Washington, September 2003.

T. Kaspar, *et al.* "Investigation of the interfacial region of (Ba,Sr)TiO_3 thin films deposited on Pt substrates by MOCVD." AVS 49th International Symposium in Denver, Colorado, November 2002.

T. Coulter, *et al.* "Oxidation of Si(100) using photolytically-generated $O(^1D)$ and $O(^3P)$." 2001 Annual Meeting of the American Institute of Chemical Engineers in Reno, Nevada, November 2001.

T. Coulter, *et al.* "Non-thermal SiO_2 film growth on Si(100) using laser-generated $O(^1D)$ and $O(^3P)$." AVS 48th International Symposium in San Francisco, California, October 2001. *Received Thin Films Division Graduate Student Award.*